Computational modeling of bacterial chromosome organization: macromolecular crowding, chain heterogeneity, and chain cross-linking

by

Amir Hosein Sadeghi Isfahani

A thesis
presented to the University of Waterloo
in fulfillment of the
thesis requirement for the degree of
Doctor of Philosophy
in
Physics

Waterloo, Ontario, Canada, 2024

© Amir Hosein Sadeghi Isfahani 2024

Examining Committee Membership

The following served on the Examining Committee for this thesis. The decision of the Examining Committee is by majority vote.

External Examiner:	James Polson Professor, the Department of Physics University of Prince Edward Island
Supervisor:	Bae-Yeun Ha Professor, the Department of Physics and Astronomy University of Waterloo
Internal Member:	Russell Thompson Associate Professor, the Department of Physics and Astronomy University of Waterloo
Internal Member:	David Yevick Professor, the Department of Physics and Astronomy University of Waterloo
External Member:	Nasser Mohieddin Abukhdeir Associate Professor, the Department of Chemical Engineering University of Waterloo

Author's declaration

I hereby declare that I am the sole author of this thesis. This is a true copy of the thesis, including any required final revisions, as accepted by my examiners.

I understand that my thesis may be made electronically available to the public.

Abstract

Chromosome organization is integral to life, as it plays a pivotal role in maintaining the integrity and functionality of genomic materials, as well as facilitating the transcription, replication, and transmission of genetic information during cell division. Despite lacking membrane-based compartmentalization strategies, bacteria compactly organize their chromosomes within the nucleoid, an unpartitioned subcellular space, in a hierarchical manner. Due to this open-plan layout, macromolecular crowding (MMC) is an essential factor in bacterial chromosome organization. Indeed, it has been known that chain molecules in a crowded medium can undergo phase-separation, transitioning into collapsed states. However, the extent to which bacteria rely on MMC for organizing their chromosomes is not fully understood. Moreover, chromosomes exhibit structural heterogeneity, being decorated with various proteins such as the cross-linking protein histone-like nucleoid-structuring (H-NS) and the key transcription enzyme RNA polymerase (RNAP). The resulting chain heterogeneity can influence chromosome organization in a crowded medium, with MMC potentially modulating the effects of these proteins on their target chromosomal segments. A comprehensive understanding of chromosome organization would necessitate acquiring a fuller picture of how chain heterogeneity, MMC, and the action of DNA binding proteins (DBPs) are orchestrated in a confined space.

In this thesis, using molecular dynamics (MD) simulations, we study how biomolecular crowding, confinement, chain heterogeneity, and chain cross-linking affect the spatial organization of "chromosome-like" polymers. Our modeling efforts are inspired by the way Escherichia coli (E. coli) chromosomes are organized. For this, we start with a simple model and gradually improve our modelling strategy by incorporating more biological details. These efforts yield quantitative insights into some key observations such as the clustering of transcription-active units into a transcription factory as well as H-NS and crowder synergy in condensing bacterial chromosomes.

First, our homogeneous-polymer model establishes a relationship between its spatial organization and the distribution of the surrounding crowders under anisotropic (cylindrical) confinement. This effort extends the applicability of the previous findings for unconfined spaces to cell-like confined spaces: in a parameter space of biological relevance, the sum of the volume fractions of monomers and crowders, rescaled by their respective size, remains constant.

We then introduce chain heterogeneity, simulating the effects of transcription on an otherwise homogeneous polymer. The resulting polymer contains large monomers dispersed along the backbone with small ones in between. This effort demonstrates that the compaction transition by crowders is well correlated with the clustering: when the large monomers are of sufficient size, chain compaction and clustering of large monomers occur concomitantly at the same narrow (biologically-relevant) range of the crowder volume fraction. It also indicates that cylindrical confinement makes MMC effects more effective.

Finally, we study the action of H-NS protein and its impact on chromosome compaction. H-NS, modeled as a mobile "binder," can bind to a chromosome-like polymer. This effort elucidates how MMC and H-NS binding each play a part in compacting a bacterial chromosome, providing a quantitative understanding of the synergistic interactions between crowders and binders. Crowders intensify the binding of H-NS to the polymer, and conversely, the presence of H-NS improves the efficiency of MMC effects, indicating a bidirectional synergy in chain compaction. Additionally, we observe that the presence of crowders facilitates the clustering of binders, where the cluster size grows as the volume fraction of crowders increases.

This thesis outlines a physical framework where phase separation and clustering, driven by MMC, are identified as the principal mechanisms in bacterial chromosome organization.

Keywords: bacterial chromosome organization, chromosome-like polymers, molecular dynamics (MD) simulations, Escherichia coli (E. coli), macromolecular crowding, depletion force, confinement, transcription, RNA polymerase (RNAP), polymer heterogeneity, histone-like nucleoid-structuring (H-NS) protein, cross-linking, DNA binding proteins (DBPs).

Acknowledgements

I seize this moment to extend my heartfelt gratitude to everyone who contributed to the fruition of this thesis. At the forefront, my deepest appreciation goes to my supervisor, Professor Bae-Yeun Ha, whose encouragement, unwavering support, and invaluable advice have greatly enriched my personal and professional journey. Additionally, my gratitude extends to the members of my defense and advisory committee. Special thanks to Professor James Polson for graciously accepting the role of external examiner. I am equally grateful to Professors Russell Thompson, David Yevick, and Nasser Mohieddin Abukhdeir, whose insightful comments and constructive suggestions have significantly enhanced my work over the years. My acknowledgments would be incomplete without mentioning Dr. Chanil Jeon and Dr. Youngkyun Jung, who were instrumental in enhancing my computational skills.

A special expression of gratitude is dedicated to my wife, Behnaz, to whom this thesis is lovingly dedicated. Her unwavering love and companionship have been the warmth and light through the challenging journey of my Ph.D. This thesis would not have been a reality without her. Equally, my parents deserve my profound gratitude for providing an extraordinary foundation and support throughout my life, playing a pivotal role in shaping my intellect and character. My in-laws also earn my appreciation for their lasting support.

I have been fortunate to be encircled by an incredible circle of friends, whose presence has brought joy and richness to my life, sharing both its highs and lows. While it is impossible to name everyone, I wish to acknowledge a few who have significantly supported during my Ph.D. Journey: Javad, Najmeh, Ali, Soheila, Dara, Joe, and Mehrdad.

Finally, I would like thank the Natural Sciences and Engineering Research Council (NSERC) of Canada and the Digital Research Alliance of Canada for their computational resources, which was indispensable to my research.

Dedication

To Behnaz, my guiding light, and to our parents, whose love and support know no bounds, this thesis is lovingly dedicated.

Table of contents

Examining Committee Membership iii

Author's declaration v

Abstract vii

Acknowledgements ix

Dedication xi

List of tables xvii

List of figures xix

List of abbreviations xxiii

1 Introduction 1

1.1 Motivation and Goals . . . 1

1.2 Organization of the thesis . . . 4

1.3 Macromolecular crowding . . . 5

1.3.1 Crowded systems . . . 6

1.3.2 Nonspecific interactions in crowded media . . . 7

1.3.3 Crowded cellular environments in molecular simulations . . . 10

1.4 Chromosome organization hierarchy in bacteria . . . 11

1.4.1 DNA double-helical structure . . . 11

1.4.2 DNA supercoiling . . . 12

1.4.2.1 Supercoiling and the ring topology of bacterial chromosomes . . . 12

1.4.2.2 Linking number . . . 13

1.4.3 Plectonemic loops . . . 14

1.4.4 Structural units . . . 14

1.4.5 Chromosomal interaction domains . . . 16

1.4.6 Macrodomains . . . 18

1.4.7 The nucleoid . . . 19

2 Theoretical background: Physics of crowded systems 21

2.1 Equilibrium thermodynamics . . . 21

2.2 Equilibrium statistical mechanics . . . 22

2.2.1 Implicit-solvent picture . . . 24

2.2.1.1 Connection with the equilibrium thermodynamics . . . 26

2.2.2 Crowded systems with preferentially-excluded crowder-tracer interactions . . . 26
2.2.2.1 The binary mixture of hard spheres . . . 27
2.2.2.2 Depletion and MMC potentials . . . 28
2.2.2.3 Free volume theory . . . 28
2.2.2.4 Asakura-Oosawa theory . . . 29
2.2.2.5 The limitations of the AO theory . . . 31
2.2.3 Effective solvent picture . . . 33
3 The interdependence between the spatial organization of a biopolymer and the distribution of crowders under confinement 35
3.1 Introduction . . . 35
3.2 Computational modeling . . . 37
3.2.1 A polymer model . . . 37
3.2.2 Simulation method . . . 39
3.3 Results . . . 42
3.4 Discussion and conclusion . . . 52
4 Compaction and clustering of a heterogeneous polymer by biomolecular crowding 57
4.1 Introduction . . . 57
4.2 Computational modeling . . . 60
4.2.1 A heterogeneous chain model . . . 60
4.2.2 Clustering of large monomers . . . 62
4.2.3 Simulation method . . . 64
4.3 Results . . . 67
4.4 Discussion and conclusion . . . 82
5 Modeling the compaction of bacterial chromosomes: biomolecular crowding and the cross-linking protein H-NS 85
5.1 Introduction[1] . . . 85
5.2 Computational Modeling . . . 87
5.2.1 Model . . . 87
5.2.2 Simulation method . . . 89
5.3 Results . . . 95
5.4 Discussions and conclusion . . . 101
6 Concluding remarks and future considerations 105

[1]A brief version of this chapter, including some figures, is published in the journal *Scientific Reports*. For an electronic copy, see here: https://doi.org/10.1038/s41598-023-50355-2

6.1 Conclusions 105
6.2 Proposals 107
6.2.1 A heterogeneous branched ring polymer model of the bacterial chromosome 107
6.2.2 Compaction and organization of of a chromosome-like polymer: The interplay between MMC, H-NS oligomerization, and chain stiffness 109
Letter's of copyright permissions **113**
Bibliography **115**
Glossary **145**

List of tables

1.1 Heterogeneity of cellular species in E. coli: Variations in weight, size, and population 8
3.1 Input parameters for polymer-crowder system in cylindrical confinement . 41
5.1 Pair coefficients of the Lennard-Jones potential 91

List of figures

1.1 Electron micrograph of the Escherichia coli cell shows the nucleoid in the middle of the cell . . . 2
1.2 Heterogeneity of cellular species in Escherichia coli heterogeneity at three magnifications: Variations in type, shape, and size of cellular species . . . 7
1.3 Electron micrograph of the rosette-like E. coli chromosome with supercoiled DNA loops radiating from the central RNA-containing core . . . 15
1.4 Bacterial chromosome is segmented into approximately 30 chromosomal interaction domains with size ranging from 30 kbp to 430 kbp. . . . 17
1.5 (A) Spatial positioning of macrodomains in the E. coli cell (B) Volumetric display of chromosomal DNA in an E. coli cell . . . 18
2.1 Depletion interaction between two hard spheres . . . 30
3.1 A flexible polymer in a crowded cylindrical confinement . . . 38
3.2 The compaction of a cylindrically-confined chain as a function of the crowder volume fraction . . . 43
3.3 Compaction of a cylindrically-confined chain as a function of the crowder volume fraction for (A) $a_c = a$ and (B) $N = 2000$ . . . 45
3.4 Interdependence between the radial distributions of monomers and crowders under MMC conditions . . . 47
3.5 Longitudinal distributions of monomers and crowders under MMC conditions, illustrating anisotropic phase separation into monomer-rich and crowder-only phases . . . 49
3.6 Sum of rescaled radial volume fractions does not yield conclusive results about the applicability of the density sum rule along the radial direction under cylindrical confinement. . . . 51
3.7 Sum of rescaled longitudinal volume fractions, verifying the (density) sum rule holds under confinement for sufficiently large cylinder to crowder size ratios . . . 52
3.8 Sum of rescaled two-dimensional number densities, supporting the two-dimensional interpretation of the (density) sum rule under confinement for sufficiently large cylinder to crowder size ratios . . . 53

4.1 Schematic overview of the E. coli chromosome highlighting the transcription machinery's role in the bacterial chromosome's heterogeneity and organization. . . . 58
4.2 Clustering of large monomers due to MMC effects . . . 62
4.3 Size and configuration of clusters formed by large monomers . . . 63
4.4 Probability distribution function of spatial distance for different pairs of large monomers with the genomic distance $\Delta n_{\alpha\beta} = 161$ . . . 68
4.5 Probability distribution function of spatial distance between large monomers across varying genomic distance Δn in the absence of MMC effects ($\phi_c = 0$) and chain heterogeneity ($a_l = 1$) . . . 69
4.6 Probability distribution function of spatial distance between large monomers for various bulk volume fractions of crowders ϕ_c in the absence of chain heterogeneity ($a_l = 1$) . . . 70
4.7 Probability distribution function of spatial distance between large monomers for various large monomer sizes a_l in the absence of macromolecular crowding (MMC) effects ($\phi_c = 0$) . . . 71
4.8 Effects of MMC, chain heterogeneity, and confinement on probability distribution function of spatial distance between larger monomers . . . 73
4.9 Probability mass function for the number of directs between large monomers across varying direct contact thresholds . . . 75
4.10 PMFs for the cluster size across different combinations of a_l (organized by rows) and ϕ_c (denoted by line colors) in free space (left column) and cylindrical confinement (right column) . . . 77
4.11 Probability distribution functions for cluster size (left column) and direct contact number (right column) across various combinations of ϕ_c (indicated by line colors) and a_l (organized by rows) in free space. . . . 78
4.12 MMC effects on the compaction and intra-chain clustering of a heterogeneous polymer in free and cylindrically-confining spaces . . . 79
4.13 Schematic representation of clustering and spatial distribution of monomers and crowders . . . 80
4.14 Spatial distributions (radial volume fractions) of monomers and crowders in free space . . . 82
5.1 A ring polymer interacting with crowders and H-NS dimers . . . 88
5.2 The distance between the center of an H-NS patch and the centers of a pair of adjacent H-NS core and DNA monomer . . . 90
5.3 Chain compaction due to MMC and H-NS binding . . . 96
5.4 MMC effects enhance H-NS binding . . . 98

5.5 Synergistic effects of MMC and H-NS binding on polymer compaction is explained. 99
5.6 H-NS cluster size distribution and average size at $\varepsilon_{hc} = \varepsilon$ and $c_h = 25.5\,\mu M$ 101
5.7 H-NS cluster size distribution and average size at $\varepsilon_{hc} = \varepsilon$ and $\phi_c = 0.32$ . . 102
6.1 Clustering and compaction of a heterogeneous branched ring polymer due to MMC effects. 108
6.2 The synergy between H-NS binding and MMC effects on a chromosome-like ring polymer: how MMC affects the DNA stiffening and bridging modes of the H-NS proteins. 110

List of abbreviations

AO Asakura-Oosawa. 22, 27, 29–33

BIA bridge-induced attraction. 87, 100

BIME bacterial interspersed mosaic element. 16

CAP chromosome-associated protein. 85, 102, 103

CDF cumulative distribution function. 72, 76

CID chromosomal interaction domain. 16–18

COM center of mass. 46, 76, 81, 95

CS Carnahan-Staring. 32

CSP chromosome structuring protein. 14

DBP DNA binding protein. 3, 4, 12, 14, 37, 58, 106

DNA deoxyribonucleic acid. 1–6, 11–19, 36, 37, 54, 55, 58, 60, 61, 83, 85–90, 92–94, 96, 97, 101, 102, 105–107, 109, 111

DNase deoxyribonuclease. 15

DNP deoxyribonucleoprotein. 108, 109

dsDNA double-stranded DNA. 11–14

E. coli Escherichia coli. 2–6, 13, 14, 16, 18, 19, 35–39, 54, 55, 59–61, 64, 82–86, 89, 102, 105–107, 109

FENE finitely extensible nonlinear elastic. 40, 66, 67, 92, 94

Fis factor for inversion stimulation. 102, 103

FMT fundamental-measure theory. 29

FVT free volume theory. 28, 29

H-NS histone-like nucleoid-structuring. 4, 5, 84–103, 106, 109, 111, 112

HIG highly expressed gene. 17

HS hard sphere. 27, 29, 31, 32, 44

HU heat-unstable. 85, 102

IHS impenetrable hard sphere. 32

LAMMPS Large-scale Atomic/Molecular Massively Parallel Simulator. 42, 67, 94

LJ Lennard-Jones. 32, 39, 40, 42, 65–67, 89, 90, 93, 97

MD macrodomain. 18, 19

MD molecular dynamics. 4, 5, 31, 36, 39, 52, 54, 59, 64, 67, 86, 94, 105, 107, 109

MMC macromolecular crowding. xx, 3–10, 21, 22, 24, 26–28, 31, 33, 35, 36, 38, 39, 42, 44–49, 51, 52, 54, 55, 57, 59, 61, 62, 64, 67, 69, 70, 72, 75, 76, 78, 80–83, 85–87, 92, 95, 97, 102, 103, 105–107, 109, 111, 112

mRNA messenger ribonucleic acid. 84

NAP nucleoid associated protein. 3, 12, 14, 16, 17, 61, 85, 86, 102, 106

NS non-structured. 18

OriC origin of replication. 18, 60, 61

PBC periodic boundary condition. 65, 89

PDF probability distribution function. 68

PFK2 phosphofructokinase 2. 6

PFR plectoneme-free region. 17

PHS penetrable hard sphere. 29, 32

PMF probability mass function. 74, 75

pre-rRNA pre-ribosonal ribonucleic acid. 60, 61, 83, 107, 109

RNA ribonucleic acid. 6, 15, 16, 19, 54, 57, 60, 109

RNAP RNA polymerase. 16, 17, 38, 58–61, 83, 102, 107–109

RNase ribonuclease. 15

RNP ribonucleoprotein. 109

ROG radius of gyration. 65, 76, 78, 95

rrn ribosomal RNA. 59–61, 83, 106, 107, 109

rRNA ribosonal ribonucleic acid. 60, 61

SDB supercoiling-diffusion barrier. 14, 16, 17

SPT scaled particle theory. 29, 32

ssDNA single-stranded DNA. 11, 12, 107

SU structural unit. 14–17, 37

TD topological domain. 14, 15

ter terminus region. 18

WCA Weeks-Chandler-Anderson. 39, 65, 74, 91

CHAPTER 1

Introduction

1.1 Motivation and Goals

The Watson-Crick model of deoxyribonucleic acid (DNA), i.e., the double-helical structure of DNA, simultaneously captures the physics and chemistry of DNA, revealing how the polymer carries out its biological tasks [1]. The double-helical structure underpins how a long sequence of base pairs encodes the genetic instructions required for maintaining cellular life. Therefore, each cellular organism has a set of genetic instructions within almost all of its cells, called the genome. In cellular species, the genome mainly consists of one or more long DNA molecules decorated with proteins, called chromosome. The long lengths of chromosomes immediately pose questions about their organization within cells. Understanding chromosome organization is crucial for comprehending how cells maintain the integrity and functionality of their genetic information, as well as how they replicate and transmit it accurately during cell division.

Eukaryotes utilize a membrane-bound compartment, called the nucleus, to organize their chromosomes within their cells [5, 6]. In contrast, prokaryotes — bacteria and archaea — rely on "an open plan architecture design" [7] for this purpose. Most prokaryotes have single circular chromosomes, residing in an unpartitioned region called the nucleoid (Fig. 1.1). Within prokaryotes, the problem of chromosome organization in bacteria is especially puzzling. Unlike archaea, bacteria lack homologs of eukaryotic histones, architectural proteins associated with DNA to form nucleosome-like structures [8, 9]. Yet, bacteria not only efficiently compact and organize their chromosome within their nucleoids [10], but also regulate the size and positioning of their nucleoids [11]. How is the chromosome compaction achieved in bacterial cells? How does the chromosome organization happen in the nucleoid? Beyond advancing our understanding of underlying physical principles of bacterial chromosome packaging, finding answers to these questions has promising technological applications. Indeed, a new paradigm has recently emerged in which the bacterial nucleoid is recognized as the most complex of "smart polymers" [12]. This class of polymers that undergo confor-

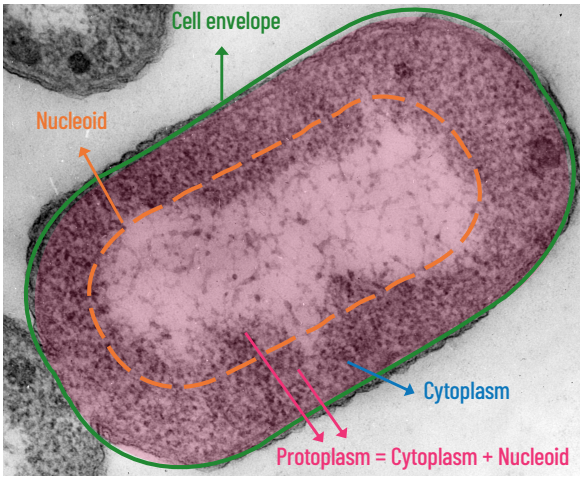


FIGURE 1.1 An electron micrograph of the E. coli cell displays the nucleoid in the middle of the cell at the x12 000 magnification. Unlike the eukaryotic nucleus, the bacterial nucleoid is an unbound region in the middle of the cell, consisting of 80 % chromosomal DNA, 10 % protein, and 10 % RNA species in weight [2, 3]. The image, modified from [4] under CC BY 3.0, highlights the protoplasm, i.e., the cell interior within the inner membrane, which includes the nucleoid and the cytoplasm.

mational transitions in response to external stimuli, e.g., growth conditions, to fulfill their functions [8, 12].

Let's further clarify the importance of chromosome compaction and nucleoid organization with some insights from the bacterium Escherichia coli (E. coli), which is used as a model system throughout this thesis. An average E. coli cell is in the shape of a spherocylinder with a size (diameter) of 1 µm and a length of 2 µm [13]. The 4.6 Mbp-long chromosome of E. coli [14] is almost 1.5 mm along its backbone, if it is considered as a long B-DNA double-helix with a helical turn of 3.5 nm per 10.5 bp [5]. Simple polymer physics calculations suggest this chromosome is approximately 555.6 µm in length if it is modeled as a semiflexible ring polymer in a cylindrical confinement of size 1 µm. Such a long length is much longer than the average 2 µm length of E. coli cells; yet, this long chromosome resides within the nucleoid, which accounts for less than 20 % of the cell volume [15, 16]. How does this chromosome, which is two orders of magnitude longer than the cell length, fit inside one-fifth of the cell volume?

Cellular conditions influencing chromosome organization can be categorized into two main groups [15]. The first category includes physical conditions like ionic strength and molecular concentration, which serve as structural and environmental determinants for the configuration and functionality of chromosomes. The second encompasses physiological conditions such as DNA replication and cell growth, representing dynamic biochemical and molecular activities that shape chromosome organization and functionality either directly or indirectly. These physical and physiological con-

ditions typically coexist, leading to structural changes in chromosomal DNA via two interconnected mechanisms, namely, supercoiling and interactions with DNA binding proteins (DBPs) [5, 17–19].

Supercoiling is already locked into bacterial chromosomes, due to the ring topology of their chromosomes [5], demonstrating itself via various supercoiled conformations (loops) [20]. A wide range of DBPs, ranging from topoisomerases and condesins to duplication and transcription machines, constantly changes the DNA structure and supercoiling at local and global levels [10, 21, 22]. A subclass of DBPs are nucleoid associated proteins (NAPs), which are low molecular weight proteins, extensively found in bacterial nucleoids. Functionally similar to eukaryotic histones, NAPs play an important role in the compaction and organization of bacterial chromosomes in two ways [10, 21]: (a) binding to DNA in different ways, including but not limited to bending and wrapping, changing DNA supercoiling; and (b) intervening with the transcription machinery, via a range of nonsequence to sequence DNA-binding specifies. Consequently, DBPs, in particular NAPs, stabilize and manipulate supercoiled loops at various levels, resulting in a hierarchical organization of the bacterial chromosome [10, 21, 22]. While supercoiling and DBPs, particularly NAPs, are central to the bacterial chromosome organization, their effects, alone or together, have been found insufficient to compact chromosomes within bacterial cells [23, 24].

In E. coli cells, macromolecules occupy a significant fraction of the total volume up to 40 %, with concentrations ranging from 50 g L^{-1} to 400 g L^{-1} [25–30]. At such high volume fractions, nontrivial effects arise from nonspecific interactions, particularly excluded-volume interactions, among macromolecules, such as proteins, which are referred to as macromolecular crowding (MMC) effects. Due to the aforementioned "open plan architecture design," cellular crowding has emerged as the third factor, in addition to supercoiling and DBPs, in the compaction and organization of bacterial chromosome [8, 31, 32]. Theoretical models and in-vitro studies have shown MMC can compact bacterial chromosomes to their in-vivo sizes [33–36]. Additionally, in-vivo experiments have shown E. coli utilize confinement to modulate its cytoplasmic MMC effects on its chromosome, thus adjusting the size and position of its nucleoid based on its cell size [11, 37, 38]. In parallel, scaling arguments and chromosome models, based on polymer physics, have suggested MMC effects play a role in the spatial clustering of transcription-active sites along the bacterial chromosome [39, 40].

Indeed, much effort has been made to clarify the previously "obvious but underappreciated" [41] role of MMC in nucleoid formation and chromosome organization. However, these efforts have posed new questions about the MMC role at different hi-

erarchies of the bacterial chromosome organization: How much the physical properties of macromolecules are important in MMC effects? What is the interplay between MMC and DNA supercoiling? How does MMC affect the interactions between DNA and DBPs? Do small cellular species such as ions and solvent molecules modify MMC effects on the chromosome? These fundamental questions have not been adequately addressed so far.

In this thesis, we employ molecular dynamics (MD) simulations to systematically investigate how biomolecular crowding, confinement, chain heterogeneity, and chain cross-linking influence the spatial organization of "chromosome-like" polymers. Our modeling approach is motivated by the hierarchical organization of E. coli chromosomes. Initially, we adopt a simple model, progressively enhancing it with additional biological details. This approach offers a quantitative understanding of several key phenomena, including the clustering of transcription-active units into a transcription factory, and the synergistic effects of histone-like nucleoid-structuring (H-NS) and MMC effects in the compaction of bacterial chromosomes.

The emerging physical view from this thesis is that MMC-driven phase separation and clustering are the primary mechanisms governing the organization of bacterial chromosomes. At the cell-size scale, MMC and anisotropic (cylindrical) confinement together modulate chromosome folding, compacting it into the nucleoid. At the intermediate level, MMC can bring genomically-distant heterogeneous chromosome segments in spatial proximity via intra-chain clustering, where confinement makes MMC effects more effective. And, at the micro level, MMC can enhance the binding of proteins to chromosomal DNA, which in turn can intensify MMC effects.

1.2 Organization of the thesis

In Section 1.1, we discussed the motivation and goals of our study on bacterial chromosome organization. We introduce crowded systems and MMC effects in Section 1.3. The chapter concludes with a succinct overview of the hierarchical organization of bacterial chromosomes in Section 1.4, with E. coli serving as our model system.

Progressing to Chapter 2, we explore the physics of MMC, establishing a theoretical framework that lays the foundational knowledge necessary to grasp the role of MMC in the subsequent chapters (Chapters 3 to 5). Specifically, this chapter elucidates the relationship between various approaches to modeling MMC effects.

Chapter 3 is dedicated to examining the role of MMC in chain compaction and interdependence between spatial distributions of monomers and crowders under cylindri-

cal confinement. We demonstrate that MMC effects are local and thus a simple density sum rule can be used to link the distributions of monomers and crowders.

In Chapter 4, we explore the impact of MMC on the compaction of a heterogeneous ring polymer in unconfined and confined spaces. Inspired by the chromosomal organization in E. coli cells, we adopt a coarse-grained model of the E. coli chromosome, composed of large and small monomers. We show how the clustering of large monomers, mimicking transcriptionally-active units along the E. coli chromosome, affects polymer organization and compaction through MD simulations.

Chapter 5 focuses on understanding how the binding of H-NS protein affects chromosome compaction. In our modeling approach, H-NS dimers (protomers) are conceptualized as spherical binders equipped with two DNA-binding sites each. Through this model, we delve into the synergistic interactions between MMC and H-NS binding.

Finally, Chapter 6 synthesizes the insights gained throughout the thesis, proposing two projects for future research. The first project investigates the role of MMC in the organization and compaction of a heterogeneous branched ring polymer. This effort extends the discussions in Chapter 4 by integrating more biological details in modeling transcriptionally-active units. In the second project, we consider H-NS oligomerization and chain stiffness, aspects not covered in our analysis in Chapter 5. By adding two H-NS-binding sites to each H-NS binder, our goal is to investigate the formation of nucleoprotein filaments under MMC conditions and its implications for chromosome compaction and organization.

1.3 Macromolecular crowding

The concept of MMC, first articulated by Minton in his groundbreaking papers [42, 43], has since been the subject of extensive study [44–46]. The interpretations of crowded systems and MMC effects vary, particularly in terms of the constituents of a crowded system and their interactions [28, 47–49].

In the following subsections, we describe MMC effects, with an emphasis on nonspecific interactions. Given the significant focus on these interactions and their connection to MMC, we will provide an in-depth yet concise account of nonspecific interactions.

Central to our subsequent discussion is the concept of a macromolecule. According to the IUPAC[1], a macromolecule is defined as “a molecule of high relative molecular

[1] International Union of Pure and Applied Chemistry.

mass, the structure of which essentially comprises the multiple repetitions of units derived, actually or conceptually, from molecules of low relative molecular mass" [50]. Common examples include proteins, molecular machines, ribonucleic acid (RNA), and DNA. For proteins, these building units are amino acids, while for DNA, they are base pairs. In polymer physics, these units are conceptualized as monomers or Kuhn segments.

1.3.1 Crowded systems

Crowded systems refer to solutions where macromolecular species, with sizes substantially larger than solvent species, occupy a high total volume fraction, despite not having high individual concentrations [69]. In the literature, the macromolecular species studied in a crowded medium, like the chromosomal segments in this thesis, is referred to as the probe, tracer, or solute, while other mobile macromolecular species in the medium are called crowders, crowding agents, or cosolutes [69].[2]

The cellular environment represents the most intricate example of a crowded system, encompassing a wide range of species. Figure 1.2 schematically illustrates the intricacy in an E. coli's cell at three snapshots in an increasing magnification from left to right. As can be seen, cellular species are not only heterogeneous in their types but also in their shapes and sizes. Table 1.1 complements this schematic picture with a short census of cellular species in E. coli, illustrating a quantitative picture of the cellular interiors.

As listed in Table 1.1, large molecular weight differences between cellular species often point to large size (volume) differences between them. For instance, a water molecule in liquid phase is 18 Da in weight and 0.320 nm [60, 61] in size while the phosphofructokinase 2 (PFK2) is 32 456 Da in weight and 4.240 nm in size [64, 67, 68]. Accordingly, a variety of interactions exist between these cellular species, most important of which are [70–72]: (a) repulsive entropic interactions (including steric-hydration interactions); (b) electrostatic interactions; (c) attractive Van der Waals interactions; (d) attractive hydrophobic interactions; and (e) attractive depletion interactions. Usually, a combination of these interactions exists between two or more particles. How can we classify these interactions in terms of their importance? What are our classification criteria? Is this classification important in understanding the interactions between tracer and crowder species? we provide answers to these questions in the following subsection, defining MMC effects based on them.

[2] More generally, mobile and structural macromolecular species, other than the tracer species, are referred to as background species [69].

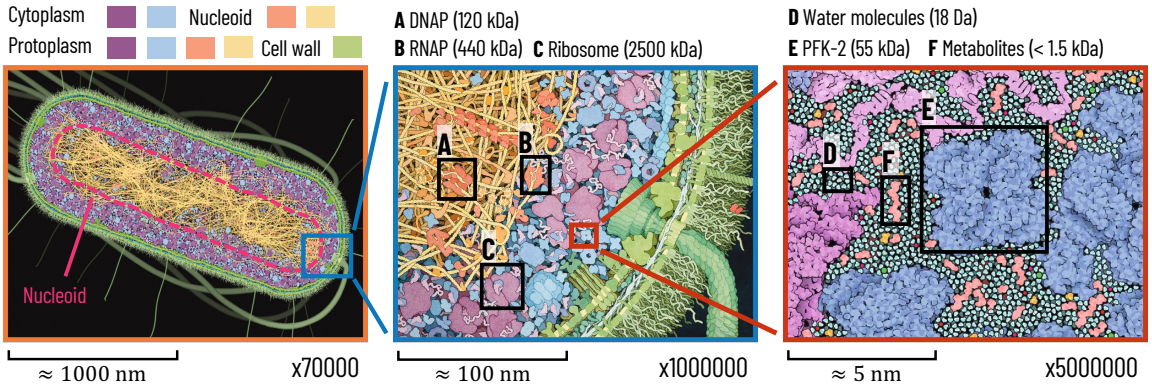


FIGURE 1.2 Schematic illustrations of E. coli cell at increasing magnifications from left to right. The three sub-figures reveal the degree of heterogeneity of cellular species in type, shape, and size, reflecting cellular environments as the most intricate crowded systems. *Left:* An E. coli cell at x70 000 magnification. Legend atop shows color themes for the main cellular parts, namely the cell wall (green), protoplasm (purple, blue, orange, and yellow), cytoplasm (purple and blue), and nucleoid (orange and yellow). This color theme is also used in the other sub-figures. Protoplasm refers to the cell interior within the inner membrane. The nucleoid, an unpartitioned region containing the bacterial chromosome, is enclosed by a dashed contour. *Middle:* Magnification of the small blue box in the left sub-figure at a resolution of x100 000, revealing that distances between macromolecules are of the same order as their sizes. For comparison, the legend atop the middle sub-figure indicates molecular weights of DNA polymerase (DNAP), RNA polymerase (RNAP), and ribosome. *Right:* Magnification at resolution of x500 000 of the small red box in the middle sub-figure, revealing the relative size of macromolecules to metabolites, water molecules, and ions. As in the middle sub-figure, some species are selected with a legend atop showing their names and molecular weights. The macromolecule PFK2 is an enzyme indirectly responsible for regulating the rates of glycolysis (a metabolic pathway that converts glucose into pyruvate and produces energy for producing ATP). The molecular weights for DNAP, RNAP, ribosome, and PFK2 are taken from refs. [51], [52], [53], and [54], respectively. The upper limit of molecular weights for metabolites is based on ref. [55]. The scale bars are loosely defined by comparing the average length of an E. coli cell (2 µm) [56, 57], average thicknesses of an Escherichia coli flagellum (20 nm) [13], and an average length of PFK2 (4.240 nm) (see Table 1.1) with their average sizes in centimeters in the left, middle, and right sub-figures, respectively. The sub-figures are modified, with permission, from [58].

1.3.2 Nonspecific interactions in crowded media

Within a crowded medium, macromolecules are often nearby, with inter-particle distances being comparable to the sizes of the macromolecules themselves [28, 41, 69, 73]. This proximity results in a wide range of interactions, as listed in Section 1.3.1. To understand the concept of MMC, it is thus crucial to distinguish these interactions based on specificity [28, 48, 49, 74].

Specific interactions, also known as site-specific or segment-dependent interactions, often occur due to the complementary geometrical shapes or specific interatomic bonds of the molecules involved [70]. These interactions vary in strength, ranging from weak

TABLE 1.1 A census of an average E. coli cell with a volume of 1.3 μm^3 [13] hints at the large differences in masses, sizes, and numbers of its cell composition. For more detailed censuses, see refs. [13, 15, 59].

Species	Mol. m.[a] (Da)	Size (nm)	Con.[b] (M)	Tot. m.[c] (fg)	Number	Vol. fra.[d] (%)
Water	18[e]	0.320 [60]	-	670 [59]	2.24×10^{10}	70 [59]
Ions (K^+)	39	0.266 [61]	100 [13]	2.8 [59]	6×10^7 [13]	0.045
Metabolites[f]	-	-	-	8.12 [59]	-	-
Glutamate[g]	147.13	0.9[h] [62]	960 [63]	-	7.57×10^{7}[i]	0.445[j]
Proteins[k]	35 750[l]	4.324[m]	-	154 [59]	2.9×10^6	9.344
PFK2	32 456 [64]	4.240[n]	-	-	-	-
RNAP	460 000 [52]	15 [52]	-	-	5000 [65]	0.675
Ribosome	2 500 000 [53]	22 [53]	-	47.7 [59]	18 700 [59]	7.965

[a] Molecular mass.
[b] Molar concentration.
[c] Total mass.
[d] Volume fraction.
[e] The molecular masses of water, K^+, and glutamate are taken from their Wikipedia entries.
[f] Metabolites are small molecules ($\leq$1500 Da) that play a key role in cell metabolism, as substrates, energy sources, intermediates, or products [66].
[g] The most abundant metabolite in E. coli.
[h] Length; the width is 0.35 nm [62].
[i] Estimated based the glutamate concentration and the cell volume.
[j] Estimated for cylindrical glutamates.
[k] The average protein length in E. coli is 325 aa [67, 68].
[l] The average size of an amino acid is 110 Da. See the Wikipedia entry for amino acids.
[m] The average protein size in E. coli is calculated by means of equation 10 in ref. [68].
[n] PFK2 is 309 aa in length [64]. The protein size is calculated employing equation 10 in [68].

to strong [49]. Specific interactions lead to the formation of structured complexes, which can be either stable or transient, and play a vital role in biological functions [49]. In essence, they are responsible for both self-assembly and self-organization in living cells [75]. A prime example of this type of interaction is the binding of a ligand to its receptor [70].

On the other hand, nonspecific interactions are driven not by the biological specificity of molecules but by their general physical characteristics, such as net charge and the polarity of surface residues [28, 48, 49, 74]. These interactions are weak noncovalent interactions and can be either attractive or repulsive [48, 49]. When attractive, they lead to the formation of transient structured complexes or aggregations, often as a result of self-organization [49, 75]. A classic example of a nonspecific interaction is steric interaction, which solely arises from mutual volume exclusions of two particles [74].

Based on this classification, MMC effects are effects arising from nonspecific in-

teractions between macromolecules in a crowded medium [49].[3] Nonspecific interactions can be hard or soft, and short- or long-ranged, depending on their magnitude, steepness, and interaction range [76]. Due to the variety of nonspecific interactions in crowded media, in particular cell interiors, MMC has been further classified based on different properties of these interactions, as discussed in what follows.

First, nonspecific interaction can be short- or long-ranged, depending on whether, as the inter-particle distance r approaches zero, the interaction potential vanishes more rapidly than r^{-3} or not [77]. For long-ranged interactions, virial coefficients are infinite. The Coulomb interaction is an example of long-range interactions.

Second, nonspecific interactions are classified as enthalpic and entropic interactions. In the framework of statistical mechanics, enthalpic interactions, such as electrostatic interactions, originate from direct forces or bare potentials between particles in a system, contributing to the internal energy of that system. In contrast, entropic interactions, exemplified by hydrophobic interactions, are the result of the collective behavior of particles at a finite temperature [70]. Such interactions stem from changes in the configurations of a system, rather than from direct inter-particle forces [28]. From a thermodynamic perspective, nonspecific interactions are classified as either enthalpic or entropic, based on their respective contributions to the enthalpic and entropic terms in the Gibbs free energy of a system [47, 78].

Third, nonspecific interactions can also be classified based on the physical and chemical properties of macromolecules. Excluded-volume interactions originate from steric (spatial arrangement of atoms) and electronic (arising from Coulomb repulsion and Pauli exclusion principle) constraints. In other words, excluded-volume interactions, primarily entropic, are repulsive nonspecific interactions, stemming from the relative sizes and shapes of macromolecules in a crowded medium [79].[4] On the other hand, chemical interactions depend on the chemical details of the the atoms from which a macromolecule is composed. Such interactions, spanning from entropic to enthalpic, are nonspecific attractive interactions arising from properties such as charge distributions and hydrophobicity of macromolecules [79].

Finally, MMC effects on tracers can be studied based on different classifications of nonspecific interactions between tracer and crowder species as well as the effective interactions between tracer species themselves. Here, effective interactions are any

[3]The terms MMC, biomolecular crowding, molecular crowding, cellular crowding, and crowding are often interchangeably used; however, the precise term is MMC.

[4]In literature, the terms excluded-volume and steric interactions are interchangeably used. Here, we argue the term excluded-volume interaction is more general and includes both repulsive interactions arising from both steric and electronic effects.

interactions other than bare (or direct) interactions between tracers that result from MMC effects. Short-range nonspecific tracer-crowder interactions can be split into preferentially- excluded and included interactions [47, 80]. Here, the term preferential refers to the binding affinity of crowders for tracers. Preferentially-excluded interactions between trace and crowders can result in an important class of effective interactions between tracers called depletion interactions. On the other hand, preferentially-included interactions between trace and crowders can result in another important class of effective interactions between tracers called bridging interactions. Here, bridging means intervening crowders induce an effective attraction between distant tracers [80]. In practice, tracer-crowder interactions are between these two extreme limits, having stabilizing or destabilizing effects on a tracer or group of tracers [47, 80].

It is noteworthy that some authors have limited cellular MMC effects to repulsive excluded-volume interactions and defined two other interactions in cells, namely, sticking and quinary interactions [81]. Sticking interactions refer to weak attractive non-specific interactions, which are the chemical interactions defined earlier. On the other hand, quinary interactions encompass electrostatic, hydrophobic, and other interactions that form transient quinary structures [81]. In line with Minton's perspective, we contend that these quinary interactions are those weak attractive non-specific interactions (MMC effects) responsible for the formation of quinary structures [48].

1.3.3 Crowded cellular environments in molecular simulations

While it is tempting to study the crowded interior of a cell in full detail [82, 83], such holistic (whole-cell) approaches [84–86] often only partially capture the underlying physical principles emerging from and/or governing such a crowded medium. Accordingly, different reductionist protocols have been developed not only to study crowded environments [87], but also to model crowders in molecular simulations [88]. These approaches have enabled us to systematically study the roles of the size, shape, and concentration of crowders as well as the details of nonspecific tracer-crowder and crowder-crowder interactions on MMC effects. Moreover, it is possible to explicitly include water molecules, ions, and small molecules (osmolytes, metabolites, etc.) in a study.

At mesoscales, tracers and crowders are usually modeled as simple beads. Consequently, heterogeneous crowded cellular environments are usually replaced with multicomponent concentrated media [46, 49, 69], where the background solvent (in particular water; see [89]) is either ignored, considered as a thermal bath (Langevin dynamics), or incorporated into effective interactions between mesoscale components. Sim-

ilarly, ions and metabolites are either integrated into effective interactions or coarse-grained into problem-specific details (for example, see [90]).

1.4 Chromosome organization hierarchy in bacteria

Bacteria mainly utilize supercoiling-based strategies to hierarchically organize their chromosomes within their tiny cellular spaces. This section aims to provide a concise description of this hierarchical organization of the bacterial chromosome.

1.4.1 DNA double-helical structure

The fundamental unit of DNA is the nucleotide, comprising a sugar molecule (deoxyribose), a negatively charged phosphate group, and one of four heterocyclic bases. The hydrophilic nature of the sugar and phosphate groups contrasts with the hydrophobic character of the bases. When a base forms a covalent bond with deoxyribose, a nucleoside is produced. Subsequently, the phosphate of one nucleotide can covalently bond to the sugar molecule of another, through a process termed phosphodiester linkage, resulting in a polynucleotide chain or single-stranded DNA (ssDNA). The alternating sequence of deoxyribose and phosphate groups along a ssDNA is commonly referred to as the backbone [5, 91].

The bases are categorized into two groups: the double-ringed purines (adenine 'A' and guanine 'G' and the single-ringed pyrimidines (thymine 'T' and cytosine 'C'). Adhering to base pairing rules, A pairs exclusively with T through two hydrogen bonds, while G pairs with C via three hydrogen bonds. These specific pairings are fundamental to the double-stranded DNA (dsDNA) structure, which encodes genetic information [5, 91].

The dsDNA adopts a double-helical structure, composed of two anti-parallel ssDNAs held together by hydrogen bonds between their base pairs. Despite the differences in individual base pairs, their geometries and external regions near their deoxyribose molecules are remarkably similar. This geometrical consistency and pseudo-symmetry enable any sequence of the four base pairs—AT, TA, GC, and CG—to seamlessly reside within the double-helical structure formed by the dsDNA backbone [5, 91].

While base pairing and geometrical consistency are essential, they alone do not suffice to stabilize the double-helical structure of dsDNA. The stacking interaction between adjacent base pairs is pivotal in reinforcing the secondary structure of DNA [5,

91]. This interaction encompasses the combined effects of Van Der Waals forces and electrostatic interactions between bases on both the same and opposite strands [92].

Among the various conformations of dsDNA, B-DNA is believed to represent the predominant form of DNA in cellular environments. In B-DNA, there are approximately 10.5 bp for every helical turn, with a spacing of 0.34 nm between turns. The crystal structure of B-DNA exhibits a diameter of 2 nm [93]. However, in aqueous solutions, the diameter of B-DNA is found to be 2.95 nm under high-salt concentrations (1 M NaCl) [94] and 4.4 nm under physiological conditions (0.2 M NaCl) [95, 96].[5]

1.4.2 DNA supercoiling

The double-helical structure of dsDNA arises from the stacking of nucleotides along a ssDNA and their pairing with complementary bases on an anti-parallel ssDNA. This structure offers evolutionary advantages, such as enhanced stability [97]. However, the double-helical nature of DNA also means that certain manipulations, like unwinding or overwinding of the helix during processes like replication or transcription, can cause the DNA helix to coil upon itself. This phenomenon, where the DNA helix undergoes additional coiling beyond its relaxed state, is termed supercoiling [5]. In other words, supercoiling refers to the spatial deformations of the helical axis of a dsDNA [18].

In bacteria, transcription machinery, topoisomerases, condensins, and NAPs are the key factors inducing, relaxing, or maintaining supercoiling throughout chromosomal DNA [10, 21, 22]. Overall, DBPs can engage ∼100 bp of DNA, affecting up to ∼1000 bp upstream or downstream of their interaction sites [22, 98]. As it turns out below, supercoiled conformations may lead to a secondary helical ordering in dsDNA.

1.4.2.1 Supercoiling and the ring topology of bacterial chromosomes

Bacterial chromosomes typically exist as long, closed-circular dsDNA molecules [99]. This ring topology restricts the rotational freedom inherent at the ends of linear dsDNA molecules. When the ends of a linear DNA molecule are sealed to form a circle, any deviation from its relaxed state can lead to supercoiling, which becomes locked into the circular dsDNA due to its topological constraint (ring topology) [5].

[5] In the rest of this thesis, we use DNA and dsDNA interchangeably unless otherwise stated or inferred from the text.

1.4.2.2 Linking number

As explained, supercoiling is locked in a circular dsDNA chain. While such a chain can be geometrically altered, its supercoiled state is preserved. In this section, we provide a quantitative description of supercoiling.

The linking number, Lk, of a closed-circular DNA molecule represents the number of times the dsDNA is intertwined before sealing the phosphodiester bond. This integer number remains constant unless one or both strands of the DNA are broken [5]. Mathematically speaking, the linking number is an invariant number determining the number of intersections between two closed curves [18]. For a given DNA chain with N_{bp} base pairs and h base pairs per helical turn in the dsDNA, the standard linking number is given by

$$Lk_\circ = N_{bp}/h, \tag{1.1}$$

which can be a noninteger representing the supercoiling of a DNA in its relaxed state, e.g., a linear dsDNA before closure or a nicked circular dsDNA. However, when DNA undergoes supercoiling, the actual observed linking number can deviate from its (most) relaxed state, leading to a *linking difference*, represented by

$$\Delta Lk = Lk - Lk_\circ. \tag{1.2}$$

This difference is a measure of the extent of supercoiling in the DNA molecule. The linking difference can be positive or negative, indicating positive or negative supercoiling, respectively. By convention, in a right-handed double-helix, positive supercoiling results from the over-winding of the DNA helix, while negative supercoiling arises from under-winding. Indeed, a non-zero linking difference is a measure of elastic stress in a DNA, which in turn is more pronounced in shorter DNA chains. To scale this elastic stress with the length of dsDNA, we rescale the linking difference with the standard linking number to have the specific linking difference [5],

$$\sigma_{Lk} = \Delta Lk/Lk_\circ. \tag{1.3}$$

In cells, almost all of the circular dsDNAs are negatively supercoiled [18]. For instance, the E. coli chromosome has a negative specific linking difference of $\sigma_{Lk} = -0.05$ [10]. However, supercoiling is unevenly distributed along the E. coli chromosome, varying across growth stages [21].

The linking difference of circular dsDNA can be changed in two ways: Twisting or writhing. The former refers to turning the double-helix around its axis while the latter is defined as the deformation of the helical axis in space [18]. Indeed, twist, Tw, is the

number of helical turns in a dsDNA while writhe, Wr, is the number of times that a dsDNA self-crosses. It can be proved that [5]

$$Lk = Tw + Wr. \tag{1.4}$$

Since the linking number is invariant, this equation states any chain in the twist number is accompanied by a change with the opposite sign in the writhe number.

Twisting does not change the helical axis of a dsDNA chain but writhing alters this helical axis, introducing a higher-order structure into the dsDNA chain. Thus, one can say the writhe conformations are the tertiary structure of DNA [100]. Writhe conformations are further split into plectonemic and toroidal conformations [5]. A plectoneme refers to a conformation where the DNA helix winds around itself, forming a higher-order helix. This interwinding is right-handed in the case of negatively supercoiled DNA. In contrast, toroids happen when the axis of the dsDNA lies on the surface of an imaginary torus. These writhe conformations can exist in either a free form or be held in a restrained form by DBPs [10, 101]. In terms of DNA compaction, plectonemic supercoils are less efficient than their toroidal counterparts [20], but they are the primary free form of DNA supercoils [5]. The supercoiled conformations play an important role in chromosome organization, as explained in the following subsection.

1.4.3 Plectonemic loops

As discussed in Section 1.1, bacteria lack dedicated chromosome structuring proteins (CSPs), such as histones in eukaryotes. Nevertheless, they effectively organize their chromosomes by managing their supercoiled conformations, which arise from the interactions between DBPs and chromosomal DNA.

In E. coli, approximately half of the chromosomal DNA exists in free plectonemes, while the remainder is organized into restrained plectonemes, toroids, or other supercoiled conformations through interactions with NAPs or other DBPs [5, 10]. Supercoiled loops not only compact DNA but also enhance DNA disentanglement by reducing DNA catenation. Furthermore, they facilitate interactions between proteins and DNA by bringing genomically distant DNA segments in spatial proximity, a phenomenon known as DNA synapsis [5, 10]. Consequently, plectonemes serve as physical representations of DNA supercoiling throughout the bacterial chromosome.

1.4.4 Structural units

Plectonemic loops are organized into structures known as structural units (SUs) or topological domains (TDs) along a bacterial chromosome, with supercoiling-diffusion

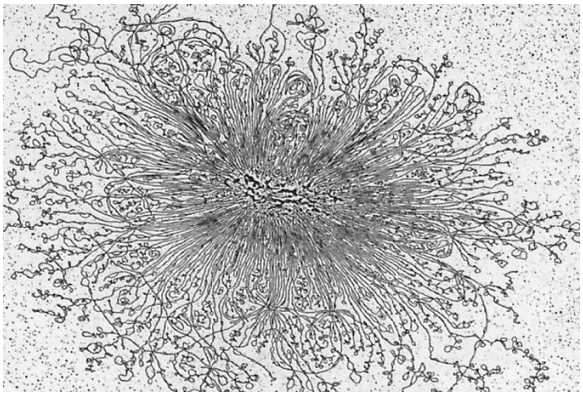


FIGURE 1.3 An electron micrograph of the E. coli chromosome released from the cell membrane, resembling a rosette-like structure with supercoiled DNA loops and a central RNA-containing core. The rosette-like structure supports the model in which the E. coli chromosome consists of several topologically-independent supercoiled DNA loops, term structural units (SUs). The image is modified, with permission, from [102] (an archived webpage). Similar images can be found in [103].

barriers (SDBs) acting as topological barriers between these SUs. Operationally, a SU or TD is defined as a region of a supercoiled chromosome that relaxes in response to a DNA disruption, such as deoxyribonuclease (DNase) treatment [101]. When erupted from the cell membrane, SUs take on a rosette-like structure radiating from a central bush-like core containing RNA [103] (Figure 1.3). Treatment with ribonuclease (RNase) changes the core's shape from bush-like material to dot-like material, revealing that the core is partly composed of RNA-based materials [103].

Early experiments reported that folded chromosomes consist of 40 to 65 SUs per cell, with sizes ranging from 40 kbp to 100 kbp [3, 15, 103–106]. In-vivo observations estimate the presence of 90 to 500 SUs per chromosome, with an average size ranging from 10 kbp to 50 kbp [23, 101]. Another experiment suggests that topological barriers typically hinder the slithering of DNA with a frequency of approximately 13 kbp [107]. SUs have consistent chromosome density and are independent of the cell membrane [2, 104]; moreover, they are relatively compact and weakly interact with each other [23]. It is estimated that an SU has a diffusion coefficient of $6.5 \pm 2.3\,\mu m^2\,s^{-1}$. Based on this estimate, the Einstein relation and Stokes law combined suggest a size (diameter) of approximately 70 ± 20 nm for spherical SUs [23]. In-vitro force-compression measurements suggest that 284 (63) SUs per cell – 71 (16) per chromosome – form a linear (ring-like) chain with an average spring constant of -2.04 ± 1.24 pN, where each SU has a size of 130 nm (440 nm) for the respective linear (ring-like) chain [35]. In summary, it can be said a SU is either a single or branched plectoneme with $\sim$50 kbp in length and $\sim$70 nm in diameter [108].

Supercoiling impacts the size of SUs. Although the average size of SUs remain con-

sistent across identical absolute magnitudes of both positive and negative supercoiling, the alteration in SU size as a result of positive and negative supercoiling exhibits asymmetry: A given absolute change in supercoiling leads to larger SUs in the context of positive supercoiling compared to negative supercoiling. This differential impact of supercoiling on SU size offers a plausible explanation for the observed variances in reported values for the size and number of SUs [23].

Experiments show that the barriers defining SUs are dynamic and depend on the rates at which a cell grows; however, neither nascent RNAs nor DNA-membrane interactions are crucial in barrier formation [105]. Domain barriers are randomly located on the genome and are created by any accidental cross-links between two parts of the chromosome due to various cellular activities [101]. While the exact nature of these barriers remains to be determined, several mechanisms have been proposed for the barrier formation. Transcription machinery plays a pivotal role in the formation of plectonemes [10], with elongating RNA polymerases (RNAPs) acting as SDBs at the 10 kbp scale [22]. NAPs complement this role by controlling supercoiling at short and long distances through mechanisms such as bending, stiffening, bunching, or bridging DNA [10, 21]. Bacterial interspersed mosaic elements (BIMEs) [10] and transertion [109, 110] are two other mechanisms for barrier formation. Based on the dynamic nature of SUs and domain barriers, it is suggested that the E. coli chromosome structurally behaves like a non-viscous fluid [23].

1.4.5 Chromosomal interaction domains

In the previous section, we introduced the concept of SUs, which partitions the bacterial chromosome based on the topological isolation of supercoiled DNA conformations. SUs provide a framework for understanding the supercoiling-driven organization of the chromosome. Now, we delve into a different aspect of bacterial chromosome organization by describing results obtained through analyzing the frequency of spatial contacts (physical interactions) between chromosomal loci, which may be genomically distant from each other. The resulting high-resolution contact maps have revealed that the bacterial chromosome is segmented into self-interacting regions called chromosomal interaction domains (CIDs), isolated with SDBs [10, 21, 22] (Fig. 1.4).

Depending on the bacterial species and growth conditions, there is approximately 30 CIDs with sizes ranging approximately from 30 kbp to 430 kbp [8, 21]. CIDs depicts a nested domain organization, where a larger domain is composed of smaller subdomains, with the smallest subdomains possibly corresponding to individual operons [21]. Notably, regions within a CID exhibit more frequent spatial interactions with

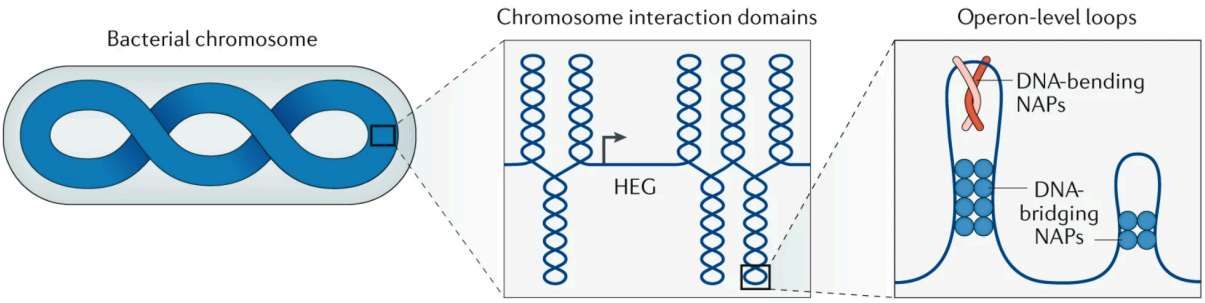


FIGURE 1.4 The bacterial chromosome is segmented into approximately 30 chromosomal interaction domains with size ranging from 30 kbp to 430 kbp. *Left:* On the global scale, the bacterial chromosome adopts a helical configuration to fit inside the bacterial cell (see Section 1.4.7). *Middle:* On a scale ranging from tens to hundreds of kilobases, the chromosome is divided into CIDs with the domain boundaries often established by HIGs. *Right:* The most fundamental unit of bacterial chromosome organization might be supercoiled loops at the level of individual operons or clusters of genes, stabilized by NAPs. The image is modified, with permission, from [21].

other regions within the same CID compared to interactions with regions within a different CID or regions outside CIDs.

Extended SDBs act as the boundaries between CIDs, with transcription playing a significant role in their formation [10, 21, 22]. In many cases, CID boundaries are plectoneme-free regions (PFRs) created by highly expressed genes (HIGs). In this context, a PFR arises as a result of high transcription activity, where active RNAPs, by unwinding DNA, help prevent the formation of plectonemic supercoils. Experiments have shown that transcription rate and transcript length are two factors determining whether a gene acts a CID boundary or not. Furthermore, It is noteworthy that long-distance interactions have been observed across CID boundaries, suggesting the presence of additional mechanisms facilitating connections between neighboring regions [22].

To summarize, transcription activity plays the main role in the formation of CIDs and the boundaries between them. Within a CID, transcription activity results in a nested domain organization. In parallel, supercoiling promotes interactions among genomic regions, and NAPs stabilize the supercoiling-mediated interactions (rightmost sub-figure in Fig. 1.4). Additionally, high transcription activity of long genes or clusters of genes leads to the formation of CID boundaries (middle sub-figure inFig. 1.4). The exact factors contributing to CID boundary formation are not fully understood [10]. Moreover, it is still unclear whether SUs and CIDs are two different realizations of the same level of organization in bacterial chromosomes or not.

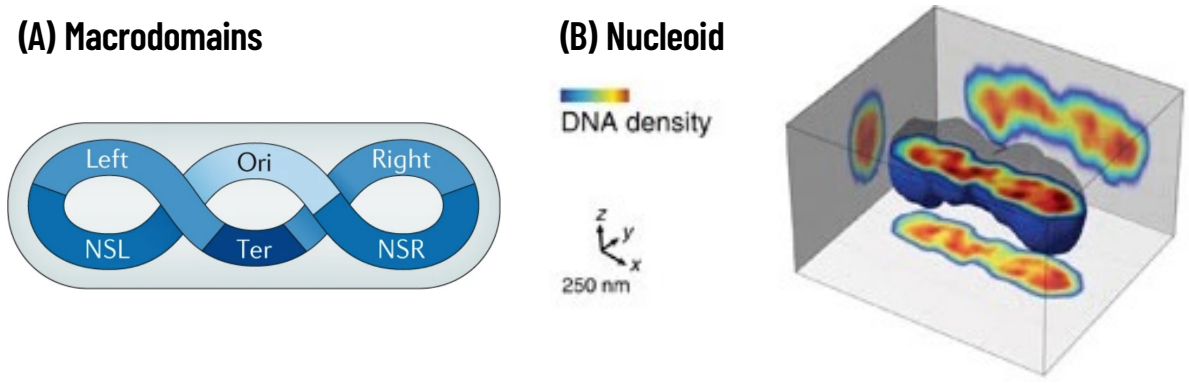


FIGURE 1.5 (A) A schematic of the E. coli chromosome illustrates the spatial positioning of macrodomainsin the cell. The image is modified, with permission, from [21]. (B) A 3D volume of chromosomal DNA marked with HU-mCherry staining. The density of nucleoid DNA in both the volumetric display and lateral projections is indicated by a color gradient from blue to red. Homologous DNA regions extend from one pole to the other, connected by a semi-continuous thread-like density. The image is taken from [111] under CC BY license.

1.4.6 Macrodomains

Macrodomains (MDs) are large, spatially distinct regions ranging in size from 600 kbp to 1000 kbp. These regions are characterized by unique DNA co-localization markers (chromosomal loci) [10, 22]. While they have been extensively studied in E. coli, similar structures have been observed in other bacterial species as well [22]. High-resolution contact maps suggest that several CIDs merge to form a MD, indicating that MDs represent a higher level of organization beyond CIDs in bacterial chromosomes [10].

In E. coli, four primary MDs have been identified (Figure 1.5A): the Ori MD (around origin of replication (OriC)), the Ter MD (encompassing the terminus region (ter)), the Left MD (adjacent to the Ter MD on the left), and the Right MD (adjacent to the Ter MD on the right). Additionally, there are two non-structured (NS) regions (NS-L and NS-R) flanking the Ori MD, known for their increased flexibility and less organized DNA interactions [10].

Chromosomal DNA within E. coli MDs exhibits restricted movement, preferentially interacting with the NS regions rather than with other MDs. High-resolution contact maps have revealed that contacts between genomic loci occur more frequently within a single MD compared to contacts between genomic loci in different MDs or with genomic loci outside that MD [10]. The positioning of the Ori MD appears to dictate the formation and organization of MDs. Repositioning OriC through genetic manipulation can result in the reorganization of MDs [10]. The replication cycle also influences the positioning of the Left and Right MDs. In general, NS regions are always closer to OriC

than the Left and Right MDs.

1.4.7 The nucleoid

As described in Section 1.1, the bacterial chromosome is compacted into a membrane-free region in the middle of the cell known as the nucleoid. Sedimentation analyses of isolated nucleoids have indicated that the nucleoid is composed of 80 % chromosomal DNA, 10 % protein, and 10 % RNA species in weight [2, 3].

The size of nucleoids varies depending on growth conditions and the age of a bacterial cell [108]. Notably, the nucleoid size is remarkably correlated with the size of the bacterial cell itself [11]. This correlation remains consistent even when there are changes in DNA content or shifts in nutrient conditions [22, 37]. For newborn cells under slow-growth conditions, the nucleoid dimensions (length multiplied by diameter) ranging from approximately 1.6 μm × 0.48 μm to 1.8 μm × 0.8 μm [108]. Fast-growing cells, on the other hand, tend to have slightly larger nucleoids, containing constantly replicating chromosomes [108].

Initial observations using conventional transmission electron microscopy images portrayed the nucleoid as an irregularly shaped region in the cell [10]. However, advanced fluorescence live 3D imaging revealed nucleoids are organized in a specific manner known as radial confinement, adopting the shape of helical ellipsoids [111–113] (Figure 1.5B).

A more detailed examination of 3D fluorescence images also revealed two notable features: curvature and longitudinal high-density regions within the nucleoid [10]. The curvature of the nucleoid shape is attributed to the radial confinement within the cylindrical E. coli cell, which is shorter than the bendable length (persistence length) of the nucleoid [113]. The extension and shortening of high-density regions result in nucleoid-longitudinal density waves throughout the nucleoid [113]. The distribution of fluorescence intensity in the cross-sections showed a density structure composed of curved, high-density areas located at the center and areas of low density around the edges of the nucleoid [113]. Interestingly, experiments showed that altering the cell radius, such as by removing the cell wall or inhibiting cell wall synthesis, leads to corresponding changes in the helical radius and pitch of the nucleoid, further supporting the radial confinement model [113].

In parallel, supporting the radial confinement hypothesis, another study has showed that large segments (approximately 140 kbp in size) excised from the chromosome can be expelled from the nucleoid and positioned at its periphery [114].

CHAPTER 2

Theoretical background: Physics of crowded systems

The purpose of this chapter is to provide a physical framework for the systematic study of MMC effects on tracer species. In Section 1.3, we discussed the heterogeneous nature of cellular environments, characterized not only by the diversity of species types and sizes but also by the interactions among them. To accommodate this heterogeneity, we defined crowded systems as those with a high total volume fraction of macromolecular species, and MMC effects as weak, nonspecific interactions occurring within these systems. Building on these definitions, we now introduce the concept of MMC free energy, which quantifies the impact of MMC effects on tracer particles within a crowded medium.

In this chapter, we will succinctly explore various theoretical approaches for defining MMC free energy. We begin by presenting the definition of MMC free energy in the context of equilibrium thermodynamics.

2.1 Equilibrium thermodynamics

From a thermodynamic viewpoint, the MMC free energy is the difference in the Gibbs free energy when transferring a tracer from an uncrowded (crowder-free) medium to a crowded medium, It is expressed as

$$\Delta\Delta G_{\mathrm{MMC}} \equiv \Delta G_{\mathrm{crowded}} - \Delta G_{\mathrm{uncrowded}}. \tag{2.1}$$

Here, $\Delta G_{\mathrm{crowded}}$ and $\Delta G_{\mathrm{uncrowded}}$ are the change in the Gibbs free energy differences between two states (e.g., folded and open) of the tracer in the crowded and uncrowded media, respectively, while temperature T and pressure P are held constant [45, 48, 49]. It is worth noting that, while we utilized the Gibbs free energy in our definition, other free energies could be equally employed. Importantly, the medium can take the form of a pure solvent (e.g., water) or a pure solution where cosolutes (ions or metabolites)

are considerably smaller in size than the tracer and crowder species, as in the case of a buffer solution.

Using the Gibbs free energy to define MMC allows us to effectively separate MMC effects into enthalpic and entropic contributions

$$\Delta\Delta G_{\text{MMC}} = \Delta\Delta H_{\text{MMC}} - T\Delta\Delta S_{\text{MMC}}, \tag{2.2}$$

where, $\Delta\Delta H_{\text{MMC}}$ and $\Delta\Delta S_{\text{MMC}}$ are the MMC enthalpy and entropy, respectively [47, 48, 78]. An exploration of the enthalpic (or energetic) and entropic contributions of MMC effects within the framework of regular solutions is introduced and discussed in refs. [80, 115]. For crowded systems characterized by preferentially-excluded tracer-crowder interactions (see Section 1.3.2), the MMC free energy simplifies to the depletion free energy. In this scenario, the enthalpic term in Eq. 2.2 vanishes [48].

In the following subsections, we connect the MMC free energy to the microscopic details of a crowded medium. Additionally, we establish a connection between MMC and depletion free energies, particularly in the framework of Asakura-Oosawa (AO) theory.

2.2 Equilibrium statistical mechanics

This subsection starts with a general definition of crowded systems, which can be used to study MMC effects at the microscopic level. This definition allows us to see how various microscopic approaches used to study crowded systems are related to each other. When possible, we also discuss the link between statistical mechanics and thermodynamics framework, in particular Eq. 2.1.

We begin by considering multi-component tracer species immersed in a crowded solution. The tracer is composed of m different components with (effective) sizes (diameters) $\{b_t\} \equiv \{b_1, b_2, \dots, b_t\}$, masses $\{M_t\}$, and numbers $\{N_t\}$ where $\{\dots\}$ show sets of values for different quantities of interest. Also, there are c different crowder species with sizes $\{a_c\}$, masses $\{m_c\}$ and numbers $\{n_c\}$. Finally, the solvent consists of s different types of particles of sizes $\{d_s\}$, masses $\{\hat{m}_s\}$, numbers $\{\hat{n}_s\}$. For simplicity, we assume that all the particles have spherical symmetry; in other words, they are beads of different sizes and masses.

The total number of particles is

$$\mathcal{N} = \mathcal{N}_t + \mathcal{N}_c + \mathcal{N}_s = \sum_{i=1}^{t} N_i + \sum_{i=1}^{c} n_i + \sum_{i=1}^{s} \hat{n}_i \tag{2.3}$$

In our classical system, the dynamical state at a given time t is fully determined with $3\mathcal{N}$ coordinates $\mathbf{r}^{\mathcal{N}} \equiv \mathbf{r}_1, \dots, \mathbf{r}_{\mathcal{N}}$ and $3\mathcal{N}$ momenta $\mathbf{p}^{\mathcal{N}} \equiv \mathbf{p}_1, \dots, \mathbf{p}_{\mathcal{N}}$, collectively representing a phase point in the $6\mathcal{N}$-dimensional phase space. We can write a Hamiltonian of our system $\mathcal{H}$ as

$$\mathcal{H}(\mathbf{r}^{\mathcal{N}}, \mathbf{p}^{\mathcal{N}}) = \mathcal{K}_{\mathcal{N}}(\mathbf{p}^{\mathcal{N}}) + \mathcal{V}_{\mathcal{N}}(\mathbf{r}^{\mathcal{N}}) + \Phi_{\mathcal{N}}(\mathbf{r}^{\mathcal{N}}), \tag{2.4}$$

where,

$$\mathcal{K}_{\mathcal{N}}(\mathbf{p}^{\mathcal{N}}) = \sum_{i=1}^{\mathcal{N}} \|\mathbf{p}_i\|^2/2m_i \tag{2.5}$$

is the total kinetic energy of the system, $\mathcal{V}(\mathbf{r}^{\mathcal{N}})$ is the total inter-particle potential of the system, and $\Phi(\mathbf{r}^{\mathcal{N}})$ is the potential energy, originating from a spatially-varying external field acting on all the particles. Above, $\|...\|$ is the (Euclidean) distance and index i runs over all particles.

We can split the interparticle potential $\mathcal{V}(\mathbf{r}^{\mathcal{N}})$ into various intra- and inter-species interactions

$$\begin{aligned}\mathcal{V}_{int}(\mathbf{r}^{\mathcal{N}}) = \mathcal{V}_t(\mathbf{r}^{\mathcal{N}_t}) + \mathcal{V}_c(\mathbf{r}^{\mathcal{N}_c}) + \mathcal{V}_{tc}(\mathbf{r}^{\mathcal{N}_t}, \mathbf{r}^{\mathcal{N}_c}) \\ \underline{+\mathcal{V}_{ss}(\mathbf{r}^{\mathcal{N}_s}) + \mathcal{V}_{ts}(\mathbf{r}^{\mathcal{N}_t}, \mathbf{r}^{\mathcal{N}_s}) + \mathcal{V}_{cs}(\mathbf{r}^{\mathcal{N}_c}, \mathbf{r}^{\mathcal{N}_s}) + \mathcal{V}_{tcs}(\mathbf{r}^{\mathcal{N}})}\end{aligned} \tag{2.6}$$

Here again, $\mathbf{r}^{\mathcal{N}_\alpha} \equiv \mathbf{r}_1, \dots, \mathbf{r}_{\mathcal{N}_\alpha}$ represents the coordinates of all particles of species α. Each term in the equation above consists of sums over double, triple, or quadruple *bare* potentials. For example, the double sum pertains to the pair bare potential, which is defined as

$$u_{\alpha\beta}(\mathbf{r}_i, \mathbf{r}_j) = u_{\alpha\beta}(r_{ij} \equiv \|\mathbf{r}_j - \mathbf{r}_i\|), \tag{2.7}$$

where α and β denote different particle species.

In practice, $\{\hat{n}_s\}$ are significantly greater than $\{N_t\}$ and $\{N_c\}$. Meanwhile, $\{d_s\}$ and $\{m_s\}$ are smaller and lighter compared to their tracer and crowder counterparts (see Fig. 1.2 and Table 1.1). These physical properties, combined with thermal energy as the energy scale, give rise to various time scales within the system. The substantial separation in these time scales precludes a complete microscopic description. Instead, the separation between microscopic and mesoscopic time scales allows the use of various coarse-graining methods in both theoretical and numerical frameworks [116–118].

If the solvent is neglected, the underlying terms in Eq. 2.6 vanish, resulting in a multicomponent system of tracer and crowder species. This *implicit-solvent* picture is further explored in the following subsection. In this picture, solvent effects can be integrated into different approaches. One approach is through effective potentials that

simulate solvent influence on tracers and crowders. In another approach, the solvent can be modeled as a continuum medium that applies friction and random forces to particles, following Langevin dynamics. We use the first approach to provide a rigorous definition of MMC free energy. In the subsequent chapters, we follow the second approach via computer simulations to study MMC effects on the behavior of a polymer in the implicit-solvent picture.

A further level of coarse-graining involves combining both crowders and solvent particles (ignoring all the terms except the first one in Eq. 2.6) into an effective potential among tracers. This *effective-solvent* or *implicit-crowder* picture implicitly includes crowder and solvent species. Again, both the effective potential and Langevin dynamics approaches are viable for studying tracer particles in a crowded solution. The effective-solvent concept is elaborated in Section 2.2.3.

2.2.1 Implicit-solvent picture

In the implicit-solvent picture, where solvent species are disregarded, the interparticle interactions between tracer and crowder species can be expressed as

$$\mathcal{V}_{\mathcal{N}_t+\mathcal{N}_c}(\mathbf{r}^{\mathcal{N}_t},\mathbf{r}^{\mathcal{N}_c}) = \mathcal{V}_t(\mathbf{r}^{\mathcal{N}_t}) + \mathcal{V}_c(\mathbf{r}^{\mathcal{N}_c}) + \mathcal{V}_{tc}(\mathbf{r}^{\mathcal{N}_t},\mathbf{r}^{\mathcal{N}_c}). \tag{2.8}$$

This equation describes the total interparticle potential in a system comprising only tracer and crowder species, as indicated by the subscript $\mathcal{N}_t + \mathcal{N}_c$. Subsequently, we employ a semi-grand canonical ensemble to describe this system, aiming to determine the free energy associated with MMC effects on tracer particles within a crowded medium.[1]

The semi-grand canonical ensemble is specified by the total volume of the medium V, temperature of the system T, numbers of tracer species $\{N_t\}$, and chemical potentials of crowder species $\{\mu_c\}$. In this ensemble, the system exchanges crowder species with a reservoir through a semipermeable membrane, exclusively permeable to crowder species. The system is at thermodynamic equilibrium when its (osmotic) pressure and the chemical potentials of its crowder species are equal to those of the crowder-only reservoir [121–125]. For this system, the semi-grand canonical partition function is given by [119, 120]

$$\Psi(V,T,\{N_t\},\{\mu_c\}) = \frac{1}{\prod_{i=1}^{t} N_i!\Lambda_i^{3N_i}} \underbrace{\sum_{n_1=0}^{\infty}\cdots\sum_{n_c=0}^{\infty}}_{c} \frac{\overbrace{z_1^{n_1}\dots z_c^{n_c}}^{c}}{\underbrace{n_1!\dots n_c!}_{c}} \mathcal{Z}(V,T,\{N_t\},\{n_c\}), \tag{2.9}$$

[1] Our approach parallels that presented in refs. [119, 120] but is extended to multi-component media.

where $\Lambda_i = \sqrt{2\pi M_i k_B T}$ with k_B as Boltzmann constant is the thermal wavelength of the tracer species i, and $z_j = \exp[\beta\mu_i/\Lambda_j^3]$ with $\beta = 1/k_B T$ is the activity of the crowder species j, $\mathcal{Z}(V,T,\{N_t\},\{n_c\})$ is the configurational integral of the system (see Eq. 2.13), and the product and sum are over the tracer and crowders species, respectively. In this ensemble, the free energy of the system, represented by $X(V,T,\{N_t\},\{\mu_c\})$, is then given by

$$X(V,T,\{N_t\},\{\mu_c\}) = -k_B T \ln[\Psi(V,T,\{N_t\},\{\mu_c\})]. \tag{2.10}$$

and is related to the Helmholtz free energy of its corresponding canonical ensemble, denoted by $A(V,T,\{N_t\},\{n_c\})$, via

$$X(V,T,\{N_t\},\{\mu_c\}) = A(V,T,\{N_t\},\{n_c\}) - \sum_c \mu_c n_c. \tag{2.11}$$

Let's now split that external potential into two terms

$$\Phi_{\mathcal{N}_t+\mathcal{N}_c}(\mathbf{r}^{\mathcal{N}_t},\mathbf{r}^{\mathcal{N}_c}) = \Phi_{\mathcal{N}_t}(\mathbf{r}^{\mathcal{N}_t}) + \Phi_{\mathcal{N}_c}(\mathbf{r}^{\mathcal{N}_c}) \tag{2.12}$$

where $\Phi_{\mathcal{N}_t}$ and $\Phi_{\mathcal{N}_c}$ are the external potentials applied to tracer and crowders species, respectively. The configuration integral of the system is

$$\begin{aligned}\mathcal{Z}(V,T,\{N_t\},\{\mu_c\}) &= \int d\mathbf{r}^{\mathcal{N}_t} d\mathbf{r}^{\mathcal{N}_c} \exp[-\beta(\mathcal{V}_{\mathcal{N}_t+\mathcal{N}_c} + \Phi_{\mathcal{N}_t+\mathcal{N}_c})] \\ &= \int d\mathbf{r}^{\mathcal{N}_t} \exp[-\beta(\mathcal{V}_t + \Phi_{\mathcal{N}_t})]\mathcal{Z}_c(V,T,\{n_c\};\mathbf{r}^{\mathcal{N}_t}),\end{aligned} \tag{2.13}$$

where

$$\mathcal{Z}_c(V,T,\{n_c\};\mathbf{r}^{\mathcal{N}_t}) = \int d\mathbf{r}^{\mathcal{N}_c} \exp[-\beta(\mathcal{V}_c + \mathcal{V}_{tc} + \Phi_{\mathcal{N}_c})]. \tag{2.14}$$

is the configuration integral of the crowder species for a given configuration of the tracer species denoted by ";" in the definition of $\mathcal{Z}_{\mathcal{N}_c}$. The grand canonical ensemble of the crowder species for $\mathcal{N}_t$ tracers at a fixed configuration is

$$\Xi_c(V,T,\{\mu_c\};\mathbf{r}^{\mathcal{N}_t}) = \underbrace{\sum_{n_1=0}^{\infty} \dots \sum_{n_c=0}^{\infty}}_{c} \frac{\overbrace{z_1^{n_1} \dots z_c^{n_c}}^{c}}{\underbrace{n_1! \dots n_c!}_{c}} \mathcal{Z}_c(V,T;\mathbf{r}^{\mathcal{N}_t}) \tag{2.15}$$

and it is related to the crowder-only grand potential with

$$\Omega_c(V,T,\{\mu_c\};\mathbf{r}^{\mathcal{N}_t}) = -k_B T \ln[\Xi_c(V,T,\{\mu_c\};\mathbf{r}^{\mathcal{N}_t})]. \tag{2.16}$$

Using Eqs. 2.13, 2.15 and 2.16, we can write Eq. 2.9 in the following form

$$\mathcal{Q}(V,T,\{N_t\},\{\mu_c\}) \equiv \frac{\int d\mathbf{r}^{\mathcal{N}_t} \exp[-\beta\mathcal{V}_t^{\text{eff}}(V,T,\{\mu_c\},\mathbf{r}^{\mathcal{N}_t})]}{\prod_{i=1}^t N_i! \Lambda_i^{3N_i}}, \tag{2.17}$$

where

$$\mathcal{V}_t^{\text{eff}}(V,T,\{\mu_c\},\mathbf{r}^{\mathcal{N}_t}) = \underline{\mathcal{V}_t(\mathbf{r}^{\mathcal{N}_t}) + \Phi_{\mathcal{N}_t}(\mathbf{r}^{\mathcal{N}_t})} + \Omega_c(V,T,\{\mu_c\};\mathbf{r}^{\mathcal{N}_t}) \tag{2.18}$$

is an effective interaction energy for the tracer-only system. The first term in this equation is the bare pair potential between tracers, the second term is the external potential applied to the tracers, and the last can be viewed as an effective interaction among tracers induced by crowder species. This last term depends on the thermodynamic state variables V, T, and $\{\mu_c\}$. Our approach suggests the semi-grand partition of the system, given by Eq. 2.9, is equivalent to the canonical partition function of tracer species, i.e., $\mathcal{Q}(V,T,\{N_t\},\{\mu_c\})$ in Eq. 2.17, for which the total potential energy is given by Eq. 2.18. Then, an effective Helmholtz free energy is given by

$$A_{\text{eff}}(V,T,\{N_t\},\{\mu_c\}) \equiv -k_B T \ln[\mathcal{Q}(V,T,\{N_t\},\{\mu_c\})], \tag{2.19}$$

where, we introduce $\mathcal{Q}$ and A_{eff} for convenience when closed-form or approximate expressions are used for $\mathcal{V}_t^{\text{eff}}$ and Ω_c [120].

Above, we split the configurational partition function into inter-species components without making any assumptions about the nature of the interparticle potentials. Thus, our approach offers a rigorous method for defining MMC free energy, as presented below. The only limitation of our approach is the assumption we made about the separation of the partition function into kinetic and configurational parts, based on the spherical, monatomic nature of the particles [126].

2.2.1.1 Connection with the equilibrium thermodynamics

We utilize Eq. 2.18 to connect our statistical mechanical description of MMC effects in the implicit-solvent picture with the thermodynamic definition of the MMC free energy, as outlined in Section 2.1. Considering two distinct configurations of the tracer species, the change in MMC free energy is expressed by

$$\Delta\Omega_{\text{MMC}} = \Delta\Omega_c(V,T,\{\mu_{n_c}\};\mathbf{r}^{\mathcal{N}_t}), \tag{2.20}$$

where, for the first two terms underlined in Eq. 2.18, the difference between the two configurations in the crowded state cancels out with their equivalent terms in the uncrowded state.

2.2.2 Crowded systems with preferentially-excluded crowder-tracer interactions

Crowded systems with preferentially-excluded crowder-tracer interactions represent the earliest approximations for cellular environments [42, 43]. These systems were

initially explored by Asakura and Oosawa, who investigated the effects of nonadsorbing macromolecules on colloidal particles [127, 128]. In such systems, MMC effects solely arise from excluded-volume interactions between tracers and crowders, resulting in attractive depletion forces among tracers, which are entropically induced by the surrounding crowders.

Within the implicit-solvent picture, this section provides a concise overview of depletion forces and their connections with MMC effects within crowded systems. Specifically, we present the AO theory as a widely used framework for studying crowded systems.

2.2.2.1 The binary mixture of hard spheres

The binary mixture of hard spheres (HSs) represents the most fundamental model of a crowded system, characterized by preferentially excluded interactions between crowders and tracers. This model is instrumental in understanding the foundational interactions within more complex crowded media.Within the implicit-solvent picture, this system is characterized by the HS potential

$$u_{\mathrm{HS}}(r_{ij}) = \begin{cases} \infty & r_{ij} \leq \sigma_{ij} \\ 0 & r_{ij} > \sigma_{ij} \end{cases}, \tag{2.21}$$

where $\sigma_{ij} = (\sigma_i + \sigma_j)/2$ denotes the effective interaction range for particles i and j.[2] In this mixture, σ_i and σ_j represent the (effective) sizes of the tracer and crowder species, respectively, designated as b_1 and a_1 in our notation. The three terms in the total potential energy, Eq. 2.8, for such a system are:

$$\mathcal{V}_t(\mathbf{r}^{N_t}) = \sum_{i=1}^{\mathcal{N}_t} \sum_{j>i}^{\mathcal{N}_t} u_{HS}(r_{ij}), \tag{2.22a}$$

$$\mathcal{V}_{tc}(\mathbf{r}^{\mathcal{N}_t}, \mathbf{r}^{\mathcal{N}_c}) = \sum_{i=1}^{\mathcal{N}_t} \sum_{j=\mathcal{N}_t+1}^{\mathcal{N}_t+\mathcal{N}_c} u_{HS}(r_{ij}), \tag{2.22b}$$

$$\mathcal{V}_c(\mathbf{r}^{\mathcal{N}_c}) = \sum_{i=\mathcal{N}_t+1}^{\mathcal{N}_t+\mathcal{N}_c} \sum_{j>i}^{\mathcal{N}_t+\mathcal{N}_c} u_{HS}(r_{ij}). \tag{2.22c}$$

Below, our discussion on the depletion forces is built upon this system.

[2] Here, we limit ourselves to additive HS system. For nonadditive HS systems, see ref. [129].

2.2.2.2 Depletion and MMC potentials

In a crowded system with preferentially-excluded crowder-tracer interactions, the depletion potential between *two* tracers [128] is defined as the difference in the grand canonical potential of crowder species, at the infinite dilute limit of tracer species, between a configuration in which a second tracer is in the proximity of a fixed tracer and one in which the second tracer is at infinite distance from the first tracer [124, 130–133]. Using the implicit-solvent picture, we can express the depletion potential as

$$w_{\text{DEP}}(V,T,\{\mu_{n_c}\};r) = \lim_{\{\rho_t\}\to 0}\Big[\Omega_c(T,\{\mu_{n_c}\};r) - \Omega_c(V,T,\{\mu_{n_c}\};r\to\infty)\Big], \tag{2.23}$$

where $r = \|\mathbf{r}_2 - \mathbf{r}_1\|$ is the distance between the two tracers and $\{\rho_t\}$ is the set of the bulk number densities of tracer species.[3]

It is important to note that our definition of the depletion attraction is beyond the implicit-solvent picture and can be used when solvent species are present. Based on this definition, we can introduce the MMC potential, $w_{\text{MMC}}(V,T,\{\mu_{n_c}\};r)$, which has the same definition as the depletion potential, except we drop the condition of preferentially-excluded crowder-tracer interactions. Mathematically, the MMC potential is given by the same equation, i.e., Eq. 2.23.

Our definitions of the depletion and MMC potentials are equivalent to the MMC free energy of two tracers if we compare $r' = r$ and $r' = \infty$ configurations:

$$w_{\text{MMC}}(T,\{\mu_{n_c}\};r) = \Delta\Omega_{\text{MMC}}(V,T,\{\mu_{n_c}\};\mathbf{r}^{\mathcal{N}_t})|_{r'=\infty}^{r'=r} \quad (\mathcal{N}_t = 2). \tag{2.24}$$

2.2.2.3 Free volume theory

The free volume theory (FVT) is based on the idea that, in the absence of additional crowders, a rigid crowder is only able to freely move in a portion of the total volume of a system, due to the space occupied by rigid tracers in that system [123, 125, 136, 137]. In other words, in the semi-grand canonical ensemble, the equilibrium (osmotic) pressure of a crowded system is equal to that of the crowder-only reservoir. This equivalence, combined with the definition of the grand potential, $\Omega = -PV$ (where P is the thermodynamic pressure), suggests that we may define an average free volume for crowders, $\langle V_{\text{free}}(\mathbf{r}^{\mathcal{N}_t})\rangle$. This volume is a complex function of the tracer configurations, $\mathbf{r}^{\mathcal{N}_t}$, within volume V. Using Widom's insertion theorem [138], $\langle V_{\text{free}}(\mathbf{r}^{\mathcal{N}_t})\rangle$ can be found by inserting a crowder in the tracer-only system. For sufficient dilution of tracers, $\langle V_{\text{free}}(\mathbf{r}^{\mathcal{N}_t})\rangle$ can be estimated by its minimum (unperturbed) value, $\langle V_{\text{free}}(\mathbf{r}^{\mathcal{N}_t})\rangle_0$,

[3] There are three other ways to define the depletion potential: The force method [130], extended Gibbs adsorption equation [125, 134], and potential distribution theorem [135].

in the absence of crowders [139, 140]. Accordingly, the grand potential of the crowder-only system, Eq. 2.16, is

$$\Omega_c(V, T, \{\mu_{n_c}\}; \mathbf{r}^{\mathcal{N}_t}) = -\Pi_c^{\text{res}} \langle V_{\text{free}}(\mathbf{r}^{\mathcal{N}_t}) \rangle_0, \tag{2.25}$$

where Π_c^{res} is the (osmotic) pressure of the crowder species in the reservoir [131, 136, 140, 141].

Given our conservative choice of the average free volume, Eq. 2.25 provides a lower limit on the grand potential of crowders. This equation implies that tracers influence the configurations of crowders, impacting their grand potential (as seen in Eq. 2.16). Consequently, the system attempts to rearrange itself to minimize this perturbation, maximizing the available free volume for crowders and reducing its overall free energy. This entropy-driven self-arrangement of the system is inherently incorporated in the FVT. The unperturbed average free volume $\langle V_{\text{free}}(\mathbf{r}^{\mathcal{N}_t}) \rangle_0$ can be derived from the scaled particle theory (SPT) and fundamental-measure theory (FMT) [140]. In practice, the FVT is valid for $q \equiv \max(\{a_c\})/\max(\{b_t\}) < 0.2$ [125].

2.2.2.4 Asakura-Oosawa theory

The Asakura-Oosawa (AO) theory describes the interactions between large spherical tracers in a solution containing small crowders [127, 128]. In their pioneering work, Asakura and Oosawa proposed that when two tracers come close to each other, the crowders are excluded from the region between them, creating a crowder-depleted zone. This exclusion leads to an osmotic pressure difference, resulting in an effective attractive force between the tracers, known as the depletion force. In the original AO model, crowders can penetrate each other, but they have excluded-volume interactions with tracers (see Fig. 2.1).

In parallel to the above thermodynamical perspective, one can explain the depletion attraction from an entropic perspective. In Fig. 2.1, each large sphere has a *depletion layer* (dashed blue circle) from which the centers of small spheres are excluded. When two large spheres approach each other, their depletion layers overlap (the *overlap volume*, shaded in magenta), increasing the volume available to crowders. While the translational entropy of large spheres decreases, that of crowders increases; however, due to the larger number of crowders, their increased entropy maximizes the entropy of the system as well, favoring the aggregation of large spheres.

Using the binary HS solution introduced in Section 2.2.2.1, we describe the AO theory: the AO system consists of a binary HS where crowders are penetrable hard spheres (PHSs) themselves but have HS interactions with tracers. Therefore, $u_c(r_{ij}) = 0$, and

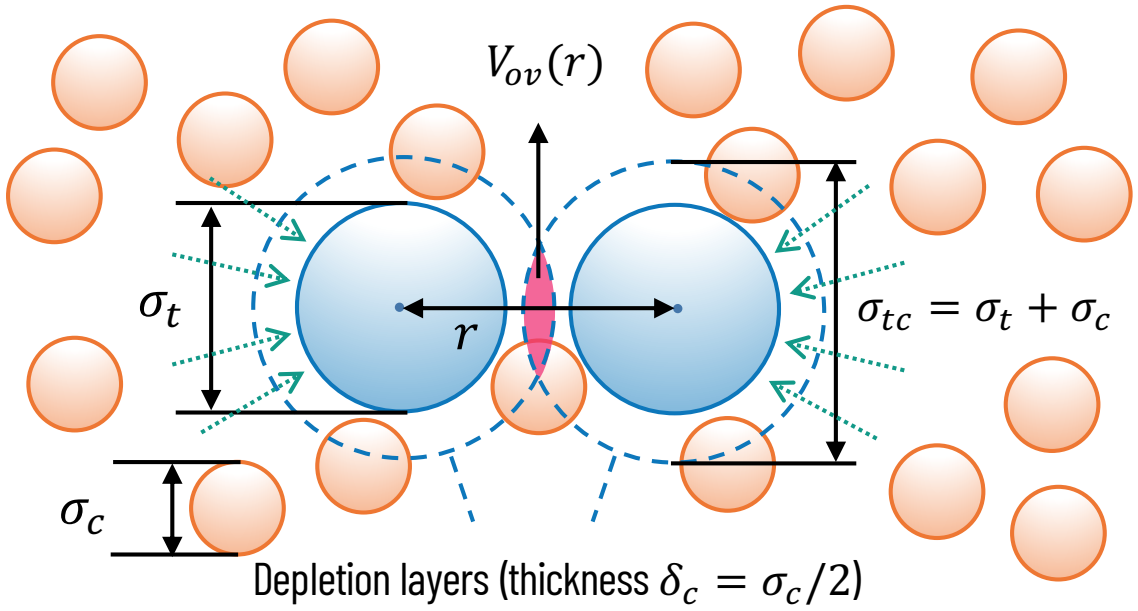


FIGURE 2.1 Two tracers (two large hard spheres with radius σ_t), in the presence of crowders (small hard spheres with radius σ_c). Each tracer has a depletion layer (dashed circle) with a size $\sigma_{tc} = \sigma_t + \sigma_c$ from which the centers of crowders are excluded. The overlap volume (hashed in magenta), $V_{\text{ov}}(r)$, of the depletion layers has the shape of a lens, the size of which depends on the distance between tracers, r. In the Asakura-Oosawa theory, crowders are treated as penetrable hard sphere, imposing an unbalanced osmotic pressure Π (dotted green arrows) between the hard spheres, which in turn results in an attractive force between them.

thus the last term in Eq. 2.8 vanishes. Moreover, with only two tracers in the system, the problem reduces to a geometrical one: finding the free volume in which the centers of small spheres can freely move. Therefore, we have

$$V_{\text{free}}(r) = \begin{cases} V - \dfrac{8\pi}{3}\sigma_{tc}^3 + V_{\text{ov}}(r) & \sigma_t \le r \le 2\sigma_{tc} \\ V - \dfrac{8\pi}{3}\sigma_{tc}^3 & r > 2\sigma_{tc} \end{cases}, \tag{2.26}$$

where $\sigma_{tc} \equiv (\sigma_t + \sigma_c)/2$, with σ_t and σ_c corresponding to b_1 and c_1, respectively, as defined in Section 2.2. Here, r represents the distance between two tracers, and

$$V_{\text{ov}}(r) = \begin{cases} \dfrac{4\pi}{3}\sigma_{tc}^3[1 - \dfrac{3}{4}\dfrac{r}{\sigma_{tc}} + \dfrac{1}{16}(\dfrac{r}{\sigma_{tc}})^3] = \dfrac{\pi}{6}[2\sigma_{tc} - r]^2[2\sigma_{tc} + \dfrac{r}{2}] & \sigma_t \le r \le 2\sigma_{tc} \\ 0 & r > 2\sigma_{tc} \end{cases},$$

is the overlap volume of two spheres with size σ_{tc} (see Fig. 2.1) [125, 128].

In the AO theory, $\langle V_{\text{free}}(\mathbf{r}^{\mathcal{N}_t})\rangle_0 = V_{\text{free}}(r)$, so we can now employ Eq. 2.25 to find the grand potential of the crowder-only system for a given configuration of two tracers:

$$\Omega_{c,\text{AO}}(V, T, \{\mu_{n_c}\}; r) = -\Pi_c^{\text{res}} V_{\text{free}}(r), \tag{2.27}$$

where Π_c^{res} is the osmotic pressure of crowders. The original AO theory is valid in the limit of a dilute concentration of tracers in a dilute solution of crowders, where the van't Hoff relation holds for the osmotic pressure of crowders

$$\Pi_c^{\text{res}} = k_b T \rho_c = k_b T \phi_c / v_c, \tag{2.28}$$

where ρ_c, ϕ_c, and v_c are the bulk number density, bulk volume fraction, and volume of crowders, respectively [129–131, 142].

2.2.2.4.1 Asakura-Oosawa depletion potential Using Eq. 2.23, we can derive the well-known attractive AO depletion potential

$$w_{\text{AO}}(r) = \begin{cases} -k_B T \rho_c V_{\text{ov}}(r) & \sigma_t \leq r \leq 2\sigma_{tc} \\ 0 & r > 2\sigma_{tc} \end{cases}, \tag{2.29}$$

where the van't Hoff's equation, $\Pi_c^{\text{res}} = k_B T \rho_c$, is used. The AO has a maximum of

$$w_{\text{AO, max}} = w_{\text{AO}}(r = \sigma_t) = -k_B T \phi_c (1 + 3\sigma_t / 2\sigma_c) \tag{2.30}$$

when the two tracers are at contact ($r = \sigma_t$).

In literature, the AO potential is generalized for two different scenarios: (a) Two rigid objects of arbitrary shapes, and (b) A rigid object and a rigid confining wall of arbitrary shapes.. In these scenarios, the AO potential is

$$w_{\text{AO, gen}}(\mathbf{r}) = \begin{cases} -k_B T \rho_c V_{\text{ov, gen}}(\mathbf{r}) & \mathbf{r} \in \mathcal{D}_{\text{ov, gen}} \\ 0 & \text{otherwise} \end{cases}, \tag{2.31}$$

where $V_{\text{ov, gen}}(\mathbf{r})$ and $\mathcal{D}_{\text{ov, gen}}$ are the overlap volume and domain of the two rigid bodies.

2.2.2.4.2 Asakura-Oosawa free energy In literature, the AO potential, Eq. 2.29, is often used as the MMC free energy. Following the assumptions employed for Eq. 2.24, this equivalence is valid if we assume that two tracers are far separated in a crowded solution (the reference configuration, where $r = \infty$ and $w_{\text{MMC}} = 0$) and then brought to distance r by MMC effects.

2.2.2.5 The limitations of the AO theory

The AO theory predicts the depletion potential is attractive, increasing from a minimum at contact ($r = \sigma_t$) to a maximum at $r = \sigma_t + \sigma_c$, and then vanishes. However, density functional treatments of HS mixtures [124] and MD simulations of HS [119]

and purely-repulsive Lennard-Jones (LJ) mixtures [143] have revealed the depletion potential follows a pattern of increasing from a minimum at contact ($r = \sigma_t$) to a maximum at $r = \sigma_t + \sigma_c$ and subsequently exhibiting decreasing oscillatory behavior with a periodicity of approximately σ_c [133, 135].

Depletion interactions are many-body in nature. Extensive studies on binary HS mixtures have identified two fundamental mechanisms giving rise to many-body effects [129, 132]: (a) Crowder-crowder correlations can induce interactions between more than two tracers, and (b) Overlaps between three or more depletion layers. The first mechanism, which always manifests as the layering of crowders around a tracer, leads to a potential profile characterized by decreasing oscillations [129, 132]. In solutions, crowder polydispersity can attenuate this oscillatory potential profile, leaving only the first potential barrier [144, 145]. The contribution from the second mechanism becomes negligible in the limit of an infinitely dilute solution of tracers. Furthermore, it has been demonstrated that three-body and higher-order overlaps do not occur in HS fluids when $q \leq \frac{2\sqrt{3}}{3} - 1 \approx 0.156$, where $q \equiv \max(\{a_c\})/\max(\{b_t\})$ represents the maximum size ratio, and $\max(\dots)$ denotes the maximum function [142].

The AO theory treats crowders as PHS and therefore neglects crowder-crowder correlations, with only the second mechanism contributing to many-body interactions. Concerning this second mechanism, a density functional treatment has found that the triplet-body term exhibits oscillatory behavior similar to the pair depletion potential, with the same decay length [146]. However, the decay becomes slower at higher bulk volume fractions of crowders [146]. Additionally, each subsequent term is almost one order of magnitude smaller than its predecessor [146].

In the modified AO theory, crowders are impenetrable hard spheres (IHSs), interacting with each other via a HS potential [125, 129]. Using a virial expansion, the osmotic pressure of IHSs cab be expressed as [120]

$$\beta\Pi_c^{\text{res}} = \rho_c + \sum_{i=2} \mathcal{B}_i \rho_c^i, \tag{2.32}$$

where $\{\mathcal{B}_n\}$ represents the virial coefficients. In the implicit-solvent picture, Π_c^{res} for the crowders is formally equivalent to the pressure of an equivalent hard-sphere fluid. For such a fluid, the virial expansion of Π_c^{res} can be replaced with the Carnahan-Staring (CS) equation [147], SPT [148], or other closed-form expressions for the pressure of a HS fluid [120]. While the modified AO theory successfully incorporates many-body crowder-crowder interactions at the whole range of the bulk crowder volume fractions at equilibrium, it lacks many-body tracer-tracer interactions. Therefore, the modified version is accurate in the context of infinite dilution of tracers [125, 132].

2.2.3 Effective solvent picture

As discussed at the end of Section 2.2.2.2, MMC potential is fundamentally many-body in nature. However, under certain conditions, it can be simplified to a pair potential denoted as $w_{\text{MMC}}(\mathbf{r}_i, \mathbf{r}_j)$ (see Eq. 2.23), for which an analytical expression is available, particularly based on the AO theory.

In the effective-solvent picture, we further disregard both crowder-crowder and tracer-crowder interactions. Consequently, Eq. 2.6 can be reduced to the following form

$$\mathcal{V}_{int}(\mathbf{r}^{\mathcal{N}}) = \mathcal{V}_{\mathcal{N}_t}(\mathbf{r}^{\mathcal{N}_t}) = \sum_{i=1}^{\mathcal{N}_t}\sum_{j>i}^{\mathcal{N}_t} v(\mathbf{r}_i, \mathbf{r}_j) + \sum_{i=1}^{\mathcal{N}_t}\sum_{j>i}^{\mathcal{N}_t}\sum_{k>i>j}^{\mathcal{N}_t} u(\mathbf{r}_i, \mathbf{r}_j, \mathbf{r}_k) + \dots, \tag{2.33}$$

where, the total pair potential $v(\mathbf{r}_i, \mathbf{r}_j)$, expressed as,

$$v(\mathbf{r}_i, \mathbf{r}_j) = u(\mathbf{r}_i, \mathbf{r}_j) + w_{\text{MMC}}(\mathbf{r}_i, \mathbf{r}_j) \tag{2.34}$$

is the sum of the total bare pair potential between two tracers, $u(\mathbf{r}_i, \mathbf{r}_j)$, and the MMC pair potential, $w_{\text{MMC}}(\mathbf{r}_i, \mathbf{r}_j)$.

CHAPTER 3

The interdependence between the spatial organization of a biopolymer and the distribution of crowders under confinement

3.1 Introduction

MMC effects arise when macromolecules within an environment occupy a significant volume fraction of the environment, limiting the available space for molecular diffusion and interactions [41, 69, 74, 149, 150]. These effects, fundamentally entropic, predominantly manifest themselves thorough the so-called depletion forces [125, 127, 128]. Cell interiors are the most obvious examples of crowded media [31, 73, 151]; for instance, cytoplasmic macromolecular concentration ranges from 50 g L^{-1} to 400 g L^{-1} in E. coli, occupying up to 40 % of the cell volume [25–30]. Within cells, depletion forces originate from excluded-volume interactions between sub-molecular units, molecules, and molecular complexes [39, 152]. Cellular MMC influences processes ranging from biomolecular aggregation [49] to cell growth [153].

In particular, MMC has garnered attention in the context of bacterial chromosome organization, for which much of our understanding is owned to the polymer models of the bacterial chromosome [35, 36, 39, 40, 152, 154–157]. MMC tends to compact single polymer chains, such that the degree of compaction and the nature (abrupt vs. continuous) of the transition depends on polymer flexibility, the size and volume fraction of crowders, and whether the polymer is confined or not [35, 36, 154, 158–162]. As it turns, the system undergoes phase separation into monomer-rich (chain-occupying) and crowder-only regions [36, 161].

A crucial aspect to understand the role of MMC in chromosome organization involves systematically analyzing the interdependence between the spatial distributions of monomers and crowders. For flexible polymers, chain compaction due to MMC effects varies with the crowder size a_c relative to the monomer size a_m. In the $a_c \leq 0.5a_m$

regime, MMC effects scale with the ratio $a_m\phi_c/a_c$ in unconfined and confined spaces, where ϕ_c is the bulk volume fraction of crowders [36, 154, 158–162]. The ratio $a_m\phi_c/a_c$ supports the view that smaller crowders are better at compacting a polymer. Notably, in this regime, MMC effects are independent of confinement details. Consequently, MMC effects can be seen as reducing solvent quality and can be fully absorbed into the effective excluded volume of monomers (the so-called effective-solvent picture), implying the locality of MMC effects [160]. Conversely, in the $a_c \geq 4a_m$ regime, chain compaction enhances with ϕ_c in an unconfined space and shows insensitivity to a_c [160, 161]. In this regime, the effective-solvent picture is still valid up to $a_c/a_m < 20$, provided that the chain size is sufficiently larger than a_c.

In unconfined spaces, a "density sum rule" emerges as a fundamental principle, linking the spatial distributions of monomers and crowders [161]. This rule extends beyond the simple two-body picture that underlies the understanding of MMC effects via the depletion interaction between monomer pairs, simultaneously capturing the entropy of both monomers and crowders. Consequently, it provides a more comprehensive understanding of MMC effects.

In this chapter, employing MD simulations, we investigate MMC effects on chain compaction and the interdependence between the spatial distributions of monomers and crowders. Our focus is on cylindrically-confined systems where $a_c > 0.5a_m$, a domain overlooked in previous studies. Our findings indicate that, at a constant ϕ_c, larger crowders more effectively compact a polymer chain up to $a_c = 4a_m$, beyond which chain compaction becomes insensitive to the value of a_c. Additionally, when the ratio of the cylinder effective diameter to the crowder size, $\kappa \equiv (D - a_c)/a$, is significantly large, confinement has minimal effects on MMC. Given the size ratio of cellular crowders to naked chromosomal DNA typically ranges from $0.5a_m$ to $10a_m$ [20, 65, 96, 163–165], our results underscore the varying impact of MMC across different hierarchies of bacterial chromosome organization.

Furthermore, our findings expand the validity of the density sum rule to cylindrically confined spaces, assuming a sufficiently large κ, thereby affirming that MMC effects are localized and largely unaffected by the geometry of confinement. This is in alignment with previous observations in unconfined spaces [161]. Importantly, our findings clarify the observed interdependence between the spatial distributions of chromosomal DNA and bimolecular crowders within E. coli cells [38, 166–171], offering insights into the intracellular organization.

3.2 Computational modeling

3.2.1 A polymer model

We examine the behavior of a flexible polymer within a cylindrical tube. This approach is akin to models our group has previously explored [36, 155, 161]. As depicted in Fig. 3.1, the polymer consists of N structureless spherical (bead-like) monomers, each with a size (diameter) a_m. These monomers experience depletion forces due to N_c bead-like crowders of size a_c each. We use the farthermost distance $L \equiv z_{\max} - z_{\min}$ [172, 173] as the chain size, where z represents the longitudinal position of monomers, with $z_{\min}$ and $z_{\max}$ marking the leftmost and rightmost positions, respectively [172, 173]. The confining cylinder is characterized by a size D and a length Z, with its wall composed of beads with a diameter of a_w. However, to calculate bulk volume fractions, the effective cylinder size is defined as $D_{\text{eff},\alpha} = D - a_\alpha$, where α is either "m" or "c"; for confined spaces, this effective cylinder determines the volume in which the center of a particle can be placed. Accordingly, the bulk number density and volume fraction of crowders are $\rho_c \equiv N_c/V_{\text{eff},c}$ and $\phi_c \equiv N_c(\pi a_c^3/6)/V_{\text{eff},c}$, respectively.

Ideally, we are interested in exploring the biologically-relevant space of parameters. However, due to physical and physiological conditions within bacterial cells, the mapping procedure is far from trivial. Factors such as growth conditions can significantly influence the cell size, affecting parameters D and Z in our model [37, 56, 57, 65]. Under minimal growth conditions, for example, the E. coli chromosome remains unreplicated, and the average dimensions ($D \times Z$) of the E. coli cell and nucleoid measure 0.5 µm × 2.5 µm and 0.21 µm × 2.21 µm, respectively, as detailed in table 1 of ref. [57].

The E. coli chromosome, approximately 4.6 Mbp in length, introduces further complexities into our model. Unlike isolated DNA segments, chromosomal DNA exhibits heterogeneous width (see Chapter 4 and ref. [40]). Factors such as ionic strength [5, 95, 96], DNA supercoiling [5, 24, 33, 174], and DNA interactions with DBPs [40, 175] are the key factors influencing a_m and N. For instance, modeling the chromosome as a semi-flexible chain suggests $N \approx 642\,000$, with each monomer having a hydrodynamic diameter of 2.4 nm and encompassing 7.23 base pairs of DNA [95]. Alternatively, the chromosome can be seen as a semi-flexible nucleoprotein chain with $N \approx 1325$ monomers, each 35 nm in size and comprising 3599 base pairs [175]. In scenarios where the E. coli chromosome behaves as a flexible chain of SUs as monomers, N might be around 100 SUs, with each monomer being 70 nm in size and approximately 50 kbp in length [108].Given the non-uniform nature of DNA supercoiling across the chromo-

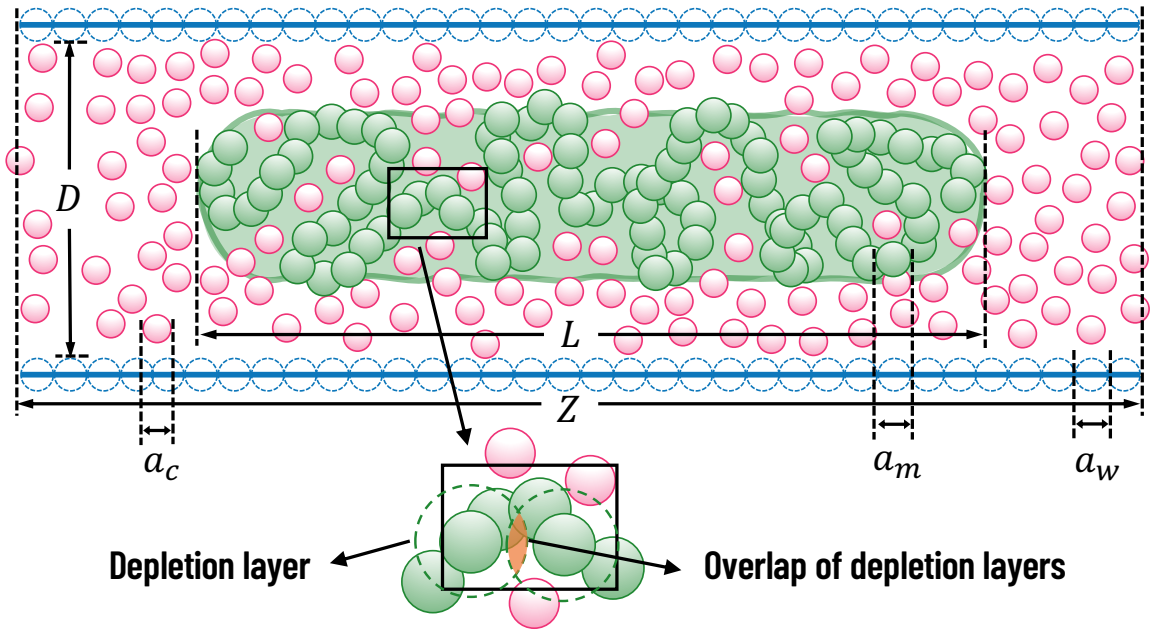


FIGURE 3.1 A schematic representation of a model polymer chromosome comprising N monomers with size (diameter) a_m. The polymer is confined within an open-ended cylinder of size D and length Z, with its wall composed of beads with a size of a_w. Under confinement, the farthermost distance of the polymer, L, is reported as its length [172, 173]. The cylinder is populated with inert crowders of size a_c and bulk volume fraction ϕ_c. Crowders exert exclude-volume effects on themselves and monomers. Illustrated at the bottom of the figure, each monomer has a depletion layer (dashed circle) of size $a_m + a_c$ from which the centers of crowders are excluded. The overlaps of depletion layers around monomers increase the available volume for crowders to translate, which in turn increases the overall entropy of the system. This process results in an entropic force known as depletion force [127, 128]. From a thermodynamical perspective, the overlaps of depletion layers perturb otherwise homogeneous osmotic pressure of crowders around each monomer, resulting in a net inwards osmotic pressure gradient that brings monomers together.

some [22], the choice between modeling it as a flexible polymer, [36], a semi-flexible polymer [156], or a flexible-semiflexible copolymer [176] depends on the specific aspects of the problem being addressed.[1]

Cellular macromolecules exhibit diverse physical properties, such as size, shape, and net charge, complicating the modeling of cellular environments [58, 177] (see Section 1.3.1). In E. coli cells, the average protein size is 4.6 nm [62, 68], whereas molecular machines like ribosomes or RNAP can reach up to 25 nm [53] (see Table 1.1). Despite this diversity, research has demonstrated that representing crowders as structureless beads of specific sizes (a_c) and volume fractions (ϕ_c) effectively captures the essence of MMC effects, particularly nonspecific excluded-volume interactions [35, 36,

[1]Ref. [176], while not directly related to modeling bacterial chromosomes, provides insights into employing flexible-semiflexible copolymers for such studies.

69, 154, 162]. Depletion forces exerted by inert polymeric crowders have been shown to compact E. coli chromosomes to their in-vivo sizes [35, 162]. Computer simulations with inert bead-like spherical crowders align with experimental outcomes, underscoring the validity of this modeling approach [36, 154, 162]. Furthermore, the impact of crowder size polydispersity can be accurately simulated using a weighted (rescaled) average across different crowder species [36, 162]. It is important to note, however, that the shape of crowders, e.g., bead-like vs short polymeric, also alters MMC effects [178]. Here, we study bead-like crowders with size ranging between 4.6 nm to 23 nm [53, 62, 68].

3.2.2 Simulation method

We use MD simulations to study a flexible linear polymer in the presence of N_c crowders with size a_c under cylindrical confinement. The polymer is modeled as a self-avoiding bead-spring chain with N monomers of size a_m. We impose the cylindrical confinement on particles via an open-ended cylindrical simulation region of size D with the periodic boundary condition along the longitudinal axis. The cylindrical wall is composed of imaginary beads, which are of the same kind of monomers. To minimize finite-size effects, the cylinder length Z is three times larger than the estimated equilibrium farthermost distance of the chain $L(\phi_c)$ at a fixed value of the bulk volume fraction of crowders ϕ_c [173, 179].

Let r_{ij} be the center-to-center distance between two particles i and j, then a pair of particles interact via a truncated and shifted LJ potential

$$U_{TSLJ,\alpha\beta}(r_{ij}) = \begin{cases} U_{LJ}(r_{ij}) - U_{LJ}(r_{cut,\alpha\beta}) & \text{for } r \le r_{cut,\alpha\beta} \\ 0 & \text{otherwise} \end{cases}, \tag{3.1}$$

where $U_{LJ}(r_{ij})$ is the (conventional) LJ potential

$$U_{LJ}(r_{ij}) = 4\varepsilon_{\alpha\beta}\left[\left(\frac{\sigma_{\alpha\beta}}{r_{ij}}\right)^{12} - \left(\frac{\sigma_{\alpha\beta}}{r_{ij}}\right)^{6}\right]. \tag{3.2}$$

Above, $\sigma_{\alpha\beta} = (\sigma_\alpha + \sigma_\beta)/2$ is the collision size (diameter) at which $U_{LJ}(\sigma_{\alpha\beta}) = 0$ (the LJ potential changes sign), and $\varepsilon_{\alpha\beta}$ is the depth of the LJ potential at $r_{min,\alpha\beta} = 2^{1/6}\sigma_{\alpha\beta}$ (the inter-species attraction strength). Here, subscripts $\alpha, \beta \in \{m, c, w\}$ refer to monomers ($\sigma_m = a_m = \sigma$), crowders ($\sigma_c = a_c$), and wall-shaping particles ($\sigma_w = a_m = \sigma$), respectively, where $\sigma_\alpha \equiv \sigma_{\alpha\alpha}$ is often referred to as the particle size and σ is the length unit. In Eq. 3.1, our choice of the cutoff distance $r_{cut,\alpha\beta} = r_{min,\alpha\beta}$ leads to the so-called fully-repulsive Weeks-Chandler-Anderson (WCA) potential that

conveniently considers excluded-volume effects between particles [180]. We set all the $\varepsilon_{\alpha\beta} = \varepsilon$, with ε as the unit of energy, except for $\varepsilon_{mw} = \varepsilon_{wm} = 5.0\varepsilon$ to prevent chain-wall adhesion [36, 155].

To enforce chain connectivity, there is the finitely extensible nonlinear elastic (FENE) potential between the adjacent monomers along the chain backbone [181]

$$U_{FENE}(r_{ij}) = \begin{cases} -\frac{1}{2}k_0 r_0^2 \ln\left[1 - (\frac{r}{r_0})^2\right] & r \leq r_0 \\ 0 & r > r_0 \end{cases}, \tag{3.3}$$

where the spring constant $k_0 = 30.0\varepsilon/\sigma^2$ and the equilibrium bond size $r_0 = 1.5\sigma$ to prevent monomers from crossing [182, 183].

In addition to the above-mentioned conservative interactions, all the particles are subjected to the viscous and random forces, both resulting from collisions with implicit solvent particles at a fixed temperature T; as a result, the motion of i-th particle is described with the Langevin equation

$$m_i \frac{d^2\vec{r}_i}{dt^2} = -\vec{\nabla}_i U_{tot}(\{\vec{r}_j\}) - \gamma m_i \frac{d\vec{r}_i}{dt} + \vec{W}_i(t), \tag{3.4}$$

where m_i, $\vec{r}_i$, and $\vec{\nabla}_i$ are the particle mass, the particle position, and the gradient operator with respect to the particle coordinates, respectively. Moreover, $U_{tot}(\{\vec{r}_j\})$ is the sum of all the inter-particle (not inter-species) interactions in the system and γ is the damping coefficient. In the right side of Eq. 3.4, the first, second, and third terms are the total conservative, viscous, and random forces exerted on i-th particle, respectively. The random force $\vec{W}_i$ satisfies

$$\langle \vec{W}_i(t) \rangle = 0, \tag{3.5a}$$

$$\langle \vec{W}_i(t)\vec{W}_j(t') \rangle = 6\gamma k_B T m_i \delta_{ij}\delta(t - t'), \tag{3.5b}$$

for i-th particle collided by j-th particle.

If $m = 1.0$ is the mass unit, then the masses of different species are given by $m_\alpha = \sigma_\alpha^3 m/\sigma^3$, assuming a uniform mass density for all particle species. We employ the velocity-Verlet algorithm to integrate the equations of motion with time step $\delta t = 0.002\tau_{LJ}$ ($\delta t = 0.005\tau_{LJ}$) for $a_c < a_m$ ($a_c \geq a_m$) where $\tau_{LJ} = \sigma\sqrt{m/\varepsilon} = 1.0$ is the LJ reduced time unit and $\sigma = 1.0$ [185, 186]. The system is kept at a fixed temperature $T = 1.0\varepsilon/k_B$ via the Langevin thermostat with a damping constant $\gamma = 0.1\tau_{LJ}^{-1}$, where $k_B = 1$ is the Boltzmann constant in the LJ reduced unit system [187]. The choices of mass and damping factor are not important in our study since they do not influence equilibrium properties.

TABLE 3.1 The input parameters for a system comprising of a flexible linear polymer in a cylindrical confinement with a size (diameter) D, interacting with bead-like crowders. The cylinder length is set to $Z \geq 3\langle L(\phi_c)\rangle$, where $\langle L(\phi_c)\rangle$ represents the farthermost distance of the chain at the bulk crowder volume fraction ϕ_c. For comparison, we provide values for the measured unperturbed ($\phi_c = 0$) farthest distance, $\langle L_0\rangle$, and the estimated unperturbed Flory radius, $R_{f,0} \approx 1.12N^{3/5}$, which characterizes the chain size in free space, where N is the number of monomers [184]. The ratios D/R_F and $\langle L_0\rangle/R_{f,0}$ indicate the degree of confinement, as described in [173]. We used different values for ϕ_c up to $\phi_c = 0.45$. Four independent simulations (replicates) were performed for each set of parameters, including N, D, crowder size a_c, and ϕ_c. Lengths are reported in the LJ length unit $\sigma = a_m = 1.0$.

N	$R_{f,0}[\sigma]$	$D[\sigma]$	$\langle L_0[\sigma]\rangle$	$a_c[\sigma]$
500	46.6	10	128.7	0.6 0.8 1.0
1000	70.7	15	190.0	1.0 2.0
2000	107.1	20	309.7	1.0 2.0
		25	259.4	1.0 2.0 4.0
		30	224.1	4.0 6.0
		60	148.3	4.0 6.0

Table 3.1 lists our choices for all the system parameters, namely a_c, N, and D, exception of ϕ_c, which takes on different values up to $\phi_c = 0.45$. We use thousands of crowders up to 250 000 based on the combination of ϕ_c, D, and Z. Initially, the chain is configured in a helical shape but crowders are randomly distributed in the cylindrical confinement. After the system equilibration for 7.1×10^7 integration steps, each simulation is run for 3×10^8 integration steps. In each simulation, we gather the system conformations every 2000 (5000) steps to calculate time averages (spatial distributions).

For each parameter set, we launched four distinct simulations, each referred to as a replicate. These replicates differ based on the unique random number seeds assigned for the Langevin thermostat and the initial crowder distribution. This strategy produces four thermodynamically identical systems, each exploring different paths within the phase space. Within each replicate, we derive ensemble averages from time averages. By averaging these values across all replicates, we enhance statistical precision. As a result, the standard errors of the mean for the presented physical properties are

so small that they are obscured by the symbols in the illustrations. Notably, unless indicated otherwise, all values discussed herein underwent this dual-layered averaging method. Equilibrium macroscopic quantities are denoted by $\langle Q \rangle$, while spatial distributions are represented as $Q(\{x_i\})$, where $\{x_i\}$ signifies a collection of spatial coordinates. Moreover, we express all measurements, using the LJ reduced unit system, where $m = \varepsilon = \sigma = a_m = 1.0$.

Our simulations are performed in the LAMMPS simulation package [188]. To reduce computational costs, we benefit from the multi-size neighbor bin algorithm in LAMMPS [189]. We employ *MDAnalysis* python package and the algorithms therein to analyze trajectory files [190–192]. The analysis phase is done in parallel with *GNU-Parallel* [193].

3.3 Results

In this study, we explore the impact of MMC on the spatial organization and compaction of a single polymer confined within a cylindrical space. Our analysis specifically targets conditions that the crowder size is comparable to or greater than the monomer size, i.e., $a_c \gtrsim a_m$. The primary parameters investigated are the crowder size a_c and the crowder volume fraction ϕ_c. To ensure meaningful results, the effective size of the cylindrical confinement $D_{eff,c}$ is consistently adjusted to be at least four times larger than a_c. Similarly, the number of monomers N is also modified to preserve a sense of confinement for the polymer chain (see Table 3.1).

First, we assessed the polymer compaction due to MMC effects. Figure 3.2 presents our result for various combinations of N, D, and a_c, as listed in Table 3.1; here, the chain size $\langle L \rangle$ is rescaled with its unperturbed value, $\langle L_0 \rangle \equiv \langle L \rangle(\phi_c = 0) \sim ND^{-2/3}$, and plotted against ϕ_c. Recall that $\phi_c = 2N_c a_c^3 / 3ZD_{\text{eff},c}^2$, with $D_{\text{eff},c} = D - a_c$.; for confined spaces, the effective volume is the volume in which the center of a crowder can be placed. From top left sub-figure (Fig. 3.2A) to bottom right one (Fig. 3.2B), the pair of N and D values increases. The same color theme and marker style are used for a_c in all the sub-figures. Overall, the findings, as depicted in Fig. 3.2, indicate that chain compaction intensifies with ϕ_c, following a continuous, second-order transition characteristic of flexible chains [35, 36, 154, 158]. Below, we further discuss these findings in three regimes: $a_c < 1$ (Fig. 3.2A), $a_c = 1$ (Figs. 3.2A to 3.2D), and $a_c > 1$ (Figs. 3.2B to 3.2E).

In the regime where $a_c < 1$, previous research has indicated chain compaction due to MMC effects are significantly different between $a_c \leq 0.5$ [36, 154, 158–162]

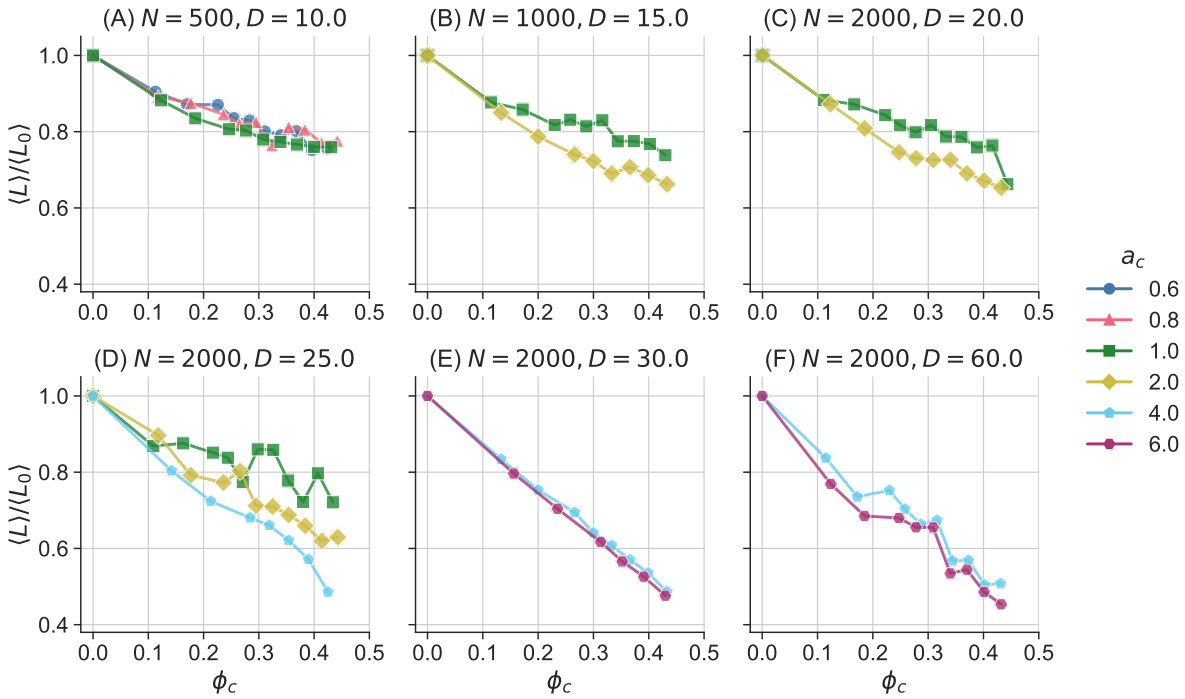


FIGURE 3.2 The compaction of a cylindrically-confined chain by crowders as a function of the crowder volume fraction ϕ_c for different crowder sizes a_c. From the top left sub-figure to bottom right one, the number of monomers N and cylinder size D increases. As displayed, the rescaled chain size $\langle L\rangle/\langle L_0\rangle$ decreases as ϕ_c grows. Chain compaction follows a continuous, second-order transition characteristic of flexible chains [35, 36, 154, 158]. For $a_c < 1$, (blue and pink curves in Fig. 3.2A), chain compaction is minimal and shows little dependence on a_c. For $a_c = 1$ (green curves in Figs. 3.2A to 3.2D), compaction remains modest without sensitivity to variations in N or D. Conversely, for $a_c > 1$ (yellow, cyan, and red curves in Figs. 3.2B to 3.2F), larger crowder compacts the chain more, beyond the effects seen at $a_c \leq 1$, still being independent of D. However, chain compaction becomes insensitive to a_c for $a_c \geq 4$.

and $0.5 < a_c < 1$ [36] ranges. Specifically, in the former range, an inverted-sigmoid compaction curve is observed, which reaches saturation at $\sim 0.2\langle L_0\rangle$ [36] across both confined [36, 160–162] and unconfined spaces [154, 158–161]. This range also shows a convergence of compaction curves for different a_c values against $a\phi_c/a_c$ (or $a\rho_c a_c^2$), with full compaction at $a\phi_c/a_c \approx 1.0$ [36, 161]. Conversely, the $0.5 < a_c < 1$ regime demonstrates weaker compaction, up to $\sim 0.75\langle L_0\rangle$, in cylindrical confinement [36], with no complementary data for unconfined spaces. Additionally, in this range, compaction curves corresponding to a_c values collapse onto a single curve when plotted against ϕ_c, having the maximum compaction at the highest ϕ_c examined [36]. As shown in Fig. 3.2A ($a_c = 0.6$ and 0.8), our results shows the chain approximately shrinks up to 80 %, almost independent of a_c, aligning with earlier studies on shorter chains in narrower confinements in the $0.5 < a_c < 1$ range [36].

For the $a_c = 1$ regime, the difference between our system and a HS fluid is chain connectivity; thus, one may argue the degree of chain compaction represents how chain connectivity, denoted by N at fixed bonding details, modulates MMC effects on the chain (see green curves with square markers in Figs. 3.2A to 3.2D). For a better comparison, we re-plotted the curves with $a_c = 1$ in Fig. 3.3A, where line color and marker style indicate D and N, respectively. This figure demonstrates that the chain condenses up to almost ∼65 % of its unperturbed size as a function of ϕ_c, independent of the combinations of N and D values (curves corresponding to different combinations of N and D collapse on each other). Our results imply chain connectivity does not significantly affect chain compaction. Moreover, for chains comprising $N = 2000$ monomers (see Figs. 3.2C to 3.2D, or curves with square marker in Fig. 3.3A), the degree of confinement shows negligible impact on compaction. Interestingly, our findings for the $a_c = 1$ regime indicate that confinement can amplify MMC effects on chain compaction up to twice as much compared to unconfined chains ($N = 50$) over the same ϕ_c range ($0 \leq \phi_c \leq 0.45$) [160].

In the $a_c > 1$ regime, earlier studies have revealed that the response of single chain to MMC effects are different in short- and large-N scenarios in unconfined space [160, 161]. A short chain ($N = 50$) compacts up to ∼80 % of its unperturbed size as ϕ_c is increased to 0.5, where chain compaction is insensitive to a_c values over the range$1 \leq a_c \leq 4$. On the other hand, chain compaction is more pronounced for long single chains ($N = 2000$): As ϕ_c grows from 0 to 0.56, the chain shrinks up to ∼20 % of its unperturbed, again independent of a_c values over the range $4 \leq a_c \leq 20$. Note that the simulation scenarios, where $a_c = 4$, have revealed the N-dependant response of a chain to MMC effects [160].

Figures 3.2B to 3.2F display our findings for a cylindrically-confined chain, revealing some disagreement with results obtained in unconfined space; under confinement, chain compaction is sensitive to a_c when $1 \leq a_c \leq 4$. As depicted in Figs. 3.2B to 3.2D, crowders with $a_c = 2$ (yellow curves with diamond marker) are more effective than crowders with $a_c = 1$ (green curves with square markers) in chain compaction (up to 10 % enhancement), independent of the combinations of N and D values, except for the largest ϕ_c value in Fig. 3.2C. In parallel, Fig. 3.2D also illustrates higher chain compaction for larger crowders, with up to 15 % enhancement for $a_c = 4$ (cyan curve with pentagon markers) over $a_c = 2$ (yellow curve with diamond markers). To further clarify chain compaction under cylindrical confinement, we re-plotted our results for $N = 2000$ in Fig. 3.3B, where line color and marker style represent different a_c and D values, respectively. The first finding is that chain compaction is insensitive to confinement; at a given a_c value (line color), the curves corresponding to different D values

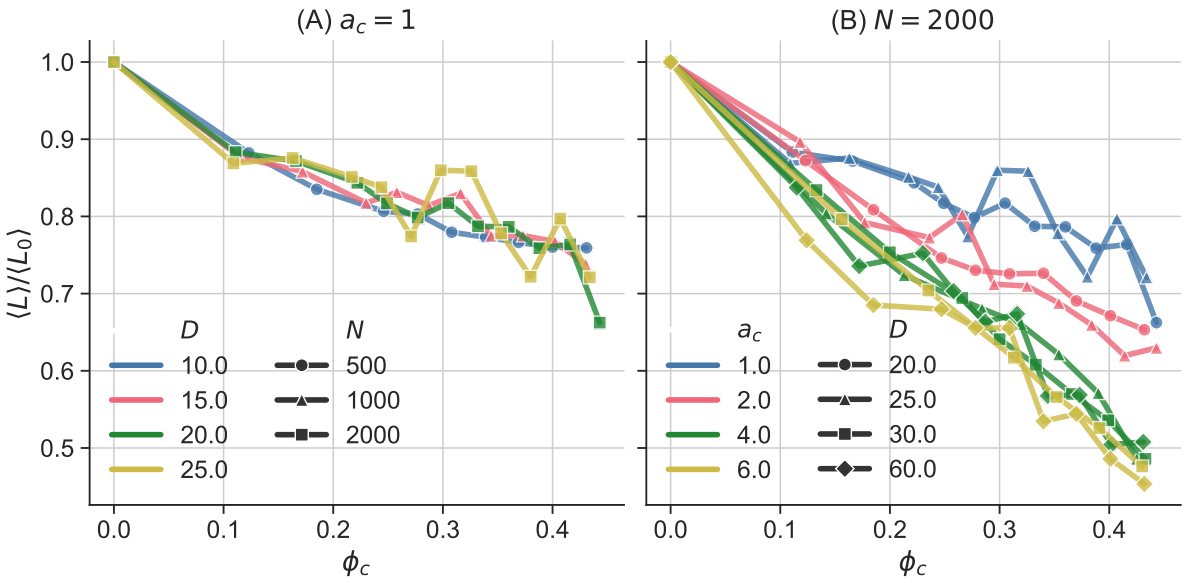


FIGURE 3.3 The compaction of a cylindrically-confined chain due to MMC effects. The results shown in Fig. 3.2 are re-plotted here for some specific choices of input parameters. (A) In scenarios where $a_c = 1$, MMC moderately compacts a single polymer chain, independent of the number of monomers N (marker style) and cylinder size D (line color). (B) For a long chain ($N = 2000$), chain compaction is insensitive to confinement (different marker styles) at a given a_c value (line color). MMC effects become stronger for larger crowders but become insensitive to a_c beyond $a_c = 4$ (green and yellow curves collapse on each other). For visual clarity, the chain size $\langle L \rangle$ is rescaled with its unperturbed value $\langle L_0 \rangle$ in the absence of crowders ($\phi_c = 0$).

(different marker styles) collapse on each other. The second, more important, finding is that MMC effects become stronger for larger crowders but become insensitive to a_c beyond $a_c = 4$ (green and yellow curves collapse on each other). In other words, our findings agree with the results obtained unconfined space [160, 161] for $a_c \geq 4$.[2]

Previous studies have shown that a confined system (i.e., a single chain vs crowders in a confinement) undergoes an anisotropic phase separation [36], unlike its unconfined counterpart [160, 161]. Here, we calculated the spatial distributions of monomers and crowders to investigate this anisotropic phase separation, extending the previous findings to the regime where $a_c \geq a$ under cylindrical confinement. As expected, our system also anisotropically phase-separate into the monomer-rich (chain-occupying) and crowder-only phases along the longitudinal direction. However, a few differences arise as discussed below.[3]

[2]As of April 29, 2024, we are still running simulations for a chain with $N = 2000$ monomers in the presence of crowders with $a_c = 2,\ 4,\ 6$ and 8 under cylindrical confinement with $D = 120$ and 240, to further support these results.

[3]To investigate the spatial distributions of monomers and crowders, we calculated the volume fraction profiles of different particle types. These quantities afford a more intuitive view of the role of volume

Figures 3.4 and 3.5 depict the radial volume fraction $\phi_\alpha(r)$ and the longitudinal volume fraction $\phi_\alpha(|z|)$ for monomers ($\alpha = m$, dashed lines) and crowders ($\alpha = c$, solid lines), respectively. Here, r and z denote radial and longitudinal distances from center of mass (COM) of the polymer. Across the figures, the parameters a_c, D, and N increase from the top-left sub-figure to the bottom-right sub-figure. Various sets of ϕ_c values are explored across the sub-figures. The top row of each figure demonstrates cases for $a_c < 1$ and $a_c = 1$ regimes, whereas the bottom row is dedicated to examining the $a_c > 1$ regime.

Within each sub-figure of Figs. 3.4 and 3.5, $\phi_\alpha(r)$ and $\phi_\alpha(|z|)$ are presented across different values of ϕ_c (indicated by line colors). We rescaled $\phi_\alpha(r)$ as $\phi_\alpha(r)/\phi_\alpha(0)$, where $\phi_\alpha(0)$ represents the radial volume fraction of α-type particles on the longitudinal axis ($r = 0$). A different rescaling method is applied in the longitudinal direction: $\phi_c(|z|)$ is rescaled as $\phi_c(|z|)/\phi_c(\infty)$, where $\phi_c(\infty)$ signifies the longitudinal volume fraction of crowders in the crowder-only region far from the COM of the polymer. Conversely, $\phi_m(|z|)$ is rescaled as $\phi_m(|z|)/\phi_m(0)$, where $\phi_m(0)$ denotes the longitudinal volume fraction of monomers at the COM of the polymer. The variables r and $|z|$ are scaled with the cylinder radius $D/2$ and the unperturbed chain size $\langle L_0 \rangle/2$, respectively. For visual clarity, the $|z|$ axis is truncated at $|z| = 1.5\langle L_0 \rangle$.

In Fig. 3.4A ($a_c = 0.6$), $\phi_m(r)$ exhibits a smooth decline from its peak at $r = 0$ to zero at $r = D/2$, highlighting the depletion of monomers from the cylinder wall. Concurrently, $\phi_c(r)$ remains relatively uniform across the radial axis but starts to oscillate with an increasing amplitude as r approaches $D/2$. This gradual decline of $\phi_m(r)$ reflects the repulsive interaction between the wall and monomers noted in earlier studies, in the absence of crowders absent [173, 194], aligning with in-vitro observations of bacterial chromosome compaction [35].[4] The oscillatory behavior of $\phi_c(r)$ indicates the wall-layering of crowders [173, 195]. Increasing ϕ_c (darkening line color) does not qualitatively influence $\phi_m(r)$, but intensifies the magnitudes of peaks and troughs in $\phi_c(r)$, increases the numbers of them, and shifts the positions of them towards the longitudinal axis (smaller r values). Insensitivity of the $\phi_m(r)$ to the degree of MMC (increasing in ϕ_c) underscores that the compaction of flexible polymers (see Figs. 3.2 and 3.5) mainly happens along the longitudinal axis, unlike their semi-flexible coun-

exclusion in MMC than other concentration profiles, such as number densities. While the calculation of local number densities of point-like particles is a standard practice in numerical statistical analysis, subtle difficulties arise in the calculation of local volume fractions of the so-called extended particles, due to the contributions of a particle volume to multiple histogram bins. We developed in-house Python routines to calculate volume fraction profiles.

[4] It is noteworthy that our chosen strength for the monomer-wall interaction ($\varepsilon_{13} = 5$) prevents chain adsorption onto the cylinder wall [36, 155].

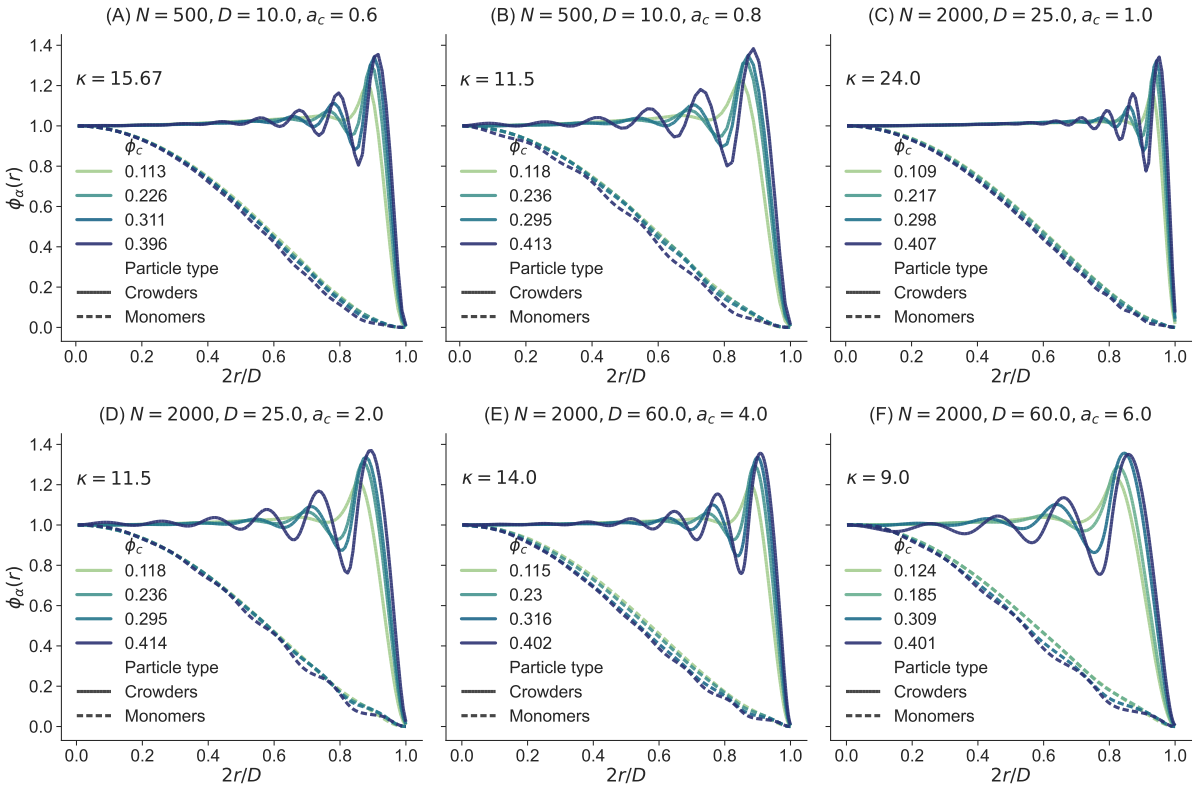


FIGURE 3.4 Interdependence between the radial distribution (volume fraction profile) $\phi_\alpha(r)$ of monomers ($\alpha = m$) and crowders ($\alpha = c$) under MMC conditions. The COM of the chain is at $r = 0$. The number of monomers N, cylinder size D, and crowders size a_c increase from the top-left sub-figure to the bottom-right sub-figure. For enhanced visibility, radial distributions $\phi_\alpha(r)$ are rescaled with their values at $r = 0$, and r is rescaled with D. The distribution of monomers $\phi_m(r)$ shows a gradual decrease from its maximum at $r = 0$ to zero as r reaches $D/2$, illustrating monomer depletion from the cylinder walls. In contrast, $\phi_c(r)$ displays a relatively constant profile across the radial axis but begins to exhibit oscillatory behavior with increasing amplitude towards $r = D/2$, revealing the wall-layering of crowders. At sufficiently high ϕ_c values, this wall-layering extends towards $r = 0$, weakly affecting $\phi_m(r)$. The impact of confinement on crowders can be quantified by the cylinder to crowder size ratio, $\kappa \equiv (D - a_c)/a_c$. As κ decreases, the effects of crowder wall-layering become increasingly evident.

terparts [196]. The longitudinal chain compaction justifies the quasi-one-dimensional approach in studying chain confined single under MMC conditions [35, 36].

Within a constant set of parameters N, D, and ϕ_c, the wall-layering of crowders becomes more pronounced and extends deeper towards the longitudinal axis ($r = 0$) for larger crowders; for instance, consider the darkest curves in Fig. 3.4E ($N = 2000$, $D = 60$, and $a_c = 4$) and Fig. 3.4F ($N = 2000$, $D = 60$, and $a_c = 6$), where $\phi_c \approx 0.4$. The penetration of crowder wall-layering near the longitudinal axis introduces a weak oscillatory pattern in $\phi_m(r)$. The impact of confinement on crowders can be quantitatively described by the cylinder to crowder size ratio, defined as $\kappa \equiv D_{\text{eff},c}/a_c$. As

κ decreases, the effects of crowder wall-layering become increasingly evident. Holding κ and ϕ_c fixed (see the darkest curves in Fig. 3.4B and Fig. 3.4D, where $\kappa = 11.5$ and $\phi_c \approx 0.4$), the impact of crowder wall-layering on $\phi_c(r)$ remains relatively similar across different systems, whereas its impact on $\phi_m(r)$ becomes more notable for smaller crowders.

Figure 3.5 depicts the longitudinal distributions across various combinations of N, D, and a_c. In Fig. 3.5A ($N = 500$, $D = 10$, and $a_c = 0.6$), both $\phi_m(|z|)$ and $\phi_c(|z|)$ exhibit almost uniform distributions near $z = 0$. However, as $|z|$ increases, $\phi_m(|z|)$ gradually diminishes at intermediate $|z|$ values, while $\phi_c(|z|)$ converges towards $\phi_c(\infty)$. This pattern suggests a coexistence of the monomer-rich (chain-occupying) and crowder-only phases, demarcated by a smooth boundary. An increase in ϕ_c (a darker curve) shifts the phase boundary towards lower $|z|$ values, signaling a more longitudinally-compacted chain (a smaller chain-occupying region). Our calculations reveal that the middle and width of the boundary region are $|z_{\text{mid}}| \approx \langle L(\phi_c)\rangle/2$ and $\Delta z_b = 2\sigma_L(\phi_c)$, respectively, where $\sigma_L(\phi_c)$ is the variance of the chain size at a given ϕ_c value. The scenario outlined for Fig. 3.5A essentially holds for other N, D, and a_c combinations, as illustrated in Figs. 3.5B to 3.5F.

Prior studies have reported that "the chain-occupying region is more permeable to crowders for smaller a_c values" in unconfined spaces [160]. The impermeability of the monomer-rich (chain-occupying) region to crowders means MMC effects are not local but rather modulated by polymer architecture and geometry of confinement [160]. Our research extends these observations to confined spaces, suggesting crowder depletion from the monomer-rich phase is determined by κ rather than a_c itself. Thus, the monomer-rich phase shows increased crowder permeability at higher κ values. Notably, Fig. 3.5C, which has the highest κ value, exhibits the smallest reduction in $\phi_c(r)$ within the monomer-rich phase, whereas Fig. 3.5F, with the lowest κ value, displays the largest decrease. Nonetheless, the reduction in $\phi_c(r)$ within the monomer-rich phase across all examined systems does not surpass 10 %. We speculate that the patterns observed in unconfined spaces would reemerge as κ approaches infinity, rendering confinement effects negligible.

In parallel, we also investigated the interdependence of monomer and crowder distributions and the validity of the so-called (density) sum rule [161] under cylindrical confinement. This sum rule, which governs the spatial distributions of crowders and monomers in unconfined spaces, is expressed as

$$\sum_{\alpha} \frac{\phi_\alpha(x)}{a_\alpha} \approx \frac{\phi_c(\infty)}{a_c} \tag{3.6}$$

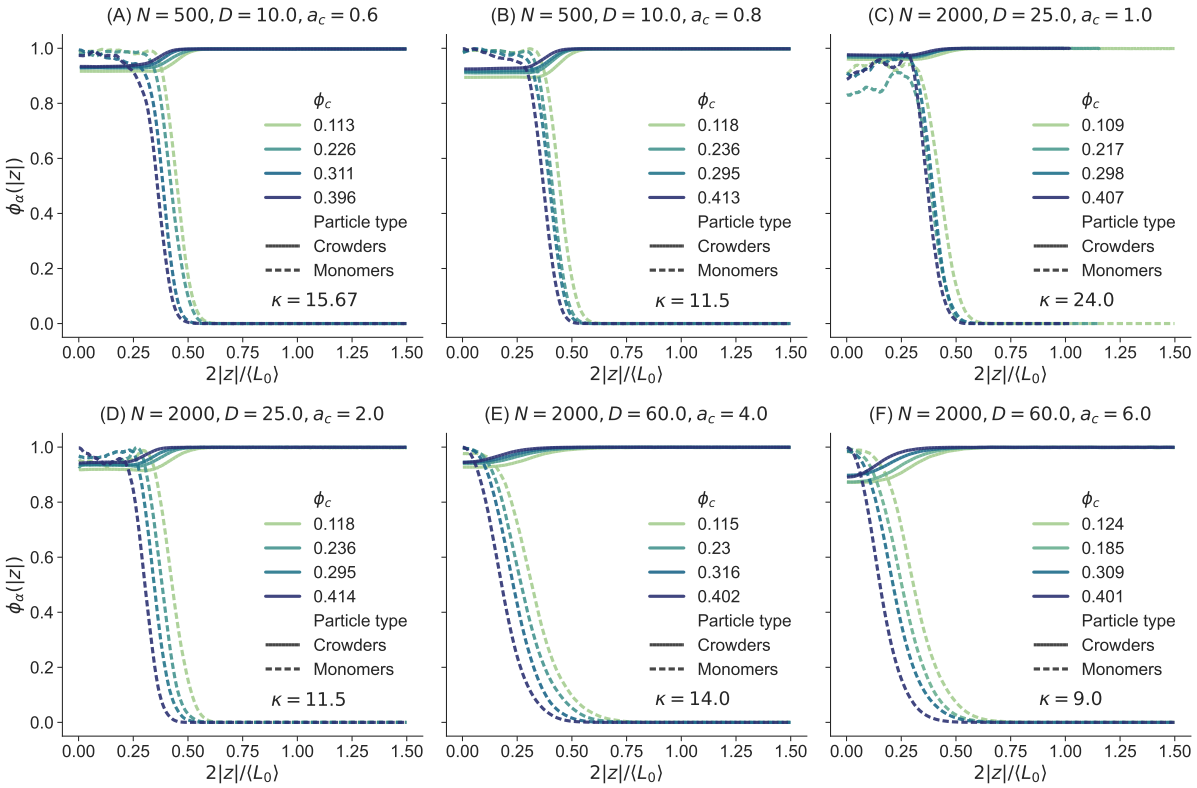


FIGURE 3.5 Longitudinal distribution $\phi_\alpha(|z|)$ of monomers ($\alpha = m$) and crowders ($\alpha = c$) under MMC conditions, illustrating anisotropic phase separation into monomer-rich and crowder-only phases. The COM of the chain is located at $z = 0$. From the top-left subfigure to the bottom-right one, the number of monomers N, cylinder size D, and crowders size a_c increase. For visual clarity, $\phi_m(|z|)$ is rescaled with its maximum value at $z = 0$, $\phi_r(|z|)$ is rescaled with its value, $\phi_c(\infty)$, deep in the crowder-only region, and $|z|$ is rescaled with the unperturbed chain size $\langle L_0 \rangle$ at $\phi_c = 0$. Near $z = 0$, both $\phi_m(|z|)$ and $\phi_c(|z|)$ display nearly uniform distributions. However, with increasing $|z|$, $\phi_m(|z|)$ gradually vanishes in intermediate zones, whereas $\phi_c(|z|)$ approaches $\phi_c(\infty)$. This indicates a coexistence of monomer-rich and crowder-only phases, separated by a smooth boundary. The midpoint and thickness of this boundary are defined by $|z_{\text{mid}}| \approx \langle L(\phi_c) \rangle/2$ and $\Delta z_b = 2\sigma_L(\phi_c)$, respectively, where $\sigma_L(\phi_c)$ represents the variance in chain length at a given ϕ_c. Crowder depletion from the monomer-rich phase is modulated by $\kappa \equiv (D - a_c)/a_c$, with increased crowder permeability observed at higher κ values. The decrease in $\phi_c(|z|)$ within the monomer-rich phase across all examined configurations does not exceed 10 %.

or, equivalently,

$$\sum_\alpha a_\alpha^2 \rho_\alpha(x) \approx a_c^2 \rho_c(\infty), \tag{3.7}$$

where $\rho_\alpha(x)$ represents the number density profile, and x can be either r or z. This rule applies in both moderate ($0.125 \leq \phi_c \leq 0.425$) and strong ($\phi_c > 0.425$) compaction regimes in unconfined spaces [161]. From the thermodynamical perspective, the sum rule simultaneously captures the entropy of crowders and monomers, being more meaningful than a two-body formalism in which MMC effects are explained via

the depletion attraction between monomers pairs.

Our results for the sum of rescaled radial volume fractions $\sum_\alpha \phi_\alpha(r)/a_\alpha$ and the sum of rescaled longitudinal volume fractions $\sum_\alpha \phi_\alpha(|z|)/a_\alpha$, where $\alpha = \{m, c\}$ are demonstrated in Figs. 3.6 and 3.7, respectively. Across the figures, a_c, D, and N increase from the top-left sub-figure to the bottom-right one. We explore various sets of ϕ_c values in the sub-figures, with the top row of each figure showcasing scenarios for $a_c < 1$ and $a_c = 1$ regimes, and the bottom row focusing on the $a_c > 1$ regime. We rescaled $\sum_\alpha \phi_\alpha(r)/a_\alpha$ and $\sum_\alpha \phi_\alpha(|z|)/a_\alpha$ with $\Big(\sum_\alpha \phi_\alpha(r)/a_\alpha\Big)/\Big(\sum_\alpha \phi_\alpha(0)/a_\alpha\Big)$ and $\Big(\sum_\alpha \phi_\alpha(|z|)/a_\alpha\Big)/\Big(\sum_\alpha \phi_\alpha(\infty)/a_\alpha\Big)$ along the radial and longitudinal directions, respectively. A solid red horizontal line in each sub-figure of Figs. 3.6 and 3.7 indicates the scaling factor. Along the longitudinal direction, the right hand side of Eq. 3.6, namely $\phi_c(\infty)/a_c$, is equal to $\sum_\alpha \phi_\alpha(\infty)/a_\alpha$, since $\phi_m(\infty) = 0$ in the crowder-only phase. Again, we rescaled r and $|z|$ with the cylinder radius $D/2$ and the unperturbed chain size $\langle L_0\rangle/2$, respectively, truncating the $|z|$ axis at $|z| = 1.5\langle L_0\rangle$ for visual clarity.

Figure 3.6 illustrates that the sum of rescaled radial volume fraction remains nearly constant, i.e., $\Big(\sum_\alpha \phi_\alpha(r)/a_\alpha\Big) \approx \Big(\sum_\alpha \phi_\alpha(0)/a_\alpha\Big)$, up to several units of a_c away from $r = 0$ when κ is sufficiently large (indicative of minimal or absent crowder wall-layering; see Figs. 3.7A, 3.7C and 3.7E where $\kappa \geq 14$). However, this constancy does not yield significant physical insights about the sum rule along the radial direction because $\phi_c(r)$ encompasses contributions from both the monomer-rich and crowder-only regions (see regions with $|z| \gtrsim 0.5$ in the (x, z) and (y, z) planes in Fig. 3.8). To conclusively determine the applicability of the sum rule along the radial direction, it is necessary to investigate the interdependence of radial volume fractions specifically within the monomer-rich region.

As depicted in Fig. 3.7, the validity of the sum rule along the longitudinal direction depends on the permeability of the chain-occupying region for crowders. In each sub-figure, the deviation of $\sum_\alpha \phi_\alpha(|z|)/a_\alpha$ from $\phi_c(\infty)/a_c$ lessens as ϕ_c increases. For higher κ values, this deviation is notably smaller, evident when comparing the brightest curves for $\phi_c \approx 0.1$ across the sub-figures. Remarkably, in the biologically-relevant intermediate ϕ_c range ($0.2 \leq \phi_c \leq 0.4$), $\sum_\alpha \phi_\alpha(|z|)/a_\alpha$ deviates by a maximum of 5 % from $\phi_c(\infty)/a_c$. This deviation is lower than that observed in unconfined spaces, where the maximum deviation reaches approximately 10 % for $N = 2000$ and $a_c = 4$ and 6 within the same ϕ_c range [161].

To further investigate the spatial interdependence between monomers and crowders, we computed two-dimensional number density profiles $\rho_\alpha(x_i, x_j)$ and their summation of rescaled profiles $\sum_\alpha a_\alpha^2 \rho_\alpha(x_i, x_j)$, where x_i and x_j span $\{x, y, z\}$, and α rep-

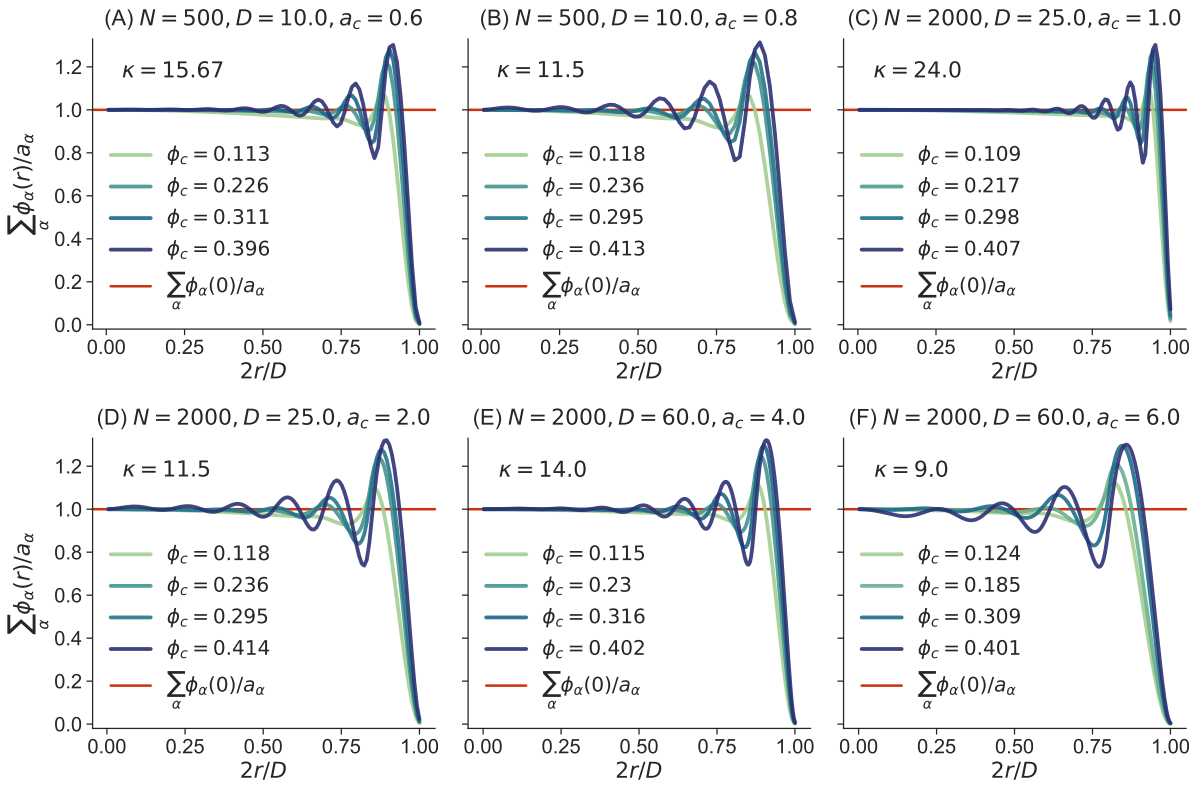


FIGURE 3.6 Sum of rescaled radial volume fractions $\sum_\alpha \phi_\alpha(r)/a_\alpha$ for different choices of the bulk crowder volume fraction, ϕ_c. The COM of the chain is at $r = 0$. The crowder size a_c, the number of monomers N, and cylinder size D grow from the top-left sub-figure to the bottom-right one. For enhanced clarity, $\sum_\alpha \phi_\alpha(r)/a_\alpha$ is rescaled with $\sum_\alpha \phi_\alpha(0)/a_\alpha$ (indicated by a solid red horizontal line) while r is rescaled with the cylinder radius $D/2$. In scenarios where the cylinder to crowder size ratio $\kappa = (D - a_c)/a_c$ is large, indicating minimal crowder wall-layering, the rescaled sum remains nearly constant close to $r = 0$. However, this observed constancy offers limited insights into the applicability of the sum rule along the radial direction since $\phi_c(r)$ has contributions from both the monomer-rich and crowder-only regions (see regions with $|z| \gtrsim 0.5$ in the (x, z) and (y, z) planes in Fig. 3.8).

resents either 'm' for monomers or 'c' for crowders. Figure 3.8 exhibits our findings under minimal crowder wall-layering and moderate MMC effects ($\kappa = 24$, $\phi_c \approx 0.3$). For visual clarity, while individual density profiles are rescaled with their respective maximum values, their sum is rescaled with the maximum of the sum deep in the crowder-only region on a given Cartesian plane, i.e., $\sum_\alpha a_{\max,\alpha}^2 \rho_\alpha(\infty, \infty)$. Recall that $\rho_{\max,m}(\infty, \infty) = 0$ in the crowder-only region, thus $\sum_\alpha a_\alpha^2 \rho_\alpha(\infty, \infty) = a_c^2 \rho_{\max,c}(\infty, \infty)$. The plot underscores the intricate relationship between monomer and crowder distributions, supporting the two-dimensional interpretation of the density sum rule, expressed as

$$\sum_\alpha a_\alpha^2 \rho_\alpha(x_i, x_j) \approx a_c^2 \rho_{\max,c}(\infty, \infty), \tag{3.8}$$

in the (x, z) and (y, z) planes. While the sum of the rescaled distributions on the (x, y)

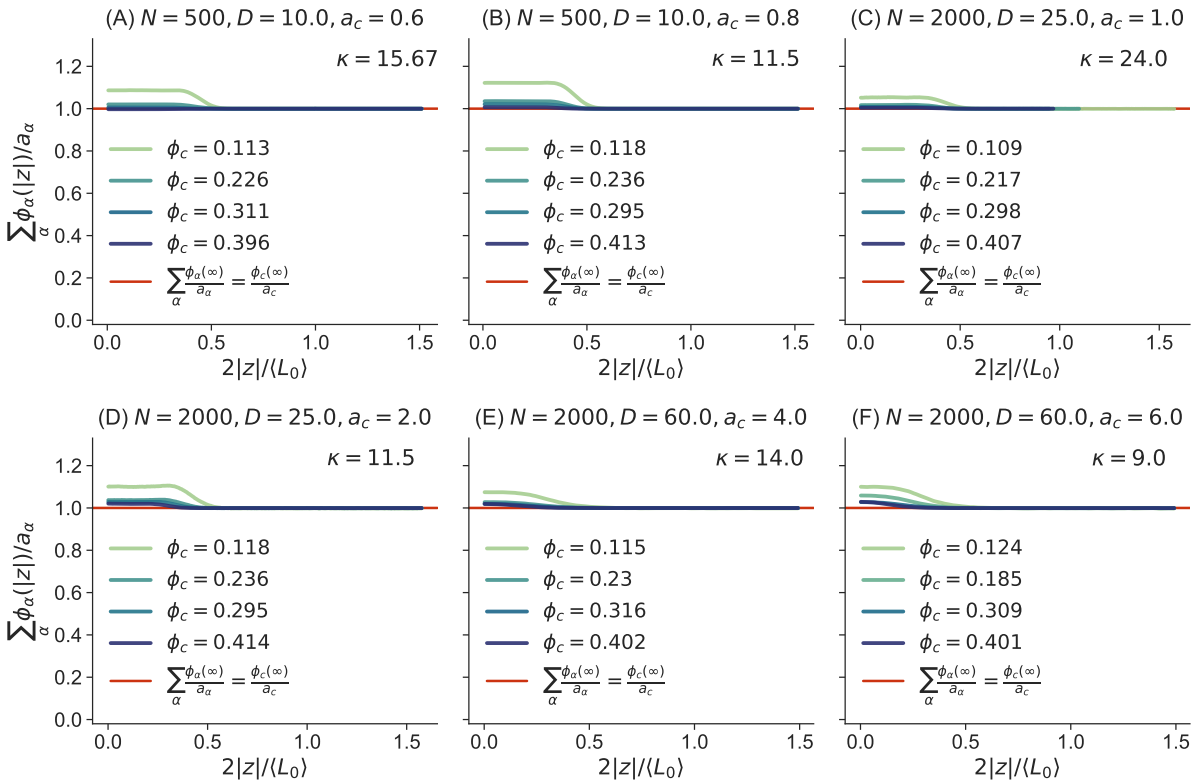


FIGURE 3.7 Sum of longitudinal volume fractions $\sum_\alpha \phi_\alpha(|z|)/a_\alpha$ for different choices of the bulk volume fraction of crowders ϕ_c, with COM of the chain at $z = 0$. The crowders size a_c, the number of monomers N, and cylinder size D grow from the top-left sub-figure to the bottom-right sub-figure. For enhanced clarity, $\sum_\alpha \phi_\alpha(|z|)/a_\alpha$ is rescaled with $\sum_\alpha \phi_\alpha(\infty)/a_\alpha$ (indicated by a solid red horizontal line) while $|z|$ is rescaled with the unperturbed chain size $\langle L_0 \rangle$ and truncated at $|z| = 1.5\langle L_0 \rangle$. Since $\phi_m(\infty) = 0$ in the crowder-only phase, $\phi_c(\infty)/a_c$ equals to $\sum_\alpha \phi_\alpha(\infty)/a_\alpha$. The validity of the sum rule depends on the permeability of the chain-occupying region for crowders. In each sub-figure, the deviation of rescaled sum $\left(\sum_\alpha \phi_\alpha(|z|)/a_\alpha\right)/\left(\sum_\alpha \phi_\alpha(\infty)/a_\alpha\right)$ from unity decreases as ϕ_c grows. At higher κ values, this deviation is notably smaller, evident when comparing the brightest curves for $\phi_c \approx 0.1$ across the sub-figures. In the biologically-relevant intermediate ϕ_c range ($0.2 \leq \phi_c \leq 0.4$), $\sum_\alpha \phi_\alpha(|z|)/a_\alpha$ deviates by a maximum of 5 % from $\phi_c(\infty)/a_c$.

plane also tends to a constant up to several a_c units away from the origin, it does not confirm the validity of the two-dimensional sum rule on this plane, due to contributions to $\rho_c(x, y)$ from the crowder-only phase (see regions with $|z| \gtrsim 0.5$ in the (x, z) and (y, z) planes in Fig. 3.8).

3.4 Discussion and conclusion

This chapter delved into the effects of MMC on chain compaction and the interdependence between the spatial distributions of monomers and crowders. Our MD simu-

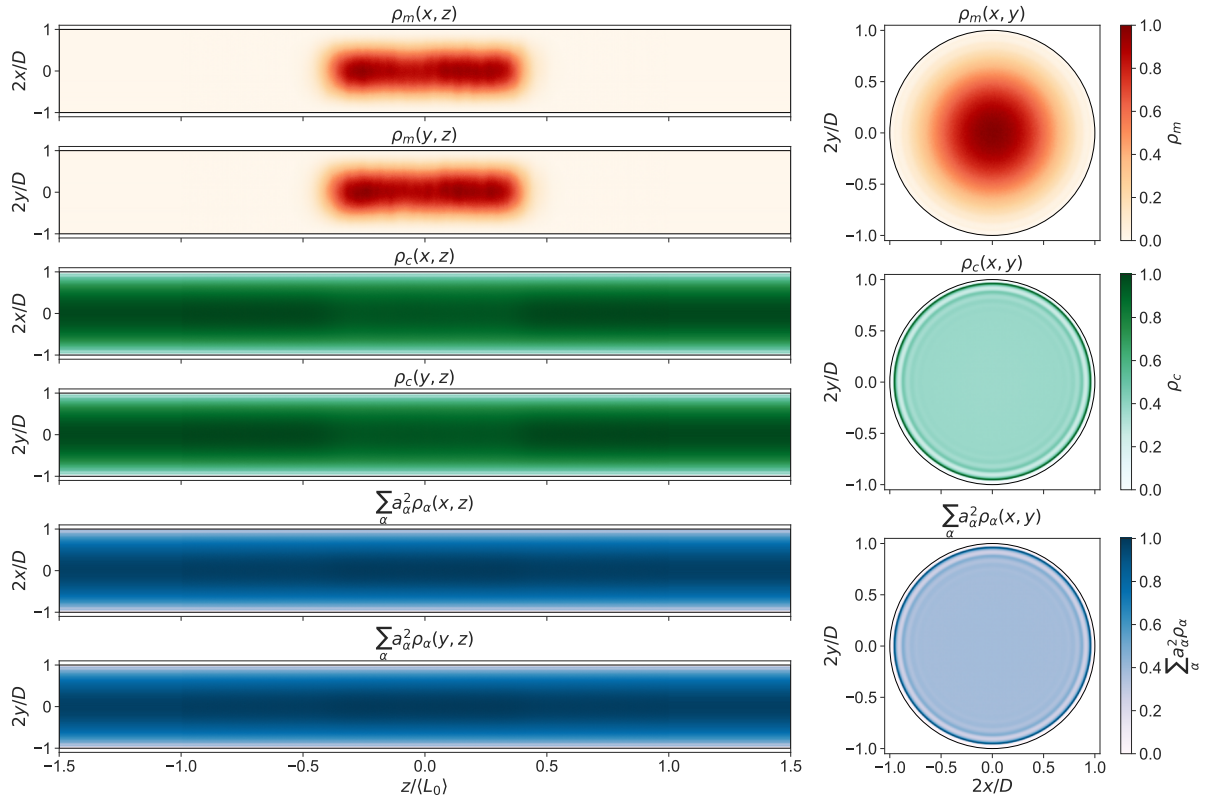


FIGURE 3.8 Two-dimensional Cartesian number density profiles for monomers (top row) and crowders (middle row), alongside their normalized summations (bottom row) under minimum crowder wall-layering ($\kappa = 24$, $N = 2000$, $D = 25$, and $a_c = 1$) and moderate MMC effects ($\phi_c = 0.298$). For monomers and crowders, each of the top two rows displays three heat maps: $\rho_\alpha(x,z)$ and $\rho_\alpha(y,z)$ profiles (stacked vertically to the left) with a $\rho_\alpha(x,y)$ profile on the right, with $\alpha =$ 'm' (monomers) or 'c' (crowders). The bottom row illustrates three normalized densities as three heat maps: $\sum_\alpha a_\alpha^2\rho_\alpha(x,z)$ and $\sum_\alpha a_\alpha^2\rho_\alpha(y,z)$ (vertically stacked on the left) alongside $\sum_\alpha a_\alpha^2\rho_\alpha(x,y)$ on the right. Here, a_α denotes the particle size of type α. Color bars to the far right of each row provide density scales for the heat maps. For visual clarity, individual density profiles are rescaled by their respective maximum values, while their summation is rescaled by the peak of the summation deep in the crowder-only region, i.e., $\sum_\alpha a_{\text{max},\alpha}^2\rho_\alpha(\infty,\infty)$. Notably, $\rho_{\text{max},m}(\infty,\infty) = 0$, making $\sum_\alpha a_\alpha^2\rho_\alpha(\infty,\infty) = a_c^2\rho_{\text{max},c}(\infty,\infty)$. The sum of rescaled distributions tends to a constant in the (x,z) and (y,z) planes, suggesting the two-dimensional version of the density sum rule is satisfied on these planes. While the sum on the (x,y) also tends to a constant up to several a_c units away from the cylinder wall, it does not suggest the validity of the two-dimensional sum rule on this plane, due to contributions from the crowder-only phase to $\rho_c(x,y)$ (see regions with $|z| \gtrsim 0.5$ in the (x,z) and (y,z) planes).

lations specifically targeted cylindrically-confined systems where the crowder size is comparable to or larger than the monomer size ($a_c \geq 0.6a_m$), a domain that has not been thoroughly explored in prior studies. To ensure robustness in our results, we consistently adjusted the cylinder size D and the number of monomers N to mitigate finite-size effects and maintain a sense of confinement for the polymer.

Prior MD findings about MMC effects on the compaction of single self-avoiding chains can be categorized into distinct regimes, based on the a_c/a_m ratio. When $0.5a_m < a_c \leq 4$, chain compaction due to MMC depends on N [160]. For the small-N case ($N \leq 100$), crowders weakly compact a short chain, and their size has marginal effects on this compaction in confined ($0.5a_m < a_c < a_m$) [36] and unconfined ($a_m \leq a_c \leq 4a_m$) [160] spaces. Our investigations extend the results obtained in the $0.5a_m < a_c < a_m$ range into large-N scenarios under cylindrical confinement; however, we found larger crowders better compact a long cylindrically-confined chain over the $a_m \leq a_c \leq 4a_m$ range. This observation contradicts theoretical findings [35, 36, 39, 127] and simulation results [36, 154, 158–162] for short chains in the $a_c \leq 0.5a_m$ regime: smaller crowders are more efficient in chain compaction in unconfined and confined spaces.

Remarkably, in the $a_c = a_m$ case, we found that chain compaction due to MMC effects is insensitive to N and D over the explored range of parameters. Additionally, our results suggest that confinement has minimal effects on MMC, provided that the ratio $\kappa \equiv (D - a_c)/a_c \gg 1$. When $a_c > 4a_m$, chain compaction is moderate over the biologically-relevant $0.2 \leq \phi_c \leq 0.4$ range in unconfined space, being insensitive to a_c: crowders with size $a_c > 4a_m$ are as good as crowders with size $a_c = 4a_m$ in compacting a long chain [160, 161]. We found similar results for long cylindrically-confined chains.

Furthermore, our work expands the applicability of the density sum rule to $a_c \geq 0.6a_m$ under cylindrical confinement, contingent on minimal crowder wall-layering ($\kappa \gg 1$). This finding aligns with previous observations in unconfined and quasi-two-dimensional slit-like spaces [161], suggesting that MMC effects remain spatially localized and largely uninfluenced by the confinement geometry. Additionally, our results show that the monomer rich (chain-occupying) phase is permeable when $\kappa \gg 1$, corroborating the concept of the effective solvent picture, where the influence of crowders on solvent quality is encapsulated within the excluded-volume parameter of monomers in high-κ regimes [160].

MMC has emerged as a significant factor in the hierarchical organization of bacterial chromosomes [36, 40, 108, 155] (also see Chapter 5). For instance, in-vitro experiments have shown that polymeric crowders can condense E. coli chromosomes to their in-vivo sizes [35]. When considering naked DNA segments as monomers, their sizes vary between 2 nm to 5 nm, depending on ionic strength [96]. The size of cellular crowders, such as cytoplasmic proteins, molecular machines like ribosomes, and RNA chains, are in range 5 nm to 25 nm [65, 163, 164]. The size ratio of cellular crowders to chromosomal monomers spans the regime examined in this work, hinting at the varying effects of MMC at different hierarchies of bacterial chromosome organization.

The applicability of the sum rule in confined spaces sheds light on the role of MMC in chromosome organization and nucleoid formation [10, 11, 22]. Experimental observations in E. coli cells have demonstrated chromosomal DNA and ribosomal species are spatially separated, with the latter predominantly located at the cell caps [38, 166–171]. These studies also revealed that the permeability of E. coli nucleoids to ribosomal species varies with the size of these species ($0.5a_m \leq a_c \leq 5a_m$, depending on coarse-graining strategy) [168]. While previous computational models successfully replicated these distribution patterns [168, 170, 197], our findings extend these efforts, revealing the interdependence between distributions of molecular species in a crowded cellular medium lead to intracellular organization.

In conclusion, our study contributes to the broader understanding of polymer behavior under MMC conditions, with specific implications for biological systems such as bacterial chromosome organization [10, 21, 22, 108]. Our findings highlight the intricate role of MMC and confinement in polymer organization, offering new insights into the polymer organization in crowded environments. Future research, especially in understanding the interplay between MMC effects and other biological processes, is essential and holds great promise for advancing our knowledge in this area. For example, it is unclear whether MMC contributes to the coexistence of condensed and extended phases seen in E. coli chromosomes [35].

CHAPTER 4

Compaction and clustering of a heterogeneous polymer by biomolecular crowding

4.1 Introduction

Living cells endeavor hard to organize their chromosomes [198, 199]. Due to the lack of internal compartments, chromosome organization is particularly challenging for bacteria. Nonetheless, the bacterial chromosome is almost isolated from other molecules, partitioning into an unbound mid-cell region called the nucleoid [199–201]. Thanks to recent efforts, the role of MMC, a previously less appreciated factor, in chromosome organization is better understood [65, 75, 152, 153, 202]. Various biomolecules, such as proteins and RNA, occupy up to 40 % of the cell interior, with a total concentration ranging from 50 g L^{-1} to 400 g L^{-1} [25–31, 41, 69, 74]. At such high total concentrations (volume fractions), inter-molecular distances are comparable to molecular sizes [73, 203]; therefore, biomolecules compete for space, exerting excluded-volume (steric) forces on each other. These MMC effects impact a variety of cellular processes ranging from protein folding and chromosome organization to bimolecular aggregation, transcription, and cell growth [35, 41, 48, 49, 204].

In a crowded environment, long polymers undergo phase separation, forming compact structures (Fig. 4.1). An excellent example is the compaction of bacterial chromosomes by MMC [19, 34–36, 40, 152–154]. Viewed from a wider lens, such phase separation is a fundamental aspect of how cellular processes and reactions are spatially organized, especially when these processes do not depend on the presence of membrane-bound compartments [75, 152, 206, 207].

In a crowded environment, polymer segments feel depletion forces exerted by crowders [125, 127, 128]. As schematically illustrated in Fig. 4.1F, each monomer is surrounded by a depletion layer (represented by a dashed circle) from which the centers of crowders are excluded [125]. The overlap of these depletion layers is favored due to the increased entropy of the crowders. This increase results in effective forces among

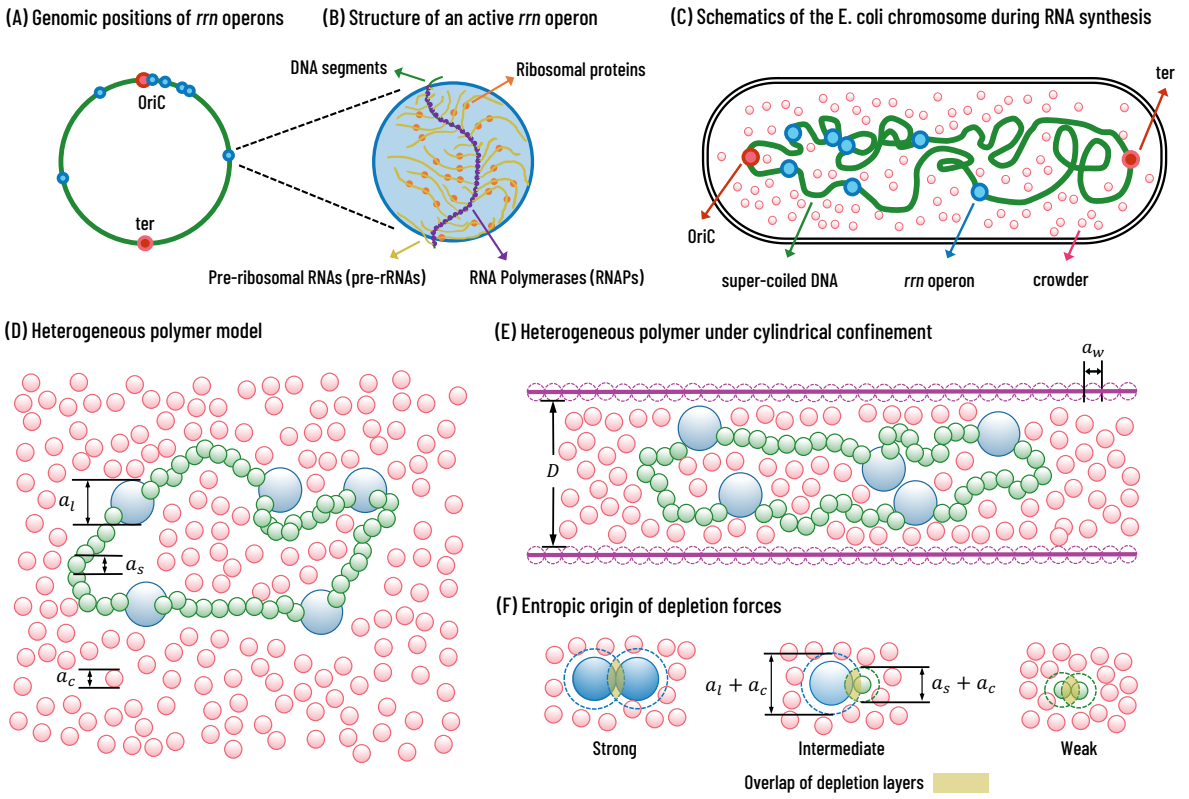


FIGURE 4.1 A schematic overview of the E. coli chromosome highlighting the role of the transcription machinery in the heterogeneity and organization of the bacterial chromosome. The chromosome inside the bacterial cell is modeled as a ring polymer in a crowded medium. (A) The depiction of approximate genomic positions of seven rrn operons with respect to the OriC and ter along the circular chromosome of E. coli. Five of these operons are within a 500 kbp distance from the OriC. (B) A depiction of an active rrn operon comprised of DNA, engaged RNAP, nascent transcripts, and ribosomal proteins, resulting in a structure reminiscent of a Christmas tree [205]. (C) A portrayal of a transcriptionally-active chromosome exhibiting heterogeneity in its structure. For simplicity, other topological complexities of the chromosome (e.g., multi-fork structure) are ignored. (D) The ring polymer comprises five large monomers and intervening small monomers, representing a transcriptionally-active heterogeneous bacterial chromosome. (E) Under cylindrical confinement, the polymer often extends along the longitudinal direction. (F) Each monomer is surrounded by a depletion layer (dashed circle) with size $a_\alpha + a_c$, where α is either s or l, from which crowders are excluded. Overlaps of depletion layers are favored by the entropy of crowders. The resulting depletion force is stronger between large monomers, weaker between small monomers, and of intermediate strength between a large monomer and a small one.

monomers, known as depletion forces, which are considered one of the key factors in the organization of bacterial chromosomes [24, 34, 35, 152]. The bacterial chromosome, as depicted in Fig. 4.1, is a long DNA molecule decorated with different DBPs, such as RNAPs, being considerably heterogeneous in structure. This heterogeneity affects depletion forces between monomers, locally modifying the spatial organization of bacterial chromosomes. Indeed, transcription has emerged as a significant determi-

nant of chromosome heterogeneity in bacteria [65, 75, 152, 202, 208, 209]. In-vivo experiments on E. coli cells have shown RNAPs, the primary molecular machine during transcription, bind to ribosomal RNA (rrn) operons distributed along the chromosome [65, 166, 202, 208, 210–218]. These transcriptionally-active rrn operons tend to form clusters, known as transcription foci, possibly driven by depletion forces, organizing the chromosome [65, 75, 152, 166, 202, 208–213, 219, 220].

This work aims to shed light on the roles of MMC and confinement in the spatial arrangement of a heterogeneous ring polymer consisting of small and large monomers distributed along its backbone, as displayed in Figs. 4.1D and 4.1E. In our model, the large monomers symbolize transcriptionally-active units. This work builds on previous investigations based on an implicit-crowder approach, in which MMC effects are viewed as inducing monomer-monomer attractions [40]. A significant finding from ref. [40] is that, under certain conditions, large monomers tend to cluster together due to depletion forces. Figure 4.1F schematically shows that the depletion force varies in strength, being strongest among larger monomers, weakest among smaller ones, and of intermediate strength between a larger and a smaller monomer. This clustering bears similarities to the formation of transcription foci seen in the chromosomes of E. coli [65, 75, 152, 166, 202, 208–213, 219, 220]. Furthermore, it has been found in ref. [40] that cylindrical confinement enhances the compaction and the clustering of the heterogeneous ring polymer.

The implicit-crowder approach [40] is founded on the depletion force between two entities, initially derived by Asakura and Oosawa (AO) [127]. This two-body picture is particularly effective for describing the behavior of extended chain conformations. However, its effectiveness and relevance are questioned when the depletion force is sufficiently strong to cause chain compaction. Moreover, a more comprehensive understanding would require a deeper exploration of how crowders are spatially distributed in response to chain compaction [161].

We utilize MD simulations to investigate the spatial organization of a heterogeneous ring polymer in a crowded medium, as displayed in Figs. 4.1D and 4.1E. Crowders are explicitly modeled as hard spheres having excluded-volume interactions with each other and monomers. Our parameter choices are inspired by the E. coli chromosome. We aim to provide a clear physical picture of how MMC effects drive the clustering of large monomers and the compaction of the polymer.

Our simulation results reveal that the compaction transition is correlated with the clustering of large monomers: both simultaneously happen at the same narrow (biologically relevant) range of ϕ_c, the bulk volume fractions of crowders. This discov-

ery differs somewhat from the earlier observation that initial compaction is primarily driven by clustering, with overall compaction occurring at larger ϕ_c [40]. Meanwhile, similarities exist between the two approaches. Both studies indicate that cylindrical confinement enhances chain compaction and the clustering of large monomers. Additionally, the compaction transition occurs within a smaller ϕ_c range when the size of large monomers, denoted as a_l, increases. This shifting is expected due to the size-dependent nature of depletion forces [40, 127, 128]. The results also suggest that large monomers within a cluster tend to adopt a close-packed configuration that maximizes direct contacts between them.

The overall insight arising from this study aligns with the notion that biomolecular aggregates, driven by intermolecular interactions, play a crucial role in enhancing biological processes or chemical reactions [75, 206, 207, 221]. In this study, it is the entropically-induced depletion force, generated by the surrounding crowders, that drives the compaction of and formation of clusters in the heterogeneous polymer, namely the E. coli chromosome. This biological manifestation of order emerging from disorder facilitates the sharing of the transcription machinery, such as RNAP, among transcriptionally-active units [152].

4.2 Computational modeling

4.2.1 A heterogeneous chain model

In this work, we largely adhere to the modeling approach outlined in ref. [40], with the notable difference that we explicitly account for crowders. We study a heterogeneous ring (circular) polymer model of the bacterial chromosome, using experimental data available about the E. coli chromosome to design this polymer model and set its parameters (Fig. 4.1C) [65, 152, 202, 215, 222]. The polymer is immersed in a crowded medium, potentially under a cell-like cylindrical confinement (Fig. 4.1E).

As can be seen in Fig. 4.1A, E. coli possesses seven rrn operons (blue spheres), five of which are located near the OriC (with distances less than 500 kbp) [215]. The term *rrn* operon refers to a set of genes responsible for the synthesis of ribosonal ribonucleic acid (rRNA), approximately spanning 5.5 kbp [208]. During RNA synthesis, an *active* rrn operon has a distinct double Christmas-tree-like structure (also called a Miller's spread), consisting of DNA, engaged RNAPs, nascent pre-ribosonal ribonucleic acids (pre-rRNAs) transcripts, and ribosomal proteins [205, 223], as schematically illustrated in Fig. 4.1B [65, 210, 215, 218, 224].

Our model, as shown in Figs. 4.1D and 4.1E, treats the active rrn operons as large spherical monomers. Certain assumptions are made in calculating their average size: (i) Components of an active rrn operon are soft and coalesce into a rigid sphere [152]; (ii) The size of this sphere is estimated via the conservation of the total surface area or volume of merging components, with our model relying on the volume conservation [152]; (iii) RNAPs and ribosomal proteins are uniformly distributed along the DNA backbone and nascent pre-rRNA chains, respectively; (iv) All nascent transcripts have the same length, and (v) We consider four possible component combinations of an active rrn operon: (a) RNAPs alone [152]; (b) RNAPs combined with DNA segments [210]; (c) RNAPs with DNA segments and nascent pre-rRNAs, and (d) RNAPs, DNA segments, nascent pre-rRNAs transcripts, and ribosomal proteins.

In slow-growth (fast-growth) cells, an rrn operon typically contains around 5 (70) RNAPs [210, 223]. The average size of an engaged RNAP is 14.7 nm [225–230]. The DNA has a width of ∼2 nm [5, 93] and has a persistence length of ∼50 nm [5, 231]. In E. coli, 5 S, 16 S, and 23 S rRNAs have genomic lengths of 120 bp, 1542 bp, and 2905 bp, respectively [232]. Hence, a nascent pre-rRNA has an average length of 1500 nt.[1] Using these numbers and the above assumptions, we crudely estimate that the size of a large monomer (an active rrn operon), denoted by a_l, ranges from 24 nm to 64 nm.

Our heterogeneous flexible ring polymer is composed of 405 monomers in total, including five large monomers that simulate the rrn operons near the OriC. Ignoring complexities, such as multi-fork replication [234], we evenly distribute these large monomers along the polymer's backbone. This simplification allows us to analyze the interplay between chain heterogeneity and MMC in chain organization. The remaining monomers are small, with size a_s, representing the backbone DNA. One might be inclined to set $a_s = 2$ nm, which corresponds to the average cross-sectional width of DNA. However, at the length scales pertinent to our study, the backbone DNA is negatively charged, super-coiled, and decorated with NAPs (see refs. [23, 35, 235] and relevant references therein). Therefore, our small monomers are designed to encapsulate the collective effects of such interactions along the DNA, as opposed to merely representing coarse-grained DNA (multiple base pairs) with a size of 2 nm. Accordingly, we assume that the small monomers have the same size as crowders, i.e., $a_s = a_c$, where the crowder size $a_c = 4.6$ nm is the average protein size in E. coli's cell [67, 68].

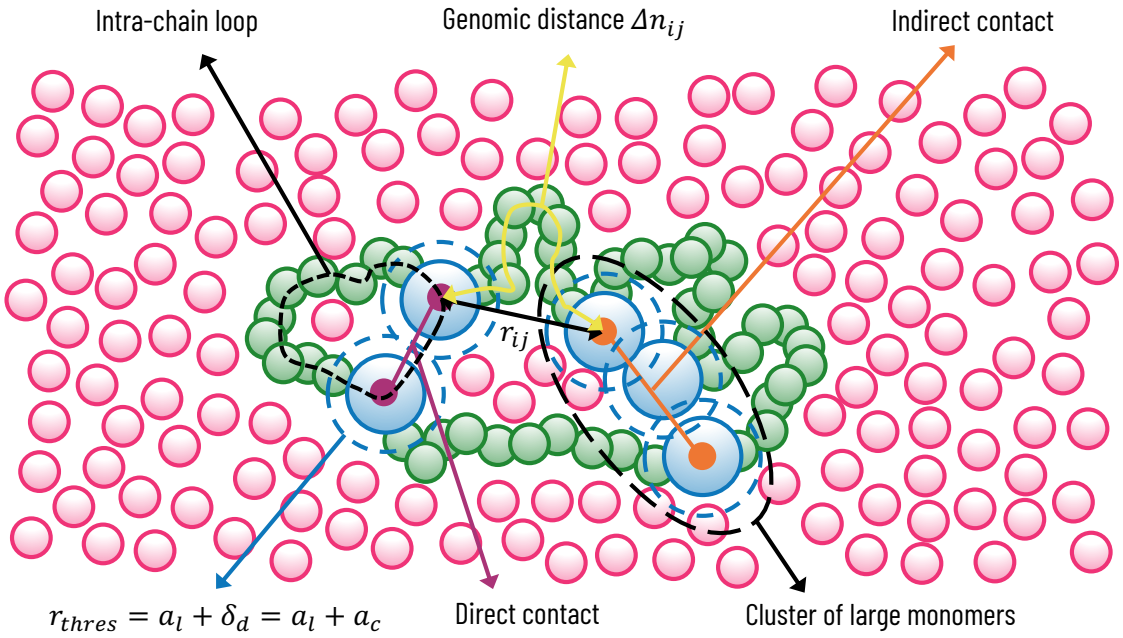


FIGURE 4.2 Clustering of large monomers under the influence of MMC. When a heterogeneous ring polymer is placed in a crowded medium, its large monomers are attracted to each other due to the depletion force induced by the surrounding crowders, being the so-called direct contact (purple dumbbell-like symbol) if their distance $r_{\alpha\beta} \leq r_{\text{thres}}$. A closely related concept is indirect contact (orange dumbbell-like symbol), which refers to a pair of large monomers connected through a chain of directly contacted monomers. A cluster of larger monomers (black dashed oval) refers to a group of directly or indirectly connected larger monomers. Clustering of large monomers results in intra-chain loops (black dashed closed contour), bringing genomically distant monomers into spatial proximity. For a pair of large monomers, the solid black double arrow illustrates the spatial distance $r_{\alpha\beta}$ between them. In contrast, the yellow dashed curved double arrow shows the genomic distances $\Delta n_{\alpha\beta}$ between them along the backbone.

4.2.2 Clustering of large monomers

In this study, one of our objectives is to examine the clustering (or aggregation) of large monomers, a phenomenon where an external agent (MMC in our discussion) brings two or more genomically distant large monomers into spatial proximity, resulting in intra-chain looping. Figure 4.2 provides a schematic depiction of how crowders trigger clustering among large monomers. We distinguish between direct and indirect contacts between two large monomers, represented by purple and orange dumbbell-like symbols, respectively, following the notation introduced in ref. [236].

A direct contact between two large monomers occurs when their center-to-center distance r_{ij} is within a threshold distance r_{thres}. Akin to the concept of the depletion layer, we define a direct-contact layer with size δ_d for each large monomer, where

[1]Bacterial genes have a mean length of 924 bp [233].

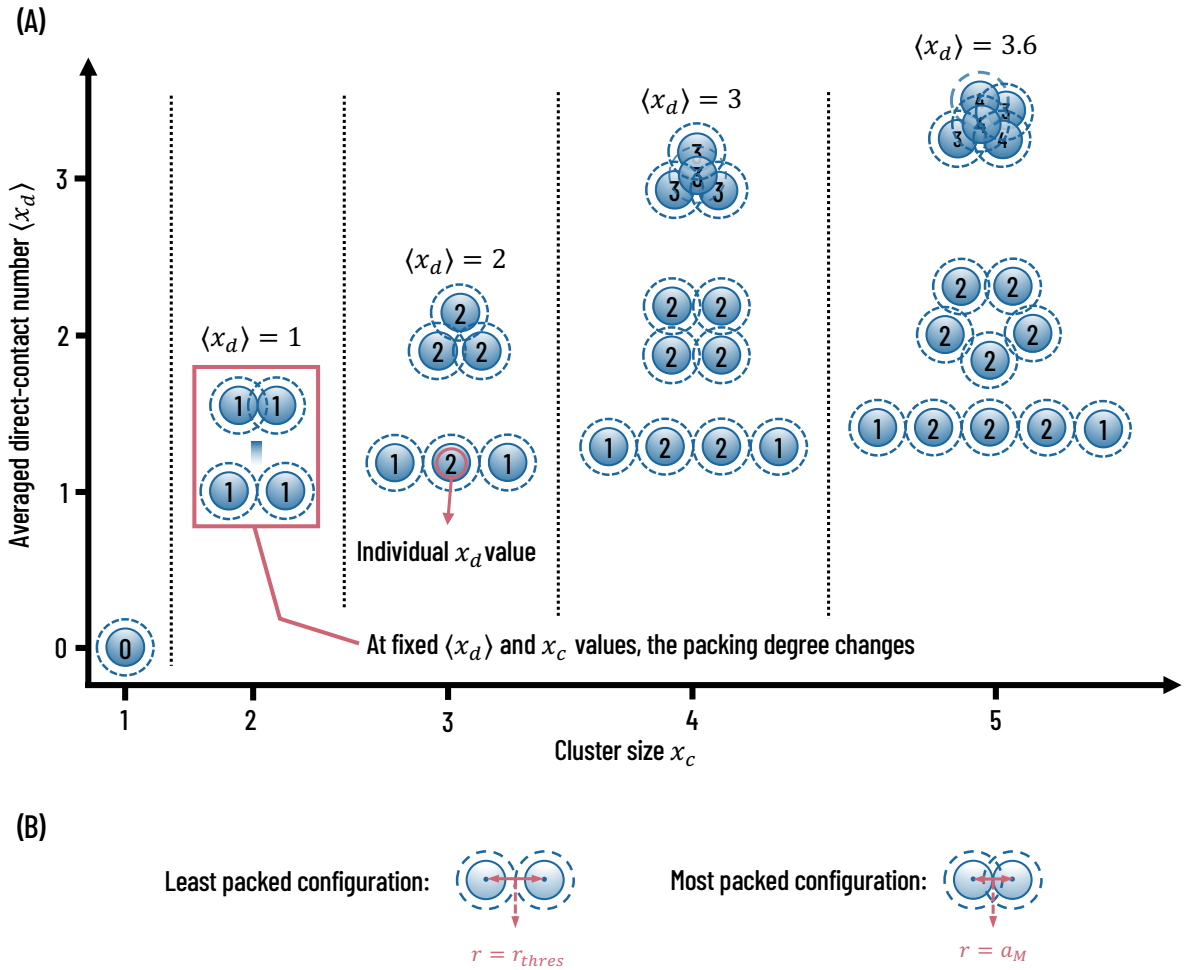


FIGURE 4.3 Cluster size x_c, the number of direct contacts x_d, and spatial distance r collectively set the morphology of large monomer clusters. (A) For N_l large monomers, x_c ranges from 1 to N_l while x_d ranges from 0 to $N_l - 1$. Within a cluster, each monomer is labeled with its x_d value. Larger clusters exhibit more configurations with varying degrees of packing and individual x_d values, as shown along the horizontal axis. When x_c is held fixed, a cluster with a higher average direct contact per monomer $\langle x_d \rangle$ is more densely packed, as depicted along the vertical axis. For a given x_c, the cluster configuration with the largest number of direct contacts is indicted by its $\langle x_d \rangle$ atop its graph. At fixed x_c and x_d values, the packing degree of a cluster changes as a function of distances between large monomers. (B) For two directly-contacted large monomers, r ranges from $r = a_l$ (the most packed configuration) to $r = r_{\text{thres}}$ (the least packed configuration). Recall that $r_{\text{thres}} = a_l + a_c$.

$r_{\text{thres}} = a_l + \delta_d$. Therefore, two large monomers are considered to be in direct contact if their direct-contact layers overlap. The value of δ_d, and consequently r_{thres}, is determined by the characteristics of the external agent promoting the clustering. Within a crowded medium, it is convenient to set $\delta_d = a_c$ (and thus, $r_{\text{thres}} = a_l + a_c$), which coincides with the range of the depletion force between two large monomers. On the other hand, an indirect contact is defined as a connection between two large monomers

through a chain of other large monomers that are directly or indirectly connected. A group of large (directly or indirectly connected) monomers forms a cluster (indicated by the dashed oval).

For a pair of monomers located at genomic positions n_i and n_j, we can define the genomic distance $\Delta n_{ij} \equiv \text{Min}(|n_i - n_j|, N - |n_i - n_j|)$ along the backbone of a circular (ring) polymer , where $|\ldots|$ and $\text{Min}(\ldots)$ are the absolute value and minimum functions. Hence, we express Δn_{ij} in units of the number of bonds between monomers.[2] Clusters of large monomers create intra-chain loops (one demonstrated by a black dashed closed contour) in the backbone of a polymer. An intra-chain loop brings genomically distant monomers ($\Delta n \gg 1$) into spatial proximity ($r \approx 0$).

A cluster of large monomers is characterized by three quantities, as schematically illustrated in Fig. 4.3: (i) The cluster size x_c denotes the number of large monomers within a cluster, ranging from 1 to N_l, as shown along the horizontal axis in Fig. 4.3A; (ii) Within a cluster, large monomers can have different numbers of direct contact, x_d, with other large monomers. In a cluster, x_d is between 1 and x_d. In the special case of $x_c = 1$, $x_d = 0$. When x_c is fixed, a cluster with a higher total number of direct contacts $X_d = \sum x_d$ or a greater average direct contact per monomer $\langle x_d \rangle$ (the metric used in our analysis; see the vertical axis in Fig. 4.3A) is more densely packed. For a given x_c, the cluster configuration with the largest number of direct contacts is indicated by its $\langle x_d \rangle$ atop its graph in Fig. 4.3A, and (iii) At fixed x_c and x_d values, the packing degree of a cluster changes as a function of distances between large monomers (Fig. 4.3B). For two large monomers in direct contact, r spans from $r = a_l$ (indicating the most compact configuration) to $r = r_{\text{thres}} = a_l + a_c$ (marking the least compact configuration).

Despite its simplicity, our polymer model is designed to capture the essential characteristics of chromosome organization by MMC. Indeed, polymer models have consistently been valuable for interpreting experimental findings [35, 157, 237]. Specifically, past research has demonstrated that when confined within a cylindrical space, the E. coli chromosome exhibits behavior akin to that of a simple polymer [35], reacting to crowders in a similar manner. Our approach in this study introduces an extra layer of complexity by incorporating chain heterogeneity into the model.

4.2.3 Simulation method

We use MD to simulate our heterogeneous ring polymer in the presence of N_c crowders in free and cylindrically confining spaces. The polymer is modeled as a flexible

[2] Moving forward, the ij subscript in r_{ij} and Δn_{ij} will be omitted when the exact indexes of a monomer pair are not important.

self-avoiding bead-spring chain with $N = N_l + N_s$ spherical monomers, including $N_l = 5$ large monomers of size a_l and $N_s = 400$ small monomers of size a_s. Large monomers are equally spaced along the backbone, with one large monomer every 80 small monomers. The polymer is examined in a cubic box with the periodic boundary conditions (PBCs) in all directions (free space) and within a cylinder of size D with the PBC along the longitudinal direction (cylindrical confinement). Under confinement, particles interact with the confining wall, composed of imaginary beads of the same kind as the small monomers. Therefore, the precise definition of D is the size of the inner cylindrical surface formed by these imaginary spheres (Fig. 4.1E). Crowders are structureless spheres (beads) of size a_c and have a volume fraction $\phi_c \equiv N_c v_c / V_T$, where $v_c = \pi a_c^3/6$ and V_T are the volumes of a crowder and the simulation box, respectively. To minimize finite-size effects, the cube side (cylinder length) Z is six (three) times larger than the estimated equilibrium radius of gyration (ROG) (farthermost distance) of the chain $R_g(\phi_c)$ ($L(\phi_c)$) at a fixed value of ϕ_c [173, 179].[3]

Let r_{ij} be the center-to-center distance between two particles i and j, then a pair of particles interact via a truncated and shifted LJ potential

$$U_{TSLJ,\alpha\beta}(r_{ij}) = \begin{cases} U_{LJ}(r_{ij}) - U_{LJ}(r_{cut,\alpha\beta}) & \text{for } r \le r_{cut,\alpha\beta} \\ 0 & \text{otherwise} \end{cases}, \tag{4.1}$$

where $U_{LJ}(r_{ij})$ is the (conventional) LJ potential,

$$U_{LJ}(r_{ij}) = 4\varepsilon_{\alpha\beta}\left[\left(\frac{\sigma_{\alpha\beta}}{r_{ij}}\right)^{12} - \left(\frac{\sigma_{\alpha\beta}}{r_{ij}}\right)^{6}\right]. \tag{4.2}$$

Above, $\sigma_{\alpha\beta} = (\sigma_\alpha + \sigma_\beta)/2$ is the collision size (diameter) at which $U_{LJ}(\sigma_{\alpha\beta}) = 0$ (the LJ potential changes sign), and $\varepsilon_{\alpha\beta}$ is the depth of the LJ potential at its minimum $r_{min,\alpha\beta} = 2^{1/6}\sigma_{\alpha\beta}$ (the inter-species attraction strength). Here, subscripts $\alpha, \beta \in \{s, l, c\}$ refer to small monomers ($\sigma_s = a_s$), large monomers ($\sigma_l = a_l$), and crowders ($\sigma_c = a_c$), where $\sigma_\alpha \equiv \sigma_{\alpha\alpha}$ is often referred to as the particle size. We use $\sigma = a_s$ as the length unit. Under confinement, an extra subscript (α or $\beta = w$) refers to wall-shaping particles ($\sigma_w = a_s$). In Eq. 4.1, our choice of the cutoff distance $r_{cut,\alpha\beta} = r_{min,\alpha\beta}$ leads to the so-called fully-repulsive WCA potential that conveniently considers excluded-volume effects between particles [180]. We set all the $\varepsilon_{\alpha\beta} = \varepsilon$, with ε as the energy unit, except for $\varepsilon_{\kappa w} = \varepsilon_{w\kappa} = 5.0\varepsilon$, where $\kappa \in \{s, l\}$, to prevent chain-wall adhesion under cylindrical confinement [36, 155].

[3]The farthermost distance is defined as $L \equiv z_{\max} - z_{\min}$ [172, 173], where z is the longitudinal distance and the subscripts min and min indicate the leftmost and rightmost positions of monomers along the longitudinal direction. For the definition of the ROG, see Section 4.3.

To enforce the chain connectivity, there is the FENE potential between the adjacent monomers along the chain backbone [181]

$$U_{FENE}(r_{\alpha\beta}) = \begin{cases} -\frac{1}{2}k_{\alpha\beta}r_{0,\alpha\beta}^2 \ln\left[1-\left(\frac{r_{\alpha\beta}}{r_{0,\alpha\beta}}\right)^2\right] & r_{\alpha\beta} \le r_{0,\alpha\beta} \\ 0 & r_{\alpha\beta} > r_{ij,0} \end{cases}, \tag{4.3}$$

where $k_{\alpha\beta} = k_0(\sigma/\sigma_{\alpha\beta})^2$ and $r_{0,\alpha\beta} = 1.5r_0(\sigma_{\alpha\beta}/\sigma)$ are the spring constant and equilibrium bond size. In Eq. 4.3, subscripts $\alpha, \beta \in \{s, l\}$. We set $k_0 = (30.0\varepsilon/\sigma^2)$ and $r_0 = 1.5\sigma$ in our simulations to prevent monomers from crossing [182, 183].

In addition to the above-mentioned conservative interactions, all the particles are subjected to the viscous and random forces, both resulting from collisions with implicit solvent particles at a fixed temperature T; as a result, the motion of α-th particle is described with the Langevin equation

$$m_i\frac{d^2\mathbf{r}_i}{dt^2} = -\boldsymbol{\nabla}_i U_{tot}(\{\mathbf{r_j}\}) - \gamma m_i\frac{d\mathbf{r}_i}{dt} + \mathbf{W}_i(t), \tag{4.4}$$

where m_i, $\mathbf{r}_i$, and $\boldsymbol{\nabla}_i$ are the particle mass, particle position, and gradient operator with respect to the particle coordinates, respectively; moreover, $U_{tot}(\{\mathbf{r}_j\})$ is the sum of all the inter-particle (not inter-species) interactions in the system, and γ is the damping constant. In the left-hand side of Eq. 4.4, the first, second, and third terms are the total conservative, viscous, and random forces exerted on α-th particle, respectively. The random force $\mathbf{W}_i$ satisfies[4]

$$\langle \mathbf{W}_i(t)\rangle = 0, \tag{4.5a}$$

$$\langle \mathbf{W}_i(t)\mathbf{W}_j(t')\rangle = 6\gamma k_B T m_i \delta_{ij}\delta(t-t'), \tag{4.5b}$$

for i-th particle collided by j-th particle.

Assuming a uniform mass density for all particle species, $m_i = m(\sigma_i/\sigma)^3$ is the mass of i-th species, where m is the mass unit. We employ the velocity-Verlet algorithm [185, 186] to integrate the equations of motion with time step $\delta t = 0.005\tau_{LJ}$ where $\tau_{LJ} = \sigma\sqrt{m/\varepsilon}$ is the LJ reduced time unit. The system is kept at a fixed temperature $T = 1.0\varepsilon/k_B$ through Langevin thermostat [187] with a damping constant $\gamma = 0.1\tau_{LJ}^{-1}$, where $k_B = 1$ is the Boltzmann constant in the LJ reduced unit system. The mass and damping factor choices are unimportant in our study since they do not influence equilibrium properties. Our initial settings include choosing $D = 20\sigma$ and $a_c = a_s = \sigma$, and we vary the values of a_l as $q\sigma$, where q ranges within $1, 3, 4, 5, 6$. For

[4] Greek subscripts are used to distinguish particle index from species index.

the crowder volume fraction, ϕ_c, we adopt values from the set 0, 0.1, 0.15, 0.2, 0.225, 0.25, 0.275, 0.3, 0.325, 0.35, 0.375 and 0.4. Depending on the specific ϕ_c value and the volume V_T, we employ a number of crowders that reaches up to 2.8×10^5 for the free space and 4×10^4 for cylindrical confinement.

The chain is initially configured in a helical shape at the center of the simulation box. We first equilibrate the chain alone for 2×10^5 timesteps with $\delta t = 0.01\tau_{LJ}$, where the FENE potential is replaced with the harmonic bond potential, i.e., $U_{Harmonic}(r_{\alpha\beta}) = \frac{1}{2}k_{\alpha\beta}(r_{\alpha\beta} - r_{0,\alpha\beta})^2$. Then, the bond potential is returned to the FENE potential, the crowders are randomly distributed in the simulation box, and the system is equilibrated for another 6×10^6 timesteps with $\delta t = 0.01\tau_{LJ}$. Once the system is fully equilibrated, each simulation is for 10^8 timesteps during the sampling phase. In each simulation, we gather the system conformations every 2000 (5000) steps to calculate time averages (spatial distributions). For each set of system parameters, we run eight independent simulations (replicates) with different random number seeds for the Langevin thermostat and initial crowder distribution, generating eight thermodynamically equivalent systems that evolve along distinct paths in the phase space. We calculate ensemble averages as time averages within each run and then do uncertainty analyses such as obtaining averages and standard errors over replicates. As a result, the standard error of the mean in a reported physical property is smaller than the symbols used in the figures. In the rest of this chapter, all the quantities are averaged over replicates and time (where applicable) unless stated otherwise; moreover, all the measurements are reported in the LJ reduced unit system ($\varepsilon = m = \sigma = 1.0$).

Our MD simulations are performed in the LAMMPS simulation package [188]. We benefit from the multi-size neighboring bin algorithm in LAMMPS [189] to reduce computational costs. We employ the MDAnalysis python package to analyze trajectory files [190–192]. The analysis phase is done in parallel with GNUParallel [193].

4.3 Results

We study the MMC effects on the compaction transition of a heterogeneous ring polymer in free and confined spaces. Specifically, we are interested in seeing whether clustering of large monomers happens; and, if it happens, what is the morphology of such clusters, and how does clustering influence the compaction transition? To this end, we first report our cluster formation and morphology results and then provide our findings of the clustering effects on the compaction transition.

In our polymer model, large monomers are evenly placed along the backbone. Does

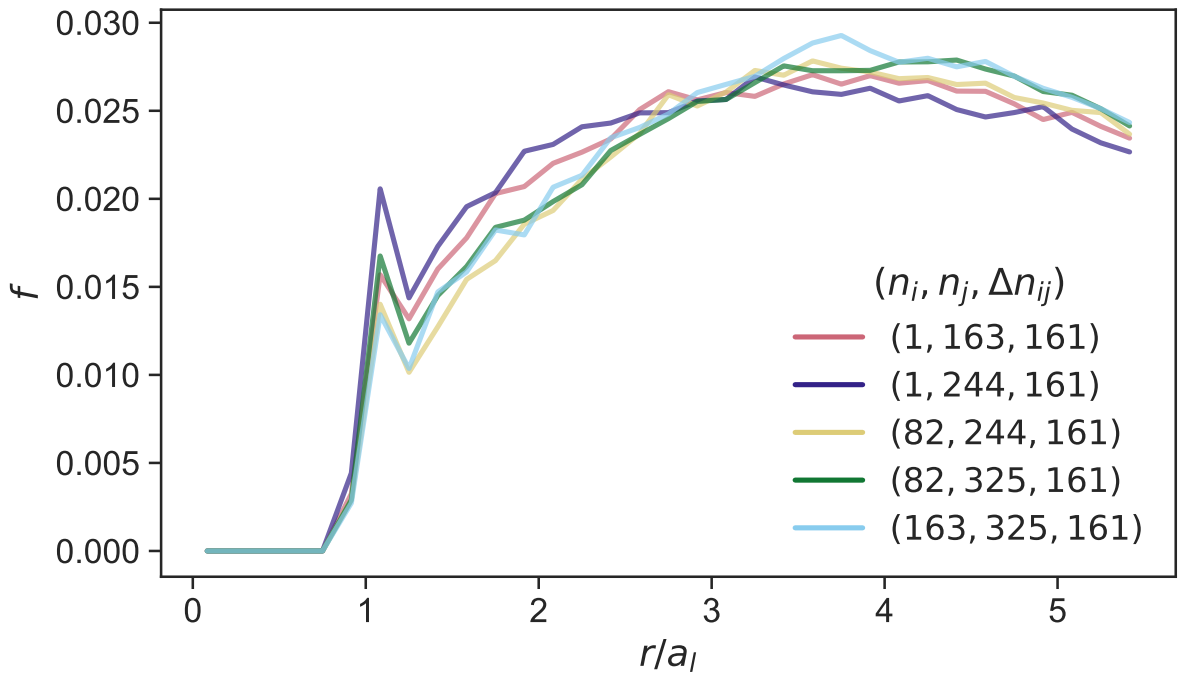


FIGURE 4.4 Probability distribution function $f(r)$ of spatial distance r for different pairs of large monomers with the genomic distance $\Delta n_{\alpha\beta} = 161$. As shown, the $f(r)$ for different (n_i, n_j) pairs (line colors) collapse onto each other, rendering $f(r)$ independent of (n_i, n_j). For visual clarity, r has been rescaled by a_l and truncated, and the area under the curve of $f(r)$ is normalized to unity ($\int_0^\infty 4\pi f(r) r^2 dr = 1$). We have chosen $a_l = 3$ and $\phi_c = 0.2$ in free space.

this translation symmetry along the backbone influence the probability distribution function (PDF) $f(r)$ for the spatial distance between a pair of large monomers? The probability distribution of the spatial distance, represented as $4\pi f(r) r^2 dr$, quantifies the likelihood of the spatial distance vector $\vec{r}$ falling within a spherical shell. This shell has a radius varying between r and $r + dr$, centered around one of the two large monomers in the pair.

To answer this question, we plotted $f(r)$ for different pairs of large monomers at a fixed value of Δn in Fig. 4.4 in free space. For visual clarity, r is rescaled with a_l while the area under the curve of $f(r)$ is normalized to unity ($\int_0^\infty 4\pi f(r) r^2 dr = 1$). Recall that Δn is measured in the number of bonds. As illustrated, the $f(r)$ for various (n_i, n_j) pairs (denoted by line colors) converge onto each other, making $f(r)$ independent of the specific (n_i, n_j) values. Our analysis demonstrates that this trend is not affected by the combinations of Δn, a_l, and ϕ_c in confined ($D = 20.0$) and unconfined ($D = \infty$) spaces. Therefore, we decided to average $f(r)$ over different large monomer pairs, (n_i, n_j), with the same Δn_{ij} value for the rest of our analysis.[5]

[5]In a ring polymer comprising of N_l large monomers, there are $N_l(N_l - 1)/2$ unique pairs of large

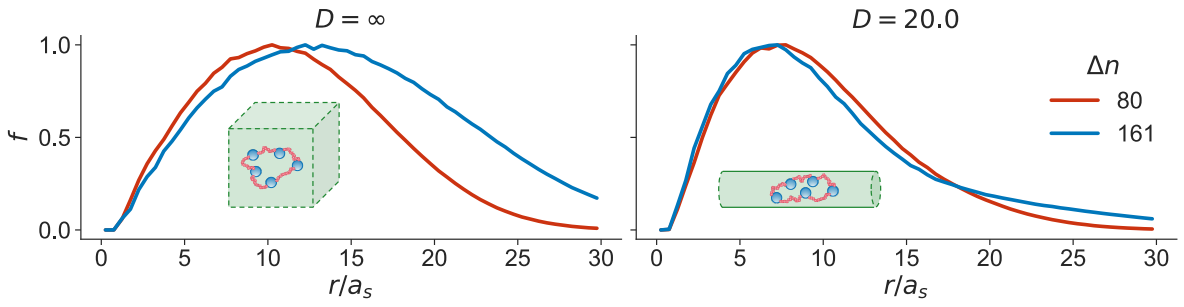


FIGURE 4.5 Probability distribution function $f(r)$ of spatial distance r between large monomers across varying genomic distances Δn (line colors) in the absence of MMC effects ($\phi_c = 0$) and chain heterogeneity ($a_l = 1$). For visual clarity, r is rescaled by a_s while $f(r)$ is rescaled by its maximum value. Recall that $f(r)$ is averaged over pairs of large monomers with different genomic positions but the same Δn. The insets display the heterogeneous polymer inside the simulation box, with dashed contours representing planes perpendicular to which the periodic boundary condition are applied. *Left:* At lower Δn, $f(r)$ peaks more sharply and declines rapidly, reflecting the tendency of genomically proximal segments to be closer in space. *Right:* Under cylindrical confinement, $f(r)$ demonstrates an opposite trend: for a larger Δn value, $f(r)$ increases almost more quickly to its maximum, then decreases more rapidly in the intermediate range of r, before transitioning to regular behavior as it vanishes to zero. This distinct trend, albeit less pronounced than the free space scenario, indicates cylindrical confinement can cause genomically distant segments within a circular polymer to become spatially proximate.

We further examined how cylindrical confinement affects $f(r)$. Figure 4.5 demonstrates the behavior of $f(r)$ for different choices of Δn in the absence of MMC effects ($\phi_c = 0$) and chain heterogeneity ($a_l = 1$). The insets in Fig. 4.5 display the heterogeneous polymer inside the simulation box, with dashed contours representing planes perpendicular to which the periodic boundary condition are applied. In free space (the left sub-figure), at lowerΔn, $f(r)$ peaks more sharply and declines rapidly, reflecting the tendency of genomically proximal segments to be closer in space. Under cylindrical confinement, $f(r)$ demonstrates an opposite trend: for a larger Δn value, $f(r)$ increases almost more quickly to its maximum, then decreases more rapidly in the intermediate range of r, before transitioning to regular behavior as it vanishes to zero. This distinct trend, albeit less pronounced than the free space scenario, indicates cylindrical confinement can cause genomically distant segments within a circular polymer to become spatially proximate. Our investigation confirms that these opposing trends do not qualitatively alter in scenarios where MMC or/and chain heterogeneity exist(s). This consistency across different scenarios is further elucidated in the following two paragraphs, where we explore the effects of MMC and chain heterogeneity separately, as demonstrated in Figs. 4.6 and 4.7. respectively.

monomers with $\lfloor N_l/2 \rfloor$ distinct Δn values. Here, $\lfloor \dots \rfloor$ is the floor function.

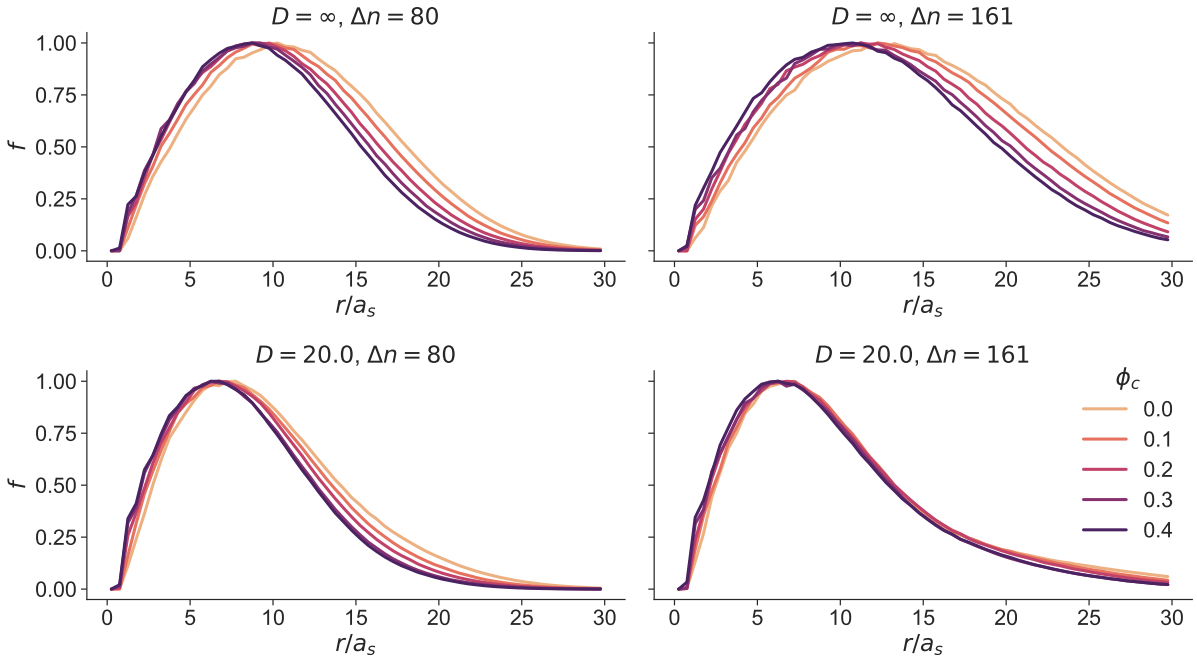


FIGURE 4.6 Probability distribution function $f(r)$ of spatial distance r between large monomers for various bulk volume fractions of crowders ϕ_c (line colors) in the absence of chain heterogeneity ($a_l = 1$). For visual clarity, r is rescaled by a_s while $f(r)$ is rescaled by its maximum value. Recall that $f(r)$ is averaged over pairs of large monomers with different genomic positions but the same genomic distance. *Top row:* In free space, with genomic distances $\Delta n = 80$ (left sub-figure) and $\Delta n = 160$ (right sub-figure), $f(r)$ shifts to smaller r for a larger ϕ_c value (darker line color), suggesting the compaction of large monomers due to MMC effects. Increasing the genomic distance from the left to the right sub-figure does not alter this trend. *Bottom row:* Under cylindrical confinement, the trend of increasing tightness with larger ϕ_c persists. However, the degree of tightness intensifies as the genomic distance increases from $\Delta n = 80$ in the left sub-figure to $\Delta n = 160$ in the right sub-figure, where the curves corresponding to different ϕ_c values converge. This convergence aligns with the enhanced spatial proximity of genomically-distant large monomers under confinement.

Previous studies have shown that MMC and confinement enhance chain compaction [36, 161]. In this vein, we explore the combined effects of MMC and confinement on our ring polymer in the absence of chain heterogeneity. Figure 4.6 displays our results. In free space (the top row), $f(r)$ becomes tighter as ϕ_c increases. This trend, suggesting the compaction of large monomers due to MMC effects, remains consistent across different genomic distances. Under cylindrical confinement, as depicted in the bottom row, the trend of increasing tightness in $f(r)$ with larger ϕ_c values is maintained. However, this effect is more pronounced for a larger Δn value. In particular, when $\Delta n = 160$ (the bottom right sub-figure), the curves corresponding to different ϕ_c values converge, highlighting the closer spatial proximity of genomically distant large monomers under confinement.

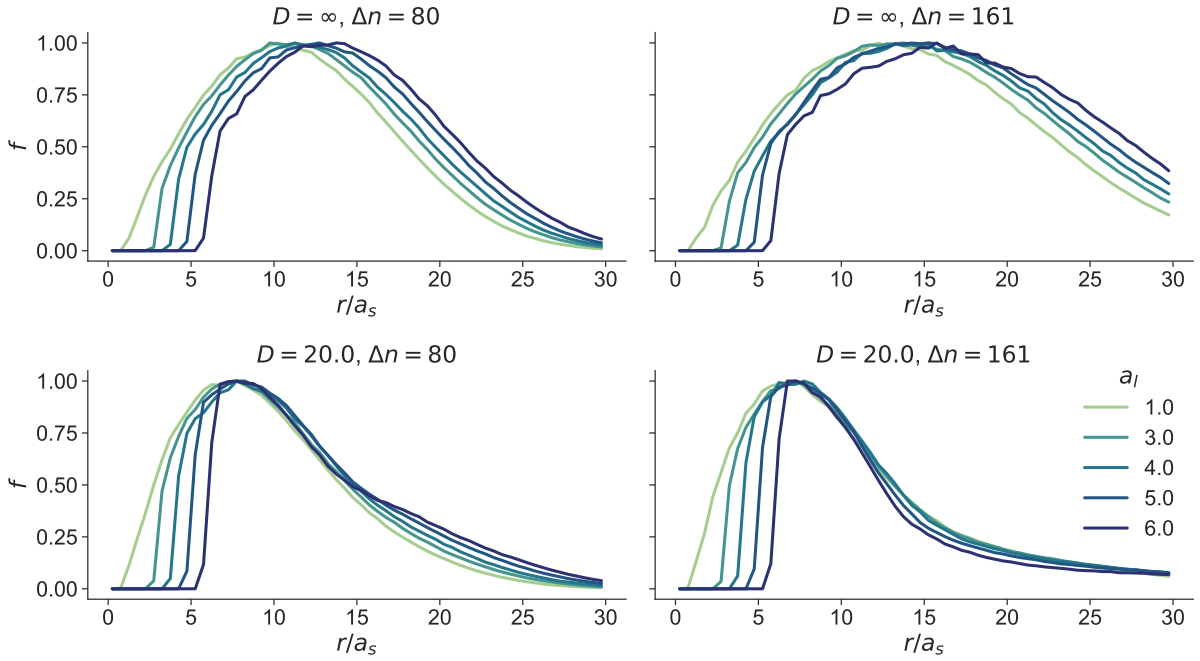


FIGURE 4.7 Probability distribution function $f(r)$ of spatial distance r between large monomers for various large monomer sizes a_l (line colors) in the absence of MMC effects ($\phi_c = 0$). For visual clarity, r is rescaled by a_s while $f(r)$ is rescaled by its maximum value. Recall that $f(r)$ is averaged over pairs of large monomers with different genomic positions but the same genomic distance. All the sub-figures show that $f(r)$ is zero for $r \leq a_l$, irrespective of any changes. *Top row:* In free space, with genomic distances $\Delta n = 80$ (left sub-figure) and $\Delta n = 160$ (right sub-figure), $f(r)$ becomes non-zero for $r > a_l$, showing a shift towards larger r values as a_l increases (darker line color). Increasing the genomic distance from the left to the right sub-figure does not alter this trend. *Bottom row:* Under cylindrical confinement, when $\Delta n = 80$ (left sub-figure), the shift diminishes for intermediate r values, where the curves corresponding to different a_l values overlap. When $\Delta n = 160$ (right sub-figure), the shift in $f(r)$ disappears, and the distribution becomes tighter with an increase in a_l, highlighting the closer spatial proximity of genomically distant large monomers under confinement.

Next, we delved into the interplay between confinement and chain heterogeneity. Figure 4.7 demonstrates how chain heterogeneity ($a_l > 1$) affects $f(r)$ in the absence of crowders ($\phi_c = 0$). A notable observation across all sub-plots is that $f(r)$ remains zero for $r \leq a_l$, regardless of any other changes. In the top left sub-figure, for $\Delta n = 80$ in free space, $f(r)$ shifts toward larger r values as a_l increases. The same trend can be seen in the top right sub-figure ($\Delta n = 160$). In the bottom left sub-figure, with $\Delta n = 80$ in confined space, the previously observed shift in $f(r)$ lessens and becomes non-uniform, leading to an overlap of the curves at intermediate r values. When the genomic distance is doubled to $\Delta n = 160$ (the bottom right sub-figure), the shift in $f(r)$ vanishes; instead, $f(r)$ becomes tighter as a_l increases. This observation corroborates our earlier conclusion from Fig. 4.5: Under cylindrical confinement, genomically distant large monomers tend to be closer in space.

Now, we turn our attention to the combined effects of MMC ($\phi_c > 0$), chain heterogeneity ($a_l > 1$), and confinement on $f(r)$, as depicted in Fig. 4.8. In this figure, a_l increases from the left column to the right, while ϕ_c grows from the top row to the bottom. Additionally, variations in system geometry and genomic distance Δn are indicated by line style and color, respectively. Scenarios previously discussed in Fig. 4.6 ($a_l = 1$) and Fig. 4.7 ($\phi_c = 0$) are excluded in what follows.

When examining the interrelation of confinement with MMC and chain heterogeneity (Figs. 4.6 and 4.7), $f(r)$ typically shows a unimodal distribution. However, in the first column Fig. 4.8, where $a_l = 3$, a second peak emerges as ϕ_c increases. This peak, located at $r \approx a_l$ and marked by a dotted-dashed vertical black line, falls within the region $r \leq r_{\text{thres}} = a_l + a_c$, defined in Section 4.2.2, which is highlighted in light green. This peak becomes more pronounced with increasing ϕ_c. In free space, denoted by solid curves, the peak is more distinct for smaller Δn values (red curves) when $0.1 \leq \phi_c \leq 0.3$. Under cylindrical confinement, represented by dashed curves, this trend nearly disappears, consistent with the behavior observed in Fig. 4.5. In the bottom row, where $\phi_c = 0.4$, this second peak becomes the most probable state of $f(r)$, independent of the system geometry or Δn value.

The prominence of the peak at $r \approx a_l$ in the last row of the first column suggests that MMC effects intensify the likelihood of direct contact between large monomers. However, it is crucial to note that this intensification does not necessarily lead to a permanent direct contact between two large monomers. The cumulative distribution function (CDF) for a pair of large monomers, defined as

$$\mathcal{P}(r_1 \leq r \leq r_2) = \int_{r_1}^{r_2} 4\pi f(r) r^2 dr \tag{4.6}$$

over the interval $[r_1, r_2]$, is smaller within the highlighted region ($r \leq r_{\text{thres}}$) around $r \approx a_l$ than outside it, highlighting the direct contact between large monomers are transient. Such a quantitative analysis aids in understanding the observed patterns in the second column of Fig. 4.8, where $a_l = 4$. Although the general trend observed with $a_l = 3$ in the first column continues, notable differences emerge. Under confinement, indicated by dashed curves, this peak is as significant as the first, even at $\phi_c = 0.1$ (the top row). As ϕ_c increases, the peak at $r \approx a_l$ becomes the most probable state in $f(r)$ at $\phi_c = 0.3$, regardless of the system geometry or Δn value. In the bottom row, where $\phi_c = 0.4$, all $f(r)$ curves converge. Notably, $f(r)$ is almost negligible across most ranges, except near $r \approx a_l$ and at a new, albeit smaller, peak, outside the green-shaded region, in the interval $[r_{\text{thres}}, 2r_l]$. In other words, $\mathcal{P} \approx 1$ within the interval $[0, r_{\text{thres}}]$, suggesting that two large monomers are almost always in direct contact. Along with

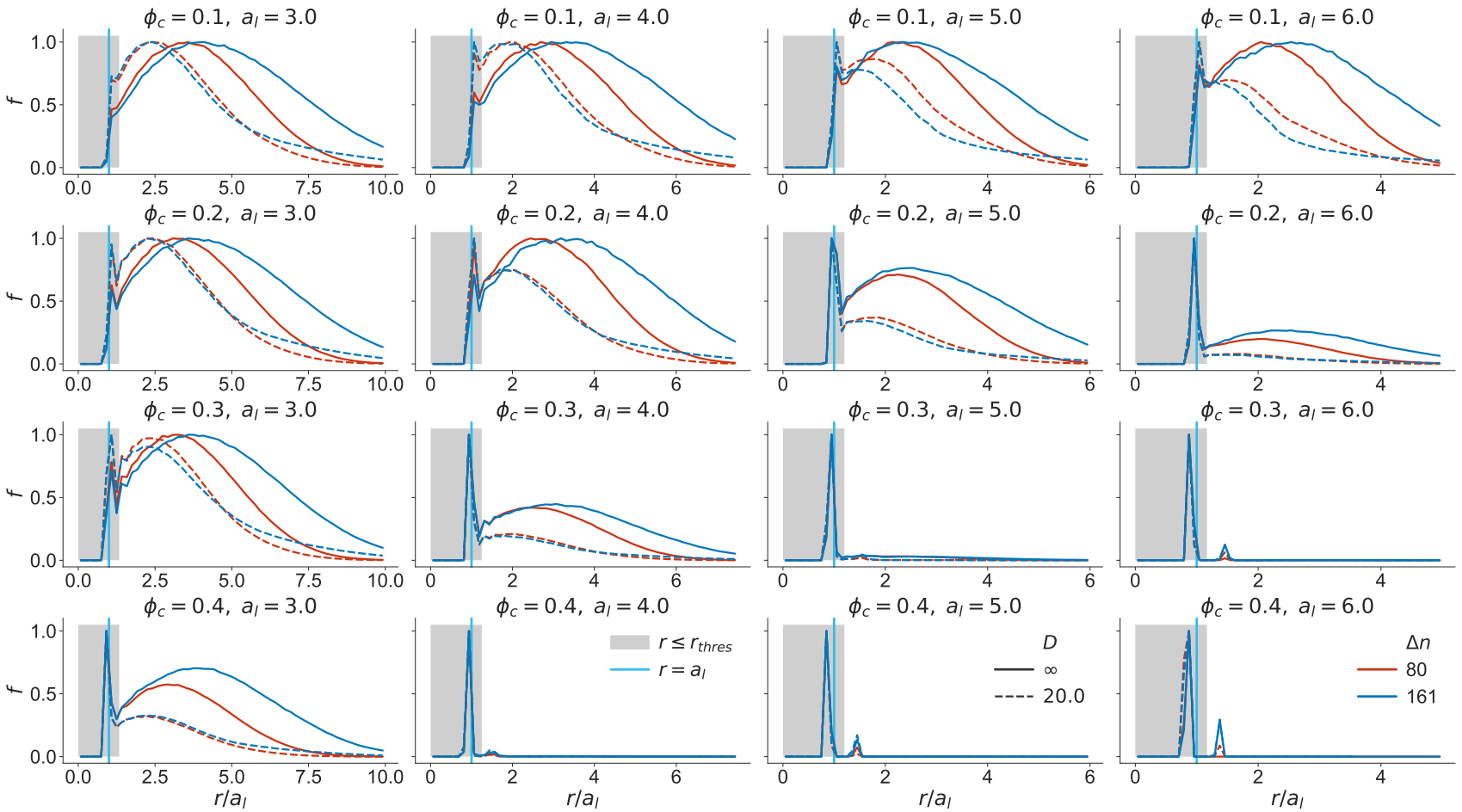


FIGURE 4.8 Probability distribution function $f(r)$ of spatial distance r between large monomers across various Δn values (line color) under different MMC ($\phi_c > 0$, varied along the rows) and chain heterogeneity ($a_l > 1$, varied along the columns) conditions in free (solid lines) and confined (dashed lines, with $D = 20$) spaces. Overall, increasing ϕ_c enhances direct contact between large monomers, maximizing $f(r)$ at $r \approx a_l$ (marked with a vertical cyan line). This trend evenatully leads to persistent direct contact between two large monomers when a_l reaches or exceeds a critical threshold a_l^{thres}. The behavior, i.e., persistent direct contact between two large monomers, is first prominent in the bottom row of the second column, where the cumulative distribution function $\mathcal{P}(r)$ (the area under the curve) nearly reaches unity within the interval $[0, r_{\text{thres}}]$, shaded in gray. In this sub-figure, an additional small peak in the range $[r_{\text{thres}}, 2a_l]$ emerges, akin to the distance between two spheres on two different layers of a lattice in the close-packing of equal spheres, indicating direct contact (or possibly clustering) of more than two large monomers. Cylindrical confinement enhances the direct contacts between large monomers. For improved visual clarity, r is rescaled by a_l and truncated, while $f(r)$ is rescaled with its maximum value. Recall that $f(r)$ is averaged over pairs of large monomers with different genomic positions but identical genomic distances.

this observation, the emergence of the new peak implies an additional significant spatial configuration of large monomer pairs. If we assume that most large monomers are in direct contact within a cluster, then the location of this second peak, i.e., the interval $[r_{\text{thres}}, 2r_l]$, resembles the center-to-center distances between spheres in the first and second layers of a lattice in the close-packing of equal spheres [238].

In the third and fourth columns of Fig. 4.8, corresponding to $a_l = 5$ and $a_l = 6$ respectively, the patterns observed in the second column ($a_l = 4$) become more pronounced. For instance, the peak at $r \approx a_l$ emerges as the most probable state at $\phi_c = 0.2$ in the second row of these columns, regardless of system geometry or the Δn value. In the third row, $\mathcal{P} \approx 1$ is observed within the range $[0, r_{\text{thres}}]$, and a distinct second peak forms within the interval $[r_{\text{thres}}, 2r_l]$. This second peak becomes particularly evident in the final row of both columns.

Our findings in Fig. 4.8 demonstrate the usefulness of our choice of $r_{\text{thres}} = a_l + a_c$, detailed in Section 4.2.2, for defining direct contact between large monomers. Building on these findings, we further explored the implications of varying r_{thres}, with the results demonstrated in Fig. 4.9. In this figure, $p(x_d)$ represents the probability mass function (PMF) of the number of direct contacts x_d between large monomers, defined as

$$p(x_d) = \frac{n_d}{\sum_{n_d} n_d}, \tag{4.7}$$

where n_d is the count of large monomers with x_d direct contacts. In a system with N_l large monomers, x_d can vary from zero to $N_l - 1$ (subject to a maximum of 12, as per the close-packing problem [238, 239]). To calculate $p(x_d)$, we first tallied the occurrences of x_d in each simulation frame, then averaged these over the total number of conformations and replicates.Furthermore, we incrementally increased the value of r_{thres} from $\sigma_{lc} = a_l + a_c$ to $r_{lc,cut} = 2^{1/6}\sigma_{lc}$. Outside this range, r_{thres} loses its meaning: When $r_{\text{thres}} \leq \sigma_{lc}$ ($r_{\text{thres}} \geq r_{lc,cut}$), the WCA potential is strongly repulsive (zero), implying a pair of large monomers are (are not) in direct contact.

As shown in Fig. 4.9 ($a_l = 5$ and $\phi_c = 0.3$ in free space), the curves corresponding to different r_{thres} values collapse on each other, indicating the insensitivity of $p(x_d)$ to changes in r_{thres}, within the tested range. Our investigation shows that changes in the combination of a_l, ϕ_c, and spatial geometry (free space vs. cylindrical confinement) do not qualitatively affect this trend. Upon integrating these findings with a detailed visual inspection of particle trajectories, we determined that $r_{\text{thres}} = \sigma_{lc} = a_l + a_c$ is the most appropriate approach for analyzing the direct contact and clustering of large monomers.

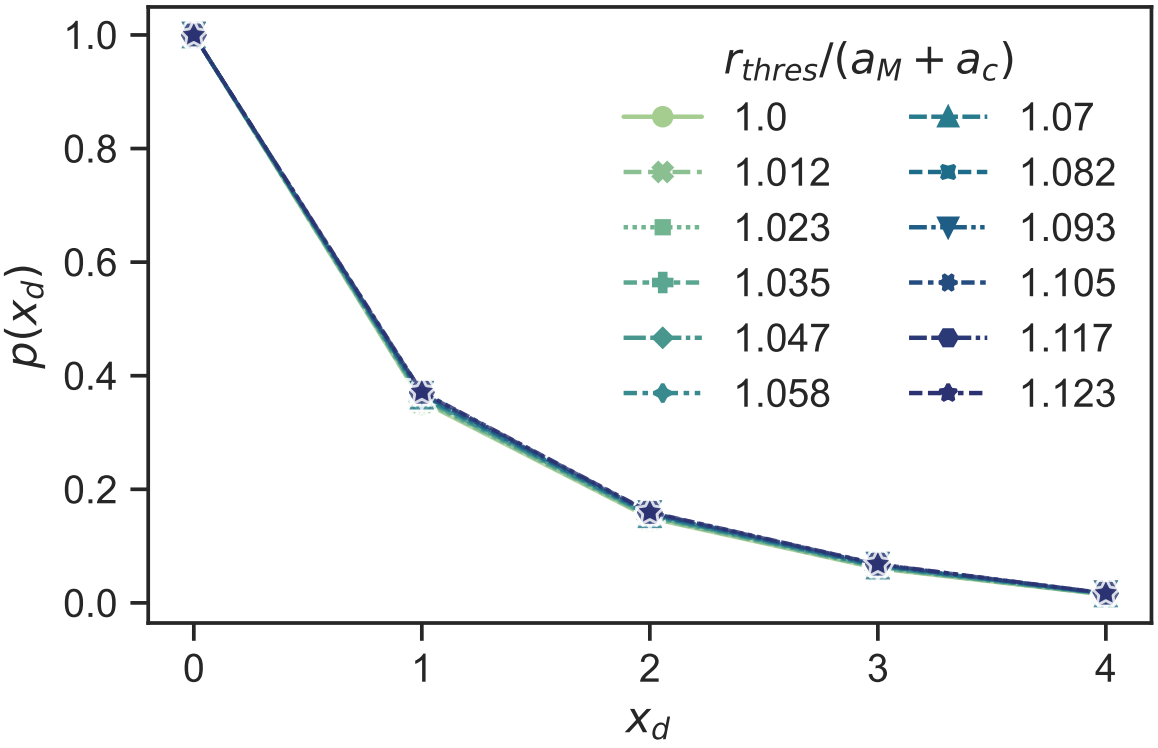


FIGURE 4.9 Probability mass function $p(x_d)$ of the number of direct contacts x_d between large monomers across various direct contact threshold r_{thres} (line styles). The range of r_{thres}, i.e., $[\sigma_{lc}, r_{lc,cut}]$, is chosen based on rationale detailed in Section 4.2.2. For visual clarity, r_{thres} has been rescaled by $a_l + a_c$. Notably, the curves corresponding to different r_{thres} values collapse on each other, indicating the insensitivity of $p(x_d)$ to changes in r_{thres}, within the tested range. The parameters $a_l = 5$, $a_c = 1$, and $\phi_c = 0.3$ were selected for this analysis in free space.

So far, our results have elucidated the effects of MMC and chain heterogeneity on the direct contacts between two large monomers. To investigate the influence of MMC and chain heterogeneity on the clustering of large monomers, we computed the PMFs for both direct contact x_d and cluster size x_c, denoted as $p(x_d)$ and $p(x_c)$, respectively. Similar to the definition of $p(x_d)$, given by Eq. 4.7, we defined $p(x_c)$ as

$$p(x_c) = \frac{n_c}{\sum_{n_c} n_c}, \tag{4.8}$$

where n_c is the count of clusters with x_c large monomers. We adopted the same procedure used for calculating $p(x_d)$ to numerically determine $p(x_c)$. Figure 4.10 showcases our results for $p(x_c)$ across various combinations of ϕ_c (represented by line colors) and a_l (organized by rows) in free (left column) and confined (right column) spaces. In both spaces, $p(x_c = 1) \approx 1$ is approximately unity for all ϕ_c values in the first two rows ($a_l = 1$ and 3), implying that clustering of large monomers does not occur when $a_l \leq 3$. However, in the third row with $a_l = 4$, $p(x_c)$ only deviates from zero under the

most intense MMC condition ($\phi_c = 0.4$, indicated by the darkest line color). Specifically, in free space, large monomers still predominantly exist as single entities, where $p(x_c = 1) \approx 0.6$. In contrast, under cylindrical confinement, they tend to form a single cluster encompassing all monomers, as indicated with $p(x_c = N_l) \approx 1$. This observation suggests that cylindrical confinement promotes the clustering of large monomers. In the final two rows, featuring $a_l = 5$ and $a_l = 6$, $p(x_c)$ shows nonzero values for $x_c > 1$ even at lower ϕ_c levels.

Next, we investigated the packing degree of large monomer clusters. Figure 4.11 shows $p(x_c)$ (left column) and $p(x_d)$ (right column) across varying ϕ_c values in both free (top row) and cylindrically confining (bottom row) spaces. We selected $a_l = 5$ for this figure, as previous findings (see Fig. 4.10) indicated substantial clustering of larger monomers at this a_l value in both free and confined spaces. Along the top row of Fig. 4.11 (free space), a single cluster encompassing all the large monomers (i.e., $x_c = N_l$) becomes the most probable state for $\phi_c \geq 0.325$ in the left column. For such clusters, the plot on the right column reveals a large monomer is mostly in direct contact with three or four other large monomers, as indicated with $\mathcal{P}(x_d \geq 3) \approx 0.85$ (area under the curves), where

$$\mathcal{P}(x_{d,1} \leq x_d \leq x_{d,2}) = \sum_{x_{d,1}}^{x_{d,2}} p(x_d), \tag{4.9}$$

is the CDF of x_d overall interval $[x_{d,1}, x_{d,2}]$. Under confinement, as illustrated along the bottom row of Fig. 4.11, a single cluster encompassing all the large monomers (i.e., $x_c = N_l$) becomes the most probable state for $\phi_c = 0.3$ in the left column, showing cylindrical confinement improves clustering of large monomers due to MMC effects. For such clusters, the plot on the right column reveals a large monomer is mostly in direct contact with three or four other large monomers, as indicated with $\mathcal{P}(x_d \geq 3) \approx 0.7$.

So far, we have established that crowders induce clustering of large monomers at high ϕ_c values, when a_l is equal to or greater than some threshold value, denoted as a_l^{thres}. We now examine the compaction of a heterogeneous polymer due to MMC effects. Below, we report the ROG of the ring polymer, given by,

$$R_g = \left[\frac{1}{N} \sum_i (\vec{r}_i - \vec{R}_{\text{COM}})^2 \right]^{1/2}, \tag{4.10}$$

as the polymer size at a given ϕ_c value in both free and cylindrical confinement. Here, $\vec{r}_i$ is the position of the i-th monomer, and $\vec{R}_{\text{COM}} = (1/N) \sum_i \vec{r}_i$ denotes the COM of

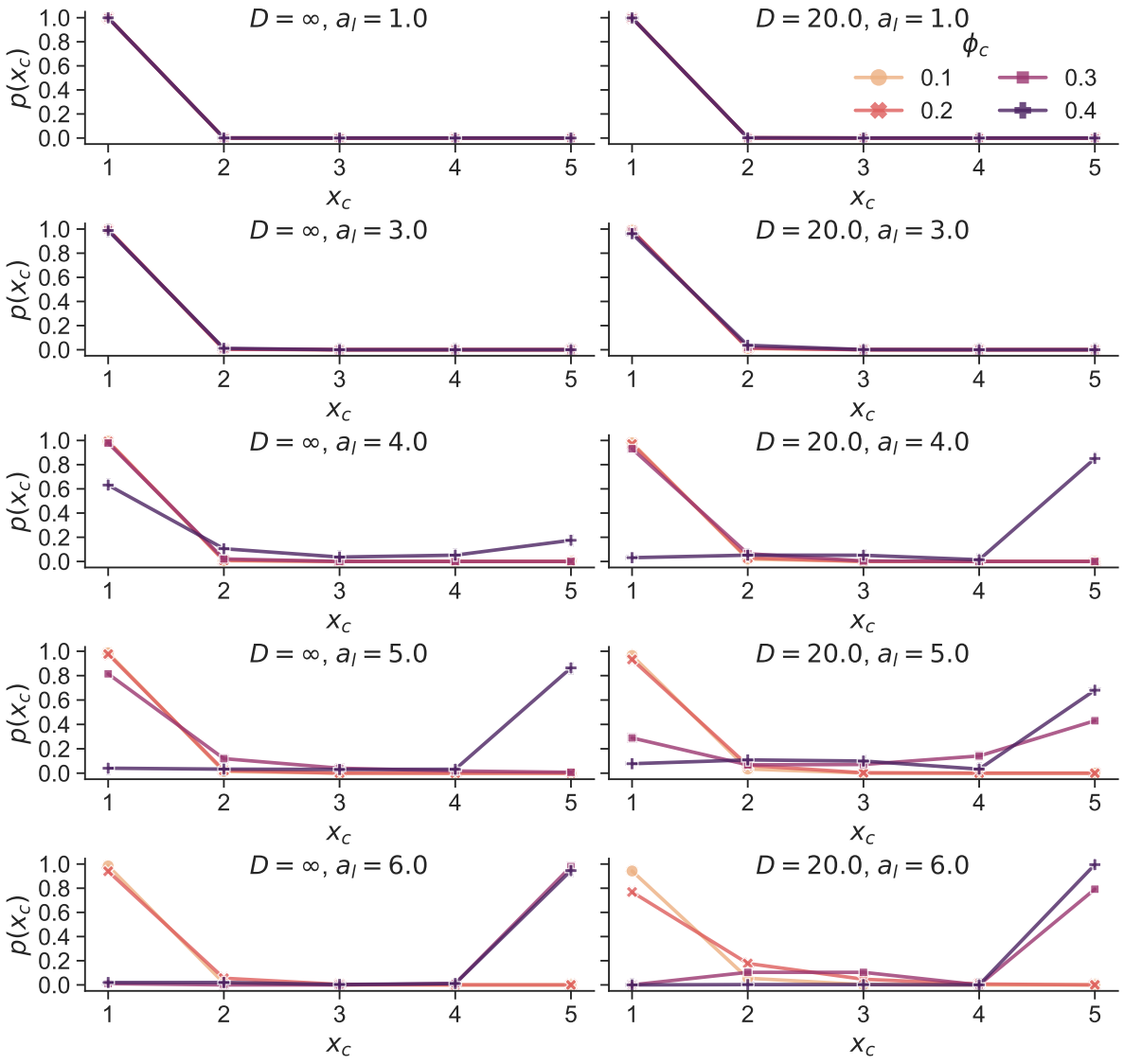


FIGURE 4.10 Probability mass function $p(x_c)$ for the cluster size x_c across various combinations of ϕ_c (represented by line colors) and a_l (organized by rows) in free space (left column) and cylindrical confinement (right column). For $a_l \leq 3$ (first two rows), $p(x_c = 1) \approx 1$ around one across all ϕ_c values in both spaces, suggesting that large monomers do not cluster. However, for $a_l = 4$ (third row), clustering becomes noticeable only under the strongest MMC condition ($\phi_c = 0.4$). Here, large monomers still mainly exist as single entities in free space, where $p(x_c = 1) \approx 0.6$, but under cylindrical confinement, they tend to form a single large cluster, as indicated with $p(x_c = N_l) \approx 1$. This pattern indicates that cylindrical confinement plays a crucial role in enhancing clustering. In cases with larger monomer sizes ($a_l = 5$ and $a_l = 6$, last two rows), the emergence of non-zero $p(x_c)$ values for $x_c > 1$ at lower ϕ_c levels suggests a higher likelihood for clustering among large monomers, especially under conditions of increased chain heterogeneity and MMC.

the polymer.[6]

[6]It is noteworthy that the farthermost distance is a more suitable measure of chain size under cylindrical confinement [173]. However, to facilitate comparison between different spaces (free vs. cylin-

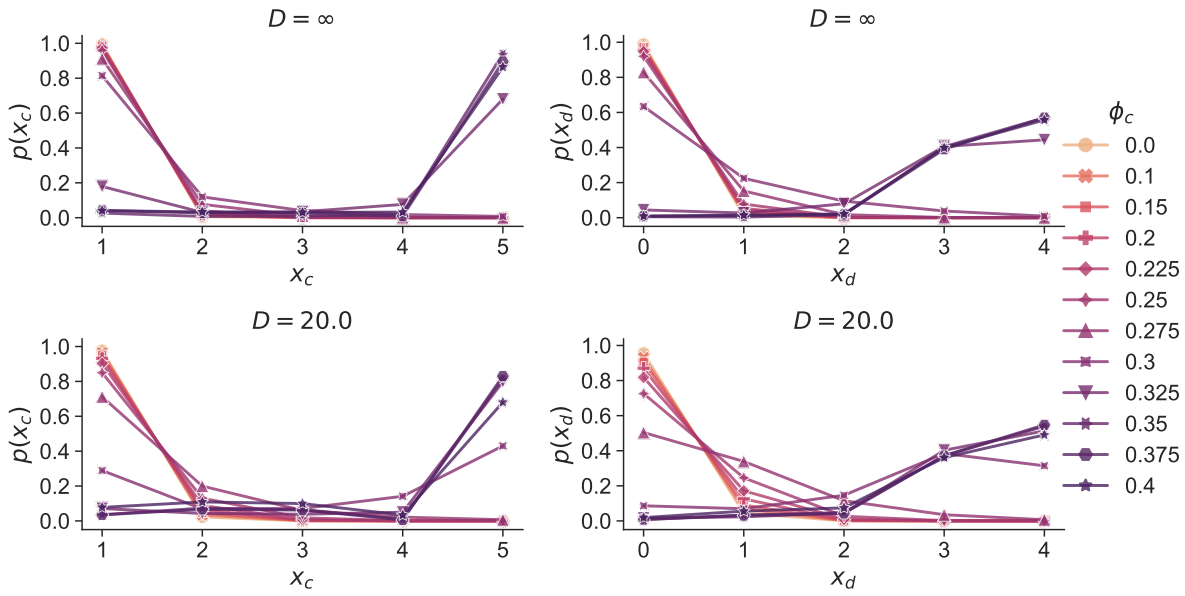


FIGURE 4.11 Probability distribution functions $p(x_c)$ and $p(x_d)$ for cluster size x_c (left column) and direct contact number x_d (right column), respectively, are shown across varying ϕ_c values (indicated by line colors) in free space (top row) and cylindrical confinement (bottom row) at $a_l = 5$. *Top row:* As ϕ_c increase (darker line colors), the peaks in $p(x_c)$ and $p(x_d)$ shift to larger x_c and x_d values, respectively. This trend highlights the formation of larger and tighter clusters under a stronger MMC condition ($\mathcal{P}(x_d \geq 3)$ for $\phi_c \geq 0.325$). *Bottom row:* Cylindrical confinement enhances the formation of large and tight clusters and ($\mathcal{P}(x_d \geq 3)$ for $\phi_c \geq 0.3$).

Figure 4.12 depicts our calculations for three interrelated quantities, namely the equilibrium (average) ROG of the polymer $\langle R_g \rangle$ (top row), number of direct contacts per large monomer $\langle x_d \rangle$ (middle row), and size of large monomer clusters $\langle x_c \rangle$ (bottom row). We reported them as functions of ϕ_c at various a_l values (denoted line colors) in free (dashed line style with circle markers; see Fig. 4.1D) and cylindrically confining (solid line style with square markers ; see Fig. 4.1E) spaces. Recall that all the physical quantities are averaged over replicates, time, and, if possible, pairs of large monomers with the same Δn value. We rescaled $\langle R_g \rangle$ with $\langle R_{g,0} \rangle \equiv \langle R_g(\phi_c = 0) \rangle$, which is the unperturbed ROG of the polymer in the absence of crowders.

The top row of Fig. 4.12 displays the compaction of a heterogeneous chain under the influence of MMC effects. As ϕ_c increases, the polymer undergoes compression, except within the high ϕ_c range, where the polymer size nearly saturates ($\langle R_g \rangle \approx 0.4 \langle R_{g,0} \rangle$) for $a_l = 5, 6$. Remarkably, this "full compaction" (collapse transition) occurs within a biologically-relevant range of ϕ_c ($0.2 \lesssim \phi_c \lesssim 0.4$). In general, confinement (solid curves with filled squares) amplifies the compaction effects of MMC, causing a shift in

drical confinement), we utilize the equilibrium ROG.

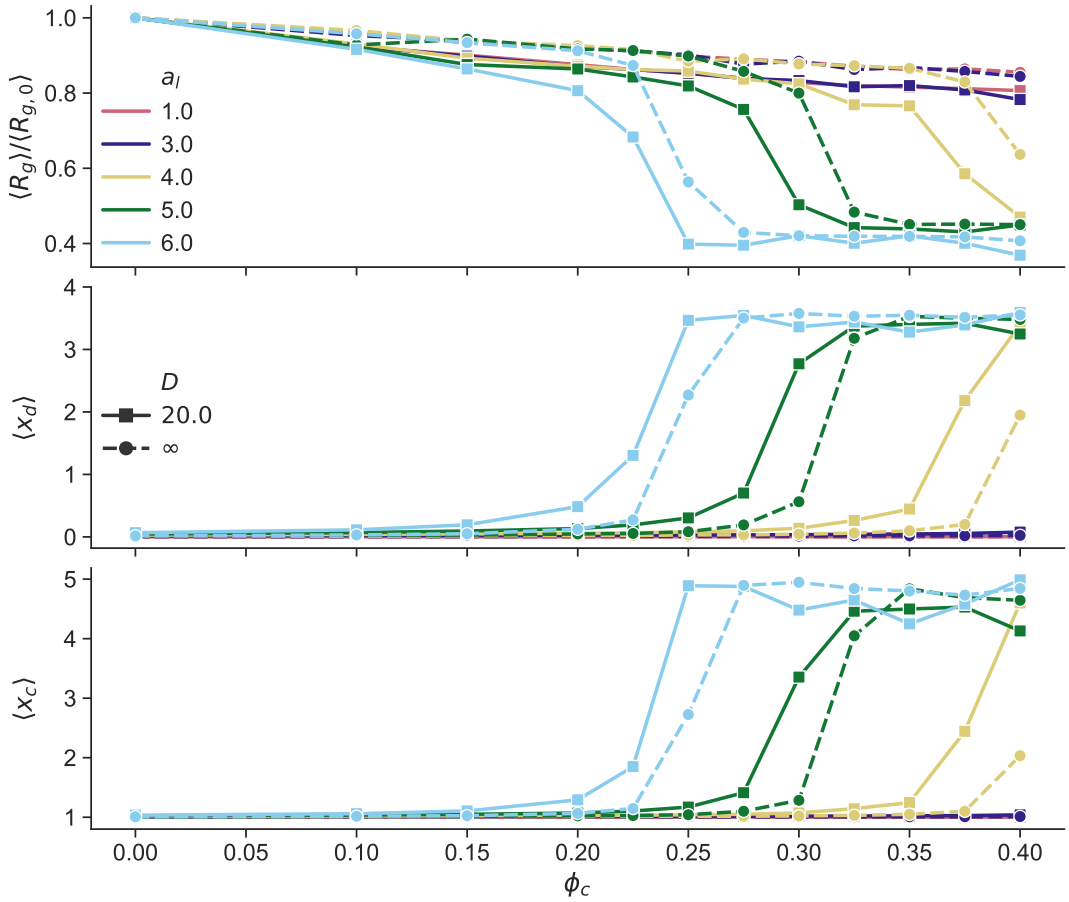


FIGURE 4.12 MMC effects on the intra-chain clustering and compaction of a heterogeneous polymer in free spaces (dashed curves with filled circles) and in cylindrically confined spaces (solid line with filled squares).From top to bottom, the rows represent the equilibrium ROG of the polymer $\langle R_g \rangle$, number of direct contacts between large monomers $\langle x_d \rangle$, and size of large monomer clusters $\langle x_c \rangle$ as functions of ϕ_c at varying a_l values (different line colors). We rescaled $\langle R_g \rangle$ by its respective value $\langle R_{g,0} \rangle$ at $\phi_c = 0$ for visual clarity. *Top row:* The chain size decreases with increasing ϕ_c, possibly except in a large ϕ_c range, where $\langle R_g \rangle$ saturates at $\langle R_g \rangle \approx 0.4 \langle R_{g,0} \rangle$ for $a_l = 5, 6$; this "full compaction" (collapse transition) occurs in a biologically-relevant range of ϕ_c ($0.2 \lesssim \phi_c \lesssim 0.4$). However, for the homogeneous case ($a_l = 1$) and even for $a_l = 3$, MMC has a marginal effect on chain compaction, especially in the free case. In all depicted cases, cylindrical confinement enhances the transition. *Middle row:* As ϕ_c increases, $\langle x_d \rangle$, which characterizes the cluster configuration (see Fig. 4.3A), increases. When $a_l \geq 4$, $\langle x_d \rangle$ initially remains nearly flat and then increases rapidly to a large value ($\langle x_d \rangle \approx 3.6$), except for the dashed yellow curve, as a function of ϕ_c; beyond full compaction, it reaches a plateau. The value of ϕ_c at which this occurs is smaller for larger a_l; for a given a_l, it is smaller for the confined case. *Bottom row:* Similar to $\langle x_d \rangle$, $\langle x_c \rangle$ increases rapidly to a large value around 4 or 5 in some narrow range of ϕ_c. The results in the middle and bottom rows suggest that for a sufficiently large value of ϕ_c, the large monomers are clustered with a close-packing configuration: $\langle x_d \rangle \approx \langle x_c \rangle - 1$. The results in the top row are mirrored by those in the bottom ones: chain compaction occurs when the large monomers form a cluster; the condition for "full compaction" (i.e., $\langle R_g \rangle \approx 0.4 \langle R_{g,0} \rangle$) coincides with that for clustering.

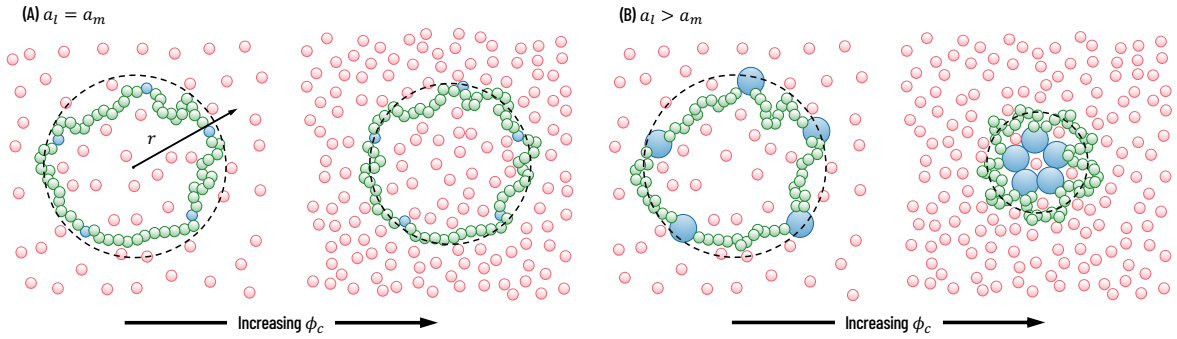


FIGURE 4.13 Clustering and spatial distribution of monomers and crowders. The dashed circle represents the boundary between monomer-rich and crowder-rich phases. Here, r denotes the radial distance from the COM of the polymer. The findings displayed in Fig. 4.12 are schematically reflected in this illustration. (A) In the case of $a_l = a$, MMC minimally impacts chain compaction. The presence of the polymer slightly perturbs the spatial distribution of crowders. (B) At low ϕ_c, polymer compaction is marginal, similar to the situation depicted in (A). However, as ϕ_c increases significantly, both chain compaction and clustering occur simultaneously. Notably, large monomers within the cluster are distinctly segregated from small monomers and crowders.

the full compaction towards lower ϕ_c values (approximately a 0.025 reduction in ϕ_c). Conversely, when $a_l = 1$ (representing a homogeneous case), MMC exerts a minimal influence on polymer compaction, especially in the free scenario (illustrated by the dashed red curve with filled circles).

In the middle row of Fig. 4.12, $\langle x_d \rangle$ is depicted as a measure of cluster configuration packing. For $a_l < 4$, $\langle x_d \rangle$ remains nearly zero across all values of ϕ_c. However, when $a_l \geq 4$, as ϕ_c increases, $\langle x_d \rangle$ initially exhibits little variation but then sharply increases towards its maximum values ($\langle x_d \rangle \approx 3.6$, except for the dashed yellow curve; see the top right cluster configuration in Fig. 4.3A). Notably, the threshold ϕ_c at which this transition occurs is smaller for larger a_l, and for a given a_l, it is further reduced under confinement.

The bottom row of Fig. 4.12 illustrates the relationship between $\langle x_c \rangle$ and ϕ_c. Similar to $\langle x_d \rangle$, $\langle x_c \rangle$ shows a rapid increase, reaching a significant value around 4 or 5 ($\langle x_c \rangle \approx N_l$) within a narrow range of ϕ_c, particularly when $a_M \geq 4a$ (again; except for the dashed yellow curve). The findings from the middle and bottom rows of Fig. 4.12 indicate that during full compaction, the large monomers are in a closely-packed cluster, with $\langle x_d \rangle \approx \langle x_c \rangle - 1$. It is noteworthy that the observations in the top row of Fig. 4.12 mirror those in the middle and bottom rows: chain compaction coincides with the clustering of larger monomers, and the criterion for "full compaction" (i.e., $\langle R_g \rangle \approx 0.4 \langle R_{g,0} \rangle$) aligns with that for clustering.

While the large monomers can cluster under the right conditions, the entire sys-

tem can phase-separate into monomer-rich and crowder-rich regions, as depicted in Fig. 4.13; the findings in Fig. 4.12 are schematically echoed in this figure. As illustrated in Fig. 4.13A, in the homogeneous case where $a_l = 1$, MMC minimally affects chain compaction; consequently, the presence of the polymer weakly perturbs the spatial distribution of crowders. The effect of MMC on a heterogeneous polymer is similarly marginal for small ϕ_c, analogous to the corresponding scenario in Fig. 4.13A for the homogeneous case. However, when ϕ_c reaches sufficiently high levels, both chain compaction and clustering occur concurrently, as illustrated in Fig. 4.13B. Therefore, the large monomers in the cluster are expected to be effectively segregated from small monomers and crowders.

To systematically examine the spatial distributions of monomers and crowders, we have plotted the radial volume fractions of monomers and crowders in free space across various combinations of a_M and ϕ_c in Fig. 4.14. Here, $\phi_\alpha(r)$ (where $\alpha = c, s, l$) denotes the local volume fraction of each species: crowders ($\alpha = c$; top row), small monomers ($\alpha = s$; middle row), and large monomers ($\alpha = l$; bottom row). The value of a_l increases from $a_l = 1$ in the leftmost column to $a_l = 6$ in the rightmost column. The COM of the heterogeneous chain is located at the origin, i.e., $r = 0$. For visual clarity, $\phi_s(r)$ and $\phi_l(r)$ ($\phi_c(r)$) are (is) rescaled with its maximum value near the origin (deep in the crowder-rich) for small and large monomers (crowders). Additionally, the radial direction r is rescaled with the unperturbed chain size $\langle R_{g,0} \rangle$ for a given a_l value.

The findings presented in Fig. 4.14 suggest that the transition between crowder-rich and monomer-rich phases exhibits a gradual crossover, rather than the sharp separation often assumed in theoretical models [34, 36] (also see in the Supplementary Information of ref. [35]). Moreover, these findings provide a visual representation of the interrelation between the distributions of monomers and crowders. In the homogeneous scenario, where $a_l = a_s = 1$, the volume fraction $\phi_c(r)$ within the monomer-rich region is approximately 10 % smaller across all values of ϕ_c used. A similar tendency persists for $a_l = 3$. Conversely, for $a_l \geq 4$, when ϕ_c is large, crowders and monomers exhibit distinct segregation, with a more pronounced separation observed for larger a_l, particularly evident in the case of $a_l = 5, 6$. Notably, for $a_l = 5, 6$, $\phi_c(r)$ almost vanishes near the origin, provided that ϕ_c attains sufficiently high values ($\phi_c \gtrsim 0.3$). This observation corresponds to the clustering phenomenon observed in Fig. 4.2: crowders are almost entirely excluded from the cluster, as schematically shown in Fig. 4.13B. Likewise, significant segregation between large and small monomers is observed under these conditions.

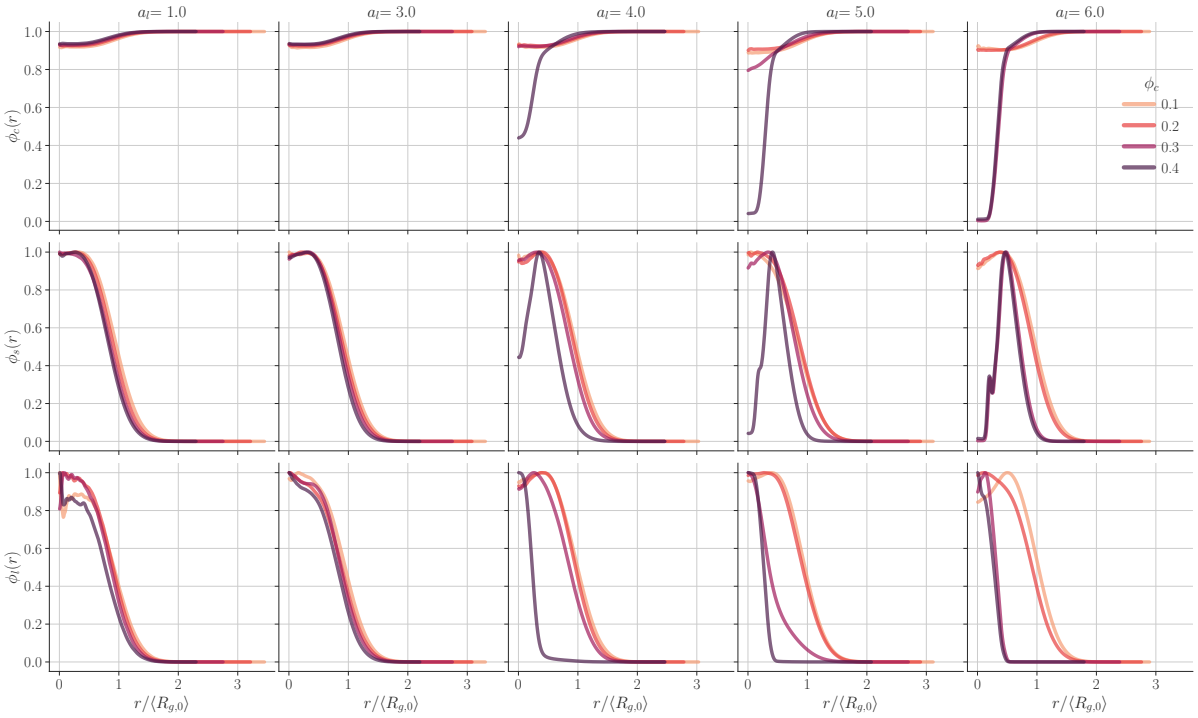


FIGURE 4.14 Spatial distribution of monomers and crowders in an free space. Here, ϕ_α (with $\alpha = c, s, l$) represents the radial volume fraction of species α: crowders ($\alpha = c$; top row), small monomers ($\alpha = s$; middle row), and large monomers ($\alpha = l$; bottom row). The value of a_l increases from $a_l = 1$ in the leftmost column to $a_l = 6$ in the rightmost column. The COM of the heterogeneous chain is located at the origin, i.e., $r = 0$. For visual clarity, $\phi_\alpha(r)$ is rescaled with its maximum value near the origin (deep in the crowder-rich) for monomers (crowders). Additionally, the radial direction r is rescaled with the unperturbed chain size $\langle R_{g,0}\rangle$ for a given a_l value. The upper two rows together indicate that the transition between crowder-rich and monomer-rich regions is a smooth crossover rather than a sharp separation. In the homogeneous case ($a_l = 1$; leftmost column), $\phi_c(r)$ is slightly lower in the monomer-rich region by approximately 10 %. This trend persists for $a_l = 3$. When $a_l = 4$, small monomers tend to segregate from large monomers, especially at high $\phi_c = 0.4$, although the segregation is somewhat modest. In the case of larger a_l, such as $a_l = 5a$, monomers and crowder are well-separated at sufficiently high ϕ_c values, typically $\phi_c \gtrsim 0.3$. A similar separation is observed between large monomers and small ones. This observation aligns well with the clustering of large monomers into a closely-packed configuration under appropriate conditions, as observed in Fig. 4.12 and schematically illustrated in Fig. 4.13B.

4.4 Discussion and conclusion

This chapter has presented simulation outcomes for the compaction of a heterogeneous ring polymer by MMC effects in unconfined (free) and confined spaces. Our study was inspired by how the chromosome is organized in E. coli cells. The polymer model we employed features large monomers evenly interspersed with small monomers along the backbone, representing key features of the E. coli chromosome at a coarse-grained level. These large monomers symbolize transcriptionally-active units along the E. coli

chromosome, particularly rrn operons, consisting of DNA, engaged RNAPs, nascent pre-rRNAs transcripts, and ribosomal proteins [65, 152, 202, 222]. The size of each large monomer reflects growth conditions, enlarging under fast growth conditions [152] (also see refs. [40, 161]).

However, our polymer model ignores certain biological details, such as the intricate Christmas-tree-like structure of rrn operons (see Fig. 4.1B) [65, 202, 205]. Here, we assume RNAPs to be closely packed into a spherical shape alongside other components, although in reality, RNAP exchange or rearrangement between nearby operons can occur. This 'soft' characteristic allows two large monomers to merge into one with a larger size, resulting in stronger depletion forces between them [161, 234]. In our modeling, this 'soft' characteristic is considered by adjusting the size of large monomers.

In spite of its simplicity, our model goes beyond the scope of recent modeling efforts [40, 152, 161, 210]. Prior studies often ignored the interdependence between monomer and crowder distributions or were based on two-body depletion interactions. Our coarse-grained computational modeling systematically captures this interdependence and depletion forces within the polymer (see Fig. 4.13).

Our simulation outcomes shed light on how polymer heterogeneity and confinement impact the compaction and clustering of a chromosome-like polymer under MMC effects. Notably, when large monomers reach a critical size, they tend to cluster into a closely-packed configuration within a biologically-relevant range of crowder volume fraction (ϕ_c), enhancing compaction, particularly under cylindrical confinement. The clustering of large monomers echoes observations made of the E. colichromosomes, where transcription-active units cluster into the so-called "transcription factories" in rapidly growing E. coli [65, 152, 202, 210]. In a manner akin to our findings, the chromosome in these instances was demonstrated to be organized into a more condensed structure [65, 202, 210]

Moreover, our results illustrate how monomer and crowder distributions are mutually dependent and how this interdependence influences polymer compaction and clustering. Specifically, when the polymer is weakly compacted as is the case for a homogeneous polymer (i.e., $a_l = a_s$), its presence minimally affects crowder distribution, slightly reducing crowder volume fraction within the polymer-occupied region (less than 10 % reduction). Conversely, for larger a_l values (e.g., $a_l = 5a_s, 6a_s$), crowders are depleted from the polymer-occupied region, almost entirely from a cluster formed by large monomers.

Our work underscores the significance of phase separation and clustering as organizing principles in biology, particularly for systems not reliant on membrane com-

partmentalization [75, 206, 207, 221]. The nucleoid formation and its internal organization, such as the clustering of transcriptionally-active units and H-NS binding sites (see next chapter), serve as prime illustrations in bacteria. Membrane compartmentalization of the nucleoid would entail substantial energy costs for bacteria. Instead, segregating the chromosome from the cytoplasm through phase separation offers an efficient alternative that supports associated processes, including transertion in E. coli — the coupling of chromosome loci with the cell membrane via membrane protein insertion [110, 240]. Additionally, this mechanism allows for the dynamic exchange of molecules with the cytoplasm. For example, free messenger ribonucleic acid (mRNA) molecules can easily move from the membraneless nucleoid to regions rich in ribosomes, facilitating efficient protein synthesis in these regions [110].

In this study, we did not observe the coexistence of extended and collapsed states seen in in-vitro experiments on the E. coli chromosomes trapped in cylindrical tubes [35]. This difference likely stems from model-chromosome variability. Primarily, the chromosome has local stiffness and is longer than the flexible model we employed. Although our findings show full polymer compaction upon clustering of large monomers, they do not provide a definite picture of the nature of the transition (abrupt vs. continuous). The collapse transition of a polymer in a poor solvent becomes more abrupt with chain stiffness and length [241]. For instance, when a block copolymer containing both flexible and semiflexible blocks is immersed in a selective implicit solvent (poor vs. good), it exhibits a coexistence of collapse and rod-like states [176]. The details of this coexistence depend on the stiffness of the polymer blocks and the solvent selectivity [176].

Finally, we did not incorporate electrostatic interactions between chain segments or between a chain segment and salt ions or charged crowders. Despite this and other features that have been omitted, our study may serve as a preliminary effort towards modeling the clustering within bacterial chromosomes. Although the model presented is considerably simplified, it is noteworthy for being the first to methodically incorporate both chain heterogeneity and the effects of crowders. As more experimental data emerge, there is significant scope for refinement and enhancement of this model.

CHAPTER 5

Modeling the compaction of bacterial chromosomes: biomolecular crowding and the cross-linking protein H-NS

5.1 Introduction[1]

In all organisms, chromosomes are densely packed yet show a high level of organization [39, 198, 199]. But what ensures they remain well structured, in a manner compatible with their essential biological functions like transcription or replication? Chromosome organization is a complex endeavor for every cell, necessitating a blend of different molecules and their physical influences [39, 198, 199]. For bacterial chromosomes, various studies have illuminated the contributions of NAPs like heat-unstable (HU) and H-NS [10, 19, 242, 243]. These proteins can bend, link, loop, or supercoil the chromosomal DNA. Moreover, the impact of MMC in cellular environments has gained prominence [24, 35, 39, 40, 108, 153, 158, 160, 161].

Within crowded cellular spaces [27, 153, 204], biopolymers like chromosomes may undergo entropic condensation and phase separation from surrounding crowders [24, 35, 39, 40, 108, 153, 158, 160, 161]; polymer segments experience entropic attractions due to MMC effects [127, 128]. While bacterial chromosome organization heavily leans on this non-specific entropy-driven mechanism, it needs to synchronize seamlessly with other cellular activities like DNA transcription, DNA segregation, and cell growth [39, 199, 244]. Recent research underscores the combined influences of crowders and the H-NS protein [245–248]. On its own, H-NS subtly affects chromosome compaction, akin to other chromosome-associated proteins (CAPs) [24]. Yet, when paired with crowders, its impact can amplify.

H-NS is among the approximately twelve well-known NAPs for E. coli [249]. It is

[1]A brief version of this chapter, including some figures, is published in the journal *Scientific Reports*. For an electronic copy, see here: https://doi.org/10.1038/s41598-023-50355-2

15.6 kDa [250] in weight, and exists in abundance, with ∼20 000 [242, 249] copies per genome during exponential phase in an E. coli cell, a rough concentration of 20 µM for one genome equivalent in an E. coli cell with an average volume of 1 µm³ [72].[2] H-NS is composed of 137 aa [250], with an N-terminal unit consisting of two oligomerization sites, a linker responsible for initial DNA binding, and C-terminal for DNA binding [243, 250–252]. It primarily exists as a dimer (more accurately, protomer) and preferentially (otherwise non-specifically) binds to AT-rich curved DNA [253, 254], playing structural and regulatory roles [243, 252, 255]. Due to this preference, characteristic of promoters, H-NS acts as a global repressor [254] of transcription [243, 252, 255]. Additionally, H-NS plays a role in condensing bacterial DNA by bridging (cross-linking) two sites on the DNA, which may be spatially distant along its sequence [10, 19, 243, 252, 255–257]. In collaboration with other NAPs, H-NS facilitates DNA compaction on a scale up to 1 kbp [10, 19].

In the context of the synergistic effects between H-NS binding and MMC, it is noteworthy to highlight the size-dependent nature of depletion interactions [39, 40, 158, 160]. When crowders are larger than monomers, their impact on chain condensation becomes minimal [158, 160]. The average size of cytoplasmic crowders ($\approx$ 5 nm [67, 68]) exceeds the typical DNA width ($\approx$ 2.5 nm [5, 93]). However, it is widely recognized that MMC plays a pivotal role in compacting bacterial chromosomes [24, 35]. Recent research supports that the binding of molecules to an otherwise homogeneous polymer results in enhanced chain condensation due to MMC effects, as distinctly observed in bacterial chromosome compaction [36, 40, 108]. This observation is consistent with the previously discussed synergy between H-NS and crowders [245–248].

Although significant efforts have been made, a definitive understanding of the interrelation between H-NS and crowders remains elusive. To shed light on the synergetics mentioned above, a mean-field type approach was utilized in ref. [247], considering the H-NS binding to DNA as a process that thickens the DNA. A computational study [258] effectively portrayed H-NS as a mobile binder but omitted crowders. Without crowders, the bridging (cross-linking) behavior of H-NS can be replicated through limited bridging connections between specific monomers spread across the chain structure [257, 259]. To achieve a deeper grasp of the interrelation between cross-linking and MMC, it is crucial to systematically examine this interrelation under well-defined conditions, without neglecting vital aspects like the presence of crowders, the binding of H-NS to DNA, and the interaction between H-NS and crowders.

In this chapter, we utilize MD simulations rooted in polymer physics to analyze

[2] We use the tradition unit of molar concentration, where $1\,\mathrm{M} = 1\,\mathrm{mol\,L^{-1}} = 1000\,\mathrm{mol\,m^{-3}}$.

the compaction of bacterial chromosomes by H-NS and crowders. Polymer models of chromosomes have significantly contributed to recent advances in our understanding chromosome organization [39, 40, 108, 157, 161, 258, 259]. Building upon recent modeling techniques [39, 40, 108, 161, 258], we examine a circular polymer interacting with mobile binders within a crowded environment. Every H-NS binder (dimer), conceptualized as a sphere with two opposing binding sites, can bridge two monomers along the polymer backbone, even if they are distant [258, 260]. In designing these binders, we follow the modeling strategy outlined in ref. [258], ensuring our mobile binders emulate the impact of H-NS on bacterial chromosomes.

The simulation outcomes presented in this chapter provide a detailed understanding of the roles of MMC and H-NS in chromosome compaction. Specifically, they give a more comprehensive insight into the synergy between crowders and H-NS than previous studies [245–248]. Our findings can be encapsulated in the following manner: Crowders amplify the ability of H-NS to bind to chromosome-like polymers by boosting H-NS cross-linking propensity. Conversely, when H-NS is present, it intensifies the impact of MMC. This mutual influence indicates a bidirectional synergy between H-NS and crowders in chromosome compaction. Additionally, our data demonstrates that MMC effects can encourage the aggregation of bound H-NS, outlining the circumstances leading to H-NS clustering. When the H-NS concentration reaches a biologically pertinent level ($\gtrsim 20\,\mu$M), H-NS forms clusters, and the size of these clusters grows with the increase in the volume fraction of crowders.

Our observation of H-NS clustering is reminiscent of H-NS oligomerization [10, 243, 252, 255]. Meanwhile, it has been demonstrated that H-NS dimers can cluster even without crowders due to the so-called bridge-induced attraction (BIA) between the dimers [258]. This phenomenon occurs when H-NS dimers connect adjacent DNA strands and form clusters. This action reduces the bending energy of DNA and the entropic consequences of DNA looping. Nonetheless, our insights drawn from MMC effects suggest that crowders can amplify the oligomerization of H-NS proteins.

5.2 Computational Modeling

5.2.1 Model

We focus on understanding the synergic effects of DNA-binding protein H-NS and MMC on the compaction of bacterial chromosomes. As depicted in Figure 5.1, we use a ring polymer, which captures the essential aspect of the bacterial chromosome [40, 108, 155, 257–259]. Our model portrays H-NS proteins as bivalent patchy particles

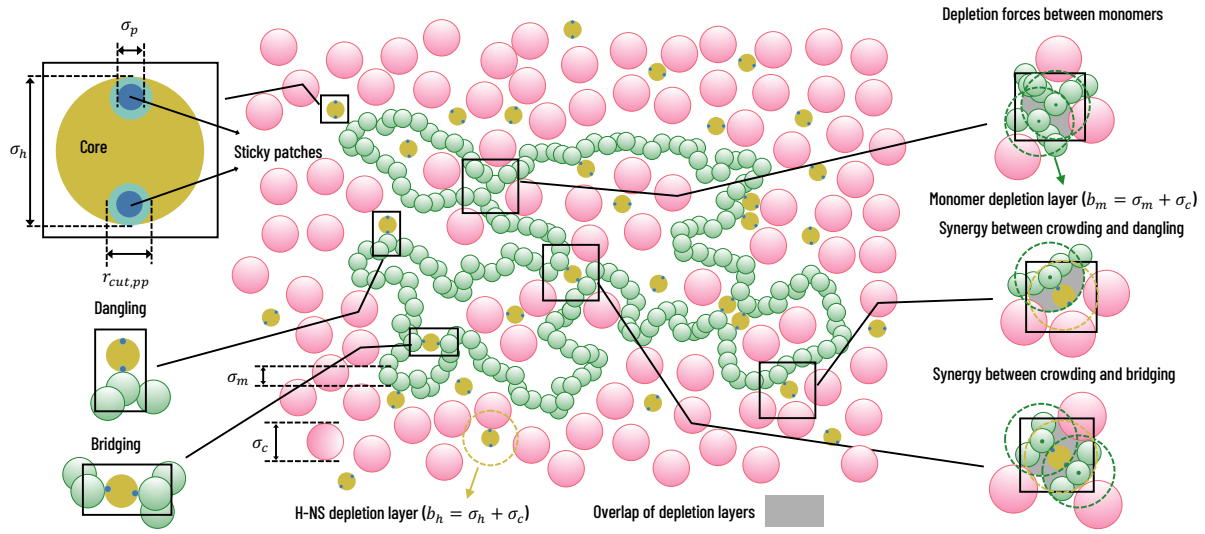


FIGURE 5.1 The synergy between H-NS binding and MMC effects on a chromosome-like ring polymer. In the top left inset, H-NS dimer is modeled as a bivalent patchy particle with a core (dark yellow) and two opposing patches (dark blue) at poles. The core interacts with monomers (shown in green) through excluded-volume interactions. On the other hand, a patch engages solely through nonspecific attractive interactions with monomers, with an interaction range depicted with a light blue ring around the patch. Accordingly, a H-NS dimer can either dangle on the polymer (one-site binding; middle-left inset) or bridge (cross-link) two polymer segments (two-site binding; lower-left inset). Crowders (shown in red) only have excluded-volume interactions with the polymer and H-NS dimers. In the right insets, dashed circles represent depletion layers around monomers and H-NS dimers, excluding the centers of the crowders. The overlap of these layers (hashed in light gray) increases the available space for crowders, favoring particle association due to the entropy of crowders, which leads to depletion forces. The spatial organization of the polymer is governed by the combined influences of MMC and H-NS binding, as highlighted in the center of the figure. The top-right inset indicates that crowders exert depletion forces onto monomers, leading to polymer compaction. H-NS plays a dual role in DNA condensation: It facilitates bridging and also amplifies the effects of MMC. H-NS dangling results in the overlap between the depletion layers of an H-NS dimer and a monomer, leading to localized chain thickening, which enhances the compaction by crowders (middle right inset). H-NS bridging creates overlaps between the depletion layers of an H-NS dimer and two monomers (lower right inset), leading to stronger crowder-induced attractions between monomers compared to those between two monomers or between a dangling H-NS protein and a monomer. Thus, H-NS binding boosts the MMC-induced chain compaction. In our model, the monomer, H-NS (core), and crowder sizes are $\sigma_m = \sigma$, $\sigma_h = \sigma$, and $\sigma_c = 2\sigma$, respectively, where σ is the length unit.

(binders, or dimers) [257–260], while crowders are depicted as structureless spherical beads [36, 108, 155].

As shown in the top left inset of Fig. 5.1, we model H-NS dimers as bivalent patchy particles (patch-core-patch triplexes) with two opposing binding sites [258, 260], each reflecting the DNA-binding capacity of a single H-NS monomer. The DNA-binding (C-terminal) domain in H-NS is structurally stable at high temperature [261]. Recent studies have shown that the linker also plays a role in the ability of H-NS to bind DNA

[262]. The Gibbs free energy (binding energy) of H-NS to DNA, ΔG, increases from $-21.09\,\mathrm{kJ\,mol^{-1}}$ to $-18.86\,\mathrm{kJ\,mol^{-1}}$ in a temperature range of 10 °C to 45 °C [263]. Accordingly, a patch interacts with DNA monomer with an interaction strength ε_{pm} with a value in the range of ΔG, where the subscripts p and m refer to the patch and monomer species, respectively.

In our model, the H-NS core and the two H-NS patches approximately capture the essence of the H-NS full protein size and DNA-binding domain, respectively. Accordingly, the core only has excluded-volume interactions with other particles while the patches only have nonspecific attractive interactions with DNA monomers. The patch size σ_p must fulfill two criteria. First, it must interact with a single DNA monomer. Second, it should not impact the excluded-volume interaction between a H-NS core with other particles. The actual patch size σ_p and the range of interaction between two patches $r_{cut,pp}$ depend on the simulation details, as discussed in Section 5.2.2.

We model crowders as structureless beads with a size approximately equal to the average protein size (≈4.6 nm) in the E. coli cytoplasm [36, 67, 68, 108, 155].

5.2.2 Simulation method

We use a ring polymer composed of $N_m = 200$ DNA monomers with size σ_m and persistence length p_m. The polymer resides in a cubic box with PBCs in all directions, resembling free space. Crowders are structureless spheres (beads) of size σ_c and have a volume fraction $\phi_c \equiv N_c v_c / V_T$, where $v_c = \pi\sigma_c^3/6$ and V_T are the volumes of a crowder and the simulation box, respectively. H-NS proteins (binders) are bivalent patchy particles [258, 260], where cores have a size of σ_h and patches have a size of σ_p and attraction strength ε_{pm} for monomers. To minimize finite-size effects, the cube side Z is six times larger than the estimated equilibrium gyration radius of the chain R_g in the absence of crowders and H-NS dimers [173, 179] (see Section 5.3 for the definition of R_g).

We employed the LJ potential for non-bonded interactions. Depending on its parameters, the repulsive and attractive components of the LJ potential capture the essence of excluded-volume and binding interactions in our system. Let $r_{ij} = \|\vec{r}_i - \vec{r}_j\|$ be the center-to-center distance between two particles i and j located positions $\vec{r}_i$and $\vec{r}_j$, where $\|...\|$ is their (Euclidean) distance. Then, a pair of particles interacts via a truncated and shifted LJ potential,

$$U_{TSLJ,\alpha\beta}(r_{ij}) = \begin{cases} U_{LJ}(r_{ij}) - U_{LJ}(r_{cut,\alpha\beta}) & \text{for } r \le r_{cut,\alpha\beta} \\ 0 & \text{otherwise} \end{cases}, \tag{5.1}$$

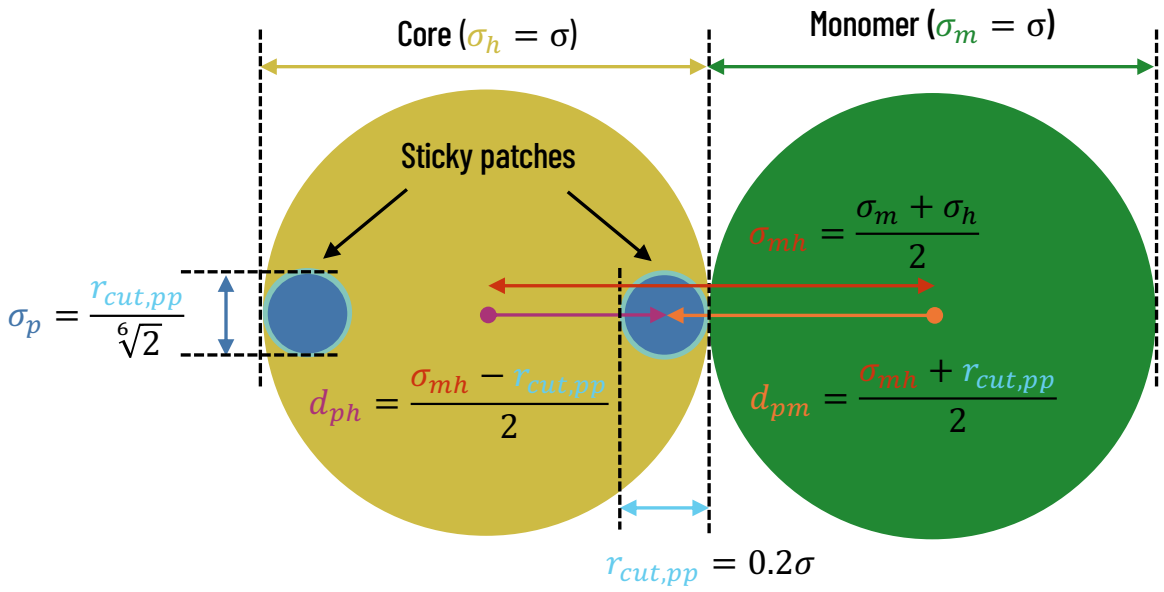


FIGURE 5.2 The distance between the center of an H-NS patch and the centers of a pair of adjacent H-NS core and DNA monomer. We set the H-NS patch size $\sigma_p = r_{cut,pp}/\sqrt[6]{2}$ such that $r_{cut,pp} = 0.2\sigma$ is buried fully within the H-NS core. Therefore, the steric repulsion of a H-NS binder only arises from its core. In this configuration, the distance of a patch from a core is $d_{ph} = (\sigma_h - r_{cut,pp})/2 = 0.4\sigma$; and when a H-NS patch is in touch with a monomer, the distance of a H-NS patch from DNA monomer is $d_{pm} = (\sigma_m + r_{cut,pp})/2 = 0.6\sigma$. In the figure, the relative size of particles matches their actual relative size.

where $U_{LJ}(r_{ij})$ is the (conventional) LJ potential,

$$U_{LJ}(r_{ij}) = 4\varepsilon_{\alpha\beta}\left[\left(\frac{\sigma_{\alpha\beta}}{r_{ij}}\right)^{12} - \left(\frac{\sigma_{\alpha\beta}}{r_{ij}}\right)^{6}\right]. \tag{5.2}$$

Above, $\sigma_{\alpha\beta}$ is the collision size (diameter) at which $U_{LJ}(r_{ij} = \sigma_{\alpha\beta}) = 0$ (the LJ potential changes sign), and $\varepsilon_{\alpha\beta}$ is the depth of the LJ potential at its minimum $r_{min,\alpha\beta} = \sqrt[6]{2}\sigma_{\alpha\beta}$ (the inter-species attraction strength). The subscripts $\alpha, \beta \in \{m, p, h, c\}$ where m, p, h, c refer to (DNA) monomers, H-NS patches, H-NS cores, and crowders, respectively. Finally, $r_{cut,\alpha\beta}$ is the inter-species cutoff distance in Eq. 5.1.

Table 5.1 list our choices for $\sigma_{\alpha\beta}$, $\varepsilon_{\alpha\beta}$, and $r_{cut,\alpha\beta}$ values. Note that the pair coefficients are symmetric. In our model, the H-NS patches do not have non-bonded interactions with H-NS cores and crowders. Thus, the relevant coefficients are not defined (see rows 6 and 7 in the Table 5.1). We set $\varepsilon_{\alpha\beta} = \varepsilon$, except for $\varepsilon_{mp} = 29.0\varepsilon$, where $\varepsilon = k_B T = 2.48\,\mathrm{kJ\,mol^{-1}}$ is the thermal energy at the absolute room temperature $T = 298.15\,\mathrm{K}$ and k_B is the Boltzmann constant. In what follows, we explain our choices for ε_{mp} and ε_{hc}.

TABLE 5.1 The pair coefficients of the LJ potential for different particle species in Eq. 5.2. Symbols m, p, h, c refer to monomers, H-NS patch, H-NS core, and crowders, respectively. We set the LJ cutoff distance between two patches $r_{cut,pp} = 0.2\sigma$ and the H-NS patch size $\sigma_{pp} = \sigma_p = r_{cut,pp}/\sqrt[6]{2}$. Accordingly, any repulsive interaction between two patches is buried in the H-NS core (see Fig. 5.2), ensuring the interaction between two H-NS binders is equal to the purely repulsive interaction between their cores. Similarly, we set $\sigma_{mp} = d_{pm}/\sqrt[6]{2}$, ensuring any repulsive interaction between a patch and monomer is fully contained within the core. Finally, we set $r_{cut,mp} = d_{mp} + \delta_{attr}$, where δ_{attr} is the range of attractive interaction. Lengths and energies are reported in the LJ reduced units of $\sigma = \sigma_m$ and $\varepsilon = k_B T$, where σ_m, k_B, and T are the monomer size, Boltzmann constant, and absolute temperature, respectively.

α-β[a]	$\varepsilon_{\alpha\beta}[\varepsilon]$	$\sigma_{\alpha\beta}[\sigma]$	$r_{cut,\alpha\beta}[\sigma]$
m-m	1.0	1.0	1.122462[b]
m-p	29.0	0.535[c]	0.685[d]
m-h	1.0	1.0	1.122462
m-c	1.0	1.5	1.5×1.122462
p-p	1.0	0.178[e]	0.2
p-h	N/A[f]	N/A	N/A
p-c	N/A	N/A	N/A
h-h	1.0	1.0	1.122462
h-c	1.0[g]	1.5	1.5×1.122462
c-c	1.0	2.0	2×1.122462

[a] Pair coefficients are symmetric, e.g., $\varepsilon_{\alpha\beta} = \varepsilon_{\beta\alpha}$.
[b] $2^{1/6} \approxeq 1.122462$.
[c] $\sigma_{mp} = d_{mp}/2^{1/6} \approxeq 0.535\sigma$; see Fig. 5.2 for the definition of d_{mp}.
[d] $r_{mp,cut} = d_{mp} + \delta_{attr} = 0.6\sigma + 0.085\sigma = 0.685\sigma$; see the table caption for the definition of δ_{attr}.
[e] $\sigma_{pp} = r_{pp,cut}/2^{1/6} \approxeq 0.178\sigma$.
[f] N/A stands for "Not applicable".
[g] $\varepsilon_{hc} = 0$ is also used in our simulations.

The arithmetic mixing rule size, i.e., $\sigma_{\alpha\beta} = (\sigma_\alpha + \sigma_\beta)/2$, is used to set the collision size for $\alpha, \beta \in \{m, h, c\}$ where $\sigma_{mm} = \sigma_m = \sigma$, $\sigma_{hh} = \sigma_h = \sigma$, and $\sigma_{cc} = \sigma_c = 2\sigma$ are often referred to as the sizes of monomers, H-NS protein (or core), and crowders, respectively. Also, our choice of the cutoff distance, i.e., $r_{cut,\alpha\beta} = r_{min,\alpha\beta}$, leads to the so-called fully-repulsive WCA potential that conveniently considers excluded-volume effects between particles [180].

As illustrated in Fig. 5.2, we set the H-NS patch size $\sigma_p = r_{cut,pp}/\sqrt[6]{2}$ such that $r_{cut,pp} = 0.2\sigma$ is buried fully within the H-NS core, in accordance with the modeling strategy described in ref. [258]. Therefore, the interaction between two H-NS proteins only equals the purely repulsive interaction between their cores. As a result, the distance of a patch from a core is $d_{ph} = (\sigma_h - r_{cut,pp})/2 = 0.4\sigma$. When a H-NS patch is in touch with a monomer, the distance of a H-NS patch from the monomer is $d_{pm} = (\sigma_m + r_{cut,pp})/2 = 0.6\sigma$.

As listed in Table 5.1, we set $\sigma_{mp} = d_{pm}/\sqrt[6]{2}$, ensuring the repulsive interaction between a patch and monomer is fully contained within the H-NS core. Finally, we set $r_{cut,mp} = d_{mp} + \delta_{attr}$, where δ_{attr} is the range of attractive interaction. To have an isotropic range of interaction for the H-NS protein, $d_{ph} + r_{cut,mp} \leq r_{cut}$; that is, $0 \leq \delta_{attr} \leq \sigma_{mh}(\sqrt[6]{2} - 1)$. The choices of $\delta_{attr} = 0$ and $\delta_{attr} = \sigma_{mh}(\sqrt[6]{2} - 1)$ mean no and full binding rate in collisions between H-NS proteins and monomers in the system, respectively.

The binding rate also depends on ε_{mp}, where a higher value means a stronger attraction between H-NS binders and monomers. With $\delta_{attr} = 0.085\sigma$ and $\varepsilon_{mp} = 29\varepsilon$, we have $U_{TSLJ,mp}|_{r=r_{min,pm}} \approxeq -8.68\varepsilon = -21.45\,\mathrm{kJ\,mol^{-1}}$, which closely matches the experimentally-measured binding energy of H-NS to DNA (see Section 5.2.1). Under these conditions, about one-third of H-NS proteins bind to DNA in the absence of crowders, regardless of the choice of ε_{hc} (see the curve corresponding to $\phi_c = 0$ in Fig. 5.4).

One way to quantify the synergy between MMC and H-NS binding effects in computer simulations is by manipulating ε_{hc}. When $\varepsilon_{hc} = \varepsilon$, H-NS dimers and crowders have excluded-volume interactions, leading to crowder-induced depletion attraction among H-NS dimers. However, at $\varepsilon_{hc} = 0$, a H-NS dimer and crowder pair can penetrate each other, thus they do not feel any mutual volume exclusion. As a result, crowders do not exert depletion forces on H-NS dimers. Note our choices of cutoff distances between H-NS patches and other particle species means the patches do not contribute to excluded-volume interaction between H-NS proteins and other particle species.

To enforce the polymer connectivity, there is the FENE potential between the adjacent monomers along the ring backbone [181]

$$U_{bond,mm}(r_{ij}) = \begin{cases} -\frac{1}{2}k_{b,mm}r_{b,mm}^2 \ln\left[1 - \left(\frac{r_{ij}}{r_{b,mm}}\right)^2\right] & r_{ij} \leq r_{b,mm} \\ 0 & r_{ij} > r_{b,mm} \end{cases}, \tag{5.3}$$

where $j = i + 1$. We set the spring constant $k_{b,mm} = 30.0\varepsilon/\sigma^2$ and equilibrium bond size $r_{b,mm} = 1.5\sigma$ in our simulations to prevent monomers from crossing [182, 183]. However, the bonding between a pair of H-NS core and patch is accomplished by the harmonic bond potential

$$U_{bond,hp}(r_{ij}) = \frac{1}{2}k_{b,hp}(r_{ij} - r_{b,hp})^2, \tag{5.4}$$

where $j = i + 1$. In our simulations, we set the spring constant $k_{b,hp} = 240\varepsilon/\sigma^2$ and equilibrium bond size $r_{b,hp} = 0.4\sigma$.

Bending rigidity is introduced by the harmonic angle potential

$$U_{bend,\alpha\beta\gamma}(\theta_i) = \frac{1}{2}k_{\theta,\alpha\beta\gamma}(\theta_i - \theta_{0,\alpha\beta\gamma})^2, \tag{5.5}$$

where $k_{\theta,\alpha\beta\gamma}$ is the bending rigidity, $\theta_{0,\alpha\beta\gamma}$ is the equilibrium angle value, and θ_i is the angle between the bonds connecting particles $i-1$, i, and $i+1$. We set patch-core-patch angles, $\theta_{0,php} = \pi$. The bending rigidity $k_{\theta,\alpha\beta\gamma}$ is related to the persistence length p via $k_{\theta,\alpha\beta\gamma} \approx k_B T p/\sigma$. However, the notion of the persistence length is meaningless for H-NS protein, so we set $k_{\theta,php} = 100\epsilon$ to rigidly fix the patches at the poles of a H-NS protein.

In addition to the above-mentioned conservative interactions, all the particles are subjected to the viscous and random forces, both resulting from collisions with implicit solvent particles at a fixed temperature T; as a result, the motion of i-th particle is described with the Langevin equation

$$m_i \frac{d^2\vec{r}_i}{dt^2} = -\vec{\nabla}_i U_{tot}(\{\vec{r}_j\}) - \gamma m_i \frac{d\vec{r}_i}{dt} + \vec{W}_i(t), \tag{5.6}$$

where m_i, $\vec{r}_i$, and $\vec{\nabla}_i$ are the particle mass, particle position, and gradient operator with respect to the particle coordinates, respectively; moreover, $U_{tot}(\{\vec{r}_j\})$ is the sum of all the inter-particle (not inter-species) interactions in the system, and γ is the damping coefficient.

In the left-hand side of Eq. 5.6, the first, second, and third terms are the total conservative, viscous, and random forces exerted on i-th particle, respectively. The random force $\vec{W}_i$ satisfies

$$\langle \vec{W}_i(t) \rangle = 0, \tag{5.7a}$$

$$\langle \vec{W}_i(t)\vec{W}_j(t') \rangle = 6\gamma k_B T m_i \delta_{ij}\delta(t-t'), \tag{5.7b}$$

for i-th particle collided by β-th particle.

Assuming a uniform mass density for all particle types, $m_\alpha = m(\sigma_\alpha/\sigma)^3$ is the mass of α-th species, where the average mass of 7.35 base pairs, $m = m_m = 4.542\,\mathrm{kg\,mol^{-1}}$, is the mass unit.[3] We employ the velocity-Verlet algorithm [185, 186] to integrate the equations of motion with time step $\delta t = 0.005\tau_{LJ}$ where $\tau_{LJ} = \sigma\sqrt{m/\varepsilon} \approxeq 3.45\,\mathrm{ns}$ is the LJ reduced time unit. The system is kept at a fixed temperature $T = 298.15\,\mathrm{K}$ through the Langevin thermostat [187] with a damping constant $\gamma = 0.1\tau_{LJ}^{-1}$. The mass

[3] For the average molecular weight of DNA double-helix, see the following on the Thermo Fisher Scientific website: https://www.thermofisher.com/ca/en/home/references/ambion-tech-support/rna-tools-and-calculators/dna-and-rna-molecular-weights-and-conversions.html

and damping factor choices are unimportant in our study since they do not influence equilibrium properties.

In our simulations, we change the crowder volume fraction ϕ_c in the range of 0 to 0.4 with a step size of 0.08; therefore, the number of crowders N_c ranges from 0 to 11 937 based on the combination of ϕ_c and a total volume V_T. We have chosen a range of $N_h = 0,\ 4,\ 8,\ 12,\ 16,\ 20$ and 30 correspond to the H-NS molar concentrations $c_h = 0,\ 3.4,\ 6.8,\ 10.2,\ 13.6,\ 17.0$ and $25.3\,\mu$M, respectively.

For each set of system parameters, we run four independent simulations (replicates) with different random number seeds for the Langevin thermostat and initial H-NS proteins and crowder distributions, generating four thermodynamically equivalent systems that evolve along distinct paths in the phase space. In each simulation, the chain is initially configured in a helical shape at the center of the simulation box. We first equilibrate the chain alone for 5.1×10^6 integration steps with $\delta t = 0.01\tau_{LJ}$, where the FENE potential is replaced with the harmonic bond potential, i.e., Eq. 5.4, where the same spring constant and equilibrium bond length are used. Then, the bond potential is returned to the FENE potential, and H-NS proteins and crowders are randomly distributed in the simulation box. The attractive interaction between H-NS patches and DNA monomers is turned off at this stage. The system is equilibrated for another 10^5 integration steps with $\delta t = 0.01\tau_{LJ}$. Once the system is fully equilibrated, the attractive interaction between H-NS patches and DNA monomers is turned on. Finally, during the sampling phase, each simulation is run for 10^9 integration steps with $\delta t = 0.005\tau_{LJ}$. In each simulation, we gather the system conformations every 5000 (10 000) steps to calculate time averages (spatial distributions).

We calculate ensemble averages as time averages within each run and then do uncertainty analyses such as obtaining averages and standard errors over replicates. As a result, the standard error of the mean in a reported physical property is smaller than the symbols used in our figures. The symbol $\langle \dots \rangle$ signifies averaging over time and replicates. In the rest of this chapter, all the quantities are averaged over replicates and time (where applicable) unless stated otherwise.

Our MD simulations are performed in the LAMMPS simulation package [188]. We benefit from the multi-size neighboring bin algorithm in LAMMPS [189] to reduce computational costs. We employ the MDAnalysis python package to analyze trajectory files [190–192]. The analysis phase is done in parallel with GNUParallel [193].

5.3 Results

In this study, the volume fraction of crowders ϕ_c and the number of H-NS dimers N_h serve as the key parameters. Following the simulation protocol described in the previous section, we measured physical quantities that clarify the synergy between MMC and H-NS binding in polymer compaction and organization. Our chromosome-like polymer is a ring chain composed of $N_m = 200$ monomers interacting with crowders and H-NS dimers in a cubic volume of size 125 nm × 125 nm × 125 nm.

Figure 5.3 shows the reduction in the rescaled ROG of the ring polymer, $\langle R_g \rangle / \langle R_{g,0} \rangle$, as a function of ϕ_c, across various choices of N_h (line colors) and ε_{hc} (line style). The ROG is defined as

$$R_g = \left[\frac{1}{N_m} \sum_i (\vec{r}_i - \vec{R}_{\text{COM}}) \right]^{1/2}, \tag{5.8}$$

where $\vec{r}_i$ is the position of the i-th monomer and $\vec{R}_{\text{COM}} = (1/N) \sum_i \vec{r}_i$ represents the COM of the polymer. The rescaling factor, $\langle R_{g,0} \rangle = 0) \rangle$, is the unperturbed gyration radius of the chain without crowders and H-NS dimers.

The chain shortens in size as ϕ_c increases for a fixed c_h value (a fixed line color). When there are no H-NS present ($c_h = 0$; represented by the lightest curve with circle marker), the ring polymer compacts to approximately 88 % of its unperturbed size with increasing ϕ_c. In contrast, when no crowders are present ($\phi_c = 0$, indicated by colored markers on a vertical dotted red line on the plot's left side), the ring polymer shrinks to 86 % of its unperturbed value as c_h increases. Across the board, as ϕ_c rises, the chain size diminishes, with a steeper decline observed at higher c_h values. For example, when $\phi_c = 0.4$ at a concentration of $c_h = 3.4\,\mu\text{M}$, the polymer compaction rate approximates 80 %. However, this rate decreases to about 50 % when $\phi_c = 0.4$ at a concentration of $c_h = 25.5\,\mu\text{M}$.

As highlighted above, the chain size contracts more swiftly with ϕ_c when c_h is higher, hinting at an interconnection between crowders and H-NS dimers. This aligns with recent findings that H-NS boosts bacterial chromosome compaction through MMC effects [245–248]. Indeed, as suggested in ref. [247] and illustrated in Fig. 5.1, H-NS not only amplifies the depletion force between chain segments by augmenting the chain thickness, but it also binds more robustly to a chromosome-like polymer as ϕ_c grows. Conversely, it can be said crowders not only compact the chain but also amplify the binding affinity of H-NS, as depicted below. Such interconnection is also reflected in the crowders and H-NS synergetics.

We have delved deeper into this interconnection between MMC and H-NS binding effects. Figure 5.4 illustrates the binding probability (a.k.a. binding affinity), θ, of H-

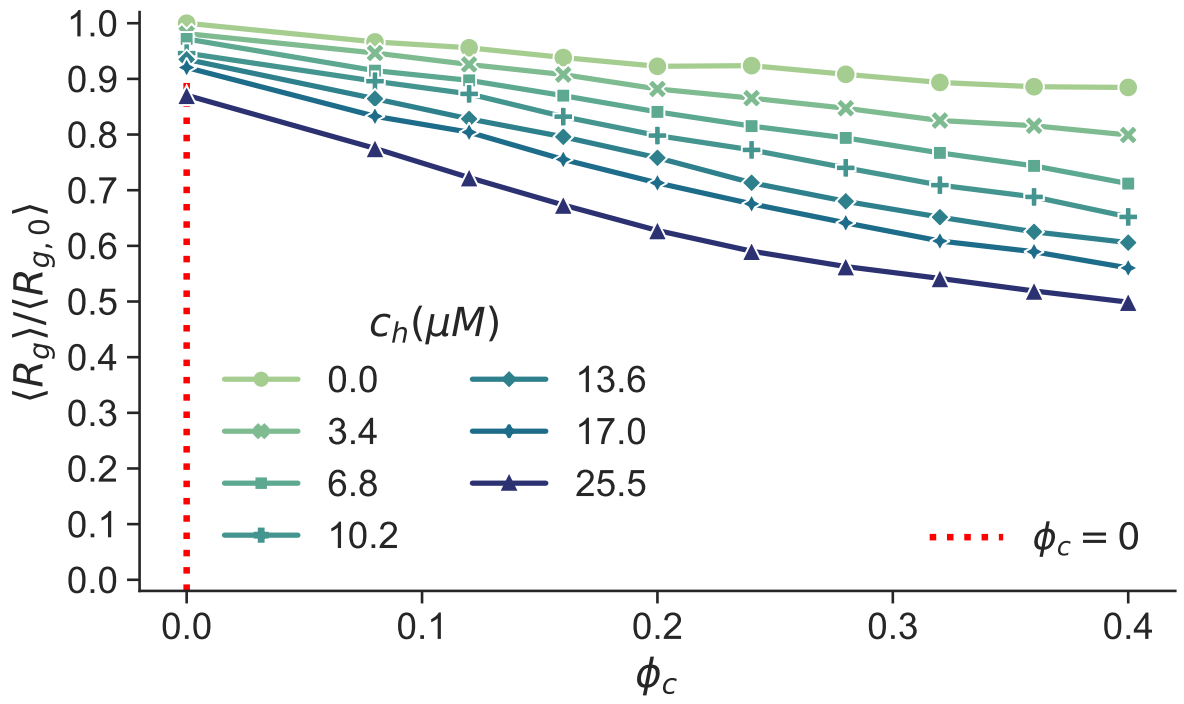


FIGURE 5.3 The effect of MMC on the compaction of polymers for different concentrations of H-NS proteins, c_h. The rescaled chain size, denoted as $\langle R_g \rangle / \langle R_{g,0} \rangle$, decreases as a function of ϕ_c. Here, $\langle R_g \rangle$ signifies the gyration radius, while $\langle R_{g,0} \rangle$ corresponds to the gyration radius in an unperturbed state (when $\phi_c = 0$ and $c_h = 0$). When no H-NS protein presents ($c_h = 0$; represented by the lightest curve with circle marker), the ring polymer compacts to approximately 88 % of its unperturbed size with increasing ϕ_c. In contrast, when no crowders are present ($\phi_c = 0$, indicated by colored markers on a vertical dotted red line on the plot's left side), the ring polymer shrinks to 86 % of its unperturbed value as c_h grows. Across the board, as ϕ_c rises, the chain size diminishes, with a steeper decline observed at higher c_h values. For example, when $\phi_c = 0.4$ at a concentration of $c_h = 3.4\,\mu M$, the polymer compaction rate approximates 80 %. However, this rate decreases to about 50 % when $\phi_c = 0.4$ at a concentration of $c_h = 25.5\,\mu M$.

NS proteins to a ring polymer. We mathematically expressed θ as

$$\theta = \frac{\langle N_{h,bound} \rangle}{N_h} \tag{5.9}$$

where $\langle N_{h,bound} \rangle$ represents the average number of bound H-NS dimers. A H-NS is deemed to be bound to a DNA monomer if their distance, r, is within the limit $r \leq r_{thres}$. In this study, we utilized $r_{thres} = r_{cut,mp}$. In an imaginary scenario where all H-NS molecules are bound to the polymer, $\theta = 1$.

The graph on the left of Fig. 5.4 depicts θ rises as c_h increases, likely saturating when c_h approaches infinity. Different colors in this graph signify different ϕ_c values. With a constant c_h (as illustrated by the dashed green line at $c_h = 3.4\,\mu M$ in Fig. 5.4), a higher ϕ_c yields a larger θ, implying crowders boost the H-NS binding affinity for the polymer.

This effect might be attributed to MMC-induced chain collapse, possibly amplifying the binding of H-NS by increasing their bridging propensity. Further details on this phenomenon are discussed below.

As depicted in Fig. 5.1, H-NS has two binding modes: *dangling* and *bridging*. A dimer with one binding site engaged with DNA is in the dangling mode. In contrast, a binder with both binding sites engaged with DNA is in the bridging mode. Additionally, the bridging mode is further categorized into *cis* and *trans* configurations, depending on the ability of H-NS dimers to bridge two nearby genomic sites. When a H-NS dimer binds to two genomic sites that are distant from each other more than two monomers or beads apart, we refer to it as a *trans* bridging. Conversely, when the dimer binds to sites that are nearby, we label it as *cis* bridging. In *cis* binding, the H-NS dimer must undergo bending, forming a 'U' shape. However, it is important to note that our modeling approach, like the one presented in ref. [258], does not account for this bending in *cis* bridging scenarios. From a physics perspective, one may assert that this intricacy does not alter the overall understanding shown in Fig. 5.3: cross-linking or bridging two adjacent monomers does not significantly enhance chain compaction compared to dangling. Further discussions on this topic are provided below. In our study, the terms *two-site binding* and *cross-linking* are used interchangeably.

The graph on the right of Fig. 5.4 shows the dangling probability (blue curve marked with 'x'), bridging probability (yellow curve marked with square), and their sum, i.e., binding probability, (red curve with marked with circle), as function of ϕ_c at a representative value of $c_h = 25.5\,\mu\text{M}$. As ϕ_c increases, there is a swift increase in the bridging probability, while the dangling probability gradually diminishes. However, the binding probability rises with ϕ_c. This graph underscores how crowders amplify the propensity of H-NS to bind in the bridging mode.

From Fig. 5.4, it is evident that crowders boost the affinity of H-NS binding to bacterial chromosomes. But does H-NS binding reciprocally intensify chain compaction? Previous research [245–248] indicates a positive correlation: H-NS augments crowders' efficiency in collapsing bacterial chromosomes. Such behavior was rationalized by the theory that H-NS binding increases polymer thickness [247]. Although this mean-field approach is valuable, a thorough comprehension would demand an in-depth examination of MMC and H-NS effects on chain compaction in a controlled setting.

To systematically examine the interplay between MMC and H-NS binding, we manipulate the strength of LJ potential between H-NS and crowders ε_{hc} as detailed in Section 5.2.2. In Fig. 5.5, we compared two sets of curves: one set derived with $\varepsilon_{hc} = 0$ (depicted as solid curves with square markers) and the other with $\varepsilon_{hc} = \varepsilon$ (illustrated as

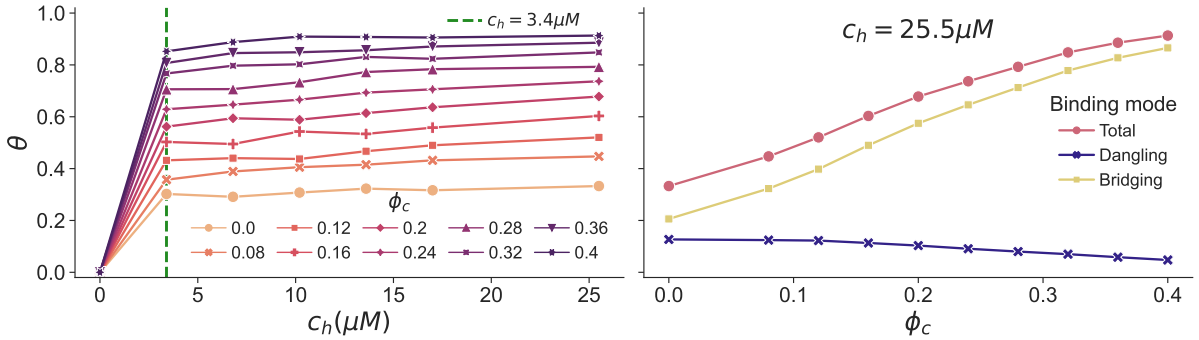


FIGURE 5.4 The binding probability θ of H-NS proteins to a model chromosome as a function of c_h (on the left) and ϕ_c (on the right). *Left:* θ increases as c_h grows, reaching a saturation point when c_h approaches infinity. With no crowders ($\phi_c = 0$; lightest curve with circle marker), θ jumps to 0.3 at $c_h = 3.4\,\mu$M (smallest non-zero c_h value) and reaches a maximum of $\theta \approx 0.33$ at $c_h = 25.6\,\mu$M. At a fixed c_h value, a larger ϕ_c increases θ more. For example, see the dashed green line illustrating this increase at $c_h = 0.4$. This indicates that when a chromosome-like polymer collapses due to MMC, it may elevate the tendency of H-NS to bind, possibly intensifying bridging between two polymer sites, as highlighted in the right-side graph. *Right:* The fraction of bound H-NS dimers splits into two binding modes: A single-site binding called dangling and a two-site binding called bridging. As ϕ_c rises, the bridging H-NS fraction surges significantly, while the dangling H-NS fraction gently diminishes. The sum of two binding modes also rises with ϕ_c. This graph underlines how crowders enhance the binding of H-NS dimers. Data is represented for $c_h = 25.5\,\mu$M.

dashed curves with circle markers). Within each set, changes in c_h are shown with different line colors. Remember, $\langle R_g \rangle$ signifies the gyration radius, whereas $\langle R_{g,0} \rangle$ stands for its undisturbed value where both crowders and H-NS dimers are absent.

When $\varepsilon_{hc} = 0$, crowders can freely move through H-NS dimers. Consequently, H-NS dimers are not subject to steric restrictions imposed by nearby crowders, implying that a pair of H-NS dimers will not be affected by any depletion forces. Therefore, the difference between the solid and dashed curves is attributable exclusively to the depletion force experienced among H-NS dimers (the dashed curves with circle markers). This can be interpreted as a metric highlighting the collaborative effect between H-NS and crowders. This difference is notably evident at higher c_h values and escalates with the growth of ϕ_c.

As previously mentioned, our model does not differentiate between the two bridging configurations: *cis* and *trans*. The contribution of H-NS dimers in the *cis* bridging to chain compaction is not as effective as those in the *trans* mode. Without crowders, their impact on chain compaction is anticipated to be minor, akin to the influence of dangling dimers. However, in the presence of crowders, H-NS dimers boost chain compaction regardless of their specific bridging mode. The extent of this enhancement is likely unaffected by their bridging mode, as the depletion free energy gain is strictly determined by the overlap of depletion layers for a given ϕ_c value, as illustrated on the

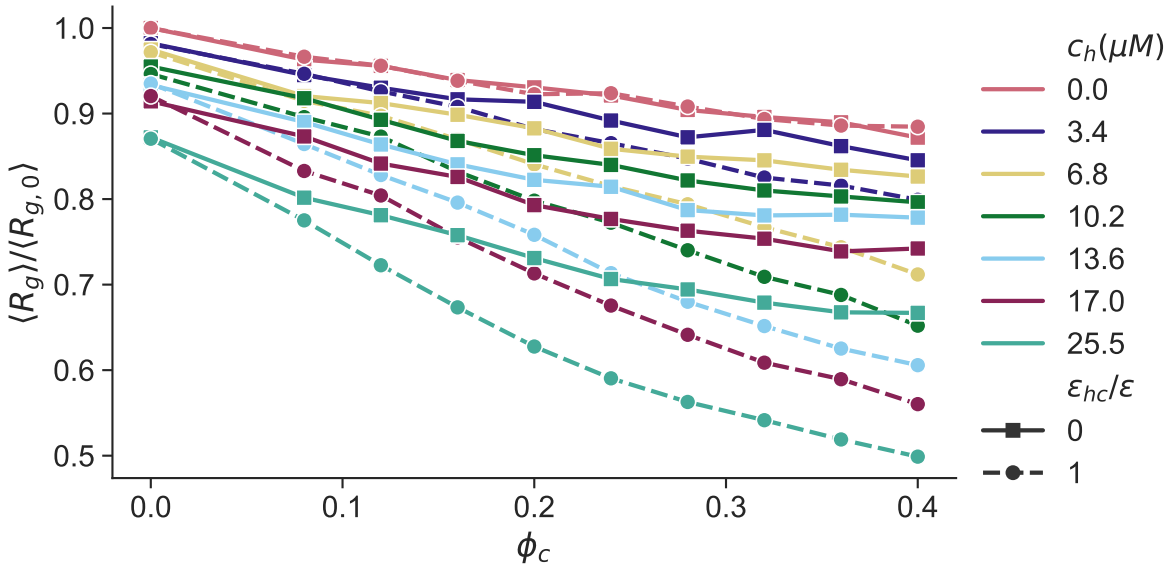


FIGURE 5.5 The synergistic effects of MMC and H-NS binding in the compaction of a chromosome-like polymer. The gyration radius of the polymer, $\langle R_g \rangle$, decreases as a function of ϕ_c for different values of c_h (denoted by line color). For clarity, $\langle R_g \rangle$ is rescaled with its unperturbed value $\langle R_{g,0} \rangle$ in the absence of both H-NS dimers and crowders. This decrease can be observed both in the absence ($\varepsilon_{hc} = 0$; solid line with square marker) and presence ($\varepsilon_{hc} = \varepsilon$; dashed line with circle marker) of excluded-volume interactions between H-NS dimers and crowders. The difference between the solid ($\varepsilon_{hc} = 0$) and dashed ($\varepsilon_{hc} = \varepsilon$) curves stems exclusively from the depletion force acting between H-NS dimers (dashed curves), exemplifying the cooperative effect of H-NS dimers and crowders. This difference becomes more pronounced with a larger c_h and intensifies as ϕ_c increases.

right of Fig. 5.1. Consequently, the core insights drawn from Fig. 5.3 are not expected to be significantly influenced by the coarse-grained model of H-NS in our study.

Figures 5.4 and 5.5 collectively present a general picture in which the synergetics between H-NS proteins and crowders in compacting bacterial chromosomes is mutual: H-NS binding intensifies the depletion forces among chain segments [245–248], while the presence of crowders amplifies the H-NS binding to the chromosome, further strengthening these depletion forces. Even if H-NS proteins and crowders, on their own, do not make a substantial difference in chain compaction, their combined presence enhances chromosome-like polymer compaction far beyond what is anticipated from their individual impacts. To illustrate, take the scenario where $c_h = 25.5\,\mu\text{M}$ and $\phi_c = 0.32$ and compare it to situations where only H-NS or crowders present. An inequality emerges: 46 % compaction (with both) surpasses 25 % compaction, which is the sum of 13 % (H-NS proteins alone) and 12 % (crowder alone). This highlights the extent of the synergic effects of H-NS and crowders in a quantitative way.

Furthermore, we have analyzed the H-NS clustering which is caused by depletion

forces. The findings are encapsulated in Figs. 5.6 and 5.7, each comprising two related sub-figures. These sub-figures respectively represent the distribution of cluster sizes $p(x_c)$ (left) and the average size of the clusters $\langle x_c \rangle$ (right) at $\varepsilon_{hc} = \varepsilon$. Clusters are identified based on the criterion that neighboring H-NS cores are within a distance of $r_{thres} = \sigma_h + \sigma_c = 3\sigma$, essentially focusing on spatial clustering. To detect these clusters, we employed custom Python scripts, implemented based on the algorithm introduced in ref. [236]. It is important to note that our analysis does not distinguish between different forms of clusters, such as a linear arrangement or a triangular formation, as long as they comprise the same number of particles. Also, our method does not differentiate between free and bound H-NS proteins.

The sub-figure on the left in Fig. 5.6 depicts $p(x_c)$ as a function of the cluster size x_c across different ϕ_c value at $c_h = 25.5\,\mu M$. The cluster size x_c is in the range of $1 \leq x_c \leq N_h$. For ϕ_c values up to 0.2, $p(x_c)$ peaks at $x_c = 1$. However, when ϕ_c exceeds 0.2, $p(x_c)$ displays two peaks, indicating the formation of larger H-NS clusters. For visual clarity, we also plotted the $p(x_c)$ for $x_c > 1$ in the inset of the sub-figure. The second graph (right) in Fig. 5.6 shows $\langle x_c \rangle$ at $h = 25.5\,\mu M$. The average cluster size $\langle x_c \rangle$ increases with ϕ_c, consistent with the sub-figure on the left. When the single-H-NS are excluded, the $\langle x_c \rangle$ increases much faster with ϕ_c, tripling at the maximum ϕ_c value, i.e., $\phi_c = 0.4$.

Figure 5.7 illustrates $p(x_c)$ for various c_h values (left sub-figure) and the relationship between $\langle x_c \rangle$ and c_h (right sub-figure), keeping the volume fraction of crowders constant at $\phi_c = 0.32$. The left sub-figure in Fig. 5.7 reveals a single-peaked $p(x_c)$ at $x_c = 1$ for all c_h values except at $c_h = 25.5\,\mu M$, where a second peak emerges at larger x_c values. For visual clarity, we also plotted the $p(x_c)$ for $x_c > 1$ in the inset of the sub-figure. The right graph in Fig. 5.7 suggests an increase in $\langle x_c \rangle$ with a higher c_c, as expected from the trend seen in the left sub-figure. This sub-figure echoes the trend seen in the right graph of Fig. 5.6, with $\langle x_c \rangle$ quadrupling at the maximum c_h value, i.e., $c_h = 25.5\,\mu M$, when excluding single H-NS clusters.

Although Figs. 5.6 and 5.7 suggest similarities between H-NS clustering and oligomerization [10, 243, 252, 255], our simplified model does not account for all biological complexities, such as interactions between H-NS proteins or chain stiffness. Nonetheless, these observations support the hypothesis that crowding effects may play a role in H-NS protein oligomerization; they also complement other findings that indicate BIA is a key factor in H-NS clustering [258].

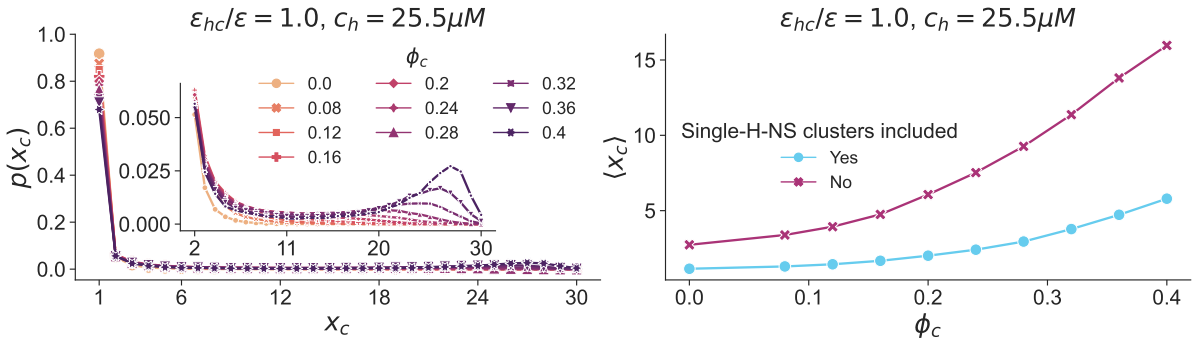


FIGURE 5.6 The cluster-size distribution $p(x_c)$ (the left sub-figure) and the average cluster size $\langle x_c \rangle$ as a function of the crowder volume fraction ϕ_c (the right sub-figure) at $c_h = 25.5\,\mu M$. Cluster size is determined by counting H-NS core particles located within a center-to-center distance of $r_{thres} = \sigma_h + \sigma_c = 3\sigma$. *Left:* When $\phi_c \leq 0.2$ is , the maximum of $p(x_c)$ occurs at $x_c = 1$. However, for $\phi_c > 0.2$, $p(x_c)$ is bimodal, with the second peak located at significantly larger x_c values (≈ 24 for $\phi_c = 0.32$), indicating the formation of large H-NS cluster. The inset graph is included to highlight the locations of these second peaks by excluding clusters with $x_c = 1$. *Right:* The average cluster size $\langle x_c \rangle$, calculated at $c_h = 25.5\,\mu M$, increases as ϕ_c rises, consistent with the trend seen in the left graph. When the single-H-NS clusters are excluded, the rate at which $\langle x_c \rangle$ increases with ϕ_c is more pronounced, for instance, jumping from ≈ 5 to ≈ 15 at $\phi_c = 0.4$.

5.4 Discussions and conclusion

This study introduced a computational model detailing how the H-NS protein and cellular crowders compact bacterial chromosomes. Our goal has been to highlight the synergistic relationship in their effects on chromosome compaction.

Our simulation portrays a H-NS dimer as a bivalent patchy particle [258, 260], featuring a core sphere with two opposing smaller patch spheres positioned at the core poles. These patch spheres can bind to a chromosome-like ring polymer. In our study, H-NS binding is divided into two modes: dangling [257, 264] and bridging [256, 257, 265]. Notably, our model excludes the *cis* configuration of bridging mode, where its two binding sites simultaneously bind to nearby DNA sites (e.g., within a few monomers) [256, 257]. In the absence of crowders, dangling and *cis* bridging both lead to DNA stiffening [256, 257, 264]. In the presence of crowders, *cis* bridging effects on DNA condensation would be possibly akin to dangling effects. Thus, while *cis* bridging is not considered, its inclusion would not drastically alter the main findings regarding chromosome compaction by H-NS dimers and crowders.

In parallel with our discussion above, it is pertinent to note that H-NS binding and its consequent effects on negatively charged DNA depends on the concentration of Mg^{2+} ions [10, 264, 266, 267]. At low concentrations, H-NS wraps around the DNA without looping; at higher levels, it bridges DNA, aiding compaction. Mg^{2+} mitigates the repul-

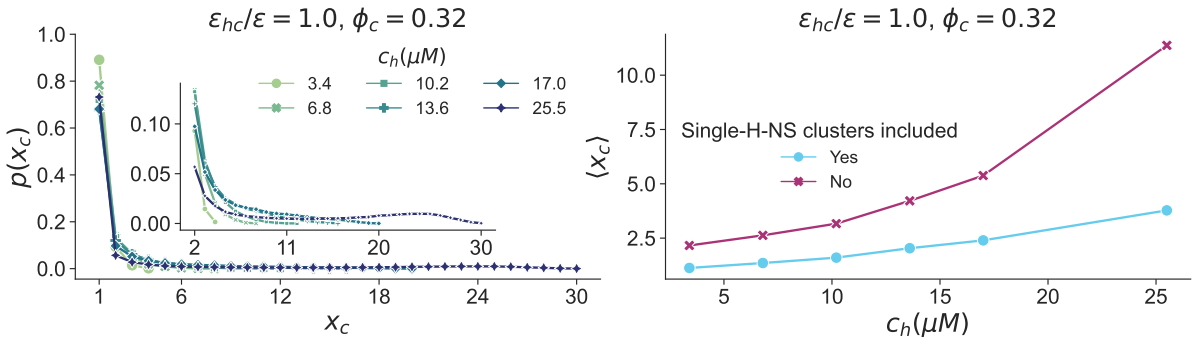


FIGURE 5.7 The cluster-size distribution $p(x_c)$ and the relationship between average cluster size $\langle x_c \rangle$ and H-NS concentration c_h are respectively plotted in the left and right sub-figures at a fixed ϕ_c value of 0.32. Clusters are identified based on whether the center-to-center distance between H-NS core particles is within $r_{thres} = \sigma_h + \sigma_c = 3\sigma$. *Left:* For all c_h values except $c_h = 25.5\,\mu M$, $p(x_c)$ shows a single peak at $x_c = 1$. However, at $c_h = 25.5\,\mu M$, a bimodal distribution emerges, with the second peak indicating a substantially larger cluster size (≈ 24), suggesting the formation of a large H-NS cluster. The inset graph shows the location of this second peak by limiting the $p(x_c)$ to $x_c > 1$. *Right:* The average cluster size $\langle x_c \rangle$, obtained at $\phi_c = 0.32$, increases with c_h. This trend aligns with the observations from the left graph. When the single-H-NS clusters are excluded, $\langle x_c \rangle$ increases with c_h at a higher rate; for example, it leaps from ≈ 2.5 to ≈ 11 at $c_h = 25.5\,\mu M$.

sion between DNA backbone charges [235], enhancing H-NS's ability to bridge DNA. This can be factored into our simulations by tweaking parameters like $\varepsilon_{\alpha\beta}$ and $r_{cut,\alpha\beta}$.

The model presented in this study effectively illustrates the cooperative interaction between H-NS dimers and crowders in compacting the polymer. This goes beyond previous research, which primarily viewed H-NS binding as a mechanism to thicken the chromosome [247]. Our findings indicate a mutual synergetics between H-NS and crowders. Specifically, crowders amplify the H-NS binding to chromosome-like polymers by promoting chain bridging. In contrast, H-NS augments the impact of crowders by enlarging local chain segments, mirroring observations made with a heterogeneous polymer in a crowded environment [40] (also see Chapter 4).

In addition to H-NS and other NAPs like HU and factor for inversion stimulation (Fis), RNAPs play a pivotal role in structuring bacterial chromosomes [39, 65, 202]. Studies have demonstrated that when RNAPs bind to E. coli chromosomes, particularly in fast-growing cells, transcriptionally active units form clusters [39], which is also supported by recent computer simulations [40] (also see Chapter 4). Both H-NS and RNAP contribute to chromosome compaction by MMC. Broadly speaking, depletion forces [127, 128], induced by MMC [28], vary with size [39, 160, 161], being stronger between larger entities, such as sites on a chromosome bound by H-NS.

It is essential to recognize the distinct roles of H-NS and RNAP or any other CAP that do not facilitate bridging. H-NS not only strengthens the depletion forces between

chromosome segments but also bridges two sites on a chromosome.

The findings presented in this study highlight the diverse roles of biomolecules. Apart from their specific biological functions, they act as physical entities that either engage in excluded volume interactions or impose steric hindrance to other molecules, as observed with H-NS. A more comprehensive understanding would benefit from a similar analysis of other proteins associated with chromosomes.

In our research, we have primarily concentrated on studying the equilibrium characteristics of chromosome compaction facilitated by H-NS proteins and crowders. As such, the data presented in Fig. 5.4 exclusively captures the equilibrium aspects of H-NS binding, omitting the dynamic aspect of H-NS binding/unbinding and cross-linking. Considering recent studies on 'facilitated' (concentration-accelerated) dissociation of CAPs (like Fis) [268, 269], it would be beneficial to expand our study to encompass the dynamics of H-NS association, dissociation, and cross-linking in the presence of crowders.

To conclude, it is worth acknowledging that biomolecular crowding can influence other biological phenomena, including protein folding and aggregation, gene regulation, and cellular growth [39, 69, 270, 271]. We hope this study inspires further investigation into the multi-faceted roles of MMC in biological systems.

CHAPTER 6

Concluding remarks and future considerations

6.1 Conclusions

Inspired by several key observations in the E. coli chromosome, this thesis was dedicated to study how biomolecular crowding, confinement, chain heterogeneity, and chain cross-linking influence the spatial organization of chromosome-like polymers. Through the development and systematic exploration of three coarse-grained polymer models, we uncovered the multifaceted roles MMC plays in the hierarchical organization of bacterial chromosomes. Employing structureless beads in our MD simulations to mimic cellular crowders, we focused on excluded-volume interactions between particles, where MMC effects give rise to depletion forces among monomers.

In Chapter 3, we studied how MMC affects chain compaction and the interdependence between the spatial distributions of monomer and crowders under confinement, using MD simulations. In particular, we focused on the conditions where the size of crowders is comparable to or exceeds that of monomers, an area previously overlooked. Our results revealed that, at a fixed bulk volume fraction of crowders, larger crowders are better in condensing a polymer within a specific range of crowder-to-monomer size ratios. Moreover, we discovered that confinement has minimal effects on MMC when the ratio of the effective cylinder size to crowder size is substantially large: chain compaction is insensitive to cylinder size and spatial distributions are unaffected by crowder wall-layering. Considering the common size ratios of cellular crowders to chromosomal monomers, our findings highlight the varying impact of MMC across different hierarchies of bacterial chromosome organization. Furthermore, we expanded the application of the density sum rule to cylindrical confinement, demonstrating that MMC effects are localized and largely unaffected by the geometry of confinement. This rule aids in elucidating the interdependence between the spatial distributions of chromosomal DNA and cellular species, such as ribosomal subunits, within bacterial cells, shedding light on the role MMC and confinement plays in nucleoid formation.

Chapter 4 investigated the MMC effects on a flexible heterogeneous ring polymer,

inspired by the spatial organization of transcriptionally-active rrn operons in E. coli cells. The polymer consisted of small and large monomers, where the large monomers mimic transcriptionally-active rrn operons. Our analysis demonstrated that upon reaching a critical size, these large monomers tend to form closely-packed clusters within a biologically-relevant range of the crowder volume fraction, thus intensifying polymer compaction. Cylindrical confinement was seen to enhance the clustering of these large monomers, reducing the crowder volume fraction required for polymer compaction. The cluster formation is reminiscent of the observed clustering of transcriptionally-active rrn operons into "transcription factories" within fast-growing E. coli cells, highlighting how MMC, in conjunction with factors like chromosome heterogeneity, drives the formation of functional complexes at the intermediate hierarchical level of chromosome organization. In parallel, our study showed a smooth crossover separates a monomer-rich phase from a crowder-only one. Thereby, the insights from Chapter 4 underpin the critical roles of phase separation and clustering as mechanisms in structuring cellular interiors beyond compartmentalization.

Chapter 5 expanded our thematic exploration by illustrating the interplay between H-NS binding and MMC effects in the compaction of bacterial chromosomes. Modeling H-NS proteins as bivalent patchy particles elucidated how their interactions with crowders contribute to chromosome compaction. Our results revealed crowders intensified H-NS binding by increasing chain bridging while the presence of H-NS dimers enhanced MMC effects by locally thickening chain segments. This chapter highlighted the effects of biomolecular crowders on the interactions between chromosomal DNA and DBPs, including NAPs, thus contributing to the bacterial chromosome organization at the micro level.

Collectively, these chapters have illuminated phase separation and clustering, induced by MMC effects, are the underlying principles in bacterial chromosome organization. Also, they have underscored the integral role of MMC in shaping the spatial organization of chromosomes across various hierarchical levels. Our findings not only advance our understanding of MMC's impact on bacterial chromosome architecture but also pave the way for future research aimed at elucidating the interplay among MMC, supercoiling, and DBPs in the organization of bacterial chromosomes.

6.2 Proposals

6.2.1 A heterogeneous branched ring polymer model of the bacterial chromosome

In Chapter 4, we built a heterogeneous ring polymer model of the bacterial chromosome, inspired by the observed role of the transcription machinery in organizing the chromosome in E. coli cells [65, 75, 202, 208, 210]. Under slow (fast) growth conditions, each rrn operon typically contains around engaged 5 (70) RNAPs, along with other components [65, 166, 202, 208, 210]. These transcriptionally-active rrn operons, known to cluster into transcription foci, are likely driven by MMC effects, contributing to chromosome organization. In Chapter 4, we simplified biological complexities, modeling an active rrn operon as a hard sphere with sizes varying between 24 nm to 64 nm based on growth conditions (see Section 4.2.1). Consequently, our model depicted the heterogeneous polymer as comprising both small and large monomers, with the larger ones evenly distributed along the backbone [65, 152, 202, 210, 222] (see Fig. 4.1). We now propose to extend this model to a coarse-grained heterogeneous branched ring polymer. Each branched sub-chain represents a transcriptionally-active rrn, mirroring the double Christmas-tree-like structure observed via electron microscopy in fast-growing cells [65, 202, 205, 223] (see Fig. 6.1).[1] Using MD simulations, we aim to explore the clustering and spatial organization of this polymer under MMC conditions.

E. coli has seven rrn operons, each spanning approximately 5.5 kbp in length [65] (see Fig. 6.1A). These operons are distributed non-uniformly along the E. coli chromosome, with the shortest genomic distance being roughly 36 kbp between the *rrnB* and *rrnE* operons [215]. In rapidly-growing E. coli cells, an active rrn operon exhibits a distinct double Christmas-tree-like structure, comprising DNA, engaged RNAPs, nascent pre-rRNAs transcripts, and ribosomal proteins [205, 223, 272], as shown in Fig. 6.1B. An engaged RNAP is approximately 14.7 nm in size, binding to 23 bp of DNA during elongation [65]. Given the average length of an rrn operon, the spacing between two consecutive engaged RNAPs is about 55 bp, equating to one RNAP every 78 bp. It is suggested that the intervening DNA between two RNAPs is ssDNA [272]. In E. coli, the 5 S, 16 S, and 23 S genes measure 120 bp, 1542 bp, and 2905 bp in length, respectively [232]. However, the nascent pre-rRNAs chains are three times shorter than their corresponding genes, due to their associated ribosomal proteins and other unknown factors [223, 272].

As depicted in Fig. 6.1C, we have simplified an active rrn operon into a branched

[1] Interestingly, such Christmas-tree-like structures, generally referred to as Miller's spreads, have been observed in different organisms beyond bacteria [272].

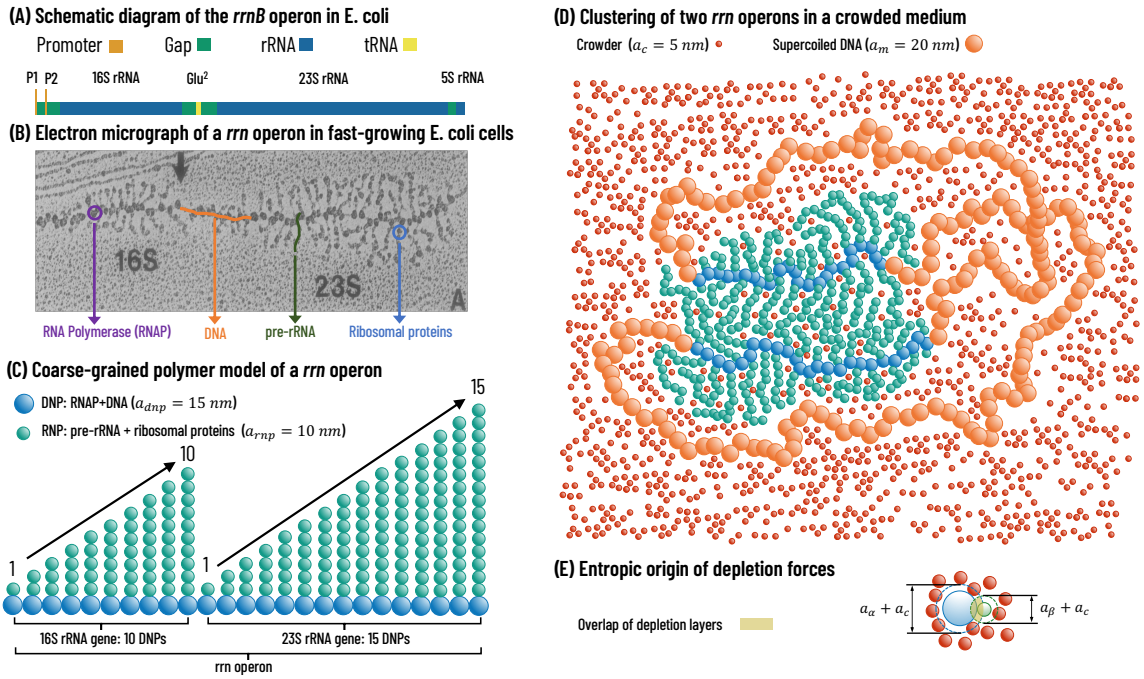


FIGURE 6.1 Clustering and compaction of a heterogeneous branched ring polymer due to MMC effects. (A) A schematic diagram of the *rrnB* operon in E. coli illustrates a single transcript undergoing transcription to produce 15S, 23S, and 5S RNAs along with a tRNA gene. Transcription is initiated from two promoters, *rrn P1* and *rrn P2* [232]. (B) An electron micrograph showcases an active rrn operon comprising DNA, engaged RNAP, nascent transcripts, and ribosomal proteins, forming a structure reminiscent of a double Christmas tree [205]. (C) Our coarse-grained branched polymer model of a rrn operon captures the essential features of the double Christmas-tree-like structure. RNAPs transcribing 16S and 23S genes are abstracted as 10 and 15 DNP monomers, respectively. Each DNP is $a_{\text{dnp}} = 15\,\text{nm}$ in size, representing an engaged RNAP and around 78 DNA base pairs. Our model maintains the actual ratio of RNAPs in these genes, albeit at the half of their numbers in fast-growing E. coli cells, excluding the 5S gene for simplicity [273]. Side-chains, comprising several RNP monomers, extend from each DNP monomer, with lengths increasing within the 16S (23S) gene region from 1 to 10 (20). Each RNP monomer encompasses several RNA nucleotide and ribosomal proteins [272], and has a $a_{\text{rnp}} = 10\,\text{nm}$, estimated by a visual comparison between the shape and size of nascent pre-rRNA chains and the RNAP-coated DNA backbone. (D) The heterogeneous branched ring polymer consists of two rrn operons, connected via two equisized linear semi-flexible sub-chains, with persistence length $l_m = 83\,\text{nm}$ [20, 165]. Each sub-chain is composed of 200 supercoiled DNA monomer of size $a_m = 20\,\text{nm}$ [20, 165]. The polymer interacts with bead-like crowders of size $a_c = 5\,\text{nm}$ in free space [67, 68]. (E) Each monomer is surrounded by a depletion layer (dashed circle) with size $a_\alpha + a_c$ or $a_\beta + a_c$, where α and β are either 'dnp', 'rnp', or 'm', from which crowders are excluded. Overlaps of depletion layers are favored by the entropy of crowders. The resulting depletion force depends on the monomer size, being stronger between larger monomers. Figure 6.2B is adapted from [223], with permission.

polymer model that captures the essential features of the double Christmas-tree-like structure: RNAPs transcribing the 16 S and 23 S genes are represented by 10 and 15 deoxyribonucleoprotein (DNP) monomers, respectively, arranged along the polymer backbone. Each DNP monomer is sized at 15 nm, consisting of an engaged RNAP and

78 DNA base pairs. The number of RNAPs along the genes is reduced to half of the actual count in rapidly growing E. coli cells, though the ratio of RNAPs in the genes remains consistent with the actual one [273]. For simplicity, the 5 S gene is omitted. From each DNP monomer, a side-chain, composed of several ribonucleoprotein (RNP) monomers, radiates out. Within the 16 S (23 S) gene region, the length of the ribosomal side-chains increases from 1 to 10 (20). Each RNP consists of several RNA nucleotides and ribosomal proteins, sized at 10 nm, estimated by visually comparing the shape and size of nascent pre-rRNA chains to the RNAP-coated DNA backbone.

We linked two such coarse-grained rrn operons via two equisized linear sub-chains to form a heterogeneous branched ring polymer model of the E. coli chromosome. Each linear sub-chain is a semi-flexible polymer with a persistence length of 83 nm and comprises 200 supercoiled DNA monomers, each 20 nm in size [20, 165]. The polymer interacts with structureless spherical (bead-like) crowders of 5 nm in free space [67, 68], as depicted in Fig. 6.1D. In our system, each monomer is surrounded by a depletion layer (illustrated with dashed circles) of size $a_\alpha + a_c$ or $a_\beta + a_c$, where α and β represent either 'dnp', 'rnp', or 'm', from which crowders are excluded. The entropy of crowders favors overlaps of depletion layers. The resulting depletion forces is stronger between larger monomers.

6.2.2 Compaction and organization of of a chromosome-like polymer: The interplay between MMC, H-NS oligomerization, and chain stiffness

In Chapter 5, we utilized MD simulations to explore the bacterial chromosome compaction by H-NS proteins and crowders. We modeled each H-NS dimer as a binder with two DNA-binding sites. This model allows H-NS dimers to cross-link two potentially distant sites along the polymer, as described in prior research [258, 260]. While our simplified model omitted biological complexities, such as interactions between H-NS proteins (oligomerization) or chain stiffness, our results demonstrated that MMC can enhance the clustering of bound H-NS dimers. This clustering mirrors the experimentally observed clustering and oligomerization of H-NS protein, which are crucial for the formation of nucleoprotein filaments and, consequently, for the gene-silencing functionality of H-NS [252, 267, 274]. Experimental studies have further shown that MMC effects facilitate the self-assembly of H-NS proteins [275].

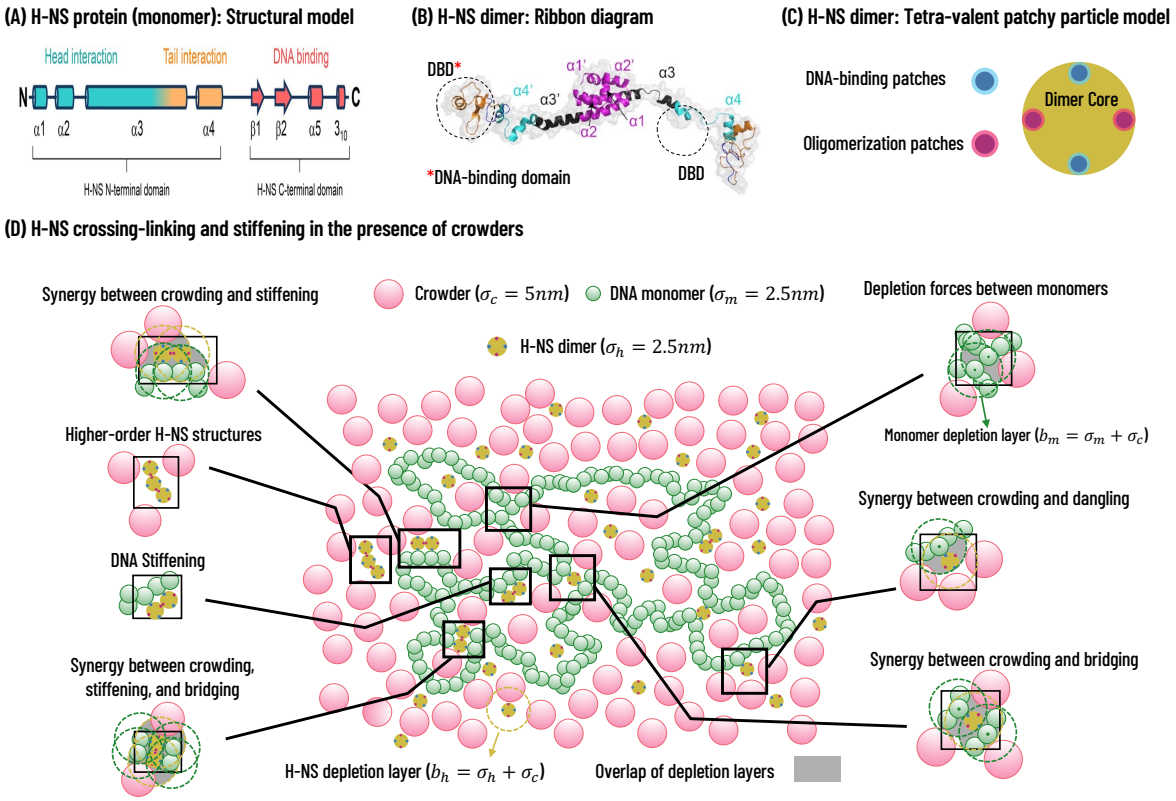


FIGURE 6.2 The synergy between H-NS binding and MMC effects on a chromosome-like ring polymer: how MMC affects the DNA stiffening and bridging modes of the H-NS proteins. (A) The diagram displays the structural components of the H-NS protein. The N-terminal domain, composed of four α-helices (cylinders), has two key regions for self-association of H-NS: The region near the N-terminus, shown in cyan, where head-to-head interactions occur, is the dimerization site. On the other hand, the region near the C-terminus of the N-terminal domain, shown in orange, where tail-to-tail interactions occur, is the oligomerization site. The linker region connects the N-terminal domain to the C-terminal (DNA-binding) domain, shown in red. The C-terminal domain includes two β-sheets (depicted as arrows), an additional α-helix, and a 3_{10} helix. (B) The ribbon diagram illustrates the dimer formation of two H-NS proteins, highlighting the head-to-head interaction at the dimerization sites, which are represented in magenta. In the diagram, the oligomerization sites are indicated in cyan, the DNA-binding domains are in orange, and the linker regions connecting these domains are shown in blue. (C) A tetra-valent patchy particle model of H-NS dimer is presented, where the opposing blue patches represents the DNA-binding domains while the opposing red patches indicate the oligomerization sites. The dimer sites and linker regions are embedded in the dimer core. The oligomerization patches enable attractive interactions between dimers, facilitating the formation of higher-order, transient structures. (D) A semi-flexible ring polymer with a persistence length of $l_p = 50\,\mathrm{nm}$ interacts with H-NS dimers in the presence of crowders in free space. This system retains the interactions described in Fig. 5.1, but now includes attractive dimer-dimer interactions. Consequently, a H-NS dimer can form higher-order structures (upper middle-left inset), induce linear stiffening in the polymer (lower middle-left inset), or both stiffen and bridge the polymer segments (bottom left inset), in addition to the previously described DNA bridging and dangling mechanisms (see Fig. 5.1). In the insets, the depletion layers surrounding monomers and H-NS dimers are visualized as dashed circles, excluding the centers of crowders. The overlap of these layers, shaded in light gray, expands the space accessible to crowders, enhancing particle association through crowder-induced depletion forces. The

Expanding on this foundation, we enhance our model by introducing a semi-flexible polymer to more accurately represent the bacterial chromosome and incorporating two opposing H-NS-binding sites on each dimer to simulate oligomerization more effectively (Fig. 6.2). This refinement allows for a more detailed investigation into the interplay between polymer stiffness, MMC, and H-NS binding. Our aim is to methodically assess how MMC impacts the stiffening and bridging modes of H-NS.

Figure 6.2A presents a schematic of the H-NS protein, showcasing its dimerization, oligomerization, and DNA-binding sites. Two H-NS proteins form a dimer through head-to-head interaction at their dimerization sites, as illustrated in Fig. 6.2B. We model an H-NS dimer as a tetra-valent patchy particle with two opposing DNA-binding patches and two oligomerization patches, as depicted in Fig. 6.2C [260]. The core of the dimer harbors the dimerization sites, while the oligomerization patches enable attractive interactions between dimers, promoting the formation of higher-order, transient H-NS structures (top middle-left inset in Fig. 6.2D). The strength of these attractions varies with factors like osmolarity and temperature [267, 274]. In our simulations, we emulate these effects by adjusting the interaction strength and range of the oligomerization patches. Figure 6.2D illustrates our system: a semi-flexible ring polymer with a persistence length $l_p = 50\,\mathrm{nm}$ interacts with H-NS dimers in the presence of crowders in free space. This system maintains the interactions outlined in Fig. 5.1 but introduces attractive binder-binder interactions. Consequently, H-NS dimers can form higher-order structures (the top middle-left inset in Fig. 6.2D), induce linear stiffening in the polymer (the top left inset in Fig. 6.2D), or both stiffen and bridge the polymer segments (the bottom left inset in Fig. 6.2D), in addition to the previously described DNA bridging and dangling mechanisms (see Fig. 5.1).

The spatial organization of the polymer arises from the combined effects of chain stiffness, MMC, and H-NS binding. As illustrated in the insets of Fig. 6.2D, depletion layers around monomers and H-NS dimers, visualized as dashed circles, exclude the centers of crowders. The overlap of these layers, shaded in light gray, increases the space available to crowders, promoting particle association through crowder-induced

FIGURE 6.2 *Continued:* spatial organization of the polymer results from the interplay between MMC and H-NS binding, significantly affecting the polymer's behavior. Notably, H-NS-induced linear stiffening leads to localized chain thickening (more effective than dangling), promoting compaction by crowders (top left inset). H-NS stiffening and bridging creates overlapping regions (lower left inset), intensifying the crowder-induced attractions and thereby enhancing MMC-driven chain compaction more effectively than the scenarios depicted in the right and top left inset. Thus, H-NS stiffening and bridging boosts the MMC-induced chain compaction more than H-NS bridging alone. In our model, the monomer, H-NS (core), and crowder sizes are $\sigma_m = 2.5\,\mathrm{nm}$, $\sigma_h = 2.5\,\mathrm{nm}$, and $\sigma_c = 5\,\mathrm{nm}$, respectively.

depletion forces. H-NS-induced linear stiffening results in localized chain thickening, more effective than dangling, thereby facilitating compaction by crowders (the top left inset in Fig. 6.2D). Notably, the H-NS stiffening and bridging creates overlapping regions (the lower left inset in Fig. 6.2D) that are larger than the overlapping regions in the scenarios depicted in the right and top left insets in Fig. 6.2D, suggesting H-NS stiffening and bridging contribute more significantly to MMC-induced chain compaction than H-NS bridging alone.

Letter's of copyright permissions

The copyright permissions are listed for Figs. 1.2 to 1.5, in order, on the following pages. Please note that archived webpages are provided as a copyright permission for the image taken from ref. [102], which is used in Fig. 1.3. Similar images to this image can be found in [103].

JOHN WILEY AND SONS LICENSE
TERMS AND CONDITIONS

Apr 24, 2024

This Agreement between Mr. Amir Hosein Sadeghi Isfahani ("You") and John Wiley and Sons ("John Wiley and Sons") consists of your license details and the terms and conditions provided by John Wiley and Sons and Copyright Clearance Center.

License Number	5775430243812
License date	Apr 24, 2024
Licensed Content Publisher	John Wiley and Sons
Licensed Content Publication	Biochemistry and Molecular Biology Education
Licensed Content Title	Escherichia coli
Licensed Content Author	David S. Goodsell
Licensed Content Date	Nov 24, 2009
Licensed Content Volume	37

Licensed Content Issue	6
Licensed Content Pages	8
Type of use	Dissertation/Thesis
Requestor type	University/Academic
Format	Electronic
Portion	Figure/table
Number of figures/tables	1
Will you be translating?	No
Title of new work	Computational modeling of bacterial chromosome organization: macromolecular crowding, chain heterogeneity, and chain cross-linking
Institution name	Univeristy of Waterloo
Expected presentation date	Apr 2024
Portions	Figures 1 and 2
	Mr. Amir Hosein Sadeghi Isfahani

Requestor Location	University Ave. Waterloo, ON N2L 3G1 Canada Attn: University of Waterloo
Publisher Tax ID	EU826007151
Total	0.00 CAD

Terms and Conditions

TERMS AND CONDITIONS

This copyrighted material is owned by or exclusively licensed to John Wiley & Sons, Inc. or one of its group companies (each a"Wiley Company") or handled on behalf of a society with which a Wiley Company has exclusive publishing rights in relation to a particular work (collectively "WILEY"). By clicking "accept" in connection with completing this licensing transaction, you agree that the following terms and conditions apply to this transaction (along with the billing and payment terms and conditions established by the Copyright Clearance Center Inc., ("CCC's Billing and Payment terms and conditions"), at the time that you opened your RightsLink account (these are available at any time at http://myaccount.copyright.com).

Terms and Conditions

- The materials you have requested permission to reproduce or reuse (the "Wiley Materials") are protected by copyright.
- You are hereby granted a personal, non-exclusive, non-sub licensable (on a stand-alone basis), non-transferable, worldwide, limited license to reproduce the Wiley Materials for the purpose specified in the licensing process. This license, **and any CONTENT (PDF or image file) purchased as part of your order,** is for a one-time use only and limited to any maximum distribution number specified in the license. The first instance of republication or reuse granted by this license must be completed within two years of the date of the grant of this license (although copies prepared before the end date may be distributed thereafter). The Wiley Materials shall not be used in any other manner or for any other purpose, beyond what is granted in the license. Permission is granted subject to an appropriate acknowledgement given to the author, title of the material/book/journal and the

publisher. You shall also duplicate the copyright notice that appears in the Wiley publication in your use of the Wiley Material. Permission is also granted on the understanding that nowhere in the text is a previously published source acknowledged for all or part of this Wiley Material. Any third party content is expressly excluded from this permission.

- With respect to the Wiley Materials, all rights are reserved. Except as expressly granted by the terms of the license, no part of the Wiley Materials may be copied, modified, adapted (except for minor reformatting required by the new Publication), translated, reproduced, transferred or distributed, in any form or by any means, and no derivative works may be made based on the Wiley Materials without the prior permission of the respective copyright owner.**For STM Signatory Publishers clearing permission under the terms of the STM Permissions Guidelines only, the terms of the license are extended to include subsequent editions and for editions in other languages, provided such editions are for the work as a whole in situ and does not involve the separate exploitation of the permitted figures or extracts,** You may not alter, remove or suppress in any manner any copyright, trademark or other notices displayed by the Wiley Materials. You may not license, rent, sell, loan, lease, pledge, offer as security, transfer or assign the Wiley Materials on a stand-alone basis, or any of the rights granted to you hereunder to any other person.

- The Wiley Materials and all of the intellectual property rights therein shall at all times remain the exclusive property of John Wiley & Sons Inc, the Wiley Companies, or their respective licensors, and your interest therein is only that of having possession of and the right to reproduce the Wiley Materials pursuant to Section 2 herein during the continuance of this Agreement. You agree that you own no right, title or interest in or to the Wiley Materials or any of the intellectual property rights therein. You shall have no rights hereunder other than the license as provided for above in Section 2. No right, license or interest to any trademark, trade name, service mark or other branding ("Marks") of WILEY or its licensors is granted hereunder, and you agree that you shall not assert any such right, license or interest with respect thereto

- NEITHER WILEY NOR ITS LICENSORS MAKES ANY WARRANTY OR REPRESENTATION OF ANY KIND TO YOU OR ANY THIRD PARTY, EXPRESS, IMPLIED OR STATUTORY, WITH RESPECT TO THE MATERIALS OR THE ACCURACY OF ANY INFORMATION CONTAINED IN THE MATERIALS, INCLUDING, WITHOUT LIMITATION, ANY IMPLIED WARRANTY OF MERCHANTABILITY, ACCURACY, SATISFACTORY QUALITY, FITNESS FOR A PARTICULAR PURPOSE, USABILITY, INTEGRATION OR NON-INFRINGEMENT AND ALL SUCH WARRANTIES ARE HEREBY EXCLUDED BY WILEY AND ITS LICENSORS AND WAIVED BY YOU.

- WILEY shall have the right to terminate this Agreement immediately upon breach of this Agreement by you.

- You shall indemnify, defend and hold harmless WILEY, its Licensors and their respective directors, officers, agents and employees, from and against any actual or threatened claims, demands, causes of action or proceedings arising from any breach of this Agreement by you.

- IN NO EVENT SHALL WILEY OR ITS LICENSORS BE LIABLE TO YOU OR ANY OTHER PARTY OR ANY OTHER PERSON OR ENTITY FOR ANY SPECIAL, CONSEQUENTIAL, INCIDENTAL, INDIRECT, EXEMPLARY OR PUNITIVE DAMAGES, HOWEVER CAUSED, ARISING OUT OF OR IN CONNECTION WITH THE DOWNLOADING, PROVISIONING, VIEWING OR USE OF THE MATERIALS REGARDLESS OF THE FORM OF ACTION, WHETHER FOR BREACH OF CONTRACT, BREACH OF WARRANTY, TORT, NEGLIGENCE, INFRINGEMENT OR OTHERWISE (INCLUDING, WITHOUT LIMITATION, DAMAGES BASED ON LOSS OF PROFITS, DATA, FILES, USE, BUSINESS OPPORTUNITY OR CLAIMS OF THIRD PARTIES), AND WHETHER OR NOT THE PARTY HAS BEEN ADVISED OF THE POSSIBILITY OF SUCH DAMAGES. THIS LIMITATION SHALL APPLY NOTWITHSTANDING ANY FAILURE OF ESSENTIAL PURPOSE OF ANY LIMITED REMEDY PROVIDED HEREIN.

- Should any provision of this Agreement be held by a court of competent jurisdiction to be illegal, invalid, or unenforceable, that provision shall be deemed amended to achieve as nearly as possible the same economic effect as the original provision, and the legality, validity and enforceability of the remaining provisions of this Agreement shall not be affected or impaired thereby.

- The failure of either party to enforce any term or condition of this Agreement shall not constitute a waiver of either party's right to enforce each and every term and condition of this Agreement. No breach under this agreement shall be deemed waived or excused by either party unless such waiver or consent is in writing signed by the party granting such waiver or consent. The waiver by or consent of a party to a breach of any provision of this Agreement shall not operate or be construed as a waiver of or consent to any other or subsequent breach by such other party.

- This Agreement may not be assigned (including by operation of law or otherwise) by you without WILEY's prior written consent.

- Any fee required for this permission shall be non-refundable after thirty (30) days from receipt by the CCC.

- These terms and conditions together with CCC's Billing and Payment terms and conditions (which are incorporated herein) form the entire agreement between you and WILEY concerning this licensing transaction and (in the absence of fraud) supersedes all prior agreements and representations of the parties, oral or written. This Agreement may not be amended except in writing signed by both parties. This Agreement shall be binding upon and inure to the benefit of the parties' successors,

legal representatives, and authorized assigns.

- In the event of any conflict between your obligations established by these terms and conditions and those established by CCC's Billing and Payment terms and conditions, these terms and conditions shall prevail.
- WILEY expressly reserves all rights not specifically granted in the combination of (i) the license details provided by you and accepted in the course of this licensing transaction, (ii) these terms and conditions and (iii) CCC's Billing and Payment terms and conditions.
- This Agreement will be void if the Type of Use, Format, Circulation, or Requestor Type was misrepresented during the licensing process.
- This Agreement shall be governed by and construed in accordance with the laws of the State of New York, USA, without regards to such state's conflict of law rules. Any legal action, suit or proceeding arising out of or relating to these Terms and Conditions or the breach thereof shall be instituted in a court of competent jurisdiction in New York County in the State of New York in the United States of America and each party hereby consents and submits to the personal jurisdiction of such court, waives any objection to venue in such court and consents to service of process by registered or certified mail, return receipt requested, at the last known address of such party.

WILEY OPEN ACCESS TERMS AND CONDITIONS

Wiley Publishes Open Access Articles in fully Open Access Journals and in Subscription journals offering Online Open. Although most of the fully Open Access journals publish open access articles under the terms of the Creative Commons Attribution (CC BY) License only, the subscription journals and a few of the Open Access Journals offer a choice of Creative Commons Licenses. The license type is clearly identified on the article.

The Creative Commons Attribution License

The Creative Commons Attribution License (CC-BY) allows users to copy, distribute and transmit an article, adapt the article and make commercial use of the article. The CC-BY license permits commercial and non-

Creative Commons Attribution Non-Commercial License

The Creative Commons Attribution Non-Commercial (CC-BY-NC)License permits use, distribution and reproduction in any medium, provided the original work is properly cited and is not used for commercial purposes.(see below)

Creative Commons Attribution-Non-Commercial-NoDerivs License

The Creative Commons Attribution Non-Commercial-NoDerivs License (CC-BY-NC-ND) permits use, distribution and reproduction in any medium, provided the original work is properly cited, is not used for commercial purposes and no modifications or adaptations are made. (see below)

Use by commercial "for-profit" organizations

Use of Wiley Open Access articles for commercial, promotional, or marketing purposes requires further explicit permission from Wiley and will be subject to a fee.

Further details can be found on Wiley Online Library
http://olabout.wiley.com/WileyCDA/Section/id-410895.html

Other Terms and Conditions:

v1.10 Last updated September 2015

Questions? customercare@copyright.com.

This page has been archived and is no longer updated

Genome Packaging in Prokaryotes: the Circular Chromosome of *E. coli*

By: Ann Griswold, Ph.D. © 2008 Nature Education

Citation: Griswold, A. (2008) Genome packaging in prokaryotes: the circular chromosome of E. coli. *Nature Education* 1(1):57

How do bacteria, lacking a nucleus, organize and pack their genome into the cell? Supercoiling enables this but forces a different kind of transcription and translation in prokaryotes.

Aa Aa Aa

Most students learn at an early age that organisms can be broadly divided into two types: prokaryotes and eukaryotes. In primary school, children are taught that the main difference between these organisms is that eukaryotic cells contain membrane-bound organelles, such as the nucleus, while prokaryotic cells do not. There is much more to the story, however, particularly with regard to chromosomal structure and organization.

E. coli: A Model Prokaryote

Much of what is known about prokaryotic chromosome structure was derived from studies of *Escherichia coli*, a bacterium that lives in the human colon and is commonly used in laboratory cloning experiments. In the 1950s and 1960s, this bacterium became the model organism of choice for prokaryotic research when a group of scientists used phase-contrast microscopy and autoradiography to show that the essential genes of *E. coli* are encoded on a single circular chromosome packaged within the cell nucleoid (Mason & Powelson, 1956; Cairns, 1963).

Prokaryotic cells do not contain nuclei or other membrane-bound organelles. In fact, the word "prokaryote" literally means "before the nucleus." The nucleoid is simply the area of a prokaryotic cell in which the chromosomal DNA is located. This arrangement is not as simple as it sounds, however, especially considering that the *E. coli* chromosome is several orders of magnitude larger than the cell itself. So, if bacterial chromosomes are so huge, how can they fit comfortably inside a cell—much less in one small corner of the cell?

DNA Supercoiling

The answer to this question lies in DNA packaging. Whereas eukaryotes wrap their DNA around proteins called histones to help package the DNA into smaller spaces, most prokaryotes do not have histones (with the exception of those species in the domain Archaea). Thus, one way prokaryotes compress their DNA into smaller spaces is through supercoiling (Figure 1). Imagine twisting a rubber band so that it forms tiny coils. Now twist it even further, so that the original coils fold over one another and form a condensed ball. When this type of twisting happens to a bacterial genome, it is known as supercoiling. Genomes can be negatively supercoiled, meaning that the DNA is twisted in the opposite direction of the double helix, or positively supercoiled, meaning that the DNA is twisted in the same direction as the double helix. Most bacterial genomes are negatively supercoiled during normal growth.

Proteins Involved in Supercoiling

During the 1980s and 1990s, researchers discovered that multiple proteins act together to fold and condense prokaryotic DNA. In particular, one protein called HU, which is the most abundant protein in



the nucleoid, works with an enzyme called topoisomerase I to bind DNA and introduce sharp bends in the chromosome, generating the tension necessary for negative supercoiling. Recent studies have also shown that other proteins, including integration host factor (IHF), can bind to specific sequences within the genome and introduce additional bends (Rice *et al.*, 1996). The folded DNA is then organized into a variety of conformations (Sinden & Pettijohn, 1981) that are supercoiled and wound around tetramers of the HU protein, much like eukaryotic chromosomes are wrapped around histones (Murphy & Zimmerman, 1997).

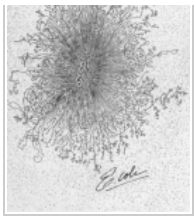


Figure 1

Once the prokaryotic genome has been condensed, DNA topoisomerase I, DNA gyrase, and other proteins help maintain the supercoils. One of these maintenance proteins, H-NS, plays an active role in transcription by modulating the expression of the genes involved in the response to environmental stimuli. Another maintenance protein, factor for inversion stimulation (FIS), is abundant during exponential growth and regulates the expression of more than 231 genes, including DNA topoisomerase I (Bradley *et al.*, 2007).

Accessing Supercoiled Genes

Supercoiling explains how chromosomes fit into a small corner of the cell, but how do the proteins involved in replication and transcription access the thousands of genes in prokaryotic chromosomes when everything is packaged together so tightly? It has been determined that prokaryotic DNA replication occurs at a rate of 1,000 nucleotides per second, and prokaryotic transcription occurs at a rate of about 40 nucleotides per second (Lewin, 2007), so bacteria must have highly efficient methods of accessing their DNA strands. But how?

Researchers have noted that the nucleoid usually appears as an irregularly shaped mass within the prokaryotic cell, but it becomes spherical when the cell is treated with chemicals to inhibit transcription or translation. Moreover, during transcription, small regions of the chromosome can be seen to project from the nucleoid into the cytoplasm (i.e., the interior of the cell), where they unwind and associate with ribosomes, thus allowing easy access by various transcriptional proteins (Dürrenberger *et al.*, 1988). These projections are thought to explain the mysterious shape of nucleoids during active growth. When transcription is inhibited, however, the projections retreat into the nucleoid, forming the aforementioned spherical shape.

Because there is no nuclear membrane to separate prokaryotic DNA from the ribosomes within the cytoplasm, transcription and translation occur simultaneously in these organisms. This is strikingly different from eukaryotic chromosomes, which are confined to the membrane-bound nucleus during most of the cell cycle. In eukaryotes, transcription must be completed in the nucleus before the newly synthesized mRNA molecules can be transported to the cytoplasm to undergo translation into proteins.

Variations in Prokaryotic Genome Structure

Recently, it has become apparent that one size does not fit all when it comes to prokaryotic chromosome structure. While most prokaryotes, like *E. coli*, contain a single circular DNA molecule that makes up their entire genome, recent studies have indicated that some prokaryotes contain as many as four linear or circular chromosomes. For example, *Vibrio cholerae*, the bacteria that causes cholera, contains two circular chromosomes. One of these chromosomes contains the genes involved in metabolism and virulence, while the other contains the remaining essential genes (Trucksis *et al.*, 1998). An even more extreme example is provided by *Borrelia burgdorferi*, the bacterium that causes Lyme disease. This organism is transmitted through the bite of deer ticks (Figure 2), and it contains up to 11 copies of a single linear chromosome



(Ferdows & Barbour, 1989). Unlike *E. coli*, *Borrelia* cannot supercoil its linear chromosomes into a tight ball within the nucleoid; rather, these strands are diffused throughout the cell (Hinnebusch & Bendich, 1997).

Figure 2: Deer tick.

This black-legged tick (*Ixodes* sp.) carries the bacterium (*Borrelia* sp.) that causes Lyme disease.
Jim Gathany and William L. Nicholson, Ph.D/CDC.

Other organisms, such as *Bacillus subtilis*, form nucleoids that closely resemble those of *E. coli*, but they use different architectural proteins to do so. Furthermore, the DNA molecules of Archaea, a taxonomic domain composed of single-celled, nonbacterial prokaryotes that share many similarities with eukaryotes, can be negatively supercoiled, positively supercoiled, or not supercoiled at all. It is important to note that archaeans are the only group of prokaryotes that use eukaryote-like histones, rather than the architectural proteins described above, to condense their DNA molecules (Sandman *et al.*, 1990). The acquisition of histones by archaeans is thought to have paved the way for the evolution of larger and more complex eukaryotic cells (Minsky *et al.*, 1997).

Other DNA Differences Between Prokaryotes and Eukaryotes

Most prokaryotes reproduce asexually and are haploid, meaning that only a single copy of each gene is present. This makes it relatively easy to generate mutations in the lab and study the resulting phenotypes. By contrast, eukaryotes that reproduce sexually generally contain multiple chromosomes and are said to be diploid, because two copies of each gene exist—with one copy coming from each of an organism's parents.

Yet another difference between prokaryotes and eukaryotes is that prokaryotic cells often contain one or more plasmids (i.e., extrachromosomal DNA molecules that are either linear or circular). These pieces of DNA differ from chromosomes in that they are typically smaller and encode nonessential genes, such as those that aid growth in specific conditions or encode antibiotic resistance. *Borrelia*, for instance, contains more than 20 circular and linear plasmids that encode genes responsible for infecting ticks and humans (Fraser *et al.*, 1997). Plasmids are often much smaller than chromosomes (i.e., less than 1,500 kilobases), and they replicate independently of the rest of the genome. However, some plasmids are capable of integrating into chromosomes or moving from cell to cell.

Perhaps due to the space constraints of packing so many essential genes onto a single chromosome, prokaryotes can be highly efficient in terms of genomic organization. Very little space is left between prokaryotic genes. As a result, noncoding sequences account for an average of 12% of the prokaryotic genome, as opposed to upwards of 98% of the genetic material in eukaryotes (Ahnert *et al.*, 2008). Furthermore, unlike eukaryotic chromosomes, most prokaryotic genomes are organized into polycistronic operons, or clusters of more than one coding region attached to a single promoter, separated by only a few base pairs. The proteins encoded by each operon often collaborate on a single task, such as the metabolism of a sugar into by-products that can be used for energy (Figure 3).

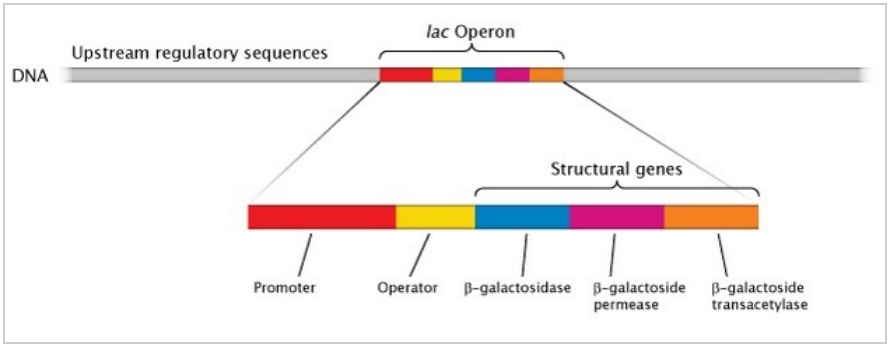


Figure 3: The prokaryotic *lac* operon.
Three structural genes code for proteins involved in lactose import and metabolism in bacteria. The genes are organized together in a cluster called the *lac* operon.
© 2013 Nature Education All rights reserved.

Figure Detail

The organization of prokaryotic DNA therefore differs from that of eukaryotes in several important ways. The most notable difference is the condensation process that prokaryotic DNA molecules undergo in order to fit inside relatively small cells. Other differences, while not as dramatic, are summarized in Table 1.

Table 1: Prokaryotic versus Eukaryotic Chromosomes

Prokaryotic Chromosomes	Eukaryotic Chromosomes
• Many prokaryotes contain a single circular chromosome. • Prokaryotic chromosomes are condensed in the nucleoid via DNA supercoiling and the binding of various architectural proteins. • Because prokaryotic DNA can interact with the cytoplasm, transcription and translation occur simultaneously. • Most prokaryotes contain only one copy of each gene (i.e., they are haploid). • Nonessential prokaryotic genes are commonly encoded on extrachromosomal plasmids. • Prokaryotic genomes are efficient and compact, containing little repetitive DNA.	• Eukaryotes contain multiple linear chromosomes. • Eukaryotic chromosomes are condensed in a membrane-bound nucleus via histones. • In eukaryotes, transcription occurs in the nucleus, and translation occurs in the cytoplasm. • Most eukaryotes contain two copies of each gene (i.e., they are diploid). • Some eukaryotic genomes are organized into operons, but most are not. • Extrachromosomal plasmids are not commonly present in eukaryotes. • Eukaryotes contain large amounts of noncoding and repetitive DNA.

References and Recommended Reading

Abbott, A. Lyme disease: Uphill struggle. *Nature* **439**, 524–525 (2006) doi:10.1038/439524a (link to article)

Ahnert, S. E., *et al.* How much non-coding DNA do eukaryotes require? *Journal of Theoretical Biology* **252**, 587–592 (2008)

Bendich, A. J., & Drlica, K. Prokaryotic and eukaryotic chromosomes: What's the difference? *Bioessays* **22**, 481–486 (2000)

Bradley, M. D., *et al.* Effects of Fis on *Escherichia coli* gene expression during different growth stages. *Microbiology* **153**, 2922–2940 (2007)

Cairns, J. The chromosome of *Escherichia coli*. *Cold Spring Harbor Symposia on Quantitative Biology* **28**, 43–46 (1963)

Dürrenberger, M., *et al.* Intracellular location of the histonelike protein HU in *Escherichia coli*. *Journal of Bacteriology* **170**, 4757–1768

(1988)

Endy, D., & Brent, R. Modelling cellular behaviour. *Nature* **409**, 391–395 (2001) doi:10.1038/35053181 (link to article)

Ferdows, M. S., & Barbour, A. G. Megabase-sized linear DNA in the bacterium *Borrelia burgdorferi*, the Lyme disease agent. *Proceedings of the National Academy of Sciences* **86**, 5969–5973 (1989)

Fraser, C. M., *et al.* Genomic sequence of a Lyme disease spirochaete, *Borrelia burgdorferi*. *Nature* **390**, 580–586 (1997) doi:10.1038/37551 (link to article)

Hinnebusch, B. J., & Bendich, A. J. The bacterial nucleoid visualized by fluorescence microscopy of cells lysed within agarose: Comparison of *Escherichia coli* and spirochetes of the genus *Borrelia*. *Journal of Bacteriology* **179**, 2228–2237 (1997)

Jacob, F., & Monod, J. Genetic regulatory mechanisms in the synthesis of proteins. *Journal of Molecular Biology* **3**, 318–356 (1961)

Lewin, B. *Genes IX* (Sudbury, MA, Jones and Bartlett, 2007)

Mason, D. J., & Powelson, D. M. Nuclear division as observed in live bacteria by a new technique. *Journal of Bacteriology* **71**, 474–479 (1956) (link to article)

Minsky, A., *et al.* Nucleosomes: A solution to a crowded intracellular environment. *Journal of Theoretical Biology* **188**, 379–385 (1997)

Murphy, L. D., & Zimmerman, S. B. Isolation and characterization of spermidine nucleoids from *Escherichia coli*. *Journal of Structural Biology* **119**, 321–335 (1997)

Rice, P. A., *et al.* Crystal structure of an IHF–DNA complex: A protein-induced DNA U-turn. *Cell* **87**, 1295–1306 (1996)

Robinow, C., & Kellenberger, E. The bacterial nucleoid revisited. *Microbiology and Molecular Biology Reviews* **58**, 211–232 (1994)

Sandman, K., *et al.* HMf, a DNA-binding protein isolated from the hyperthermophilic archaeon *Methanothermus fervidus*, is most closely related to histones. *Proceedings of the National Academy of Sciences* **87**, 5788–5791 (1990)

Sandman, K., *et al.* Diversity of prokaryotic chromosomal proteins and the origin of the nucleosome. *Cellular and Molecular Life Sciences* **54**, 1350–1364 (1998)

Sauvonnet, N., *et al.* Pilus formation and protein secretion by the same machinery in *Escherichia coli*. *EMBO Journal* **19**, 2221–2228 (2000) doi:10.1093/emboj/19.10.2221

Sinden, R. R., & Pettijohn, D. E. Chromosomes in living *Escherichia coli* cells are segregated into domains of supercoiling. *Proceedings of the National Academy of Sciences* **78**, 224–228 (1981)

Snyder, L., & Champness, W. *Molecular Genetics of Bacteria*, 2nd ed. (Washington, DC, ASM Press, 2003)

Trucksis, M., *et al.* The *Vibrio cholerae* genome contains two unique circular chromosomes. *Proceedings of the National Academy of Sciences* **95**, 14464–14469 (1998)

Willenbrock, H., & Ussery, D. W. Chromatin architecture and gene expression in *Escherichia coli*. *Genome Biology* **5**, 252 (2004)

Yasuzawa, K., *et al.* Histone-like proteins are required for cell growth and constraint of supercoils in DNA. *Gene* **122**, 9–15 (1992).

Outline | **Keywords** | **Add Content to Group** FEEDBACK

Explore This Subject

CHROMOSOME ANALYSIS

- Chromosome Mapping: Idiograms
- Chromosome Territories: The Arrangement of Chromosomes in the Nucleus
- Cytogenetic Methods and Disease: Flow Cytometry, CGH, and FISH
- Diagnosing Down Syndrome, Cystic Fibrosis, Tay-Sachs Disease and Other Genetic Disorders
- Fluorescence *In Situ* Hybridization (FISH)
- Human Chromosome Translocations and Cancer
- Karyotyping for Chromosomal Abnormalities
- Microarray-based Comparative Genomic Hybridization (aCGH)
- Prenatal Screen Detects Fetal Abnormalities
- Synteny: Inferring Ancestral Genomes

CHROMOSOME STRUCTURE

- Chromosome Mapping: Idiograms
- Chromosome Segregation in Mitosis: The Role of Centromeres
- Chromosome Territories: The Arrangement of Chromosomes in the Nucleus
- DNA Packaging: Nucleosomes and Chromatin
- Genome Packaging in Prokaryotes: the Circular Chromosome of *E. coli*
- Telomeres of Human Chromosomes

MUTATIONS AND ALTERATIONS IN CHROMOSOMES

- Chromosomal Abnormalities: Aneuploidies
- Chromosome Abnormalities and Cancer Cytogenetics

Copy Number Variation and Human Disease

Cytogenetic Methods and Disease: Flow Cytometry, CGH, and FISH

DNA Deletion and Duplication and the Associated Genetic Disorders

Genetic Recombination

Human Chromosome Number

Human Chromosome Translocations and Cancer

Karyotyping for Chromosomal Abnormalities

Prenatal Screen Detects Fetal Abnormalities

Synteny: Inferring Ancestral Genomes

Trisomy 21 Causes Down Syndrome

X Chromosome: X Inactivation

CHROMOSOME NUMBER

Chromosomal Abnormalities: Aneuploidies

Human Chromosome Number

Polyploidy

Trisomy 21 Causes Down Syndrome

CHROMOSOME THEORY AND CELL DIVISION

Chromosome Segregation in Mitosis: The Role of Centromeres

Chromosome Theory and the Castle and Morgan Debate

Developing the Chromosome Theory

Meiosis, Genetic Recombination, and Sexual Reproduction

Mitosis and Cell Division

SEX CHROMOSOMES

Genetic Mechanisms of Sex Determination

Sex Chromosomes and Sex

Determination

Sex Chromosomes in Mammals: X Inactivation

Sex Determination in Honeybees

X Chromosome: X Inactivation

Your Privacy

We use cookies to make sure that our website works properly, as well as some optional cookies to personalise content and advertising, provide social media features and analyse how people use our site. By accepting some or all optional cookies you give consent to the processing of your personal data, including transfer to third parties, some in countries outside of the European Economic Area that do not offer the same data protection standards as the country where you live. You can decide which optional cookies to accept by clicking on "Manage preferences", where you can also find more information about how your personal data is processed. Further information can be found in our privacy policy.

Accept all cookies Manage preferences

This page has been archived and is no longer updated

Visual Browse

Close

Supercoiled chromosome of E. coli.

- Author: R. Kavanoff

Keywords

Keywords for this Article

Add keywords to your Content
Save | Cancel
Share | Cancel
Revoke | Cancel

Rate & Certify

Rate Me
!

Comment
Save | Cancel

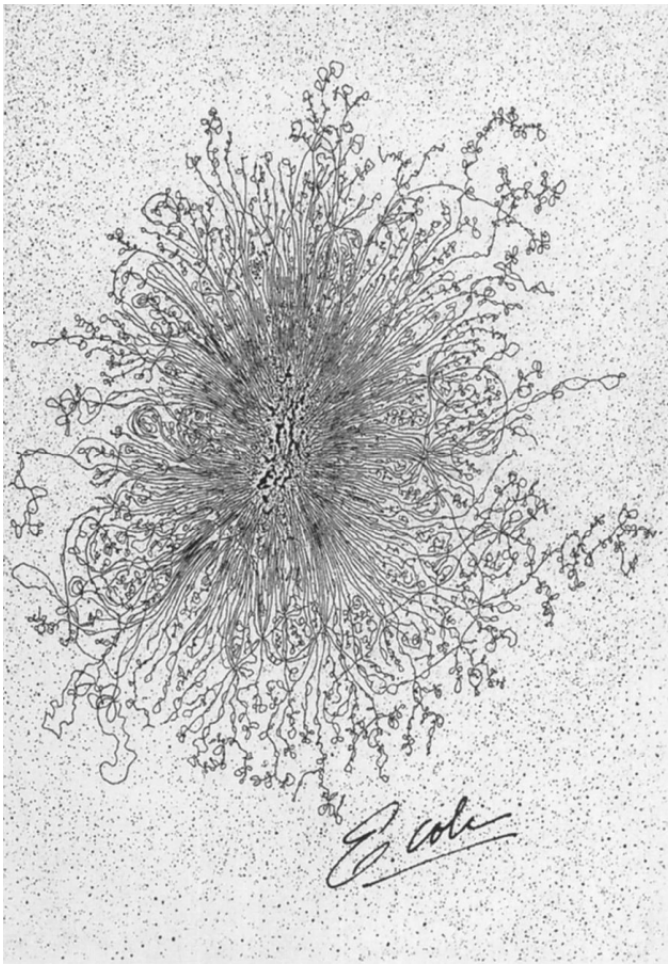
Flag Inappropriate

The Content is
- Objectionable
- Explicit
- Offensive
- Inaccurate

Comment
Flag Content | Cancel

Delete Content

Reason
Delete | Cancel
Close



Supercoiled chromosome of *E. coli*.
Supercoiled chromosome of E. coli.

This image is linked to the following Scitable pages:



Genome Packaging in Prokaryotes: the Circular Chromosome of *E. coli*

How do bacteria, lacking a nucleus, organize and pack their genome into the cell? Supercoiling enables this but forces a different kind of transcription and translation in prokaryotes.

- Add Content to Group
- |
- Bookmark
- |
- Keywords
- |
- Flag Inappropriate

share

Close

- Digg
- Facebook
- MySpace
- Google+

Comments

Please Post Your Comment

No comments yet.

Save Note

Note

View Public Private Friends & Groups

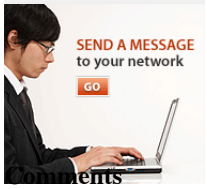
Save | Cancel | Delete

Next | Prev | Close | Edit | Delete

Topic Rooms

Genetics
Cell Biology
Scientific Communication
Career Planning

Connect



Comments

Close

© 2014 Nature Education

- About|
- Contact|
- Press Room|
- Sponsors|
- Terms of Use|
- Privacy Notice|
- Glossary|
- Catalog|
- Home|
- Library|
- Blogs

Please Post Your Comment*

Submit Post Cancel

* Required

SPRINGER NATURE LICENSE
TERMS AND CONDITIONS

Apr 24, 2024

This Agreement between Mr. Amir Hosein Sadeghi Isfahani ("You") and Springer Nature ("Springer Nature") consists of your license details and the terms and conditions provided by Springer Nature and Copyright Clearance Center.

License Number	5775430716095
License date	Apr 24, 2024
Licensed Content Publisher	Springer Nature
Licensed Content Publication	Nature Reviews Genetics
Licensed Content Title	Chromosome organization in bacteria: mechanistic insights into genome structure and function
Licensed Content Author	Remus T. Dame et al
Licensed Content Date	Nov 25, 2019
Type of Use	Thesis/Dissertation
Requestor type	academic/university or research institute
Format	electronic

Portion	figures/tables/illustrations
Number of figures/tables/illustrations	1
Would you like a high resolution image with your order?	no
Will you be translating?	no
Circulation/distribution	1 - 29
Author of this Springer Nature content	no
Title of new work	Computational modeling of bacterial chromosome organization: macromolecular crowding, chain heterogeneity, and chain cross-linking
Institution name	Univeristy of Waterloo
Expected presentation date	Apr 2024
Portions	Figure 5
Requestor Location	Mr. Amir Hosein Sadeghi Isfahani University Ave. Waterloo, ON N2L 3G1 Canada Attn: University of Waterloo
Total	0.00 CAD

Terms and Conditions

Springer Nature Customer Service Centre GmbH Terms and Conditions

The following terms and conditions ("Terms and Conditions") together with the terms specified in your [RightsLink] constitute the License ("License") between you as Licensee and Springer Nature Customer Service Centre GmbH as Licensor. By clicking 'accept' and completing the transaction for your use of the material ("Licensed Material"), you confirm your acceptance of and obligation to be bound by these Terms and Conditions.

1. Grant and Scope of License

1. 1. The Licensor grants you a personal, non-exclusive, non-transferable, non-sublicensable, revocable, world-wide License to reproduce, distribute, communicate to the public, make available, broadcast, electronically transmit or create derivative works using the Licensed Material for the purpose(s) specified in your RightsLink Licence Details only. Licenses are granted for the specific use requested in the order and for no other use, subject to these Terms and Conditions. You acknowledge and agree that the rights granted to you under this License do not include the right to modify, edit, translate, include in collective works, or create derivative works of the Licensed Material in whole or in part unless expressly stated in your RightsLink Licence Details. You may use the Licensed Material only as permitted under this Agreement and will not reproduce, distribute, display, perform, or otherwise use or exploit any Licensed Material in any way, in whole or in part, except as expressly permitted by this License.

1. 2. You may only use the Licensed Content in the manner and to the extent permitted by these Terms and Conditions, by your RightsLink Licence Details and by any applicable laws.

1. 3. A separate license may be required for any additional use of the Licensed Material, e.g. where a license has been purchased for print use only, separate permission must be obtained for electronic re-use. Similarly, a License is only valid in the language selected and does not apply for editions in other languages unless additional translation rights have been granted separately in the License.

1. 4. Any content within the Licensed Material that is owned by third parties is expressly excluded from the License.

1. 5. Rights for additional reuses such as custom editions, computer/mobile applications, film or TV reuses and/or any other derivative rights requests require additional permission and may be subject to an additional fee. Please apply to journalpermissions@springernature.com or bookpermissions@springernature.com for these rights.

2. Reservation of Rights

Licensor reserves all rights not expressly granted to you under this License. You acknowledge and agree that nothing in this License limits or restricts Licensor's rights in or use of the Licensed Material in any way. Neither this License, nor any act, omission, or statement by Licensor or you, conveys any ownership right to you in any Licensed Material, or to any element or portion thereof. As between Licensor and you, Licensor owns and retains all right, title, and interest in and to the Licensed Material subject to the license granted in Section 1.1. Your permission to use the Licensed Material is expressly conditioned on you not impairing Licensor's or the applicable copyright owner's rights in the Licensed Material in any way.

3. Restrictions on use

3. 1. Minor editing privileges are allowed for adaptations for stylistic purposes or formatting purposes provided such alterations do not alter the original meaning or intention of the Licensed Material and the new figure(s) are still accurate and representative of the Licensed Material. Any other changes including but not limited to, cropping, adapting, and/or omitting material that affect the meaning, intention or moral rights of the author(s) are strictly prohibited.

3. 2. You must not use any Licensed Material as part of any design or trademark.

3. 3. Licensed Material may be used in Open Access Publications (OAP), but any such reuse must include a clear acknowledgment of this permission visible at the same time as the figures/tables/illustration or abstract and which must indicate that the Licensed Material is not part of the governing OA license but has been reproduced with permission. This may be indicated according to any standard referencing system but must include at a minimum 'Book/Journal title, Author, Journal Name (if applicable), Volume (if applicable), Publisher, Year, reproduced with permission from SNCSC'.

4. STM Permission Guidelines

4. 1. An alternative scope of license may apply to signatories of the STM Permissions Guidelines ("STM PG") as amended from time to time and made available at https://www.stm-assoc.org/intellectual-property/permissions/permissions-guidelines/.

4. 2. For content reuse requests that qualify for permission under the STM PG, and which may be updated from time to time, the STM PG supersede the terms and conditions contained in this License.

4. 3. If a License has been granted under the STM PG, but the STM PG no longer apply at the time of publication, further permission must be sought from the Rightsholder. Contact journalpermissions@springernature.com or

bookpermissions@springernature.com for these rights.

5. Duration of License

5. 1. Unless otherwise indicated on your License, a License is valid from the date of purchase ("License Date") until the end of the relevant period in the below table:

Reuse in a medical communications project	Reuse up to distribution or time period indicated in License
Reuse in a dissertation/thesis	Lifetime of thesis
Reuse in a journal/magazine	Lifetime of journal/magazine
Reuse in a book/textbook	Lifetime of edition
Reuse on a website	1 year unless otherwise specified in the License
Reuse in a presentation/slide kit/poster	Lifetime of presentation/slide kit/poster. Note: publication whether electronic or in print of presentation/slide kit/poster may require further permission.
Reuse in conference proceedings	Lifetime of conference proceedings
Reuse in an annual report	Lifetime of annual report
Reuse in training/CME materials	Reuse up to distribution or time period indicated in License
Reuse in newsmedia	Lifetime of newsmedia
Reuse in coursepack/classroom materials	Reuse up to distribution and/or time period indicated in license

6. Acknowledgement

6. 1. The Licensor's permission must be acknowledged next to the Licensed Material in print. In electronic form, this acknowledgement must be visible at the same time as the figures/tables/illustrations or abstract and must be hyperlinked to the journal/book's homepage.

6. 2. Acknowledgement may be provided according to any standard referencing system and at a minimum should include "Author, Article/Book Title, Journal name/Book imprint, volume, page number, year, Springer Nature".

7. Reuse in a dissertation or thesis

7. 1. Where 'reuse in a dissertation/thesis' has been selected, the following terms apply: Print rights of the Version of Record are provided for; electronic rights for use only on institutional repository as defined by the Sherpa guideline (www.sherpa.ac.uk/romeo/) and only up to what is required by the awarding institution.

7. 2. For theses published under an ISBN or ISSN, separate permission is required. Please contact journalpermissions@springernature.com or bookpermissions@springernature.com for these rights.

7. 3. Authors must properly cite the published manuscript in their thesis according to current citation standards and include the following acknowledgement: '*Reproduced with permission from Springer Nature*'.

8. License Fee

You must pay the fee set forth in the License Agreement (the "License Fees"). All amounts payable by you under this License are exclusive of any sales, use, withholding, value added or similar taxes, government fees or levies or other assessments. Collection and/or remittance of such taxes to the relevant tax authority shall be the responsibility of the party who has the legal obligation to do so.

9. Warranty

9. 1. The Licensor warrants that it has, to the best of its knowledge, the rights to license reuse of the Licensed Material. **You are solely responsible for ensuring that the material you wish to license is original to the Licensor and does not carry the copyright of another entity or third party (as credited in the published version).** If the credit line on any part of the Licensed Material indicates that it was reprinted or adapted with permission from another source, then you should seek additional permission from that source to reuse the material.

9. 2. EXCEPT FOR THE EXPRESS WARRANTY STATED HEREIN AND TO THE EXTENT PERMITTED BY APPLICABLE LAW, LICENSOR PROVIDES THE LICENSED MATERIAL "AS IS" AND MAKES NO OTHER REPRESENTATION OR WARRANTY. LICENSOR EXPRESSLY DISCLAIMS ANY LIABILITY FOR ANY CLAIM ARISING FROM OR OUT OF THE CONTENT, INCLUDING BUT NOT LIMITED TO ANY ERRORS, INACCURACIES, OMISSIONS, OR DEFECTS CONTAINED THEREIN, AND ANY IMPLIED OR EXPRESS WARRANTY AS TO MERCHANTABILITY OR FITNESS FOR A PARTICULAR PURPOSE. IN NO EVENT SHALL LICENSOR BE LIABLE TO YOU OR ANY OTHER PARTY OR ANY OTHER PERSON OR FOR ANY SPECIAL, CONSEQUENTIAL, INCIDENTAL, INDIRECT, PUNITIVE, OR EXEMPLARY DAMAGES, HOWEVER CAUSED, ARISING OUT OF OR IN CONNECTION WITH THE DOWNLOADING, VIEWING OR USE OF THE LICENSED MATERIAL REGARDLESS OF THE FORM OF

ACTION, WHETHER FOR BREACH OF CONTRACT, BREACH OF WARRANTY, TORT, NEGLIGENCE, INFRINGEMENT OR OTHERWISE (INCLUDING, WITHOUT LIMITATION, DAMAGES BASED ON LOSS OF PROFITS, DATA, FILES, USE, BUSINESS OPPORTUNITY OR CLAIMS OF THIRD PARTIES), AND WHETHER OR NOT THE PARTY HAS BEEN ADVISED OF THE POSSIBILITY OF SUCH DAMAGES. THIS LIMITATION APPLIES NOTWITHSTANDING ANY FAILURE OF ESSENTIAL PURPOSE OF ANY LIMITED REMEDY PROVIDED HEREIN.

10. Termination and Cancellation

10. 1. The License and all rights granted hereunder will continue until the end of the applicable period shown in Clause 5.1 above. Thereafter, this license will be terminated and all rights granted hereunder will cease.

10. 2. Licensor reserves the right to terminate the License in the event that payment is not received in full or if you breach the terms of this License.

11. General

11. 1. The License and the rights and obligations of the parties hereto shall be construed, interpreted and determined in accordance with the laws of the Federal Republic of Germany without reference to the stipulations of the CISG (United Nations Convention on Contracts for the International Sale of Goods) or to Germany´s choice-of-law principle.

11. 2. The parties acknowledge and agree that any controversies and disputes arising out of this License shall be decided exclusively by the courts of or having jurisdiction for Heidelberg, Germany, as far as legally permissible.

11. 3. This License is solely for Licensor's and Licensee's benefit. It is not for the benefit of any other person or entity.

Questions? For questions on Copyright Clearance Center accounts or website issues please contact springernaturesupport@copyright.com or +1-855-239-3415 (toll free in the US) or +1-978-646-2777. For questions on Springer Nature licensing please visit https://www.springernature.com/gp/partners/rights-permissions-third-party-distribution

Other Conditions:

Version 1.4 - Dec 2022

Questions? customercare@copyright.com.

SPRINGER NATURE LICENSE
TERMS AND CONDITIONS

Apr 24, 2024

This Agreement between Mr. Amir Hosein Sadeghi Isfahani ("You") and Springer Nature ("Springer Nature") consists of your license details and the terms and conditions provided by Springer Nature and Copyright Clearance Center.

License Number	5775430988425
License date	Apr 24, 2024
Licensed Content Publisher	Springer Nature
Licensed Content Publication	Nature Reviews Genetics
Licensed Content Title	Chromosome organization in bacteria: mechanistic insights into genome structure and function
Licensed Content Author	Remus T. Dame et al
Licensed Content Date	Nov 25, 2019
Type of Use	Thesis/Dissertation
Requestor type	academic/university or research institute
Format	electronic

Portion	figures/tables/illustrations
Number of figures/tables/illustrations	2
Would you like a high resolution image with your order?	no
Will you be translating?	no
Circulation/distribution	1 - 29
Author of this Springer Nature content	no
Title of new work	Computational modeling of bacterial chromosome organization: macromolecular crowding, chain heterogeneity, and chain cross-linking
Institution name	Univeristy of Waterloo
Expected presentation date	Apr 2024
Portions	Figures 3 and 5
Requestor Location	Mr. Amir Hosein Sadeghi Isfahani University Ave. Waterloo, ON N2L 3G1 Canada Attn: University of Waterloo
Total	0.00 CAD

Terms and Conditions

Springer Nature Customer Service Centre GmbH Terms and Conditions

The following terms and conditions ("Terms and Conditions") together with the terms specified in your [RightsLink] constitute the License ("License") between you as Licensee and Springer Nature Customer Service Centre GmbH as Licensor. By clicking 'accept' and completing the transaction for your use of the material ("Licensed Material"), you confirm your acceptance of and obligation to be bound by these Terms and Conditions.

1. Grant and Scope of License

1. 1. The Licensor grants you a personal, non-exclusive, non-transferable, non-sublicensable, revocable, world-wide License to reproduce, distribute, communicate to the public, make available, broadcast, electronically transmit or create derivative works using the Licensed Material for the purpose(s) specified in your RightsLink Licence Details only. Licenses are granted for the specific use requested in the order and for no other use, subject to these Terms and Conditions. You acknowledge and agree that the rights granted to you under this License do not include the right to modify, edit, translate, include in collective works, or create derivative works of the Licensed Material in whole or in part unless expressly stated in your RightsLink Licence Details. You may use the Licensed Material only as permitted under this Agreement and will not reproduce, distribute, display, perform, or otherwise use or exploit any Licensed Material in any way, in whole or in part, except as expressly permitted by this License.

1. 2. You may only use the Licensed Content in the manner and to the extent permitted by these Terms and Conditions, by your RightsLink Licence Details and by any applicable laws.

1. 3. A separate license may be required for any additional use of the Licensed Material, e.g. where a license has been purchased for print use only, separate permission must be obtained for electronic re-use. Similarly, a License is only valid in the language selected and does not apply for editions in other languages unless additional translation rights have been granted separately in the License.

1. 4. Any content within the Licensed Material that is owned by third parties is expressly excluded from the License.

1. 5. Rights for additional reuses such as custom editions, computer/mobile applications, film or TV reuses and/or any other derivative rights requests require additional permission and may be subject to an additional fee. Please apply to journalpermissions@springernature.com or bookpermissions@springernature.com for these rights.

2. Reservation of Rights

Licensor reserves all rights not expressly granted to you under this License. You acknowledge and agree that nothing in this License limits or restricts Licensor's rights in or use of the Licensed Material in any way. Neither this License, nor any act, omission, or statement by Licensor or you, conveys any ownership right to you in any Licensed Material, or to any element or portion thereof. As between Licensor and you, Licensor owns and retains all right, title, and interest in and to the Licensed Material subject to the license granted in Section 1.1. Your permission to use the Licensed Material is expressly conditioned on you not impairing Licensor's or the applicable copyright owner's rights in the Licensed Material in any way.

3. Restrictions on use

3. 1. Minor editing privileges are allowed for adaptations for stylistic purposes or formatting purposes provided such alterations do not alter the original meaning or intention of the Licensed Material and the new figure(s) are still accurate and representative of the Licensed Material. Any other changes including but not limited to, cropping, adapting, and/or omitting material that affect the meaning, intention or moral rights of the author(s) are strictly prohibited.

3. 2. You must not use any Licensed Material as part of any design or trademark.

3. 3. Licensed Material may be used in Open Access Publications (OAP), but any such reuse must include a clear acknowledgment of this permission visible at the same time as the figures/tables/illustration or abstract and which must indicate that the Licensed Material is not part of the governing OA license but has been reproduced with permission. This may be indicated according to any standard referencing system but must include at a minimum 'Book/Journal title, Author, Journal Name (if applicable), Volume (if applicable), Publisher, Year, reproduced with permission from SNCSC'.

4. STM Permission Guidelines

4. 1. An alternative scope of license may apply to signatories of the STM Permissions Guidelines ("STM PG") as amended from time to time and made available at https://www.stm-assoc.org/intellectual-property/permissions/permissions-guidelines/.

4. 2. For content reuse requests that qualify for permission under the STM PG, and which may be updated from time to time, the STM PG supersede the terms and conditions contained in this License.

4. 3. If a License has been granted under the STM PG, but the STM PG no longer apply at the time of publication, further permission must be sought from the Rightsholder. Contact journalpermissions@springernature.com or

bookpermissions@springernature.com for these rights.

5. Duration of License

5. 1. Unless otherwise indicated on your License, a License is valid from the date of purchase ("License Date") until the end of the relevant period in the below table:

Reuse in a medical communications project	Reuse up to distribution or time period indicated in License
Reuse in a dissertation/thesis	Lifetime of thesis
Reuse in a journal/magazine	Lifetime of journal/magazine
Reuse in a book/textbook	Lifetime of edition
Reuse on a website	1 year unless otherwise specified in the License
Reuse in a presentation/slide kit/poster	Lifetime of presentation/slide kit/poster. Note: publication whether electronic or in print of presentation/slide kit/poster may require further permission.
Reuse in conference proceedings	Lifetime of conference proceedings
Reuse in an annual report	Lifetime of annual report
Reuse in training/CME materials	Reuse up to distribution or time period indicated in License
Reuse in newsmedia	Lifetime of newsmedia
Reuse in coursepack/classroom materials	Reuse up to distribution and/or time period indicated in license

6. Acknowledgement

6. 1. The Licensor's permission must be acknowledged next to the Licensed Material in print. In electronic form, this acknowledgement must be visible at the same time as the figures/tables/illustrations or abstract and must be hyperlinked to the journal/book's homepage.

6. 2. Acknowledgement may be provided according to any standard referencing system and at a minimum should include "Author, Article/Book Title, Journal name/Book imprint, volume, page number, year, Springer Nature".

7. Reuse in a dissertation or thesis

7. 1. Where 'reuse in a dissertation/thesis' has been selected, the following terms apply: Print rights of the Version of Record are provided for; electronic rights for use only on institutional repository as defined by the Sherpa guideline (www.sherpa.ac.uk/romeo/) and only up to what is required by the awarding institution.

7. 2. For theses published under an ISBN or ISSN, separate permission is required. Please contact journalpermissions@springernature.com or bookpermissions@springernature.com for these rights.

7. 3. Authors must properly cite the published manuscript in their thesis according to current citation standards and include the following acknowledgement: '*Reproduced with permission from Springer Nature*'.

8. License Fee

You must pay the fee set forth in the License Agreement (the "License Fees"). All amounts payable by you under this License are exclusive of any sales, use, withholding, value added or similar taxes, government fees or levies or other assessments. Collection and/or remittance of such taxes to the relevant tax authority shall be the responsibility of the party who has the legal obligation to do so.

9. Warranty

9. 1. The Licensor warrants that it has, to the best of its knowledge, the rights to license reuse of the Licensed Material. **You are solely responsible for ensuring that the material you wish to license is original to the Licensor and does not carry the copyright of another entity or third party (as credited in the published version).** If the credit line on any part of the Licensed Material indicates that it was reprinted or adapted with permission from another source, then you should seek additional permission from that source to reuse the material.

9. 2. EXCEPT FOR THE EXPRESS WARRANTY STATED HEREIN AND TO THE EXTENT PERMITTED BY APPLICABLE LAW, LICENSOR PROVIDES THE LICENSED MATERIAL "AS IS" AND MAKES NO OTHER REPRESENTATION OR WARRANTY. LICENSOR EXPRESSLY DISCLAIMS ANY LIABILITY FOR ANY CLAIM ARISING FROM OR OUT OF THE CONTENT, INCLUDING BUT NOT LIMITED TO ANY ERRORS, INACCURACIES, OMISSIONS, OR DEFECTS CONTAINED THEREIN, AND ANY IMPLIED OR EXPRESS WARRANTY AS TO MERCHANTABILITY OR FITNESS FOR A PARTICULAR PURPOSE. IN NO EVENT SHALL LICENSOR BE LIABLE TO YOU OR ANY OTHER PARTY OR ANY OTHER PERSON OR FOR ANY SPECIAL, CONSEQUENTIAL, INCIDENTAL, INDIRECT, PUNITIVE, OR EXEMPLARY DAMAGES, HOWEVER CAUSED, ARISING OUT OF OR IN CONNECTION WITH THE DOWNLOADING, VIEWING OR USE OF THE LICENSED MATERIAL REGARDLESS OF THE FORM OF

ACTION, WHETHER FOR BREACH OF CONTRACT, BREACH OF WARRANTY, TORT, NEGLIGENCE, INFRINGEMENT OR OTHERWISE (INCLUDING, WITHOUT LIMITATION, DAMAGES BASED ON LOSS OF PROFITS, DATA, FILES, USE, BUSINESS OPPORTUNITY OR CLAIMS OF THIRD PARTIES), AND WHETHER OR NOT THE PARTY HAS BEEN ADVISED OF THE POSSIBILITY OF SUCH DAMAGES. THIS LIMITATION APPLIES NOTWITHSTANDING ANY FAILURE OF ESSENTIAL PURPOSE OF ANY LIMITED REMEDY PROVIDED HEREIN.

10. Termination and Cancellation

10. 1. The License and all rights granted hereunder will continue until the end of the applicable period shown in Clause 5.1 above. Thereafter, this license will be terminated and all rights granted hereunder will cease.

10. 2. Licensor reserves the right to terminate the License in the event that payment is not received in full or if you breach the terms of this License.

11. General

11. 1. The License and the rights and obligations of the parties hereto shall be construed, interpreted and determined in accordance with the laws of the Federal Republic of Germany without reference to the stipulations of the CISG (United Nations Convention on Contracts for the International Sale of Goods) or to Germany´s choice-of-law principle.

11. 2. The parties acknowledge and agree that any controversies and disputes arising out of this License shall be decided exclusively by the courts of or having jurisdiction for Heidelberg, Germany, as far as legally permissible.

11. 3. This License is solely for Licensor's and Licensee's benefit. It is not for the benefit of any other person or entity.

Questions? For questions on Copyright Clearance Center accounts or website issues please contact springernaturesupport@copyright.com or +1-855-239-3415 (toll free in the US) or +1-978-646-2777. For questions on Springer Nature licensing please visit https://www.springernature.com/gp/partners/rights-permissions-third-party-distribution

Other Conditions:

Version 1.4 - Dec 2022

Questions? customercare@copyright.com.

RightsLink

SPRINGER NATURE

Bacterial partition complexes segregate within the volume of the nucleoid

Author: Antoine Le Gall et al
Publication: Nature Communications
Publisher: Springer Nature
Date: Jul 5, 2016

Copyright © 2016, The Author(s)

Creative Commons

This is an open access article distributed under the terms of the Creative Commons CC BY license, which permits unrestricted use, distribution, and reproduction in any medium, provided the original work is properly cited.

You are not required to obtain permission to reuse this article.
To request permission for a type of use not listed, please contact Springer Nature

© 2024 Copyright - All Rights Reserved | Copyright Clearance Center, Inc. | Privacy statement | Data Security and Privacy | For California Residents | Terms and ConditionsComments? We would like to hear from you. E-mail us at customercare@copyright.com

Bibliography

[1] J. D. WATSON and F. H. C. CRICK. “Molecular Structure of Nucleic Acids: A Structure for Deoxyribose Nucleic Acid”. In: *Nature* 171.4356 (1953), pp. 737–738. doi: 10.1038/171737a0 (cit. on p. 1).

[2] O. Gordon Stonington and David E. Pettijohn. “The Folded Genome of Escherichia coli Isolated in a Protein-DNA-RNA Complex”. In: *Proceedings of the National Academy of Sciences* 68.1 (1971), pp. 6–9. issn: 0027-8424. doi: 10.1073/pnas.68.1.6 (cit. on pp. 2, 15, 19).

[3] A. Worcel and E. Burgi. “On the structure of the folded chromosome of Escherichia coli”. In: *Journal of Molecular Biology* 71.2 (1972), pp. 127 –147. issn: 0022-2836. doi: https://doi.org/10.1016/0022-2836(72)90342-7 (cit. on pp. 2, 15, 19).

[4] James D. Jamieson. *Escherichia coli*. 2012. doi: https://doi.org/doi:10.7295/W9CIL37254 (cit. on p. 2).

[5] Andrew D. Bates and Maxwell Anthony. *DNA topology*. eng. 2nd ed. Oxford ; Oxford University Press, 14 April 2005. isbn: 9780198506553. url: https://global.oup.com/booksites/content/0198506554/ (cit. on pp. 1–3, 11–14, 37, 61, 86, 145).

[6] Ivana Jerkovic´ and Giacomo Cavalli. “Understanding 3D genome organization by multidisciplinary methods”. In: *Nature Reviews Molecular Cell Biology* 22.8 (2021), pp. 511–528. doi: 10.1038/s41580-021-00362-w (cit. on p. 1).

[7] Ivan V. Surovtsev and Christine Jacobs-Wagner. “Subcellular Organization: A Critical Feature of Bacterial Cell Replication”. In: *Cell* 172.6 (2018), pp. 1271–1293. doi: 10.1016/j.cell.2018.01.014 (cit. on p. 1).

[8] Remus Thei Dame Marco Cosentino Lagomarsino Marco Gherardi Vittore Scolari. “Modeling the 3D Conformation of Genomes”. In: ed. by G. Tiana and L. Giorgetti. Computational Biophysics 9. CRC Press, Taylor & Francis Group, 2019. Chap. Chromosome Structure and Dynamics in Bacteria: Theory and Experiments. isbn: 9781315144009. doi: https://www.taylorfrancis.com/books/edit/10.1201/9781315144009/modeling-3d-conformation-genomes-guido-tiana-luca-giorgetti (cit. on pp. 1–3, 16).

[9] Naomichi Takemata and Stephen D. Bell. “Emerging views of genome organization in Archaea”. In: *Journal of Cell Science* 133.10 (May 2020), jcs243782. issn: 0021-9533. doi: 10.1242/jcs.243782 (cit. on p. 1).

[10] Subhash C. Verma, Zhong Qian, and Sankar L. Adhya. “Architecture of the Escherichia coli nucleoid”. In: *PLOS Genetics* 15.12 (Dec. 2019), pp. 1–35. doi: 10.1371/journal.pgen.1008456 (cit. on pp. 1, 3, 12–14, 16–19, 55, 85–87, 100, 101).

[11] Handuo Shi and Kerwyn Casey Huang. “Chromosome Organization: Making Room in a Crowd”. In: *Current Biology* 29.13 (2019), R630–R632. issn: 0960-9822. doi: https://doi.org/10.1016/j.cub.2019.06.002 (cit. on pp. 1, 3, 19, 55).

[12] Vittore F. Scolari, Bianca Sclavi, and Marco Cosentino Lagomarsino. “The nucleoid as a smart polymer”. In: *Frontiers in Microbiology* 6 (2015). issn: 1664-302X. doi: 10.3389/fmicb.2015.00424 (cit. on pp. 1, 2).

[13] Rob Phillips, Jane Kondev, and Julie Theriot. “Physical biology of the cell”. In: 2nd ed. New York: Garland Science New York, 2012. Chap. 2, pp. 66–117. isbn: 9780429168833. doi: https://doi.org/10.1201/9781134111589 (cit. on pp. 2, 7, 8).

[14] Frederick R. Blattner et al. “The Complete Genome Sequence of Escherichia coli K-12”. In: *Science* 277.5331 (1997), pp. 1453–1462. issn: 0036-8075. doi: 10.1126/science.277.5331.1453 (cit. on p. 2).

[15] Conrad L. Woldringh and Theo Odijk. “Structure of DNA within the Bacterial Cell: Physics and Physiology”. In: *Organization of the Prokaryotic Genome*. Ed. by Robert L. Charlebois. American Society of Microbiology, 1999, pp. 171–187. doi: 10.1128/9781555818180.ch10BuythisChapterDigital(?)$15.00 (cit. on pp. 2, 8, 15).

[16] CONRAD L Woldringh and NANNE Nanninga. “Structure of nucleoid and cytoplasm in the intact cell”. In: *Molecular Cytology of Escherichia coli*. Ed. by NANNE Nanninga. Academic Press, 1989, pp. 161–197 (cit. on p. 2).

[17] Alexander Vologodskii. “DNA–protein interaction”. In: *Biophysics of DNA*. Cambridge University Press, 2015. Chap. 5, pp. 165–183. doi: 10.1017/CBO9781139542371.006 (cit. on p. 3).

[18] Alexander Vologodskii. “Circular DNA”. In: *Biophysics of DNA*. Cambridge University Press, 2015. Chap. 6, pp. 184–250. doi: 10.1017/CBO9781139542371.007 (cit. on pp. 3, 12, 13).

[19] Joel Stavans and Amos Oppenheim. “DNA-protein interactions and bacterial chromosome architecture”. In: *Physical Biology* 3.4 (2006), R1. url: http://stacks.iop.org/1478-3975/3/i=4/a=R01 (cit. on pp. 3, 57, 85, 86).

[20] T. Christian Boles, James H. White, and Nicholas R. Cozzarelli. “Structure of plectonemically supercoiled DNA”. In: *Journal of Molecular Biology* 213.4 (1990), pp. 931 –951. issn: 0022-2836. doi: https://doi.org/10.1016/S0022-2836(05)80272-4 (cit. on pp. 3, 14, 36, 108, 109).

[21] Remus T. Dame, Fatema-Zahra M. Rashid, and David C. Grainger. “Chromosome organization in bacteria: mechanistic insights into genome structure and function”. In: *Nature Reviews Genetics* 21.4 (2020), pp. 227–242. doi: 10.1038/s41576-019-0185-4 (cit. on pp. 3, 12, 13, 16–18, 55).

[22] Virginia S. Lioy, Ivan Junier, and Frédéric Boccard. “Multiscale Dynamic Structuring of Bacterial Chromosomes”. In: *Annual Review of Microbiology* 75.1 (2021). PMID: 34343019, pp. 541–561. doi: 10.1146/annurev-micro-033021-113232 (cit. on pp. 3, 12, 16–19, 38, 55).

[23] Tatyana Romantsov, Itzhak Fishov, and Oleg Krichevsky. “Internal Structure and Dynamics of Isolated Escherichia coli Nucleoids Assessed by Fluorescence Correlation Spectroscopy”. In: *Biophysical Journal* 92.8 (2007), pp. 2875 – 2884. issn: 0006-3495. doi: https://doi.org/10.1529/biophysj.106.095729 (cit. on pp. 3, 15, 16, 61).

[24] Renko de Vries. “DNA condensation in bacteria: Interplay between macromolecular crowding and nucleoid proteins”. In: *Biochimie* 92.12 (Dec. 2010), pp. 1715–1721. issn: 0300-9084. doi: 10.1016/j.biochi.2010.06.024 (cit. on pp. 3, 37, 58, 85, 86).

[25] Scott Cayley et al. “Characterization of the cytoplasm of Escherichia coli K-12 as a function of external osmolarity: Implications for protein-DNA interactions in vivo”. In: *Journal of Molecular Biology* 222.2 (1991), pp. 281–300. issn: 0022-2836. doi: https://doi.org/10.1016/0022-2836(91)90212-O (cit. on pp. 3, 35, 57).

[26] Steven B. Zimmerman and Stefan O. Trach. “Estimation of macromolecule concentrations and excluded volume effects for the cytoplasm of Escherichia coli”. In: *Journal of Molecular Biology* 222.3 (1991), pp. 599–620. doi: 10.1016/0022-2836(91)90499-V (cit. on pp. 3, 35, 57).

[27] R. John Ellis and Allen P. Minton. “Join the crowd”. In: *Nature* 425.6953 (2003), pp. 27–28. doi: 10.1038/425027a (cit. on pp. 3, 35, 57, 85).

[28] Huan-Xiang Zhou, Germán Rivas, and Allen P. Minton. “Macromolecular Crowding and Confinement: Biochemical, Biophysical, and Potential Physiological Consequences”. In: *Annual Review of Biophysics* 37.1 (2008). PMID: 18573087, pp. 375–397. doi: 10.1146/annurev.biophys.37.032807.125817 (cit. on pp. 3, 5, 7–9, 35, 57, 102).

[29] Francois-Xavier Theillet et al. “Physicochemical Properties of Cells and Their Effects on Intrinsically Disordered Proteins (IDPs)”. In: *Chemical Reviews* 114.13 (July 2014), pp. 6661–6714. doi: 10.1021/cr400695p (cit. on pp. 3, 35, 57).

[30] Shruti Mittal, Rimpy Kaur Chowhan, and Laishram Rajendrakumar Singh. “Macromolecular crowding: Macromolecules friend or foe”. In: *Biochimica et Biophysica Acta (BBA) - General Subjects* 1850.9 (2015), pp. 1822–1831. issn: 0304-4165. doi: https://doi.org/10.1016/j.bbagen.2015.05.002 (cit. on pp. 3, 35, 57).

[31] Alice B. Fulton. “How crowded is the cytoplasm?” In: *Cell* 30.2 (1982), pp. 345–347. issn: 0092-8674. doi: https://doi.org/10.1016/0092-8674(82)90231-8 (cit. on pp. 3, 35, 57).

[32] Steven B. Zimmerman and Lizabeth D. Murphy. “Macromolecular crowding and the mandatory condensation of DNA in bacteria”. In: *FEBS Letters* 390.3 (1996), pp. 245–248. doi: https://doi.org/10.1016/0014-5793(96)00725-9 (cit. on p. 3).

[33] Theo Odijk. “Osmotic compaction of supercoiled DNA into a bacterial nucleoid”. In: *Biophysical Chemistry* 73.1 (1998), pp. 23 –29. issn: 0301-4622. doi: https://doi.org/10.1016/S0301-4622(98)00115-X (cit. on pp. 3, 37).

[34] Sónia Cunha, Conrad L Woldringh, and Theo Odijk. “Polymer-Mediated Compaction and Internal Dynamics of Isolated Escherichia coli Nucleoids”. In: *Journal of Structural Biology* 136.1 (2001), pp. 53 –66. issn: 1047-8477. doi: https://doi.org/10.1006/jsbi.2001.4420 (cit. on pp. 3, 57, 58, 81).

[35] James Pelletier et al. “Physical manipulation of the Escherichia coli chromosome reveals its soft nature”. In: *Proceedings of the National Academy of Sciences* 109.40 (2012), E2649–E2656. doi: 10.1073/pnas.1208689109 (cit. on pp. 3, 15, 35, 38, 39, 42, 43, 46, 47, 54, 55, 57, 58, 61, 64, 81, 84–86).

[36] Juin Kim et al. “A polymer in a crowded and confined space: effects of crowder size and poly-dispersity”. In: *Soft Matter* 11.10 (2015), pp. 1877–1888. issn: 1744-683X. doi: 10.1039/C4SM02198C (cit. on pp. 3, 35–40, 42, 43, 45–47, 54, 57, 65, 70, 81, 86, 88, 89).

[37] Fabai Wu et al. “Cell Boundary Confinement Sets the Size and Position of the E. coli Chromosome”. In: *Current Biology* 29.13 (2019), 2131–2144.e4. doi: https://doi.org/10.1016/j.cub.2019.05.015 (cit. on pp. 3, 19, 37).

[38] W. T. Gray et al. “Nucleoid Size Scaling and Intracellular Organization of Translation across Bacteria”. In: *Cell* 177.6 (2019), 1632–1648.e20. doi: 10.1016/j.cell.2019.05.017 (cit. on pp. 3, 36, 55).

[39] Davide Marenduzzo, Kieran Finan, and Peter R. Cook. “The depletion attraction: an underappreciated force driving cellular organization ”. In: *Journal of Cell Biology* 175.5 (Dec. 2006), pp. 681–686. issn: 0021-9525. doi: 10.1083/jcb.200609066 (cit. on pp. 3, 35, 54, 85–87, 102, 103).

[40] Youngkyun Jung and Bae-Yeun Ha. “Collapse transition of a heterogeneous polymer in a crowded medium”. In: 155.5 (2021), p. 054902. doi: 10.1063/5.0056446 (cit. on pp. 3, 35, 37, 54, 57, 59, 60, 83, 85–87, 102).

[41] R.John Ellis. “Macromolecular crowding: obvious but underappreciated”. In: *Trends in Biochemical Sciences* 26.10 (2001), pp. 597–604. issn: 0968-0004. doi: 10.1016/S0968-0004(01)01938-7 (cit. on pp. 3, 7, 35, 57).

[42] Allen P. Minton. “Excluded volume as a determinant of macromolecular structure and reactivity”. In: *Biopolymers* 20.10 (1981), pp. 2093–2120. doi: https://doi.org/10.1002/bip.1981.360201006 (cit. on pp. 5, 26).

[43] A. P. Minton and J. Wilf. “Effect of macromolecular crowding upon the structure and function of an enzyme: glyceraldehyde-3-phosphate dehydrogenase”. In: *Biochemistry* 20.17 (Aug. 1981), pp. 4821–4826. doi: 10.1021/bi00520a003 (cit. on pp. 5, 26).

[44] Dimitrios Tsiapalis and Dimitrios I. Zeugolis. “It is time to crowd your cell culture media – Physicochemical considerations with biological consequences”. In: *Biomaterials* 275 (2021), p. 120943. issn: 0142-9612. doi: https://doi.org/10.1016/j.biomaterials.2021.120943 (cit. on p. 5).

[45] Shannon L. Speer et al. “Macromolecular Crowding Is More than Hard-Core Repulsions”. In: *Annual Review of Biophysics* 51.1 (2022). PMID: 35239418, pp. 267–300. doi: 10.1146/annurev-biophys-091321-071829 (cit. on pp. 5, 21).

[46] Arohan R. Subramanya and Cary R. Boyd-Shiwarski. “Molecular Crowding: Physiologic Sensing and Control”. In: *Annual Review of Physiology* 86.1 (2023). PMID: 37931170, null. doi: 10.1146/annurev-physiol-042222-025920 (cit. on pp. 5, 10).

[47] Liel Sapir and Daniel Harries. “Wisdom of the Crowd”. In: *Bunsen-Magazin* 19 (July 2017), pp. 152–162. doi: https://doi.org/10.26125/dw2b-m249 (cit. on pp. 5, 9, 10, 22).

[48] Germán Rivas and Allen P. Minton. “Toward an understanding of biochemical equilibria within living cells”. In: *Biophysical Reviews* 10.2 (2018), pp. 241–253. doi: https://doi.org/10.1007/s12551-017-0347-6 (cit. on pp. 5, 7, 8, 10, 21, 22, 57, 145).

[49] Germán Rivas and Allen P. Minton. “Influence of Nonspecific Interactions on Protein Associations: Implications for Biochemistry In Vivo”. In: *Annual Review of Biochemistry* 91.1 (2022). PMID: 35287477, pp. 321–351. doi: 10.1146/annurev-biochem-040320-104151 (cit. on pp. 5, 7–10, 21, 35, 57).

[50] A. D. Jenkins et al. “Glossary of basic terms in polymer science (IUPAC Recommendations 1996)”. In: Pure and Applied Chemistry 68.12 (1996), pp. 2287–2311. doi: https://doi.org/10.1351/pac199668122287 (cit. on p. 6).

[51] D. L. Ollis, C. Kline, and T. A. Steitz. “Domain of E. coli DNA polymerase I showing sequence homology to T7 DNA polymerase”. In: *Nature* 313.6005 (1985), pp. 818–819. doi: https://doi.org/10.1038/313818a0 (cit. on p. 7).

[52] Richard H. Ebright. “RNA Polymerase: Structural Similarities Between Bacterial RNA Polymerase and Eukaryotic RNA Polymerase II”. In: *Journal of Molecular Biology* 304.5 (2000), pp. 687–698. issn: 0022-2836. doi: https://doi.org/10.1006/jmbi.2000.4309 (cit. on pp. 7, 8).

[53] Sergey Melnikov et al. “One core, two shells: bacterial and eukaryotic ribosomes”. In: *Nature Structural & Molecular Biology* 19.6 (2012), pp. 560–567. doi: 10.1038/nsmb.2313 (cit. on pp. 7, 8, 38, 39).

[54] Ricardo Cabrera et al. “The Crystal Complex of Phosphofructokinase-2 of Escherichia coli with Fructose-6-phosphate: KINETIC AND STRUCTURAL ANALYSIS OF THE ALLOSTERIC ATP INHIBITION”. In: *Journal of Biological Chemistry* 286.7 (2011), pp. 5774–5783. doi: 10.1074/jbc.M110.163162 (cit. on p. 7).

[55] Benjamin P. Bowen and Trent R. Northen. “Dealing with the unknown: Metabolomics and Metabolite Atlases”. In: *Journal of The American Society for Mass Spectrometry* 21.9 (2010), pp. 1471–1476. doi: 10.1016/j.jasms.2010.04.003 (cit. on p. 7).

[56] F J Trueba and C L Woldringh. “Changes in cell diameter during the division cycle of Escherichia coli.” In: *Journal of Bacteriology* 142.3 (1980), pp. 869–878. issn: 0021-9193. eprint: https://jb.asm.org/content/142/3/869.full.pdf (cit. on pp. 7, 37).

[57] J A Valkenburg and C L Woldringh. “Phase separation between nucleoid and cytoplasm in Escherichia coli as defined by immersive refractometry.” In: *Journal of Bacteriology* 160.3 (1984), pp. 1151–1157. eprint: http://jb.asm.org/content/160/3/1151.full.pdf+html (cit. on pp. 7, 37).

[58] David S. Goodsell. “Escherichia coli”. In: *Biochemistry and Molecular Biology Education* 37.6 (2009), pp. 325–332. doi: https://doi.org/10.1002/bmb.20345 (cit. on pp. 7, 38).

[59] Frederick C Neidhardt. “Chemical composition of Escherichia coli”. In: *Escherichia coli and Salmonella: cellular and molecular biology*. Ed. by Ingraham J L Lin E C C Low K B Magasanik B Reznikoff W S Riley M Schaechter M Umbarger H E Neidhardt F C Curtiss III R. ASM press, 1996. Chap. 3, pp. 13–16 (cit. on p. 8).

[60] John L. Finney. “The water molecule and its interactions: the interaction between theory, modelling, and experiment”. In: *Journal of Molecular Liquids* 90.1 (2001), pp. 303–312. issn: 0167-7322. doi: https://doi.org/10.1016/S0167-7322(01)00134-9 (cit. on pp. 6, 8).

[61] Youxue Zhang and Zhengjiu Xu. “Atomic radii of noble gas elements in condensed phases”. In: *American Mineralogist* 80.7-8 (Aug. 1995), pp. 670–675. issn: 0003-004X. doi: 10.2138/am-1995-7-803 (cit. on pp. 6, 8).

[62] C. B. Ching, K. Hidajat, and M. S. Uddin. “Evaluation of Equilibrium and Kinetic Parameters of Smaller Molecular Size Amino Acids on KX Zeolite Crystals via Liquid Chromatographic Techniques”. In: *Separation Science and Technology* 24.7-8 (June 1989), pp. 581–597. doi: 10.1080/01496398908049793 (cit. on pp. 8, 38, 39).

[63] Bryson D Bennett et al. “Absolute metabolite concentrations and implied enzyme active site occupancy in Escherichia coli”. In: *Nature Chemical Biology* 5.8 (2009), pp. 593–599. doi: 10.1038/nchembio.186 (cit. on p. 8).

[64] The UniProt Consortium. “UniProt: the Universal Protein Knowledgebase in 2023”. In: *Nucleic Acids Research* 51.D1 (Nov. 2022), pp. D523–D531. issn: 0305-1048. doi: 10.1093/nar/gkac1052 (cit. on pp. 6, 8).

[65] Ding Jun Jin, Cedric Cagliero, and Yan Ning Zhou. “Role of RNA Polymerase and Transcription in the Organization of the Bacterial Nucleoid”. In: *Chemical Reviews* 113.11 (Nov. 2013), pp. 8662–8682. doi: 10.1021/cr4001429 (cit. on pp. 8, 36, 37, 54, 57, 59, 60, 83, 102, 107).

[66] Kim Ji Hyun Hwang Shin Yoo Hyun Ju Kim Su Jung Kim Su Hee. “Understanding Metabolomics in Biomedical Research”. In: *enm* 31.1 (2016), pp. 7–16. doi: 10.3803/EnM.2016.31.1.7 (cit. on p. 8).

[67] Jianzhi Zhang. “Protein-length distributions for the three domains of life”. In: *Trends in Genetics* 16.3 (2000), pp. 107–109. doi: 10.1016/s0168-9525(99)01922-8 (cit. on pp. 6, 8, 61, 86, 89, 108, 109).

[68] Ken A. Dill, Kingshuk Ghosh, and Jeremy D. Schmit. “Physical limits of cells and proteomes”. In: *Proceedings of the National Academy of Sciences* 108.44 (2011), pp. 17876–17882. doi: 10.1073/pnas.1114477108 (cit. on pp. 6, 8, 38, 39, 61, 86, 89, 108, 109).

[69] S B Zimmerman and A P Minton. “Macromolecular Crowding: Biochemical, Biophysical, and Physiological Consequences”. In: *Annual Review of Biophysics and Biomolecular Structure* 22.1 (1993). PMID: 7688609, pp. 27–65. doi: 10.1146/annurev.bb.22.060193.000331 (cit. on pp. 6, 7, 10, 35, 38, 57, 103).

[70] Jacob N. Israelachvili. *Intermolecular and Surface Forces*. Third Edition. San Diego: Academic Press, 2011. isbn: 978-0-12-391927-4. doi: https://doi.org/10.1016/C2011-0-05119-0 (cit. on pp. 6–9).

[71] Ken A. Dill and Sarina Bromberg. *Molecular driving forces: statistical thermodynamics in biology, chemistry, physics, and nanoscience*. 2nd ed. London: Garland Science New York, 2010. Chap. xx, 756 pages : illustrations ; 28 cm. isbn: 9780203809075. doi: https://doi.org/10.4324/9780203809075 (cit. on p. 6).

[72] Rob Phillips, Jane Kondev, and Julie Theriot. *Physical biology of the cell*. 2nd ed. New York: Garland Science New York, 2012. isbn: 9780429168833. doi: https://doi.org/10.1201/9781134111589 (cit. on pp. 6, 86).

[73] Kim A. Sharp. “Unpacking the origins of in-cell crowding”. In: *Proceedings of the National Academy of Sciences* 113.7 (2016), pp. 1684–1685. doi: 10.1073/pnas.1600098113 (cit. on pp. 7, 35, 57).

[74] Allen P. Minton. “The Influence of Macromolecular Crowding and Macromolecular Confinement on Biochemical Reactions in Physiological Media”. In: *Journal of Biological Chemistry* 276.14 (Apr. 2001), pp. 10577–10580. doi: 10.1074/jbc.R100005200 (cit. on pp. 7, 8, 35, 57).

[75] Peter R. Cook. “Predicting three-dimensional genome structure from transcriptional activity”. In: *Nature Genetics* 32.3 (2002), pp. 347–352. doi: 10.1038/ng1102-347 (cit. on pp. 8, 57, 59, 60, 84, 107).

[76] Mohona Sarkar, Conggang Li, and Gary J. Pielak. “Soft interactions and crowding”. In: *Biophysical Reviews* 5.2 (2013), pp. 187–194. doi: 10.1007/s12551-013-0104-4 (cit. on p. 9).

[77] Benjamin Widom. “Statistical mechanics: a concise introduction for chemists”. In: Cambridge University Press, 2002. Chap. 6, pp. 81–100. isbn: 9780521811194. url: https://www.cambridge.org/ca/universitypress/subjects/chemistry/physical-chemistry/statistical-mechanics-concise-introduction-chemists?format=HB&isbn=9780521811194 (cit. on p. 9).

[78] Liel Sapir and Daniel Harries. “Is the depletion force entropic? Molecular crowding beyond steric interactions”. In: *Current Opinion in Colloid & Interface Science* 20.1 (2015), pp. 3–10. issn: 1359-0294. doi: https://doi.org/10.1016/j.cocis.2014.12.003 (cit. on pp. 9, 22).

[79] Allen P. Minton. “Quantitative assessment of the relative contributions of steric repulsion and chemical interactions to macromolecular crowding”. In: *Biopolymers* 99.4 (2013), pp. 239–244. doi: https://doi.org/10.1002/bip.22163 (cit. on p. 9).

[80] Liel Sapir and Daniel Harries. “Macromolecular compaction by mixed solutions: Bridging versus depletion attraction”. In: *Current Opinion in Colloid Interface Science* 22 (2016), pp. 80–87. issn: 1359-0294. doi: https://doi.org/10.1016/j.cocis.2016.02.010 (cit. on pp. 10, 22).

[81] Drishti Guin and Martin Gruebele. “Weak Chemical Interactions That Drive Protein Evolution: Crowding, Sticking, and Quinary Structure in Folding and Function”. In: *Chemical Reviews* 119.18 (Sept. 2019), pp. 10691–10717. doi: 10.1021/acs.chemrev.8b00753 (cit. on p. 10).

[82] Michael Feig et al. “Complete atomistic model of a bacterial cytoplasm for integrating physics, biochemistry, and systems biology”. In: *Journal of Molecular Graphics and Modelling* 58 (2015), pp. 1–9. issn: 1093-3263. doi: https://doi.org/10.1016/j.jmgm.2015.02.004 (cit. on p. 10).

[83] Isseki Yu et al. “Biomolecular interactions modulate macromolecular structure and dynamics in atomistic model of a bacterial cytoplasm”. In: *eLife* 5.NOVEMBER2016 (2016). Cited by: 206; All Open Access, Gold Open Access, Green Open Access. doi: 10.7554/eLife.19274 (cit. on p. 10).

[84] Graham T. Johnson et al. “Building the next generation of virtual cells to understand cellular biology”. In: *Biophysical Journal* 122.18 (2023), pp. 3560–3569. doi: 10.1016/j.bpj.2023.04.006 (cit. on p. 10).

[85] Syma Khalid et al. “Computational microbiology of bacteria: Advancements in molecular dynamics simulations”. In: *Structure* 31.11 (2023), pp. 1320–1327. doi: 10.1016/j.str.2023.09.012 (cit. on p. 10).

[86] Jan A. Stevens et al. “Molecular dynamics simulation of an entire cell”. In: *Frontiers in Chemistry* 11 (2023). issn: 2296-2646. doi: 10.3389/fchem.2023.1106495 (cit. on p. 10).

[87] Fabio Trovato and Giordano Fumagalli. “Molecular simulations of cellular processes”. In: *Biophysical Reviews* 9.6 (2017), pp. 941–958. doi: 10.1007/s12551-017-0363-6 (cit. on p. 10).

[88] Natalia Ostrowska, Michael Feig, and Joanna Trylska. “Modeling Crowded Environment in Molecular Simulations”. In: *Frontiers in Molecular Biosciences* 6 (2019). issn: 2296-889X. doi: 10.3389/fmolb.2019.00086 (cit. on p. 10).

[89] Paulette Sofia Romero-Perez et al. “When Phased without Water: Biophysics of Cellular Desiccation, from Biomolecules to Condensates”. In: *Chemical Reviews* 123.14 (July 2023), pp. 9010–9035. doi: 10.1021/acs.chemrev.2c00659 (cit. on p. 10).

[90] Wayne G. Lilyestrom et al. “Monoclonal Antibody Self-Association, Cluster Formation, and Rheology at High Concentrations”. In: *The Journal of Physical Chemistry B* 117.21 (May 2013), pp. 6373–6384. doi: 10.1021/jp4008152 (cit. on p. 11).

[91] Alexander Vologodskii. “DNA structures”. In: *Biophysics of DNA*. Cambridge University Press, 2015. Chap. 1, pp. 1–22. doi: 10.1017/CBO9781139542371.002 (cit. on p. 11).

[92] Christopher A. Hunter. “Sequence-dependent DNA Structure: The Role of Base Stacking Interactions”. In: *Journal of Molecular Biology* 230.3 (1993), pp. 1025–1054. issn: 0022-2836. doi: https://doi.org/10.1006/jmbi.1993.1217 (cit. on p. 12).

[93] Richard Wing et al. “Crystal structure analysis of a complete turn of B-DNA”. In: *Nature* 287.5784 (1980), pp. 755–758. doi: 10.1038/287755a0 (cit. on pp. 12, 61, 86).

[94] William R. Bauer. “STRUCTURE AND REACTIONS OF CLOSED DUPLEX DNA”. In: *Annual Review of Biophysics and Bioengineering* 7.1 (1978), pp. 287–313. doi: 10.1146/annurev.bb.07.060178.001443 (cit. on p. 12).

[95] John A. Schellman and Dirk Stigter. “Electrical double layer, zeta potential, and electrophoretic charge of double-stranded DNA”. In: *Biopolymers* 16.7 (1977), pp. 1415–1434. doi: https://doi.org/10.1002/bip.1977.360160704 (cit. on pp. 12, 37).

[96] Dirk Stigter. “Interactions of highly charged colloidal cylinders with applications to double-stranded DNA”. In: *Biopolymers* 16.7 (1977), pp. 1435–1448. doi: https://doi.org/10.1002/bip.1977.360160705 (cit. on pp. 12, 36, 37, 54).

[97] Rebecca; Johnson Alexanderl; Morgan David; Raff Martin; Roberts Keith; Walter Peter Alberts Bruce; Heald. “Molecular biology of the cell”. In: 7th ed. W.W. Norton & Company, 2022. Chap. 4. url: https://wwnorton.com/books/9780393884821/about-the-book/product-details (cit. on p. 12).

[98] V.R. Chechetkin. “Statistics of genome architecture”. In: *Physics Letters A* 377.45 (2013), pp. 3312–3316. issn: 0375-9601. doi: https://doi.org/10.1016/j.physleta.2013.10.021 (cit. on p. 12).

[99] Miriam Land et al. “Insights from 20 years of bacterial genome sequencing”. In: *Functional & Integrative Genomics* 15.2 (2015), pp. 141–161. doi: 10.1007/s10142-015-0433-4 (cit. on p. 12).

[100] T.-S. Hsieh. “DNA Supercoiling”. In: *Encyclopedia of Biological Chemistry (Second Edition)*. Ed. by William J. Lennarz and M. Daniel Lane. Second Edition. Waltham: Academic Press, 2013, pp. 154–156. isbn: 978-0-12-378631-9. doi: https://doi.org/10.1016/B978-0-12-378630-2.00244-9 (cit. on p. 14).

[101] Lisa Postow et al. “Topological domain structure of the Escherichia coli chromosome”. In: *Genes & Development* 18.14 (2004), pp. 1766–1779. doi: 10.1101/gad.1207504 (cit. on pp. 14–16).

[102] A Griswold. “Genome Packaging in Prokaryotes: the Circular Chromosome of E. coli”. In: *Nature Education* 1.1 (2008), p. 57. url: https://www.nature.com/scitable/topicpage/genome-packaging-in-prokaryotes-the-circular-chromosome-9113/# (cit. on pp. 15, 113).

[103] Ruth Kavenoff and Brian C. Bowen. “Electron microscopy of membrane-free folded chromosomes from Escherichia coli”. In: *Chromosoma* 59.2 (1976), pp. 89–101. doi: 10.1007/BF00328479 (cit. on pp. 15, 113).

[104] Ruth Kavenoff and Oliver A. Ryder. “Electron microscopy of membrane-associated folded chromosomes of Escherichia coli”. In: *Chromosoma* 55.1 (1976), pp. 13–25. doi: 10.1007/BF00288323 (cit. on p. 15).

[105] R R Sinden and D E Pettijohn. “Chromosomes in living Escherichia coli cells are segregated into domains of supercoiling”. In: *Proceedings of the National Academy of Sciences* 78.1 (1981), pp. 224–228. issn: 0027-8424. doi: 10.1073/pnas.78.1.224 (cit. on pp. 15, 16).

[106] D. E. Pettijohn and Ralph Hecht. “RNA Molecules Bound to the Folded Bacterial Genome Stabilize DNA Folds and Segregate Domains of Supercoiling”. In: *Cold Spring Harbor Symposia on Quantitative Biology* 38 (1974), pp. 31–41. doi: 10.1101/SQB.1974.038.01.006 (cit. on p. 15).

[107] Richard A. Stein, Shuang Deng, and N. Patrick Higgins. “Measuring chromosome dynamics on different time scales using resolvases with varying half-lives”. In: *Molecular Microbiology* 56.4 (2005), pp. 1049–1061. doi: https://doi.org/10.1111/j.1365-2958.2005.04588.x (cit. on p. 15).

[108] Bae-Yeun Ha and Youngkyun Jung. “Polymers under confinement: single polymers, how they interact, and as model chromosomes”. In: *Soft Matter* 11 (12 2015), pp. 2333–2352. doi: 10.1039/C4SM02734E (cit. on pp. 15, 19, 37, 54, 55, 85–89).

[109] Manuela Roggiani and Mark Goulian. “Chromosome-Membrane Interactions in Bacteria”. In: *Annual Review of Genetics* 49.1 (2015). PMID: 26436460, pp. 115–129. doi: 10.1146/annurev-genet-112414-054958 (cit. on p. 16).

[110] Somenath Bakshi, Heejun Choi, and James C. Weisshaar. “The spatial biology of transcription and translation in rapidly growing Escherichia coli”. In: *Frontiers in Microbiology* 6 (2015), p. 636. issn: 1664-302X. doi: 10.3389/fmicb.2015.00636 (cit. on pp. 16, 84).

[111] Antoine Le Gall et al. “Bacterial partition complexes segregate within the volume of the nucleoid”. In: *Nature Communications* 7.1 (2016), p. 12107. doi: 10.1038/ncomms12107 (cit. on pp. 18, 19).

[112] Nancy Kleckner et al. “The bacterial nucleoid: nature, dynamics and sister segregation”. In: *Current Opinion in Microbiology* 22 (2014). Growth and development: eukaryotes/ prokaryotes, pp. 127–137. issn: 1369-5274. doi: https://doi.org/10.1016/j.mib.2014.10.001 (cit. on p. 19).

[113] Jay K. Fisher et al. “Four-Dimensional Imaging of E. coli Nucleoid Organization and Dynamics in Living Cells”. In: *Cell* 153.4 (2013), pp. 882–895. doi: 10.1016/j.cell.2013.04.006 (cit. on p. 19).

[114] Charlène Planchenault et al. “Intracellular Positioning Systems Limit the Entropic Eviction of Secondary Replicons Toward the Nucleoid Edges in Bacterial Cells”. In: *Journal of Molecular Biology* 432.3 (2020). Perspectives on Chromosome Folding, pp. 745–761. issn: 0022-2836. doi: https://doi.org/10.1016/j.jmb.2019.11.027 (cit. on p. 19).

[115] Liel Sapir and Daniel Harries. “Macromolecular Stabilization by Excluded Cosolutes: Mean Field Theory of Crowded Solutions”. In: *Journal of Chemical Theory and Computation* 11.7 (July 2015), pp. 3478–3490. doi: 10.1021/acs.jctc.5b00258 (cit. on p. 22).

[116] Jaroslaw Piasecki, Lydéric Bocquet, and Jean-Pierre Hansen. “Multiple time scale derivation of the Fokker-Planck equation for two Brownian spheres suspended in a hard sphere fluid”. In: *Physica A: Statistical Mechanics and its Applications* 218.1 (1995), pp. 125–144. issn: 0378-4371. doi: https://doi.org/10.1016/0378-4371(95)00090-T (cit. on p. 23).

[117] Jean-Pierre Hansen and Ian R. McDonald. “Applications to Soft Matter”. In: *Theory of Simple Liquids*. Fourth Edition. Oxford: Academic Press, 2013. Chap. 12, pp. 511–584. isbn: 978-0-12-387032-2. doi: https://doi.org/10.1016/C2010-0-66723-X (cit. on p. 23).

[118] Michael P. Allen and Dominic J. Tildesley. “Mesoscale methods”. In: *Computer Simulation of Liquids*. 2nd ed. Oxford University Press, June 2017. Chap. 12, pp. 382–405. isbn: 9780198803195. doi: 10.1093/oso/9780198803195.003.0012 (cit. on p. 23).

[119] Thierry Biben, Peter Bladon, and Daan Frenkel. “Depletion effects in binary hard-sphere fluids”. In: *Journal of Physics: Condensed Matter* 8.50 (1996), pp. 10799–10821. doi: 10.1088/0953-8984/8/50/008 (cit. on pp. 24, 31).

[120] Jean-Pierre Hansen and Ian R. McDonald. *Theory of Simple Liquids: with Applications to Soft Matter*. Fourth Edition. Oxford: Academic Press, 2013, p. 636. isbn: 978-0-12-387032-2. doi: https://doi.org/10.1016/C2010-0-66723-X (cit. on pp. 24, 26, 32).

[121] William G. McMillan and Joseph E. Mayer. “The Statistical Thermodynamics of Multicomponent Systems”. In: *The Journal of Chemical Physics* 13.7 (1945), pp. 276–305. issn: 1089-7690. doi: 10.1063/1.1724036 (cit. on p. 24).

[122] John G. Kirkwood and Frank P. Buff. “The Statistical Mechanical Theory of Solutions. I”. In: *The Journal of Chemical Physics* 19.6 (Dec. 1954), pp. 774–777. issn: 0021-9606. doi: 10.1063/1.1748352 (cit. on p. 24).

[123] Terrell L Hill. *An introduction to statistical thermodynamics*. Courier Corporation, 1986 (cit. on pp. 24, 28).

[124] R. Roth, R. Evans, and S. Dietrich. "Depletion potential in hard-sphere mixtures: Theory and applications". In: *Phys. Rev. E* 62 (4 2000), pp. 5360–5377. doi: 10.1103/PhysRevE.62.5360 (cit. on pp. 24, 28, 31).

[125] Henk N. W Lekkerkerker and R Tuinier. *Colloids and the depletion interaction*. eng. Lecture notes in physics ; 833. Dordrecht ; New York: Springer, 2011. isbn: 9789400712232. doi: https://doi.org/10.1007/978-94-007-1223-2 (cit. on pp. 24, 28–30, 32, 35, 57).

[126] C. G. Gray and Keith E. Gubbins. *Theory of molecular fluids*. eng. The international series of monographs on chemistry. Oxford: Clarendon Press, 1984. isbn: 0198556020 (cit. on p. 26).

[127] Sho Asakura and Fumio Oosawa. "On Interaction between Two Bodies Immersed in a Solution of Macromolecules". In: *The Journal of Chemical Physics* 22.7 (July 1954), pp. 1255–1256. issn: 0021-9606. doi: 10.1063/1.1740347 (cit. on pp. 27, 29, 35, 38, 54, 57, 59, 60, 85, 102).

[128] Sho Asakura and Fumio Oosawa. "Interaction between particles suspended in solutions of macromolecules". In: *Journal of Polymer Science* 33.126 (1958), pp. 183–192. issn: 1542-6238. doi: 10.1002/pol.1958.1203312618 (cit. on pp. 27–30, 35, 38, 57, 60, 85, 102).

[129] R. Roth, R. Evans, and A. A. Louis. "Theory of asymmetric nonadditive binary hard-sphere mixtures". In: *Phys. Rev. E* 64 (5 2001), p. 051202. doi: 10.1103/PhysRevE.64.051202 (cit. on pp. 27, 31, 32).

[130] Phil Attard. "Spherically inhomogeneous fluids. II. Hard□sphere solute in a hard□sphere solvent". In: *The Journal of Chemical Physics* 91.5 (1989), pp. 3083–3089. doi: 10.1063/1.456931 (cit. on pp. 28, 31).

[131] Evert Jan Meijer and Daan Frenkel. "Computer simulation of polymer-induced clustering of colloids". In: *Phys. Rev. Lett.* 67 (9 1991), pp. 1110–1113. doi: 10.1103/PhysRevLett.67.1110 (cit. on pp. 28, 29, 31).

[132] B. Götzelmann, R. Evans, and S. Dietrich. "Depletion forces in fluids". In: *Phys. Rev. E* 57 (6 1998), pp. 6785–6800. doi: 10.1103/PhysRevE.57.6785 (cit. on pp. 28, 32).

[133] Marjolein Dijkstra, René van Roij, and Robert Evans. "Phase diagram of highly asymmetric binary hard-sphere mixtures". In: *Phys. Rev. E* 59 (5 1999), pp. 5744–5771. doi: 10.1103/PhysRevE.59.5744 (cit. on pp. 28, 32).

[134] Y. Mao, M.E. Cates, and H.N.W. Lekkerkerker. “Depletion force in colloidal systems”. In: *Physica A: Statistical Mechanics and its Applications* 222.1 (1995), pp. 10 –24. issn: 0378-4371. doi: https://doi.org/10.1016/0378-4371(95)00206-5 (cit. on p. 28).

[135] B. Götzelmann et al. “Depletion potential in hard-sphere fluids”. In: *Europhysics Letters* 47.3 (1999), p. 398. doi: 10.1209/epl/i1999-00402-x (cit. on pp. 28, 32).

[136] H. N. W Lekkerkerker et al. “Phase Behaviour of Colloid + Polymer Mixtures”. In: *Europhysics Letters (EPL)* 20.6 (1992), pp. 559–564. doi: 10.1209/0295-5075/20/6/015 (cit. on pp. 28, 29).

[137] Terrell L Hill. *Statistical mechanics : principles and selected applications*. eng. New York: Dover Publications Inc., 1987 (cit. on p. 28).

[138] B. Widom. “Some Topics in the Theory of Fluids”. In: *The Journal of Chemical Physics* 39.11 (1963), pp. 2808–2812. doi: 10.1063/1.1734110 (cit. on p. 28).

[139] Henk N. W. Lekkerkerker and Remco Tuinier. “Phase Transitions of Hard Spheres Plus Depletants; Basics”. In: *Colloids and the Depletion Interaction*. Dordrecht: Springer Netherlands, 2011. Chap. 3, pp. 109–129. isbn: 978-94-007-1223-2. doi: 10.1007/978-94-007-1223-2_3 (cit. on p. 29).

[140] S. M. Oversteegen and R. Roth. “General methods for free-volume theory”. In: *The Journal of Chemical Physics* 122.21 (June 2005), p. 214502. issn: 0021-9606. doi: 10.1063/1.1908765 (cit. on p. 29).

[141] Gerard J. Fleer and Remco Tuinier. “Analytical phase diagrams for colloids and non-adsorbing polymer”. In: *Advances in Colloid and Interface Science* 143.1 (2008), pp. 1–47. issn: 0001-8686. doi: https://doi.org/10.1016/j.cis.2008.07.001 (cit. on p. 29).

[142] A.P Gast, C.K Hall, and W.B Russel. “Polymer-induced phase separations in nonaqueous colloidal suspensions”. In: *Journal of Colloid and Interface Science* 96.1 (1983), pp. 251 –267. issn: 0021-9797. doi: https://doi.org/10.1016/0021-9797(83)90027-9 (cit. on pp. 31, 32).

[143] Giorgio Cinacchi et al. “Large attractive depletion interactions in soft repulsive–sphere binary mixtures”. In: *The Journal of Chemical Physics* 127.21 (Dec. 2007), p. 214501. issn: 0021-9606. doi: 10.1063/1.2804330 (cit. on p. 32).

[144] Roland Roth and Masahiro Kinoshita. “Depletion potential between large spheres immersed in a multicomponent mixture of small spheres”. In: *The Journal of Chemical Physics* 125.8 (Aug. 2006), p. 084910. issn: 0021-9606. doi: 10.1063/1.2345200 (cit. on p. 32).

[145] Arieh Ben-Naim. *Molecular theory of solutions*. eng. Oxford ; New York: Oxford University Press, 2006. isbn: 9780199299690. url: https://global.oup.com/academic/product/molecular-theory-of-solutions-9780199299690?cc=ca&lang=en& (cit. on p. 32).

[146] Dave Goulding and Simone Melchionna. "Accurate calculation of three-body depletion interactions". In: *Phys. Rev. E* 64 (1 2001), p. 011403. doi: 10.1103/PhysRevE.64.011403 (cit. on p. 32).

[147] Norman F. Carnahan and Kenneth E. Starling. "Equation of State for Nonattracting Rigid Spheres". In: *The Journal of Chemical Physics* 51.2 (1969), pp. 635–636. doi: 10.1063/1.1672048 (cit. on p. 32).

[148] H. Reiss, H. L. Frisch, and J. L. Lebowitz. "Statistical Mechanics of Rigid Spheres". In: *The Journal of Chemical Physics* 31.2 (1959), pp. 369–380. doi: 10.1063/1.1730361 (cit. on p. 32).

[149] R.John Ellis. "Macromolecular crowding: an important but neglected aspect of the intracellular environment". In: *Current Opinion in Structural Biology* 11.1 (2001), pp. 114–119. issn: 0959-440X. doi: https://doi.org/10.1016/S0959-440X(00)00172-X (cit. on p. 35).

[150] Kim A. Sharp. "Analysis of the size dependence of macromolecular crowding shows that smaller is better". In: *Proceedings of the National Academy of Sciences* 112.26 (2015), pp. 7990–7995. doi: 10.1073/pnas.1505396112 (cit. on p. 35).

[151] R. Hancock. "Crowding, Entropic Forces, and Confinement: Crucial Factors for Structures and Functions in the Cell Nucleus". In: *Biochemistry (Moscow)* 83.4 (Apr. 2018), pp. 326–337. issn: 1608-3040. doi: 10.1134/S0006297918040041 (cit. on p. 35).

[152] Davide Marenduzzo, Cristian Micheletti, and Peter R. Cook. "Entropy-Driven Genome Organization". In: *Biophysical Journal* 90.10 (2006), pp. 3712 –3721. issn: 0006-3495. doi: https://doi.org/10.1529/biophysj.105.077685 (cit. on pp. 35, 57–61, 83, 107).

[153] Suckjoon Jun. "Chromosome, Cell Cycle, and Entropy". In: *Biophysical Journal* 108.4 (Feb. 2015), pp. 785–786. issn: 0006-3495. doi: 10.1016/j.bpj.2014.12.032 (cit. on pp. 35, 57, 85).

[154] Tyler N. Shendruk et al. “Simulating the Entropic Collapse of Coarse-Grained Chromosomes”. In: *Biophysical Journal* 108.4 (Feb. 2015), pp. 810–820. issn: 0006-3495. doi: 10.1016/j.bpj.2014.11.3487 (cit. on pp. 35, 36, 39, 42, 43, 54, 57).

[155] Chanil Jeon, Youngkyun Jung, and Bae-Yeun Ha. “A ring-polymer model shows how macromolecular crowding controls chromosome-arm organization in Escherichia coli”. In: *Scientific Reports* 7.1 (2017), p. 11896. doi: 10.1038/s41598-017-10421-y (cit. on pp. 35, 37, 40, 46, 54, 65, 87–89).

[156] Marc Joyeux. “A segregative phase separation scenario of the formation of the bacterial nucleoid”. In: *Soft Matter* 14 (36 2018), pp. 7368–7381. doi: 10.1039/C8SM01205A (cit. on pp. 35, 38).

[157] G. Tiana and L. Giorgetti. *Modeling the 3D Conformation of Genomes*. Computational Biophysics. CRC Press, Taylor & Francis Group, 2019. isbn: 9781315144009. doi: https://www.taylorfrancis.com/books/edit/10.1201/9781315144009/modeling-3d-conformation-genomes-guido-tiana-luca-giorgetti (cit. on pp. 35, 64, 87).

[158] Hongsuk Kang et al. “Effects of Macromolecular Crowding on the Collapse of Biopolymers”. In: *Phys. Rev. Lett.* 114 (6 2015), p. 068303. doi: 10.1103/PhysRevLett.114.068303 (cit. on pp. 35, 36, 42, 43, 54, 85, 86).

[159] Tyler N. Shendruk et al. “Coarse-grained molecular dynamics simulations of depletion-induced interactions for soft matter systems”. In: *The Journal of Chemical Physics* 141.24 (2014), p. 244910. doi: 10.1063/1.4903992 (cit. on pp. 35, 36, 42, 43, 54).

[160] Chanil Jeon, Youngkyun Jung, and Bae-Yeun Ha. “Effects of molecular crowding and confinement on the spatial organization of a biopolymer”. In: *Soft Matter* 12.47 (2016), pp. 9436–9450. issn: 1744-683X. doi: 10.1039/C6SM01184E (cit. on pp. 35, 36, 42–45, 48, 54, 85, 86, 102).

[161] Chanil Jeon et al. “How are molecular crowding and the spatial organization of a biopolymer interrelated”. In: *Soft Matter* 12.48 (2016), pp. 9786–9796. issn: 1744-6848. doi: 10.1039/c6sm01924b (cit. on pp. 35–37, 42–45, 48–50, 54, 59, 70, 83, 85, 87, 102).

[162] Da Yang et al. “The effects of polydisperse crowders on the compaction of the Escherichia coli nucleoid”. In: *Molecular Microbiology* 113.5 (2020), pp. 1022–1037. doi: https://doi.org/10.1111/mmi.14467 (cit. on pp. 35, 36, 39, 42, 43, 54).

[163] W.E. Hill, J.D. Thompson, and J.W. Anderegg. “X-ray scattering study of ribosomes from Escherichia coli”. In: *Journal of Molecular Biology* 44.1 (1969), pp. 89 –102. issn: 0022-2836. doi: https://doi.org/10.1016/0022-2836(69)90406-9 (cit. on pp. 36, 54).

[164] Barbara S. Schuwirth et al. “Structures of the Bacterial Ribosome at 3.5 Å Resolution”. In: *Science* 310.5749 (2005), pp. 827–834. doi: 10.1126/science.1117230 (cit. on pp. 36, 54).

[165] Job Ubbink and Theo Odijk. “Electrostatic-Undulatory Theory of Plectonemically Supercoiled DNA”. In: *Biophysical Journal* 76.5 (1999), pp. 2502–2519. doi: 10.1016/S0006-3495(99)77405-9 (cit. on pp. 36, 108, 109).

[166] Julio E. Cabrera and Ding J. Jin. “The distribution of RNA polymerase in Escherichia coli is dynamic and sensitive to environmental cues”. In: *Molecular Microbiology* 50.5 (2003), pp. 1493–1505. doi: 10.1046/j.1365-2958.2003.03805.x (cit. on pp. 36, 55, 59, 107).

[167] Julio E. Cabrera et al. “Active Transcription of rRNA Operons Condenses the Nucleoid in Escherichia coli: Examining the Effect of Transcription on Nucleoid Structure in the Absence of Transertion”. In: *Journal of Bacteriology* 191.13 (2009), pp. 4180–4185. doi: 10.1128/jb.01707-08 (cit. on pp. 36, 55).

[168] Arash Sanamrad et al. “Single-particle tracking reveals that free ribosomal subunits are not excluded from the Escherichia coli nucleoid”. In: *Proceedings of the National Academy of Sciences* 111.31 (2014), pp. 11413–11418. issn: 0027-8424. doi: 10.1073/pnas.1411558111 (cit. on pp. 36, 55).

[169] Qian Chai et al. “Organization of Ribosomes and Nucleoids in Escherichia coli Cells during Growth and in Quiescence”. In: *Journal of Biological Chemistry* 289.16 (2014), pp. 11342–11352. doi: 10.1074/jbc.M114.557348 (cit. on pp. 36, 55).

[170] Somenath Bakshi et al. “Time-dependent effects of transcription- and translation-halting drugs on the spatial distributions of the Escherichia coli chromosome and ribosomes”. In: *Molecular Microbiology* 94.4 (2014), pp. 871–887. doi: 10.1111/mmi.12805 (cit. on pp. 36, 55).

[171] Somenath Bakshi et al. “Superresolution imaging of ribosomes and RNA polymerase in live Escherichia coli cells”. In: *Molecular Microbiology* 85.1 (2012), pp. 21–38. doi: 10.1111/j.1365-2958.2012.08081.x (cit. on pp. 36, 55).

[172] Yanwei Wang et al. “Proof of the identity between the depletion layer thickness and half the average span for an arbitrary polymer chain”. In: *The Journal of Chemical Physics* 129.7 (2008), p. 074904. doi: 10.1063/1.2970935 (cit. on pp. 37, 38, 65).

[173] Juin Kim et al. “Elasticity of flexible polymers under cylindrical confinement: appreciating the blob scaling regime in computer simulations”. In: *Soft Matter* 9.26 (2013), pp. 6142–6150. issn: 1744-683X. doi: 10.1039/C3SM50742D (cit. on pp. 37–39, 41, 46, 65, 77, 89).

[174] Renko de Vries. “Flexible Polymer-Induced Condensation and Bundle Formation of DNA and F-Actin Filaments”. In: *Biophysical Journal* 80.3 (2001), pp. 1186–1194. issn: 0006-3495. doi: https://doi.org/10.1016/S0006-3495(01)76095-X (cit. on p. 37).

[175] Ivan Junier, Frédéric Boccard, and Olivier Espéli. “Polymer modeling of the E. coli genome reveals the involvement of locus positioning and macrodomain structuring for the control of chromosome conformation and segregation”. In: *Nucleic Acids Research* 42.3 (Nov. 2013), pp. 1461–1473. issn: 0305-1048. doi: 10.1093/nar/gkt1005 (cit. on p. 37).

[176] I. R. Cooke and D. R. M. Williams. “Collapse of Flexible-Semiflexible Copolymers in Selective Solvents: Single Chain Rods, Cages, and Networks”. In: *Macromolecules* 37.15 (2004), pp. 5778–5783. doi: 10.1021/ma0355406 (cit. on pp. 38, 84).

[177] Håkan Wennerström et al. “Colloidal stability of the living cell”. In: *Proceedings of the National Academy of Sciences* 117.19 (2020), pp. 10113–10121. doi: 10.1073/pnas.1914599117 (cit. on p. 38).

[178] Anpu Chen and Nanrong Zhao. “Comparative study of the crowding-induced collapse effect in hard-sphere, flexible polymer and rod-like polymer systems”. In: *Phys. Chem. Chem. Phys.* 21 (23 2019), pp. 12335–12345. doi: 10.1039/C9CP01731C (cit. on p. 39).

[179] Burkhard Dünweg and Kurt Kremer. “Molecular dynamics simulation of a polymer chain in solution”. In: *The Journal of Chemical Physics* 99.9 (1993), pp. 6983–6997. doi: 10.1063/1.465445 (cit. on pp. 39, 65, 89).

[180] John D. Weeks, David Chandler, and Hans C. Andersen. “Role of Repulsive Forces in Determining the Equilibrium Structure of Simple Liquids”. In: *The Journal of Chemical Physics* 54.12 (June 1971), pp. 5237–5247. issn: 0021-9606. doi: 10.1063/1.1674820 (cit. on pp. 40, 65, 91).

[181] Marvin Bishop, M. H. Kalos, and H. L. Frisch. “Molecular dynamics of polymeric systems”. In: *The Journal of Chemical Physics* 70.3 (1979), pp. 1299–1304. doi: 10.1063/1.437567 (cit. on pp. 40, 66, 92).

[182] Gary S. Grest and Kurt Kremer. “Molecular dynamics simulation for polymers in the presence of a heat bath”. In: *Phys. Rev. A* 33 (5 1986), pp. 3628–3631. doi: 10.1103/PhysRevA.33.3628 (cit. on pp. 40, 66, 92).

[183] Kurt Kremer and Gary S. Grest. “Dynamics of entangled linear polymer melts: A molecular□dynamics simulation”. In: *The Journal of Chemical Physics* 92.8 (1990), pp. 5057–5086. doi: 10.1063/1.458541 (cit. on pp. 40, 66, 92).

[184] Michael Rubinstein and Ralph H Colby. *Polymer physics*. Vol. 23. Oxford University Press New York, 2003 (cit. on p. 41).

[185] Loup Verlet. “Computer ”Experiments” on Classical Fluids. I. Thermodynamical Properties of Lennard-Jones Molecules”. In: *Phys. Rev.* 159 (1 1967), pp. 98–103. doi: 10.1103/PhysRev.159.98 (cit. on pp. 40, 66, 93).

[186] William C. Swope et al. “A computer simulation method for the calculation of equilibrium constants for the formation of physical clusters of molecules: Application to small water clusters”. In: *The Journal of Chemical Physics* 76.1 (1982), pp. 637–649. doi: 10.1063/1.442716 (cit. on pp. 40, 66, 93).

[187] T. Schneider and E. Stoll. “Molecular-dynamics study of a three-dimensional one-component model for distortive phase transitions”. In: *Phys. Rev. B* 17 (3 1978), pp. 1302–1322. doi: 10.1103/PhysRevB.17.1302 (cit. on pp. 40, 66, 93).

[188] Steve Plimpton. “Fast Parallel Algorithms for Short-Range Molecular Dynamics”. In: *Journal of Computational Physics* 117.1 (1995), pp. 1 –19. issn: 0021-9991. doi: https://doi.org/10.1006/jcph.1995.1039 (cit. on pp. 42, 67, 94).

[189] Tom Shire, Kevin J. Hanley, and Kevin Stratford. “DEM simulations of polydisperse media: efficient contact detection applied to investigate the quasi-static limit”. In: *Computational Particle Mechanics* 8.4 (2021), pp. 653–663. doi: 10.1007/s40571-020-00361-2 (cit. on pp. 42, 67, 94).

[190] Ruxandra I. Dima and D. Thirumalai. “Asymmetry in the Shapes of Folded and Denatured States of Proteins”. In: *The Journal of Physical Chemistry B* 108.21 (May 2004), pp. 6564–6570. doi: 10.1021/jp037128y (cit. on pp. 42, 67, 94).

[191] Naveen Michaud-Agrawal et al. “MDAnalysis: A toolkit for the analysis of molecular dynamics simulations”. In: *Journal of Computational Chemistry* 32.10 (2011), pp. 2319–2327. doi: 10.1002/jcc.21787 (cit. on pp. 42, 67, 94).

[192] Richard J. Gowers et al. “MDAnalysis: A Python Package for the Rapid Analysis of Molecular Dynamics Simulations”. In: *Proceedings of the 15th Python in Science Conference*. Ed. by Sebastian Benthall and Scott Rostrup. 2016, pp. 98 –105. doi: 10.25080/Majora-629e541a-00e (cit. on pp. 42, 67, 94).

[193] Ole Tange. *GNU Parallel 2018*. Ole Tange, Mar. 2018. isbn: 9781387509881. doi: 10.5281/zenodo.1146014 (cit. on pp. 42, 67, 94).

[194] Youngkyun Jung, Suckjoon Jun, and Bae-Yeun Ha. “Self-avoiding polymer trapped inside a cylindrical pore: Flory free energy and unexpected dynamics”. In: *Phys. Rev. E* 79 (6 2009), p. 061912. doi: 10.1103/PhysRevE.79.061912 (cit. on p. 46).

[195] Axel Arnold et al. “Unexpected relaxation dynamics of a self-avoiding polymer in cylindrical confinement”. In: *The Journal of Chemical Physics* 127.16 (Oct. 2007), p. 164903. issn: 0021-9606. doi: 10.1063/1.2799513 (cit. on p. 46).

[196] Jeremy J. Jones, Johan R. C. van der Maarel, and Patrick S. Doyle. “Effect of Nanochannel Geometry on DNA Structure in the Presence of Macromolecular Crowding Agent”. In: *Nano Lett.* 11.11 (Nov. 2011), pp. 5047–5053. issn: 1530-6984. doi: 10.1021/nl203114f (cit. on p. 47).

[197] Jagannath Mondal et al. “Entropy-Based Mechanism of Ribosome-Nucleoid Segregation in E. coli Cells”. In: *Biophysical Journal* 100.11 (2011), pp. 2605–2613. issn: 0006-3495. doi: https://doi.org/10.1016/j.bpj.2011.04.030 (cit. on p. 55).

[198] Boyan Bonev and Giacomo Cavalli. “Organization and function of the 3D genome”. In: *Nature Reviews Genetics* 17.11 (2016), pp. 661–678. doi: 10.1038/nrg.2016.112 (cit. on pp. 57, 85).

[199] Anjana Badrinarayanan, Tung B.K. Le, and Michael T. Laub. “Bacterial Chromosome Organization and Segregation”. In: *Annual Review of Cell and Developmental Biology* 31.1 (2015). PMID: 26566111, pp. 171–199. doi: 10.1146/annurev-cellbio-100814-125211 (cit. on pp. 57, 85).

[200] C Robinow and E Kellenberger. “The bacterial nucleoid revisited”. In: *Microbiological Reviews* 58.2 (1994), pp. 211–232. doi: 10.1128/mr.58.2.211-232.1994 (cit. on p. 57).

[201] David E Pettijohn. “The Nucleoid”. eng. In: *Escherichia coli and Salmonella typhimurium : cellular and molecular biology*. Ed. by Frederick C Neidhardt. 2nd ed. Vol. 1. Washington, D.C: American Society for Microbiology, 1996. Chap. 12, pp. 158–166. isbn: 0914826891 (cit. on p. 57).

[202] Ding Jun Jin and Julio E. Cabrera. “Coupling the distribution of RNA polymerase to global gene regulation and the dynamic structure of the bacterial nucleoid in Escherichia coli”. In: *Journal of Structural Biology* 156.2 (2006), pp. 284 –291. issn: 1047-8477. doi: https://doi.org/10.1016/j.jsb.2006.07.005 (cit. on pp. 57, 59, 60, 83, 102, 107).

[203] Sean R. McGuffee and Adrian H. Elcock. “Diffusion, Crowding & Protein Stability in a Dynamic Molecular Model of the Bacterial Cytoplasm”. In: *PLOS Computational Biology* 6.3 (Mar. 2010), pp. 1–18. doi: 10.1371/journal.pcbi.1000694 (cit. on p. 57).

[204] Huan-Xiang Zhou. “Influence of crowded cellular environments on protein folding, binding, and oligomerization: Biological consequences and potentials of atomistic modeling”. In: *FEBS Letters* 587.8 (2013), pp. 1053–1061. issn: 1873-3468. doi: 10.1016/j.febslet.2013.01.064 (cit. on pp. 57, 85).

[205] O. L. Miller, Barbara A. Hamkalo, and C. A. Thomas. “Visualization of Bacterial Genes in Action”. In: *Science* 169.3943 (1970), pp. 392–395. issn: 0036-8075. doi: 10.1126/science.169.3943.392 (cit. on pp. 58, 60, 83, 107, 108).

[206] Anthony A. Hyman, Christoph A. Weber, and Frank Jülicher. “Liquid-Liquid Phase Separation in Biology”. In: *Annual Review of Cell and Developmental Biology* 30.1 (2014). PMID: 25288112, pp. 39–58. doi: 10.1146/annurev-cellbio-100913-013325 (cit. on pp. 57, 60, 84).

[207] Salman F. Banani et al. “Biomolecular condensates: organizers of cellular biochemistry”. In: *Nature Reviews Molecular Cell Biology* 18.5 (2017), pp. 285–298. doi: 10.1038/nrm.2017.7 (cit. on pp. 57, 60, 84).

[208] Ding Jun Jin, Cedric Cagliero, and Yan Ning Zhou. “Growth rate regulation in Escherichia coli”. In: *FEMS Microbiology Reviews* 36.2 (Mar. 2012), pp. 269–287. issn: 0168-6445. doi: 10.1111/j.1574-6976.2011.00279.x (cit. on pp. 59, 60, 107).

[209] Peter R. Cook and Davide Marenduzzo. “Transcription-driven genome organization: A model for chromosome structure and the regulation of gene expression tested through simulations”. In: *Nucleic Acids Research* 46 (19 Nov. 2018), pp. 9895–9906. issn: 13624962. doi: 10.1093/nar/gky763 (cit. on p. 59).

[210] Ulrike Endesfelder et al. “Multiscale Spatial Organization of RNA Polymerase in Escherichia coli”. In: *Biophysical Journal* 105.1 (2013), pp. 172 –181. issn: 0006-3495. doi: https://doi.org/10.1016/j.bpj.2013.05.048 (cit. on pp. 59–61, 83, 107).

[211] Zhe Sun Cedric Cagliero Ding Jun Jin Carmen Mata Martin and Yan Ning Zhou. "Nucleolus-like compartmentalization of the transcription machinery in fast-growing bacterial cells". In: *Critical Reviews in Biochemistry and Molecular Biology* 52.1 (2017). PMID: 28006965, pp. 96–106. doi: 10.1080/10409238.2016.1269717 (cit. on p. 59).

[212] Anne-Marie Ladouceur et al. "Clusters of bacterial RNA polymerase are biomolecular condensates that assemble through liquid–liquid phase separation". In: *Proceedings of the National Academy of Sciences* 117.31 (2020), pp. 18540–18549. doi: 10.1073/pnas.2005019117 (cit. on p. 59).

[213] Ding J. Jin et al. "The dynamic nature and territory of transcriptional machinery in the bacterial chromosome". In: *Frontiers in Microbiology* 6 (2015). issn: 1664-302X. doi: 10.3389/fmicb.2015.00497 (cit. on p. 59).

[214] Mathew Stracy et al. "Live-cell superresolution microscopy reveals the organization of RNA polymerase in the bacterial nucleoid". In: *Proceedings of the National Academy of Sciences* 112.32 (2015), E4390–E4399. doi: 10.1073/pnas.1507592112 (cit. on p. 59).

[215] Tamas Gaal et al. "Colocalization of distant chromosomal loci in space in E. coli: a bacterial nucleolus". In: *Genes & Development* 30.20 (2016), pp. 2272–2285. doi: 10.1101/gad.290312.116 (cit. on pp. 59, 60, 107).

[216] Carmen Mata Martin et al. "Extrachromosomal Nucleolus-Like Compartmentalization by a Plasmid-Borne Ribosomal RNA Operon and Its Role in Nucleoid Compaction". In: *Frontiers in Microbiology* 9 (2018). issn: 1664-302X. doi: 10.3389/fmicb.2018.01115 (cit. on p. 59).

[217] Xiaoli Weng et al. "Spatial organization of RNA polymerase and its relationship with transcription in Escherichia coli". In: *Proceedings of the National Academy of Sciences* 116.40 (2019), pp. 20115–20123. doi: 10.1073/pnas.1903968116 (cit. on p. 59).

[218] +Jun Fan et al. "RNA polymerase redistribution and increased gene dosage support growth in E. coli strains with a minimal number of ribosomal RNA operons". In: *bioRxiv* (2022). doi: https://doi.org/10.1101/2022.02.10.479894 (cit. on pp. 59, 60).

[219] Peter R. Cook. "A Model for all Genomes: The Role of Transcription Factories". In: *Journal of Molecular Biology* 395.1 (2010), pp. 1–10. issn: 0022-2836. doi: https://doi.org/10.1016/j.jmb.2009.10.031 (cit. on p. 59).

[220] Anne R. Shim et al. “Dynamic Crowding Regulates Transcription”. In: *Biophysical Journal* 118.9 (2020), pp. 2117–2129. issn: 0006-3495. doi: https://doi.org/10.1016/j.bpj.2019.11.007 (cit. on p. 59).

[221] Marina Feric and Tom Misteli. “Phase separation in genome organization across evolution”. In: *Trends in Cell Biology* 31.8 (2021), pp. 671–685. doi: 10.1016/j.tcb.2021.03.001 (cit. on pp. 60, 84).

[222] Davide Marenduzzo, Inês Faro-Trindade, and Peter R. Cook. “What are the molecular ties that maintain genomic loops?” In: *Trends in Genetics* 23.3 (2007), pp. 126 –133. issn: 0168-9525. doi: https://doi.org/10.1016/j.tig.2007.01.007 (cit. on pp. 60, 83, 107).

[223] S L French and O L Miller. “Transcription mapping of the Escherichia coli chromosome by electron microscopy”. In: *Journal of Bacteriology* 171.8 (1989), pp. 4207–4216. doi: 10.1128/jb.171.8.4207-4216.1989 (cit. on pp. 60, 61, 107, 108).

[224] Mikel Irastortza-Olaziregi and Orna Amster-Choder. “Coupled Transcription-Translation in Prokaryotes: An Old Couple With New Surprises”. In: *Frontiers in Microbiology* 11 (2021). doi: 10.3389/fmicb.2020.624830 (cit. on p. 60).

[225] Willem TICHELAAR et al. “The quaternary structure of Escherichia coli RNA polymerase studied with (scanning) transmission (immuno)electron microscopy”. In: *European Journal of Biochemistry* 135.2 (1983), pp. 263–269. doi: https://doi.org/10.1111/j.1432-1033.1983.tb07647.x (cit. on p. 61).

[226] Seth A. Darst, Elizabeth W. Kubalek, and Roger D. Kornberg. “Three-dimensional structure of Escherichia coli RNA polymerase holoenzyme determined by electron crystallography”. In: *Nature* 340.6236 (1989), pp. 730–732. doi: 10.1038/340730a0 (cit. on p. 61).

[227] Andrey Polyakov, Elena Severinova, and Seth A. Darst. “Three-dimensional structure of E. coil core RNA polymerase: Promoter binding and elongation conformations of the enzyme”. In: *Cell* 83.3 (1995), pp. 365–373. issn: 0092-8674. doi: https://doi.org/10.1016/0092-8674(95)90114-0 (cit. on p. 61).

[228] Katsuhiko S. Murakami, Shoko Masuda, and Seth A. Darst. “Structural Basis of Transcription Initiation: RNA Polymerase Holoenzyme at 4 Å Resolution”. In: *Science* 296.5571 (June 2002), pp. 1280–1284. doi: 10.1126/science.1069594 (cit. on p. 61).

[229] Katsuhiko S. Murakami et al. “Structural Basis of Transcription Initiation: An RNA Polymerase Holoenzyme-DNA Complex”. In: *Science* 296.5571 (2002), pp. 1285–1290. doi: 10.1126/science.1069595 (cit. on p. 61).

[230] Katsuhiko S. Murakami. “X-ray Crystal Structure of Escherichia coli RNA Polymerase σ^{70} Holoenzyme”. In: *Journal of Biological Chemistry* 288.13 (2013), pp. 9126–9134. doi: 10.1074/jbc.M112.430900 (cit. on p. 61).

[231] Christoph G. Baumann et al. “Ionic effects on the elasticity of single DNA molecules”. In: *Proceedings of the National Academy of Sciences* 94.12 (1997), pp. 6185–6190. doi: 10.1073/pnas.94.12.6185 (cit. on p. 61).

[232] Jürgen Brosius et al. “Gene organization and primary structure of a ribosomal RNA operon from Escherichia coli”. In: *Journal of Molecular Biology* 148.2 (1981), pp. 107–127. issn: 0022-2836. doi: https://doi.org/10.1016/0022-2836(81)90508-8 (cit. on pp. 61, 107, 108).

[233] Lin Xu et al. “Average Gene Length Is Highly Conserved in Prokaryotes and Eukaryotes and Diverges Only Between the Two Kingdoms”. In: *Molecular Biology and Evolution* 23.6 (Apr. 2006), pp. 1107–1108. issn: 0737-4038. doi: 10.1093/molbev/msk019 (cit. on p. 62).

[234] Brenda Youngren et al. “The multifork Escherichia coli chromosome is a self-duplicating and self-segregating thermodynamic ring polymer”. In: *Genes & Development* 28.1 (2014), pp. 71–84. doi: 10.1101/gad.231050.113 (cit. on pp. 61, 83).

[235] William M. Gelbart et al. “DNA□Inspired Electrostatics”. In: *Physics Today* 53.9 (Sept. 2000), pp. 38–44. issn: 0031-9228. doi: 10.1063/1.1325230 (cit. on pp. 61, 102).

[236] E. M. Sevick, P. A. Monson, and J. M. Ottino. “Monte Carlo calculations of cluster statistics in continuum models of composite morphology”. In: *The Journal of Chemical Physics* 88.2 (1988), pp. 1198–1206. doi: 10.1063/1.454720 (cit. on pp. 62, 100).

[237] Guang Shi et al. “Interphase human chromosome exhibits out of equilibrium glassy dynamics”. In: *Nature Communications* 9.1 (2018), p. 3161. doi: 10.1038/s41467-018-05606-6 (cit. on p. 64).

[238] Charles Kittel. *Introduction to solid state physics*. John Wiley & Sons, 2004. isbn: 978-0-471-41526-8. url: https://www.wiley.com/en-us/Introduction+to+Solid+State+Physics%2C+8th+Edition-p-9780471415268 (cit. on p. 74).

[239] Thomas C. Hales. “A Proof of the Kepler Conjecture”. In: *Annals of Mathematics* 162.3 (2005), pp. 1065–1185. issn: 0003486X. doi: https://doi.org/10.4007/annals.2005.162.1065 (cit. on p. 74).

[240] Conrad L. Woldringh. “The role of co-transcriptional translation and protein translocation (transertion) in bacterial chromosome segregation”. In: *Molecular Microbiology* 45.1 (2002), pp. 17–29. issn: 1365-2958. doi: 10.1046/j.1365-2958.2002.02993.x (cit. on p. 84).

[241] V. A. Ivanov, W. Paul, and K. Binder. “Finite chain length effects on the coil–globule transition of stiff-chain macromolecules: A Monte Carlo simulation”. In: *The Journal of Chemical Physics* 109.13 (Oct. 1998), pp. 5659–5669. issn: 0021-9606. doi: 10.1063/1.477184 (cit. on p. 84).

[242] M. Falconl et al. “Proteins from the prokaryotic nucleoid: primary and quaternary structure of the 15-kD Escherichia coli DNA binding protein H-NS”. In: *Molecular Microbiology* 2.3 (1988), pp. 323–329. doi: https://doi.org/10.1111/j.1365-2958.1988.tb00035.x (cit. on pp. 85, 86).

[243] Charles J. Dorman. “H-NS: a universal regulator for a dynamic genome”. In: *Nature Reviews Microbiology* 2.5 (2004), pp. 391–400. doi: 10.1038/nrmicro883 (cit. on pp. 85–87, 100).

[244] Suckjoon Jun and Andrew Wright. “Entropy as the driver of chromosome segregation”. In: *Nature Reviews Microbiology* 8.8 (2010), pp. 600–607. doi: 10.1038/nrmicro2391 (cit. on p. 85).

[245] M. Cristofalo et al. “Cooperative effects on the compaction of DNA fragments by the nucleoid protein H-NS and the crowding agent PEG probed by Magnetic Tweezers”. In: *Biochimica et Biophysica Acta (BBA) - General Subjects* 1864.12 (2020), p. 129725. issn: 0304-4165. doi: https://doi.org/10.1016/j.bbagen.2020.129725 (cit. on pp. 85–87, 95, 97, 99).

[246] Sravani K. Ramisetty et al. “In vitro studies of DNA condensation by bridging protein in a crowding environment”. In: *International Journal of Biological Macromolecules* 103 (2017), pp. 845–853. issn: 0141-8130. doi: https://doi.org/10.1016/j.ijbiomac.2017.05.079 (cit. on pp. 85–87, 95, 97, 99).

[247] Anna S. Wegner et al. “Compaction of isolated Escherichia coli nucleoids: Polymer and H-NS protein synergetics”. In: *Journal of Structural Biology* 194.1 (2016), pp. 129–137. issn: 1047-8477. doi: https://doi.org/10.1016/j.jsb.2016.02.009 (cit. on pp. 85–87, 95, 97, 99, 102).

[248] Sravani Keerthi Ramisetty and Rita S. Dias. “Synergistic role of DNA-binding protein and macromolecular crowding on DNA condensation. An experimental and theoretical approach”. In: *Journal of Molecular Liquids* 210 (2015). Surfactants in Solution. Selected Papers presented at the 20th International Symposium on Surfactants in Solution, 22 - 27 June 2014, pp. 64–73. issn: 0167-7322. doi: https://doi.org/10.1016/j.molliq.2015.04.051 (cit. on pp. 85–87, 95, 97, 99).

[249] Talukder Ali Azam et al. “Growth Phase-Dependent Variation in Protein Composition of the Escherichia coli Nucleoid”. In: *Journal of Bacteriology* 181.20 (1999), pp. 6361–6370. doi: 10.1128/jb.181.20.6361-6370.1999 (cit. on pp. 85, 86).

[250] M. Falconl et al. “Proteins from the prokaryotic nucleoid: primary and quaternary structure of the 15-kD Escherichia coli DNA binding protein H-NS”. In: *Molecular Microbiology* 2.3 (1988), pp. 323–329. doi: https://doi.org/10.1111/j.1365-2958.1988.tb00035.x (cit. on p. 86).

[251] Charles J Dorman, Jay C. D Hinton, and Andrew Free. “Domain organization and oligomerization among H-NS-like nucleoid-associated proteins in bacteria”. In: *Trends in Microbiology* 7.3 (1999), pp. 124–128. doi: 10.1016/S0966-842X(99)01455-9 (cit. on p. 86).

[252] David C. Grainger. “Structure and function of bacterial H-NS protein”. In: *Biochemical Society Transactions* 44.6 (Dec. 2016), pp. 1561–1569. issn: 0300-5127. doi: 10.1042/BST20160190 (cit. on pp. 86, 87, 100, 109).

[253] Taku Oshima et al. “Escherichia coli Histone-Like Protein H-NS Preferentially Binds to Horizontally Acquired DNA in Association with RNA Polymerase”. In: *DNA Research* 13.4 (Jan. 2006), pp. 141–153. issn: 1340-2838. doi: 10.1093/dnares/dsl009 (cit. on p. 86).

[254] Blair R. G. Gordon et al. “Structural basis for recognition of AT-rich DNA by unrelated xenogeneic silencing proteins”. In: *Proceedings of the National Academy of Sciences* 108.26 (2011), pp. 10690–10695. doi: 10.1073/pnas.1102544108 (cit. on p. 86).

[255] L. Qin et al. “The architects of bacterial DNA bridges: a structurally and functionally conserved family of proteins”. In: *Open Biology* 9.12 (2019), p. 190223. doi: 10.1098/rsob.190223 (cit. on pp. 86, 87, 100).

[256] Paul A. Wiggins et al. “Protein-Mediated Molecular Bridging: A Key Mechanism in Biopolymer Organization”. In: *Biophysical Journal* 97.7 (2009), pp. 1997–2003. doi: 10.1016/j.bpj.2009.06.051 (cit. on pp. 86, 101).

[257] Marc Joyeux and Jocelyne Vreede. “A Model of H-NS Mediated Compaction of Bacterial DNA”. In: *Biophysical Journal* 104.7 (2013), pp. 1615–1622. doi: 10.1016/j.bpj.2013.02.043 (cit. on pp. 86–88, 101).

[258] Chris A. Brackley et al. “Nonspecific bridging-induced attraction drives clustering of DNA-binding proteins and genome organization”. In: *Proceedings of the National Academy of Sciences* 110.38 (2013), E3605–E3611. doi: 10.1073/pnas.1302950110 (cit. on pp. 86–89, 91, 97, 100, 101, 109).

[259] Vittore F. Scolari and Marco Cosentino Lagomarsino. “Combined collapse by bridging and self-adhesion in a prototypical polymer model inspired by the bacterial nucleoid”. In: *Soft Matter* 11 (9 2015), pp. 1677–1687. doi: 10.1039/C4SM02434F (cit. on pp. 86–88).

[260] C A Brackley. “Polymer compaction and bridging-induced clustering of protein-inspired patchy particles”. In: *Journal of Physics: Condensed Matter* 32.31 (2020), p. 314002. doi: 10.1088/1361-648X/ab7f6c (cit. on pp. 87–89, 101, 109, 111).

[261] Clare P. Smyth et al. “Oligomerization of the chromatin-structuring protein H-NS”. In: *Molecular Microbiology* 36.4 (2000), pp. 962–972. doi: https://doi.org/10.1046/j.1365-2958.2000.01917.x (cit. on p. 88).

[262] Yunfeng Gao et al. “Charged residues in the H-NS linker drive DNA binding and gene silencing in single cells”. In: *Proceedings of the National Academy of Sciences* 114.47 (2017), pp. 12560–12565. doi: 10.1073/pnas.1716721114 (cit. on p. 89).

[263] Shusuke Ono et al. “H-NS is a part of a thermally controlled mechanism for bacterial gene regulation”. In: *Biochemical Journal* 391.2 (Oct. 2005), pp. 203–213. issn: 0264-6021. doi: 10.1042/BJ20050453 (cit. on p. 89).

[264] Yingjie Liu et al. “A divalent switch drives H-NS/DNA-binding conformations between stiffening and bridging modes”. In: *Genes & Development* 24.4 (Feb. 2010), pp. 339–344. url: http://genesdev.cshlp.org/content/24/4/339 (cit. on p. 101).

[265] Remus T. Dame, Maarten C. Noom, and Gijs J. L. Wuite. “Bacterial chromatin organization by H-NS protein unravelled using dual DNA manipulation”. In: *Nature* 444.7117 (2006), pp. 387–390. doi: 10.1038/nature05283 (cit. on p. 101).

[266] Ramon A van der Valk et al. “Mechanism of environmentally driven conformational changes that modulate H-NS DNA-bridging activity”. In: *eLife* 6 (2017). Ed. by Gisela Storz, e27369. issn: 2050-084X. doi: 10.7554/eLife.27369 (cit. on p. 101).

[267] Liang Qin et al. “Structural basis for osmotic regulation of the DNA binding properties of H-NS proteins”. In: *Nucleic Acids Research* 48.4 (Jan. 2020), pp. 2156–2172. issn: 0305-1048. doi: 10.1093/nar/gkz1226 (cit. on pp. 101, 109, 111).

[268] Min-Yeh Tsai et al. “Molecular Mechanism of Facilitated Dissociation of Fis Protein from DNA”. In: *Journal of the American Chemical Society* 138.41 (Oct. 2016), pp. 13497–13500. doi: 10.1021/jacs.6b08416 (cit. on p. 103).

[269] Ramsey I. Kamar et al. “Facilitated dissociation of transcription factors from single DNA binding sites”. In: *Proceedings of the National Academy of Sciences* 114.16 (2017), E3251–E3257. doi: 10.1073/pnas.1701884114 (cit. on p. 103).

[270] Fabio C. Zegarra et al. “Crowding-Induced Elongated Conformation of Urea-Unfolded Apoazurin: Investigating the Role of Crowder Shape in Silico”. In: *The Journal of Physical Chemistry B* 123.17 (May 2019), pp. 3607–3617. doi: 10.1021/acs.jpcb.9b00782 (cit. on p. 103).

[271] Vinícius G. Contessoto et al. “Small Neutral Crowding Solute Effects on Protein Folding Thermodynamic Stability and Kinetics”. In: *The Journal of Physical Chemistry B* 125.42 (Oct. 2021), pp. 11673–11686. doi: 10.1021/acs.jpcb.1c07663 (cit. on p. 103).

[272] B A Hamkalo and O L Miller. “Electronmicroscopy of Genetic Activity”. In: *Annual Review of Biochemistry* 42.1 (1973). PMID: 4581229, pp. 379–396. doi: 10.1146/annurev.bi.42.070173.002115 (cit. on pp. 107, 108).

[273] Selwyn Quan et al. “Transcriptional Polarity in rRNA Operons of Escherichia coli nusA and nusB Mutant Strains”. In: *Journal of Bacteriology* 187.5 (2005), pp. 1632–1638. doi: 10.1128/jb.187.5.1632-1638.2005 (cit. on pp. 108, 109).

[274] Bincy Lukose et al. “Molecular and thermodynamic determinants of self-assembly and hetero-oligomerization in the enterobacterial thermo-osmo-regulatory protein H-NS”. In: *Nucleic Acids Research* (Feb. 2024), gkae090. issn: 0305-1048. doi: 10.1093/nar/gkae090 (cit. on pp. 109, 111).

[275] Theodoros Pittas and Arnold J. Boersma. “Self-association of a nucleoid-binding protein increases with macromolecular crowding in Escherichia coli”. In: *bioRxiv* (2023). doi: 10.1101/2023.02.23.529735 (cit. on p. 109).

Glossary

23 S The 23 S ribosomal RNA in E. coli. 61, 107–109

16 S The 16 S ribosomal RNA in E. coli. 61, 107–109

5 S The 5 S ribosomal RNA in E. coli. 61, 107, 109

B-DNA Refers to the most common form of DNA in cells, characterized by a right-handed double helix structure with about 10.5 base pairs per turn and major and minor grooves that facilitate protein binding. 2

chromosome A long DNA molecule, decorated with various protein, contains some or entire genetic instructions in an organism. 1

eukaryote A unicellular or multicellular organism with a membrane-bound nucleus, multi-chromosome geonome, and membrane-bound organelles. 1

genome The entire set of genetic instructions in an organism. 1

operon A set of prokaryotic genes expressed for similarly-functioning proteins under the control of a shared promoter. 16

prokaryote A unicellular organism that lacks membrane-bound nucleus and other membrane-bound organelles. 1

quinary structure According to Vaĭnshteĭn, a combination of biomolecules, including proteins, nucleic acids, and nucleoproteins, forming a functional aggregation. There are two types of quinary structures: native, such as viruses, ribosomes, chromosomes, and membranes; and synthetic, such as planar monomolecular films, tubes, or crystals [48]. 10

slithering The motion of DNA as it moves along a stationary superhelical axis, which occurs in plectonemically supercoiled DNA. It is also described as a 'conveyor-belt' movement [5]. 15

transertion The association of chromosome loci encoding membrane proteins with the inner cell membrane during the coupled events of transcription, translation, and membrane insertion. 16